SKIPSTEKNISK AVDELING – NORGES TEKNISKE HØGSKOLE
UNIVERSITETET I TRONDHEIM

DEPARTMENT OF MARINE TECHNOLOGY - THE NORWEGIAN INSTITUTE OF TECHNOLOGY
THE UNIVERSITY OF TRONDHEIM

report

UR-83-34

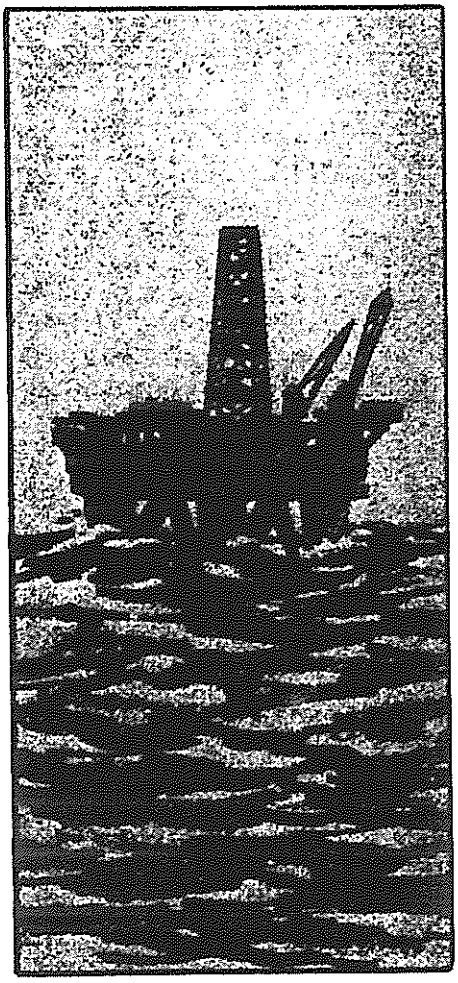

Energy absorption in ship-platform impacts

BY
JØRGEN AMDAHL
DIVISION OF MARINE STRUCTURES

MARINTEKNISK SENTER
MARINE TECHNOLOGY CENTRE
TRONDHEIM, NORWAY

Publications from
The Department of Marine Technology
The Norwegian Institute of Technology

UR-83-28 Utviklingsplan for Marinteknisk avdeling, NTH.

Division of Combustion Engines and Marine Engineering

UR-80-06 Analysis of stationary and transient heat conduction by the use of the finite element method. Dr.Ing.Thesis. By Nils Sandsmark.
UR-80-08 Methods for material response calculation and life prediction of thermally loaded engine components. By Odd Tore Saugerud.
UR-81-11 Fatigue life prediction on thermally loaded engine components. Dr.Ing.Thesis. By O.T. Saugerud.
UR-80-12 Thermal barriers in combustion engine cylinders. Part I - Four stroke diesel engines. By Harald Valland and Grzegorz K. Wyspianski.
UR-80-13 Thermal barriers in combustion engine cylinders. Part II - Two stroke diesel engines. By Harald Valland and Grzegorz K. Wyspianski.

Division of Marine Hydrodynamics

UR-82-18 Ocean wave groups. Dr.Ing.Thesis. By Henrik Rye.

Division of Marine Structures

UR-79-01 The finite element method used in a fatigue evaluation of fixed offshore platforms. Dr.Ing.Thesis. By Brigt Hatlestad.
UR-79-02 Analysis and design of cellular structures. Dr.Ing.Thesis. By Erik Pettersen.
UR-79-03 Finite difference and finite element methods applied to nonlinear analysis of plated structures. Dr.Ing.Thesis. By Sverre Valsgård.
UR-79-04 Finite element collapse analysis of structural members considering imperfections and stresses due to fabrication. Dr.Ing.Thesis. By Nils T. Nordsve.
UR-79-05 Analysis of towline forces in ocean towing systems. Dr.Ing.Thesis. By Ivar J. Fylling.
UR-80-09 Analysis of uncertainties related to the stochastic modelling of ocean waves. Dr.Ing.Thesis. By Sverre Haver.
UR-81-15 On the strength of welded ring stiffened cylindrical shells primarily subjected to axial compression. Dr.Ing.Thesis. By Jonas Odland.
UR-82-17 Analysis of uncertainties in the fatigue capacity of welded joints. Dr.Ing.Thesis. By Knut M. Engesvik.
UR-83-30 On cumulative fatigue damage in steel welded joints. Dr.Ing.Thesis. By Oddvar Inge Eide.
UR-83-33 Stochastic time domain analysis of slender offshore structures. Dr.Ing.Thesis. By Olav Mo.
UR-83-34 Energy absorption in ship-platform impacts. Dr.Ing.Thesis. By Jørgen Amdahl.

Division of Marine System Design

UR-80-07 Motstandsutrekning for kolmuletrål. By Atle Kalve.
UR-81-10 Prosjektering og konkurranse. By Stian Erichsen.
UR-81-14 Temperature distribution in the workpiece by welding. By O. Westby.
UR-81-16 Brukerbeskrivelse for DEFDEL. Generering av 2- og 3-dimensjonale produkter og/eller deler ved hjelp av grafisk databehandling. By Alf E. Pedersen.
UR-82-19 Marine traffic and platform collision risk. By Svein Kristiansen.
UR-82-20 Modell for analyse og valg av marked. By Bjørn Baggerud og Harald Ellingsen.
UR-82-21 Demonstrations and exercises in CAD/CAM of ships and platforms. By Ola Westby.
UR-83-22 Populær beskrivelse av CAD-systemet ODIN. By B. Baggerud and O. Westby.
UR-83-23 EDB for skipstekniske beregninger. Oversikt over programsystemer og kontakter innen NSFI/NTH-miljøet. By H. Ellingsen and E. Næstvold.
UR-83-24 Teoretisk og eksperimentell analyse av pelagisk trål. Dr.Ing.Thesis. By Terje Gustafson.
UR-83-25 PROJECTMAN. EDB-hjelpemiddel for prosjektstyring. By Jan O. Bakkland, Inge M. Ofstad and Ola Westby.
UR-83-26 Bruk av EDB ved prosjektering av marine systemer. By Harald Ellingsen.
UR-83-27 Datamaskinassistert konstruksjon og produksjon innen verftsindustrien. By Bjørn Baggerud.
UR-83-29 Hurtiggående kystfiskefartøy - en fiskerifaglig og skipsteknisk analyse. Dr.Ing. Thesis. By Halvard Aasjord.
UR-83-31 Fotogrammeri på marine konstruksjoner - Sluttrapport. By Bjørn Aage Østbye.
UR-83-32 Fotogrammeri på marine konstruksjoner - Systemdokumentasjon. By Bjørn Aage Østbye.

ENERGY ABSORPTION IN SHIP-PLATFORM IMPACTS

by

Jørgen Amdahl

Trondheim, September 1983

Division of Marine Structures
The University of Trondheim
The Norwegian Institute of Technology

CONTENTS

PAGE

ABSTRACT

The report deals with analysis of impacts between supply vessels and offshore structures. In particular two areas are studied, namely; energy dissipation in ship's bow and stern structures and the deformation behaviour of tubular bracings.

Various mechanisms of energy dissipation in a ship structure subjected to collision loads are identified and described. It is shown that simple closed form solutions can be obtained for such mechanisms, termed basic elements, applying the kinematic methods of plasticity. Analytic solutions are compared with experiments on single elements.

The ship cross-section is considered as an assemblage of basic elements. The total load-deformation relationship is found by adding the contribution to the energy dissipation from all elements. For verification of the theoretical procedure a fairly comprehensive test series is carried out with simplified models of ship structures, including sections of normal bow, ice-strengthened bow, bulbous bow and stern structure. Comparisons are also made with results from a number of similar tests published in the literature.

Finally, design curves are proposed for bow and stern impacts with supply vessels. The predictions are compared with present design curves recommended by Det norske VERITAS.

As to analysis of tubular bracings various modes of energy dissipation are described. Main emphasis is put on assessment of the load-carrying capacity in the beam mode of deformation accounting for the detrimental effect of local indentation. Analytic solutions based on plastic theory are presented along with calculations by a simple finite element beam program which accounts for non-linear geometry and strain hardening. Theoretical predictions are compared with experiments on scale models of brace members. Two idealized boundary conditions are simulated; fully restrained against axial displacement and axially free ends. The different effects on the deformation behaviour are clearly observed.

ACKNOWLEDGEMENT

This study has been made possible by scolarships from the Norwegian Institute of Technology.

The work has been carried out under the supervision of Professor Tore H. Søreide, to whom the author wishes to express his deepest gratitude. A major part of the experimental programme has been funded by participation in a VERITAS research project sponsored by Amoco Norway Oil Co., ESSO Expl. and Prod. Norway Inc., A/S Norske Shell, NTNF and Det norske Veritas. Grants by Anders Jahres fond til vitenskapens fremme and NIF's jubileums-fond av 1974 are also acknowledged.

The project leader at VERITAS, Helge Kjeøy, is most sincerly thanked for his kind support and cooperation during the study.

Thanks are also extended to Reijo Äyhynmäki and Hilfred K. Rønning for excellent fabrication of test specimens and to the laboratory staff for execution of experiments. Guri Berge is thanked for preparation of figures.

NOTATION

A_i = coefficient for energy term

C = flange width of basic element

C_1, C_2 = coefficients in Minorsky's equation

C_p = plate buckling coefficient

C_z = buckling coefficient for curved panel

C_{eu} = buckling augmentation factor for elliptical cylinder

D = diameter

D_s = height of ship side

E = Young's modulus

E_a = total absorbed energy in Minorsky's equation

E_i = internal energy dissipation

E_e = external work

F = cross sectional area

F_c = contact area

H = half folding wave length

L = total length of flanges

M_o = plastic moment capacity of unit plate strip

N_o = axial yield load of unit plate strip

P = axial load

P_{av} = average crushing load

P_{max} = maximum crushing load

R = radius of curved panel

R_s = radius of stern end

R_T = resistance factor in Minorsky's equation

R_c = radius of column

V = rate of deformation

V_H = horizontal velocity for basic element

V_t = tangential velocity for basic element

$V_x\ V_y\ V_z$ = displacement rates in a cortesian coordinate system

Z	=	Batdorf parameter
a	=	panel length
b	=	panel width
b_e	=	effective width
c	=	constant for dynamic flow stress
g	=	number of cuts and flanges
h	=	plate thickness
h_s	=	thickness of skin plates
h_w	=	web height
i	=	iteration number
k	=	angle coefficient
k_s	=	coefficient for energy contribution
l	=	stiffener spacing
m	=	constant for maximum load
n	=	constant for dynamic yield stress
$n_A n_T n_C$	=	number of angles, T-sections and cruciforms in a composite structure
q	=	constant for average dynamic flow stress
r	=	rolling radius
r_s	=	final radius of stationary hinge
t	=	time
u, v, w	=	displacement components parallell to x,y,z-axis
x, y, z	=	Cartesion coordinates
α	=	rotation angle for basic element
β	=	plate slenderness factor
γ	=	angle in basic mechanism
δ	=	deformation, indentation
δ_H	=	horizontal displacement
δ_o	=	maximum/reference indentation

δ_{eff} = reduced deformation

ε = strain

ε_{av} = average strain

ε_o = reference strain

$\emptyset_o$ = circumferential angle on toroidal surface

Θ = meridional coordinate for toroidal surface

κ = curvature

κ_{av} = average curvature

$\bar{\lambda}$ = reduced slenderness ratio

μ = coefficient for maximum load

ν = Poisson's ratio

σ = stress

σ_{av} = average stress

σ_E = Euler buckling stress

σ_{max} = maximum stress

σ_u = ultimate stress

σ_y = yield stress

σ_y^1 = dynamic yield stress

σ_0 = flow stress

σ_0^1 = dynamic flow stress

ϕ = reduction factor for elasto-plastic buckling

ψ = semi-angle between flanges of basic element

ω = semi-vertex angle for cone

$\dot{\bullet}$ = differentiation with respect to time

Subscripts:

b = buckling

m = membrane

1. INTRODUCTION

1.1 General

Ship collisions against platforms have been identified as one of the major hazards to oil exploration and production offshore. Potential consequences may vary from minor structural damages to major damages where the structural integrity of the platform is threatened, production downtime, pollutions, and which in its ultimate state, may result in the loss of numerous human lives.

Indeed, a large number of ship-platform collisions have occurred worldwide, some with serious consequences. Fortunately, the collisions experienced in the North Sea so far have mainly resulted in minor damages. However, the costs associated with repair as well as some few more serious incidents and some near-misses have made designers increasingly aware of the need to design for accidental loads from ship impacts.

Ship impact loads did also gain recognition in design codes. However, specific methods for estimating the frequency of occurrence as well as the degree of structural damages were not given. In fact, the detailed data and methods for collision analysis were not available.

On this background VERITAS launched the research project "Impacts and Collisions Offshore" in 1977. This was originally sponsored jointly by NTNF and VERITAS and was continued as a joint industry research project in 1980. The objective of the project was given as follows /1/:

> "To provide a rational and systematic foundation for a safe design against collisions and impact loads."

In order to achieve this objective the project was organized into five part projects:

i) Probability of Collisions
ii) Energy Absorption and Deformation of Ships
iii) Impact Capacity of Concrete Platforms
iv) Impact Capacity of Steel Platforms
v) Design Criteria for Impact Loads

The present work relates to item ii) Energy Absorption and Deformation of Ships and item iv) Impact Capacity of Steel Platforms

In the first phase of the project a computer program was developed for analysis of the force-deformation characteristics of ships in sideway collisions with rigid, circular columns (2,3). However, the need for corresponding information as to bow-and stern impacts was recognized at an early stage. Thus, it was decided to carry out a comprehensive experimental program on scale models of ship's bow and stern structures along with development of theoretical calculation methods. The execution of these tasks have been assigned to the Division of Marine Structures, NTH in Trondheim in the form of a dr.ing.study.

The present report summarizes the experimental results, describes the theoretical approach and presents application of the theory to actual impact cases.

The work on energy absorption of steel platform brace members has not been an integral part of the Veritas project but has been financed by University funds. However, also in this case there has been a close cooperation between the University and Veritas; results have been mutually available so that unnecessary parallel work has been avoided.

1.2 Design Against Collision

In the following is given an extract of the rules and guidelines for design against collisions as laid down by Det norske VERITAS, Ref. /4-6/.

In a complete safety evaluation the entire spectrum of collision events should be considered, the probabilities and consequences associated with it should be assessed and compared with given acceptance criteria. The fulfilment of the acceptance criteria may be obtained by the principles of:

- Reduction of Probability
- Reduction of Consequence

The above principles may be achieved by

- Event Control
- Indirect Design
- Direct Design

Event Control relates to measures taken to reduce the probability such as operational procedures, manoeuvrability standards, traffic regulations, field lay-out etc.

Indirect Design relates to general measures taken to improve the resistance of the structure without directly considering the loads in question. For impact loads the structure is to absorb a certain amount of impact energy rather than transfer of a specific load. Energy absorption requires the structure to behave in a ductile manner.

Measures to obtain adequate ductility are:

- Connections of primary members to develop a strength in excess of that of the member

- Provide redundancy in the structure so that alternative load distributions may be developed

- Avoid dependency on energy absorption in slender struts with a non-ductile postbuckling behaviour

- Avoid pronounced weak sections and abrupt change in strength or stiffness

- Non-brittle materials

In direct design, so-called design collision events are used as the basis for the analysis. Normally two levels of impact loads are considered:

i) An operational impact load caused by a supply boat when approaching or leaving the structure. The impact velocity is assumed to be 0.5 m/sec.

ii) An accidental impact load caused by a supply boat out of control drifting against the structure. The impact velocity is to be taken as

$$V = 0.5\ H_S \text{ (m/sec.)}$$

where H_S is the maximum significant wave height for servicing the structure. For North Sea conditions the accidental impact velocity should not be asssumed less than 2.0 m/sec.

In both cases the impact loads should be calculated for the maximum authorized vessel assumed to service the installation, normally not less than 5000 tonnes displacement in the North Sea.

The calculations of the impact loads should be based on energy distribution between boat, structure and possible fendering system. The energy absorption in the boat should be based on force-indentatiaon characteristics for the assumed point of impact.

The design collision effects are to be assessed as follows:

The ultimate limit state (ULS) corresponding to the maximum load carrying capacity is to be checked for given combinations of:

P - Permanent loads
L - Live loads
D - Deformation loads
E - Environmental loads
A - Accidental loads

and using relevant load and material coefficients.

An operational ship impact load should be assumed as a live load.

The limit state of progressive collapse is to be checked for the most unfavourable combination of P - Permanent loads, L - Live loads, D - Deformation loads, E - Environmental loads and A - Accidental loads. For accidental loads of the impact type (e.g. collisions, dropped objects) loads of the type E may be ignored. For this check, which may be based on a simplified analysis, all load coefficients may be taken equal to unity. Localized damage may be accepted, but is not to be disproportionate to the original cause.

1.3 Aim of Present Study

The aim of the present study is to identify and describe mechanisms of energy dissipation in ship's bow and stern structures as well as brace members in steel platforms subject to collision by carrying out experiments with scale models. The cases to be studied are:

- Bow impact against a rigid, plane barrier
- Stern impact against a rigid circular column
- Bow impact against a brace member
- Brace member subjected to a point load through a rigid indenter

On this background theoretical calculation models for the energy dissipation will be developed and compared with experimental results. The analysis of ship structures is based on simple closed form solutions applying the kinematical methods of plasticity. For brace members a comparative study is performed between simple analytic solutions and a non-linear finite element beam computer program.

The ultimate goal is as follows:

- Develop a general method to assess the average crushing load of composite structures with particular application to ship bows

- Predict force-indentation curves for supply vessel bow-and stern structures in collision with a rigid tower

- Investigate the interaction between a horizontal bracing of a jacket and a supply vessel bow in a collision

- Verify a computer program for analyzing the force-deformation behaviour of a platform bracing

In chapter 2 the present study is put into perspective by presenting a brief review of various approaches to analysis of energy absorption in ship and platform structures. No extensive literature review is given; instead some of the most important works are considered.

Chapter 3 contains some topics from fundamental continuum theory relevant to analytic calculations of elements undergoing very large deformations. In particular the concepts of a stationary and a moving hinge line are introduced.

From the structural points of view, the ship cross-section can be considered as an assembly of basic elements. In chapter 4 the crushing mechanics of various basic elements are studied. Introducing simple displacement and velocity fields closed-form solutions for the average crushing force are derived and compared with own tests or results published in the literature. Dynamic effects are also dealt with to some extent.

In chapter 5 the crushing resistance of integrated ship structures are developed based on the deformation characteristics of each individual basic element. The expression for a bow section is shown to depend on two free parameters which are determined by minimization.

Various levels of energy dissipation in a steel jacket subjected to ship impact are identified in chapter 6. Alternative techniques for analyzing the beam mode of deformation are described taking into account the detrimental effect from local denting on the beam section modulus.

Chapter 7 contains details from a series of static tests on simplified models of ship structures such as general bows, bulbous bows, ice-strengthened bow in collision with platform bracing and stern section. Test results are compared along with theoretical predictions. Comparisons are also performed with data from tests carried out at other institutions.

Based on the experience obtained during the comparative study, the theory developed is applied to full scale ship structures in chapter 8. Load deformation characteristics representative of offshore supply vessels are derived for the case of bow and stern impact with a rigid structure (concrete shaft) and bow-bracing impact. Suggestions for design curves are presented along with comparisons with present design loads.

In chapter 9 static and dynamic experiments with models of platform bracing are described. Comparisons between theory and experiments are also included.

Finally, conclusions and suggestions for further work are given in chapter 10.

2. LITERATURE REVIEW

2.1 Energy Absorption in Ships

One of the first studies in the area of ship collisoin damage assessment was carried out by Minorsky /7/ who developed an empirical relationship between the volume of damaged material and the amount of energy absorbed, based on investigations of a number of real collisions. The formula is very simple, but is yet crude and unreliable for minor impacts.

Most of the research has been carried out in connection with the construction of nuclear powered ships /8,9/. However, the main emphasis has been on experimental verification of the protective structures of the reactor compartment and few attempts have been made to develop analytical tools on a fundamental basis. In recent years a considerable number of experiments with relatively large scale models has also been carried out, particularly in Japan, for the purpose of evaluating low-energy collisions of ships carrying hazardous cargo and ship collisions with bridge piers /10,11,12/. Along with the tests numerical and analytical techniques are developed.

Some investigators have considered the maximum compressive strength of integrated structural elements using e.g. the semi-empirical approach suggested by Gerard /13/. Although the initial buckling phase may be decisive with regard to subsequent deformation pattern, it is realized that the elastic or elasto-plastic energy dissipation is of minor significance as compared with the energy dissipated in the plastic regime.

Plastic analysis combined with construction of yield line mechanism has proved useful in many applications. Studies of the crushing behaviour of simple strength components, e.g. tubes of circular and rectangular cross-sections have served widely as a basis for impact design in the space, aircraft and automobile industry. A number of the most important papers are listed in Ref. /14/.

In the United States an ambitious plan to conduct large and full scale ship collision tests has been prepared for the U.S.Coast Guard /15/. Unfortunately, it was decided to put this project on the shelf, presumably due to the high costs involved. Prior to the development of this test plan a comprehensive literature review on the subject of ship collision damage

assessment was undertaken /16-18/. Thus, such a review will not be repeated. Instead, the present work will be put into perspective by giving a brief description of the most important and widely used methods.

2.1.1 The Semi-Empirical Approach proposed by Minorsky

A widely used method is the semi-empirical approach proposed by Minorsky /17/ based on investigations of a number of actual ship collisions reported to the U.S. Coast Guard.

It is assumed that most of the energy is absorbed plastically. Applying fundamental principles of impact mechanics a relationship is developed between the strain energy absorbed during collision, and ship displacement, speed of striking ship along with added mass of struck ship assumed to be 40% of its displacement.

A linear relationship was found to exist between the energy absorbed, E_a, and a resistance factor, R_T, which represents the volume of damaged material in the ships.

$$E_a = C_1 R_T + C_2 \qquad (2.1)$$

This comprises members having depth in the direction of penetration such as decks, flats in both ships, longitudinal bulkheads of striking vessel and a longitudinal component of the shell of the striking ship (normally assumed at 0.7 of shell area).

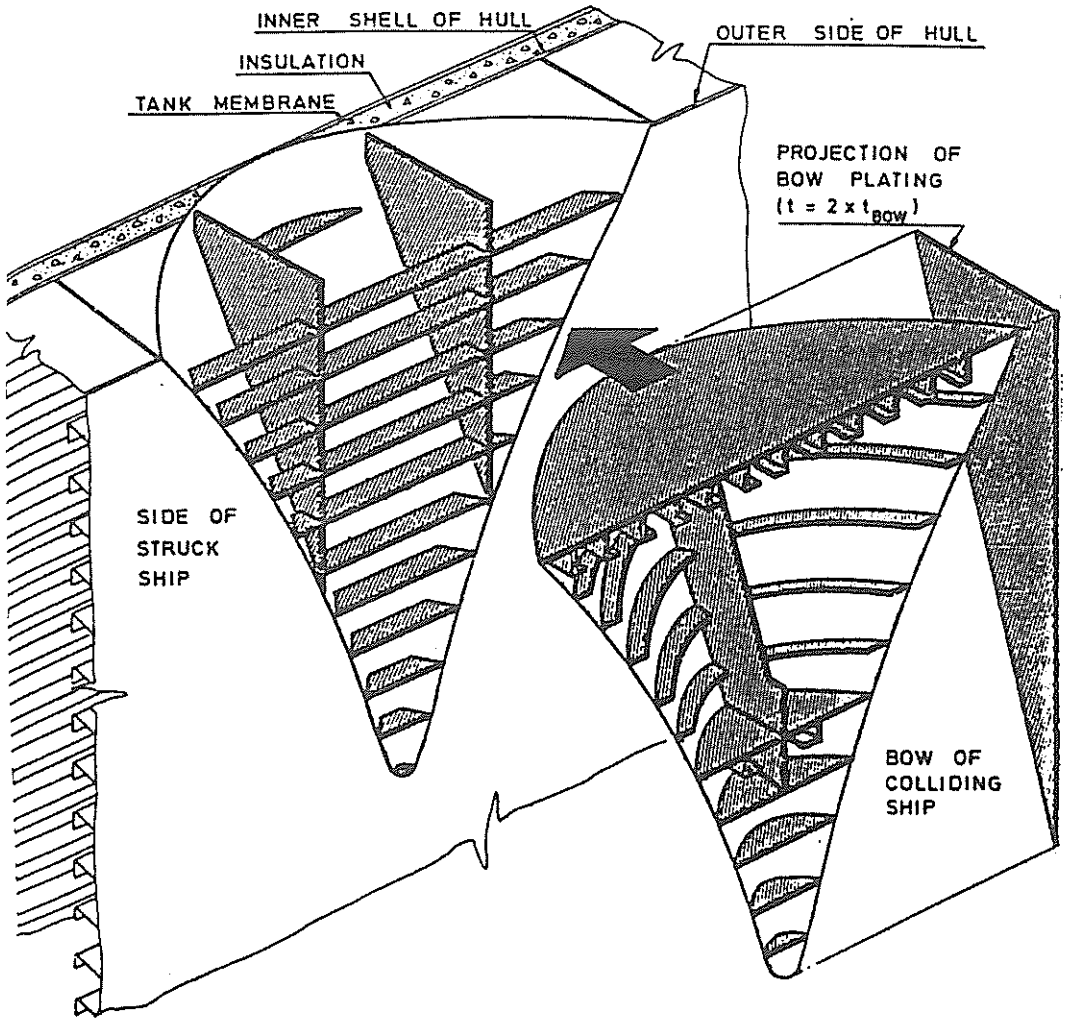

Fig. 2.1 Damaged volume included in the resistance factor.

The definition of damaged volume is illustrated by Figure 2.1. The calculated R_T was increased by 33% to allow for the forward speed of the struck vessel.

The empirical correlation between the resistance to penetration and energy absorbtion is shown in Fig. 2.2.

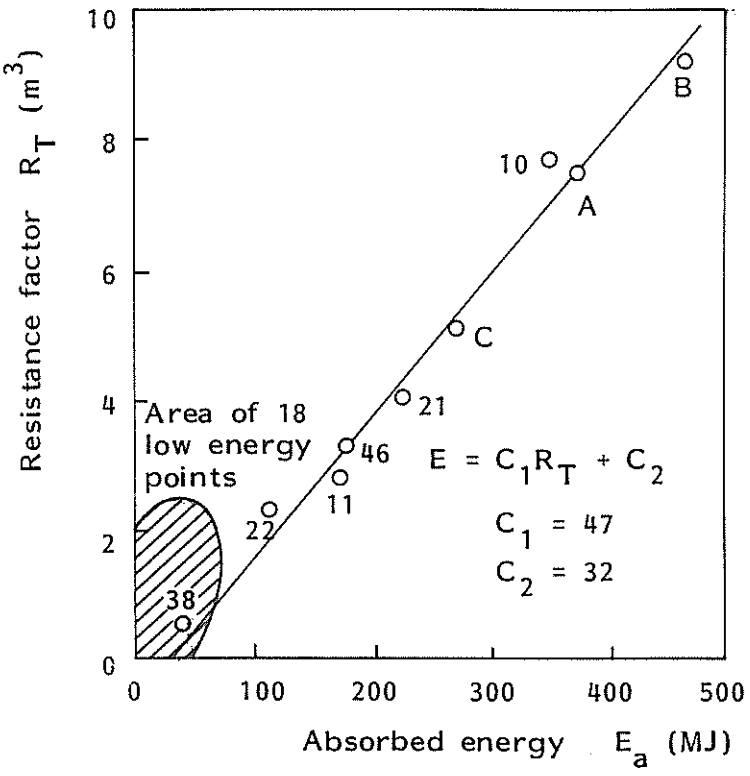

Figure 2.2 Correlation between energy absorbed in collision, and volume of damaged material according to Minorsky /7/ (Actual collisions plotted)

A significant scatter exists in the low energy region where generally more damage is done than predicted by the method. It was suggested that this stems from the fact that the pilots tend to underestimate their speeds for low speed impacts.

It is important to keep in mind that Minorsky's investigation is made of ships probably built between 1940 and 1955. A number of changes in ship design has emerged since then, e.g. relative softening of the bow structures. At the time the paper was released, 1958, the bow structures were relatively stiff and consequently more damage occurred to the struck ship. A soft bow may be deemed to absorb most of the collision energy. In this case the damage to the struck ship will be overestimated by Minorsky's method. This has been confirmed by model tests /19/. Despite its inherent weakness this easily applied method has been widely accepted. It is particularly useful for conventional ships where the side protection is of the absorbent type.

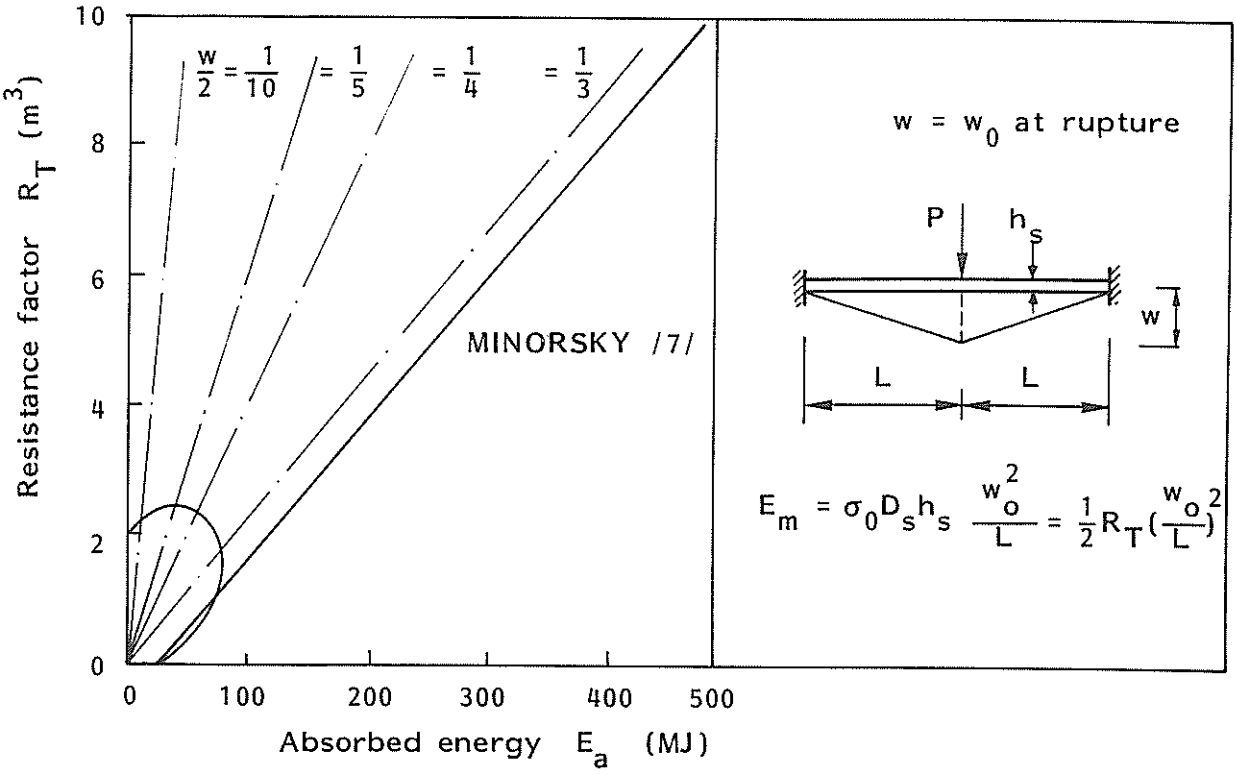

Figure 2.3 Influence from membrane forces on energy absorption

The shell plating of the struck ship is not included in the resistance factor R_T. In minor collision the side plating may contribute significantly to the energy absorption by membrane deformation to the point of rupture. An approximate method to account for this effect is suggested in Refs. /16,18/. The energy dissipated in the side plating is estimated utilizing the load-deflection curve in the membrane-phase for a rigid-plastic beam. A basic assumption is the limit displacement at rupture. In Fig. 2.3 different curves are plotted for various amounts of maximum displacement. The significance of determining this parameter is demonstrated. A family of curves radiates from the origin traversing the entire area of low energy collisions. Evidently, some of the scatter in this region originates from the uncertainty as to the energy absorbed by the side of the struck ship.

Another modification of Minorsky's method has been proposed by Woisin /20/. The membrane effects are taken care of by substituting the constant in Eq. (2.1) with

$$C_2^1 = 5000\ \Sigma D_s h_s^2 \qquad (2.2)$$

where

D_S = height of broken or heavily deformed side shell plating and possibly distorted longitudinal bulkhead

h_S = thickness of plating

This expression differs from that of Fig. 2.2 by the quadratic dependency on the plate thickness rather than the more natural linear relationship.

2.1.2 Approximate Low-Energy Collision Damage Theories

M. Rosenblatt and Son Inc. /21,22/ conducted a series of studies during the period 1971-75 intended to develop a methodology for the analysis of minor collisions in which the struck ship was a tanker. A similar approach is also used in a later work by T. Hysing /2/. A brief outline of the latter method is given below.

An array of assumptions are involved such as

- The collision bodies are at right angle
- A static deformation process is assumed
- The bow of the striking ship is considered infinitely stiff
- The indentation of the hull is constant over the height of the ship and longitudinally symmetric with respect to the incursion line
- The energy is completely absorbed as plastic deformation energy
- Cutting and puncturing of the side shell of the struck ship does not occur

The principal idea of this calculation scheme is illustrated by Fig. 2.4 showing the collapse model for the ship side.

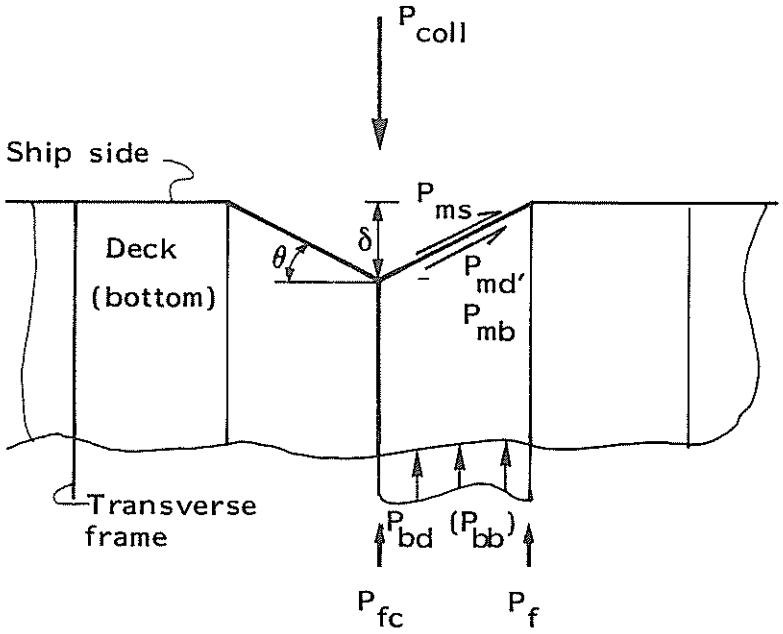

Figure 2.4 Collapse model for ship side

Initially, only the part of the hull between the incursion line and the neighbouring transverse frames is considered to be affected by the distortion of the hull. The collision load is calculated for selected indentations of the ship's side and is in static equilibrium with the membrane tension force in the side, deck and bottom (P_{ms}, P_{md}, P_{mb} respectively) and the plastic bucking load of the deck, bottom and frames (P_{bd}, P_{bb}, P_{bf} respectively).

$$P_{coll} = 2\{P_{ms}\sin\theta + (P_{md} + P_{mb})\sin\theta + (P_{bd} + P_{bb}) + P_{bf}\} \qquad (2.3)$$

The reaction force at the neighbouring transverse frame at the end of the collapse model is

$$P_f = (P_{ms} + P_{md} + P_{mb})\sin\theta \qquad (2.4)$$

If the reaction force P_f is less than the buckling load of the frame, P_{fc}, the calculations are repeated with an increased indentation of the side. Otherwise, the collapse model is extended with two more frames, and the deformations at the buckled frame and the corresponding impact load of the revised collapse model are derived. In a similar manner the load-deformation

relationships can be elaborated for a collapse model involving an increasing number of buckled frames. Due to bending and tension of the shell plating, rupture of the side occurs at a particular indentation. Beyond this limit membrane forces of the ship's side are neglected.

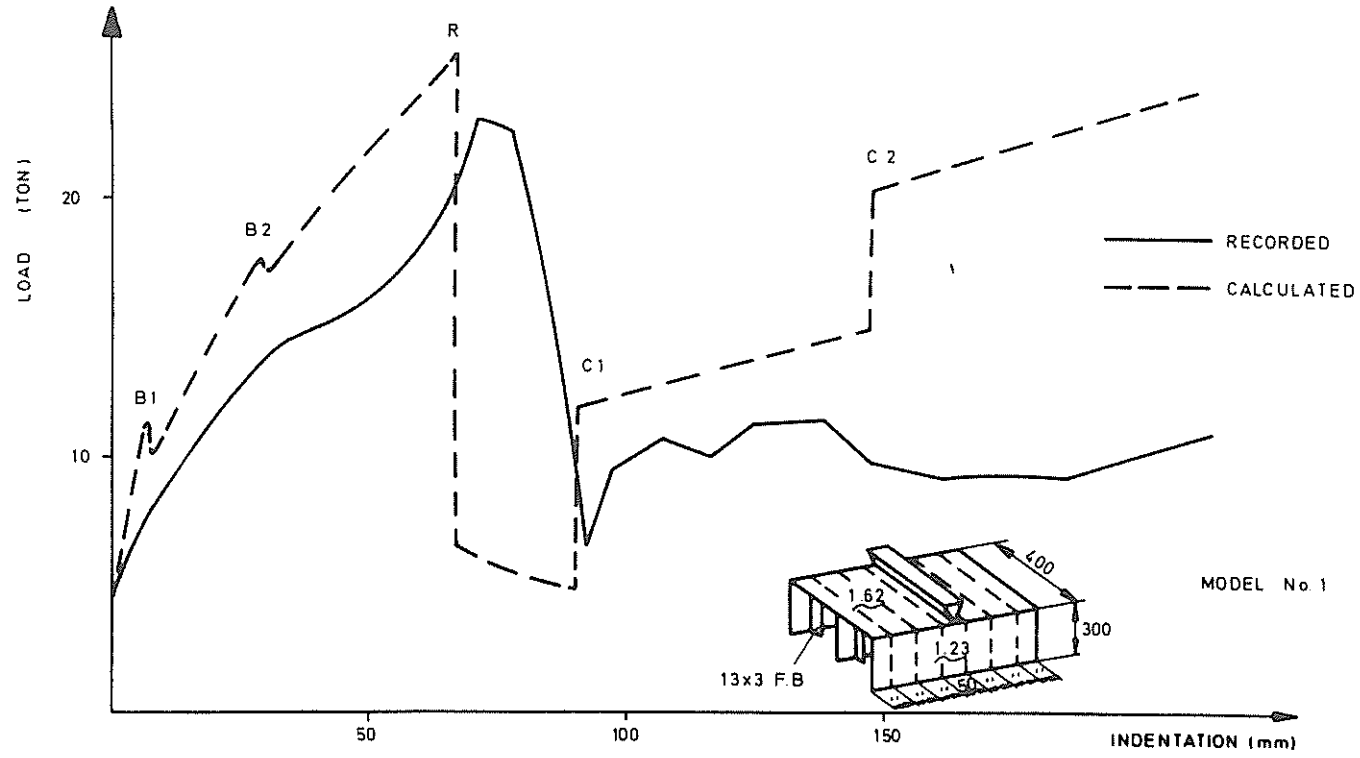

Fig. 2.5 Load-deformation relationship for side model

Fig. 2.5 shows a comparison between the theoretical prediction and the load-indentation relationship recorded in a test with a small-scale model of a ship side /9/. A considerable drop of the load is caused by rupture of the side plating.

Owing to the large contribution to the load carrying capacity from the membrane forces developed in the side plating it is of vital importance to establish a rational rupture criterion. The actual approach depends naturally on the complexity of the calculation procedure. For the present model an average tensile strain limit of 10-30% has been used extensively.

It has been argued /23/ that the rupture strain is highly scale dependent and will be much smaller for real ships. A fracture mechanics approach indicates an average strain limit of the order of 1-2 percent in welded ship plate materials.

2.1.3 Gerard's Method

Ultimate Strength of Compression Panels

A widely used semi-empirical method of calculating the ultimate load of sheet metal structures is due to Gerard /13,24,25/. The method was originally developed for aircraft structures but has found application in automobile /26/ and ship /27,28/ engineering. The method postulates that the maximum strength is a function of the plate slenderness ratio defined as

$$\beta = \frac{b}{h}\sqrt{\frac{\sigma_y}{E}} \tag{2.5}$$

so that

$$\frac{\sigma_{max}}{\sigma_y} = \mu \left(\frac{1}{\beta}\right)^m \tag{2.6}$$

where b and h are width and thickness of element considered, σ_y is the compressive yield stress and E is Young's modulus.

The constants μ and m are subject to fitting with experimental data. A clear distinction is made between elements where unloaded edges remain straight during postbuckling and those where the unloaded edges are free to warp in the plane of the plate. For straight edges a best fit was obtained with

$$\mu = 0.67, \quad m = 0.40 \tag{2.7}$$

and for distorted edges

$$\mu = 0.56, \quad m = 0.85 \tag{2.8}$$

Complex members belong to the first category (straight edges) if two or more flanges meet at a common junction and to the second group (distorted edges) when only two elements meet at a junction. A generalization of Eq. (2.6) is made by substituting the width to thickness ratio by

$$\frac{b}{h} = \frac{A}{2h^2} = \frac{A}{gh^2} \tag{2.9}$$

which gives

$$\frac{\sigma_{max}}{\sigma_y} = \mu g \left(\frac{gt^2}{A}\sqrt{\frac{E}{\sigma_y}}\right)^m \qquad (2.10)$$

As illustrated in Fig. 2.6 ,g represents the number of flanges and cuts required to reduce the section to a series of flange elements. The virtue of this scheme is that the results of several tests are reduced to a single equation for the ultimate load.

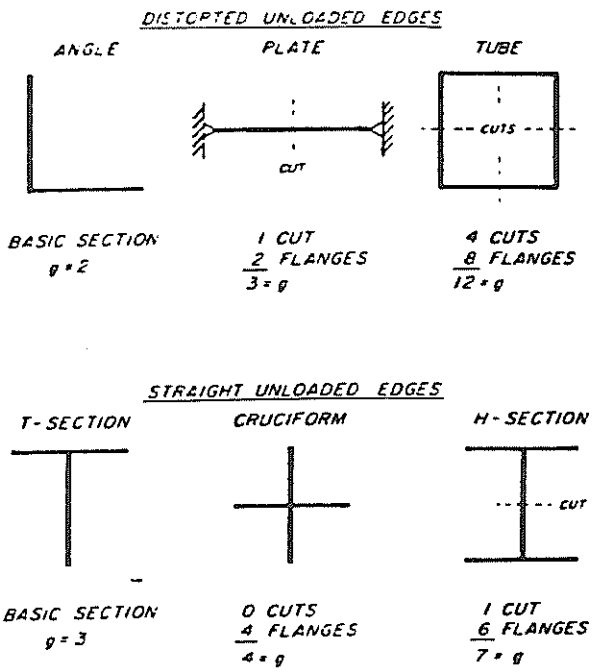

Fig. 2.6 Determination of the g - factor for simple elements.

Eq. (2.10) applies also to stiffened panels and built-up cross-sections with different thicknesses and yield strength provided that a weighting factor is introduced. The thickness effect is often sufficiently accounted for by the modified equation

$$\frac{\sigma_{max}}{\sigma_y} = \mu g \left(\frac{gt_s t_w}{A}\sqrt{\frac{E}{\sigma_y}}\right)^m \qquad (2.11)$$

where t_s and t_w are thickness of the skin and stiffener, respectively.

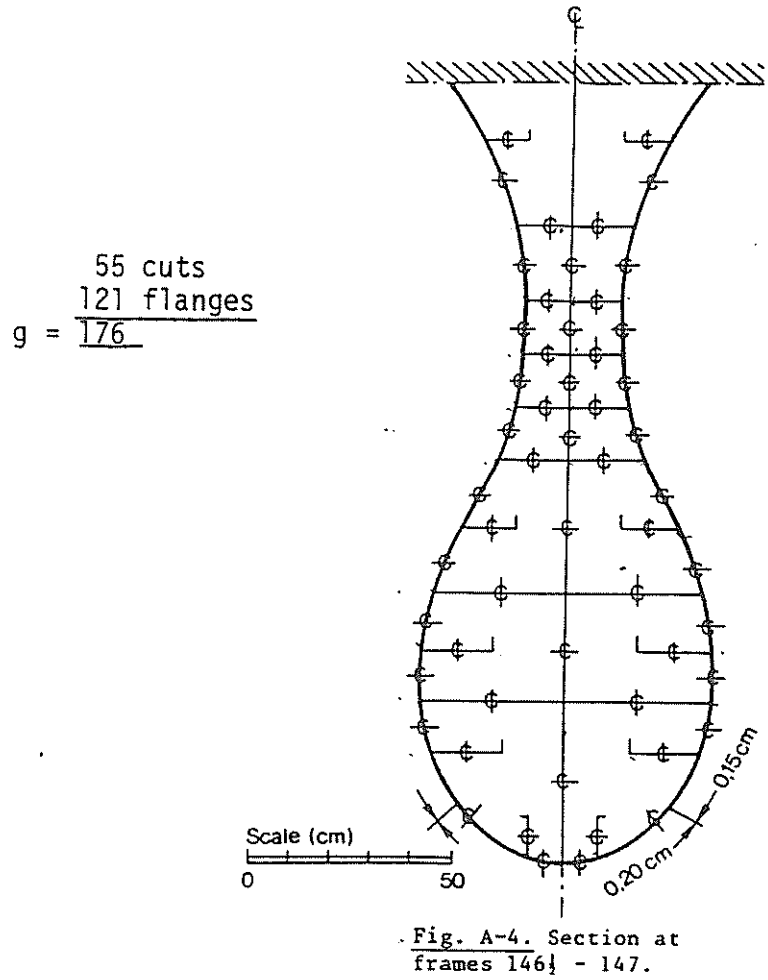

Figure 2.7 Determination of the g-factor for a tanker model cross-section /28/

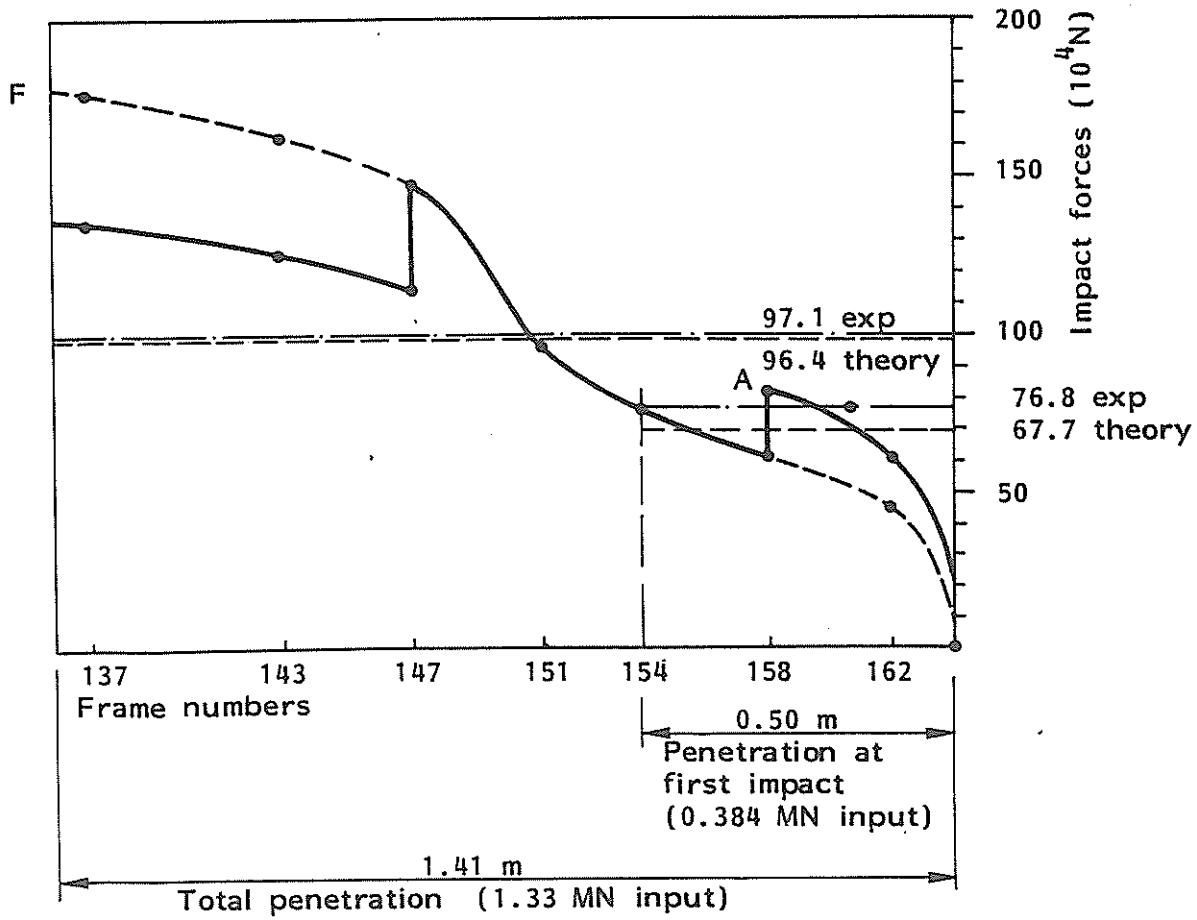

Figure 2.8 Load-penetration curve for bow model test of GKSS /28/

Eq. (2.11) with constants pertaining to distorted edges (Eq. (2.8)) has been used in several occasions to assess the crushing resistance of ship bows. In Fig. 2.7 the g-correlation scheme is shown for a frame section of the model of a 195.000 dwt tanker which was tested by GKSS /28/. The calculated impact force - penetration relationship is plotted in Fig. 2.8. Unfortunately, there are no valid experimental data to compare with the calculated values. However, the average impact force in the two consecutive tests can be obtained from the impact energy and penetration depth.

Gerard's approach is intended for the maximum strength only. Hence, it is amazing to observe the good agreement between the experimental results and the theory. The average crushing resistance should be considerably lower, especially because panels located some distance from the bow will not experience the idealized boundary conditions during failure. However, this may be counteracted by various effects such as strain rate, strain hardening, limited compressibility etc. Furthermore the strength prediction is throughout based on the formula for distorted unloaded edges while several joints in an actual cross-section will be of the cruciform and T-section type.

2.1.4 Model Collision Tests

The introduction of nuclear powered merchant vessels made the need for development of satisfactory collision-protective systems for the reactor plant. In the period from 1967 to 1976 Gesellschaft für Kernenergieverwertung in Schiffbau und Schiffahrt mbH, GKSS conducted a series of 12 collision tests at the shipyard Deutsche Werft in Hamburg /7/. Each test simulated the impact from a true-to-detail model of a ship bow structure perpendicular to the protective structure of the side model. The scale was 1:7.5 and 1:12.

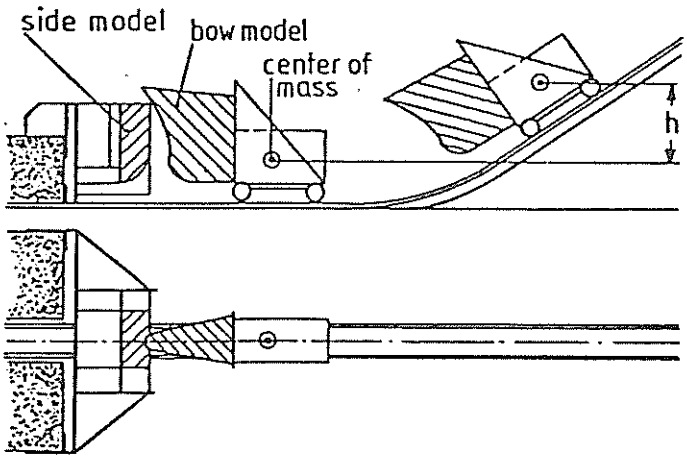

Fig. 2.9 Test set-up for collision tests /7/.

The test stand shown in Fig. 2.9 consisted of a carriage of appropriate mass with a foreship model attached in the front. The side model was mounted to a rigid counter bearing. The overall bending of the hull girder in a collision was simulated by connecting the ends of the side model to a flexible girder. The necessary velocity and impact energy were achieved by raising the model on an inclined rail path.

Several types of bow configurations were examined, ranging from sharp bows of fast passenger ships to cylindrical bow of an obo-carrier and a bulbous bow of a large crude carrier.

The first tests aimed at examining a reconstruction of the side barrier of the German nuclear vessel "Otto Hahn". Later, various configurations of the side structures were fabricated in order to develop a penetration protection of the resisting barrier type applicable to the planned second generation nuclear ships, the realization of which was stopped later on. The collision protection which was proposed as a result of the tests is shown in Fig. 2.10.

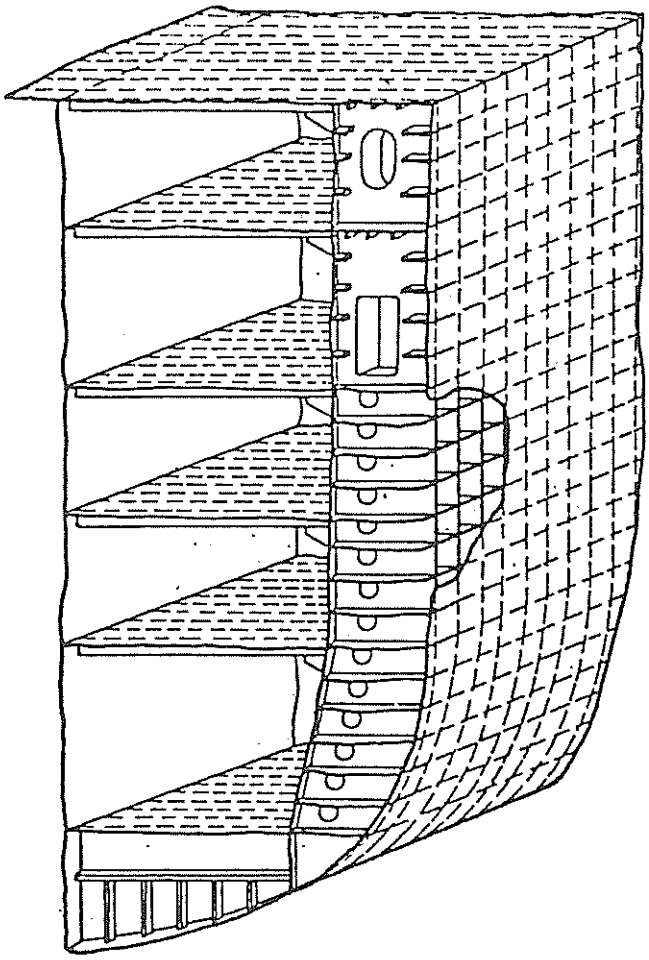

Fig. 2.10 Proposed collision barrier.

It consists of a 38 mm thick shell plating reinforced by a closely spaced square cell structure between the inner and outer shell. The distance and thickness of the frames are 900 mm and 18 mm respectively.

The main application of the test results was to extrapolate the damages to real collisions by applying scale laws with respect to impact energies.

The models were otherwise sparsely instrumented and acceleration recordings which could be used to determine the overall load history were unsatisfactory.

A comprehensive work was performed on studying different scale laws pertaining to inertia forces, strain rate effect, the microstructure of welded plate material related to crack initiation, added mass of ship during impact etc.

2.2 Energy Absorption in Platform Bracing

Collision effects analysis of jacket-type platforms is normally based upon the following decomposition into modes of energy dissipation

- Local denting of hit member at location of contact
- Beam deformation between neighbouring joints
- Overall deformation of the structure

There are important interaction effects between the different modes. Due to the complexity of incorporating all the behavioural effects simultaneously each mode is often analyzed separately.

Analysis of local energy absorption is mostly based upon ring models. The crushing of tubes between rigid plates was considered in Ref. /29/ applying rigid-plastic methods. Experimental results were found to lie above the theoretical curve. This was attributed to strain hardening, not merely due to the increased stress level but also to the effect on the deformation pattern /30/.

The local character of the deformations produced by a sharp indenter has been analyzed by various indentation models. A so-called bow-tie deformation pattern was proposed in Ref. /31/ for a tube under the action of two opposed wedge-shaped indenters. The total plastic work required to convert the tube into the assumed mechanism could easily be calculated.

The indentation of a cylindrical shell was analyzed in Ref. /32/ using a series of upper bound calculations. However, this method is valid for small deflections, not larger than a few times the thickness.

Wedge shaped yield line models have been used by several authors /33,34/. In addition to rotation across yield lines and removal of tube curvature, membrane effects are also included in such studies.

The energy absorption capacity in the beam mode of deformation can be assessed by the kinematic methods of plasticity. It is well known that the post-collapse behaviour is strongly influenced by the degree of restraint provided by the supports. Hodge /35/ presented a model in which the restraint against axial displacement was represented by linear springs.

This approach was advanced to tubular beams by Oliveira /33,36/ who also included rotational flexibility.

Few attempts have been made to assess interaction effects between the different modes of energy dissipation, However, an analytical method which simultaneously accounts for local denting and beam deformation has been presented in Ref. /37/.

Analysis of the overall deformation behaviour of the structure is normally limited to a check on the static capacity against the maximum impact load. A linear elastic, dynamic analysis of a four legged jacket is reported in Ref. /34/. There appears to be no systematic studies conducted in the non-linear regime, but a computer programme recently developed seems to have a high potential for such applications /38/.

3. FUNDAMENTAL CONTINUUM THEORY

3.1 Flow Theory of Plasticity

Crushing strength analysis requires the non-linear behaviour to be taken into account. The deformation theory and the flow theory are the two major plasticity theories. The deformation theory assumes a unique relation between total stresses and total strains while the flow theory gives an incremental relationship between stresses and strains. The two approaches coincide only along radial paths in the stress space.

The flow theory which is used subsequently is based on three major assumptions. The first is that the elastic and plastic strains may be added

$$\varepsilon_{ij} = \varepsilon^{e}_{ij} + \varepsilon^{p}_{ij} \tag{3.1}$$

The second assumption is that there exists a loading function (yield condition and hardening behaviour) at every stage of plastic deformation. The specific value

$$f\,(\sigma_{ij}) = 0 \tag{3.2}$$

constitutes the yield condition.

The third assumption is Druckers postulate on positive plastic work which implies convexity of the yield surface and normality of the plastic strain increment to the yield surface

$$d\varepsilon^{p}_{ij} = d\lambda \frac{\partial f}{\partial \sigma_{ij}} \qquad d\lambda \geqslant 0 \tag{3.3}$$

The specific plastic strain energy increment is defined by

$$dE^{p} = \sigma_{ij}\, d\varepsilon^{p}_{ij} = \bar{\sigma}\, d\bar{\varepsilon}^{\,p} \tag{3.4}$$

where $\bar{\sigma}$ is an equivalent stress and $d\bar{\varepsilon}^{p}$ is an equivalent plastic strain increment which depends on the yield condition used. Adopting the von Mises yield criterion gives

$$\sigma = \sqrt{\frac{3}{2} S_{ij} S_{ij}} \tag{3.5}$$

and

$$d\bar{\varepsilon}^p = \sqrt{\frac{2}{3} d\varepsilon^p_{ij} d\varepsilon^p_{ij}} \tag{3.6}$$

where S_{ij} is the deviatoric stress tensor.

For the dissipative part of the deformation process the plastic strain increment is often substituted by the rate of plastic strain

$$\dot{E}^p = \frac{dE^p}{dt} = \sigma_{ij} \dot{\varepsilon}^p_{ij} \tag{3.7}$$

In several occasions, and in particular where plastic strains are concentrated over narrow zones, it may be more convenient to work with stress and strain resultants, rather than directly with stresses and strains. Which resultants to use depends on the actual problem.

Consider a structure subjected to n generalized stresses (resultants) Q_i with associated generalized strain increments dq^p_i. The yield condition, the normality law and the strain energy increment, Eqs. (3.2)-(3.4), can be rearranged in the format of generalized variables

$$f(Q_i) = 0 \tag{3.8}$$

$$dq^p_i = d\lambda \frac{\partial f}{\partial Q_i} \tag{3.9}$$

$$dE^p = Q_i dq^p_i \tag{3.10}$$

Eq. (3.10) specifies that the generalized stresses and strains are energy conjugate. The resultants are obtained by integration of the physical components of stresses strains. Thus, for pure bending

$$dE^p = \int_V \sigma d\varepsilon^p dV = \int_L M d\kappa^p dx \tag{3.11}$$

so that the curvature κ^p is the correct generalized strain to be associated with the bending moment. If the longitudinal extension of large curvature is small, it is convenient to perform a limit consideration

$$dE = \int_{L \to 0} M d\kappa^p \, dx = M d\alpha^p \qquad (3.12)$$

where α^p denotes a permanent slope discontinuity between two adjacent segments. This interface is termed a yield hinge.

3.2 The Bound Theorems

A useful tool in the analysis of perfectly plastic material is the limit theorems of plasticity:

i) Upper Bound Theorem
If the rate of work of a system of applied loads with an associated kinematically admissible velocity field (collapse mechanism) is equal to the corresponding rate of internal energy dissipation, then that system of loads will cause collapse of the structure.

ii) Lower Bound Theorem
If a system of generalized stresses can be found which is in equilibrium with the applied loads and which nowhere violates the yield condition, then the structure will not collapse.

The attractiveness of these theorems is the uncoupling of the equilibrium and kinematic requirements. This simplifies significantly analytical studies. The kinematic method is particularly well suited since the mode of collapse (mechanism) is often obvious from geometrical considerations.

The bound theorems are only valid for infinitesimal strains. Thus, little information is provided as to the accuracy of approximate solutions to crushing problems where very large strains and displacements are involved. Thus predictions based on kinematic methods should be accompanied by experimental verification.

3.3 The Concept of Folding Mechanism

It is generally observed that plastic deformations in compressed members are not spread uniformly throughout the structure but are confined to narrow zones where strain and strain rates reach high magnitudes. Such zones are called hinge lines. As a result, a more or less regular pattern of wrinkles and folds is formed. The resulting shortening is comparable to the initial length of the member.

The crumpling process is strongly path dependent. The dissipated energy depends on the whole deformation history. Generally, several paths may lead to the same final state; the preferred mode is such that it renders the work a minimum. Physically this means that the structure tends to assume an inextensible deformation mode, predominantly with bending effects and as little stretching as possible. Mathematically, the transformation of surfaces after which angles and length of lines are preserved, is designated an isometric transformation. Most crushing is quasi-isometric since some extension is inevitable. Examples of isometric transformation of surfaces are given in Sec. 3.4.

Occasionally, a compressed member can be folded about stationary yield lines in the inextensional collapse mode. Normally, this can be accomplished only if sufficient freedom is left for the boundaries to deform. However, if a part of the boundary is subjected to motion constraints, the yield line may not remain stationary but is forced to travel. Thus a shape distortion is produced which does not require global inplane extension.

The conditions of continuity at a propagating hinge line is studied in Sec. 3.4.

3.4 Analysis of Discontinuities

The boundaries between a rigid and a deforming region is termed a yield hinge. The conditions of continuity at yield hinges were formulated by Hopkins /39/.

Let Γ denote a yield hinge line travelling down a surface S. The instantaneous position of Γ is given by $X = X(t)$. The line divides the surface

into two separable regions, the undeformed part S+ in front of Γ and the deformed part S- behind Γ.

Let **u** denote the displaceemnt field for the surface. It is assumed that the displacement **u** and velocities $\partial u/\partial t$ are continuous in space at any time and at any point of the shell. Hence, the velocity across the yield line must also be continuos.

Taking the derivative with respect to time t of the displacement of a material point on the yield line, there comes out

$$\left[\frac{du}{dt}\right] = \left[\frac{\partial u}{\partial t}\right] + \mathbf{v} \cdot [\text{grad } \mathbf{u}] = 0 \tag{3.13}$$

where the velocity of the yield line is $\mathbf{v} = \frac{dX}{dt}$. The brackets denote possible discontinuities across T, i.e.

$$[\dot{u}] = [\dot{u}]^{+} - [\dot{u}]^{-} \tag{3.14}$$

If $\partial u/\partial t$ is continuous, Eq. (3.13) shows that grad **u** can be discontinuous only across stationary hinges for which $\mathbf{v} = 0$. If the yield hinge is not stationary grad **u** must be continuous across Γ.

In a similar manner there is obtained

$$\left[\frac{d}{dt} \text{ grad } \mathbf{u}\right] = \left[\frac{\partial}{\partial t} \text{ grad } \mathbf{u}\right] + \mathbf{v} \cdot [\text{grad}^2 \mathbf{u}] = 0$$

provided that $\mathbf{v} \neq 0$.

On a component basis Eqs. (3.13) and (3.15) can be written

$$\left[\frac{du_i}{dt}\right] = \left[\frac{\partial u_i}{\partial t}\right] + V_k[u_{i,k}] = 0 \tag{3.16}$$

$$\left[\frac{du_{i,j}}{dt}\right] = \left[\frac{\partial u_{i,j}}{\partial t}\right] + V_k[u_{i,jk}] = 0 \tag{3.17}$$

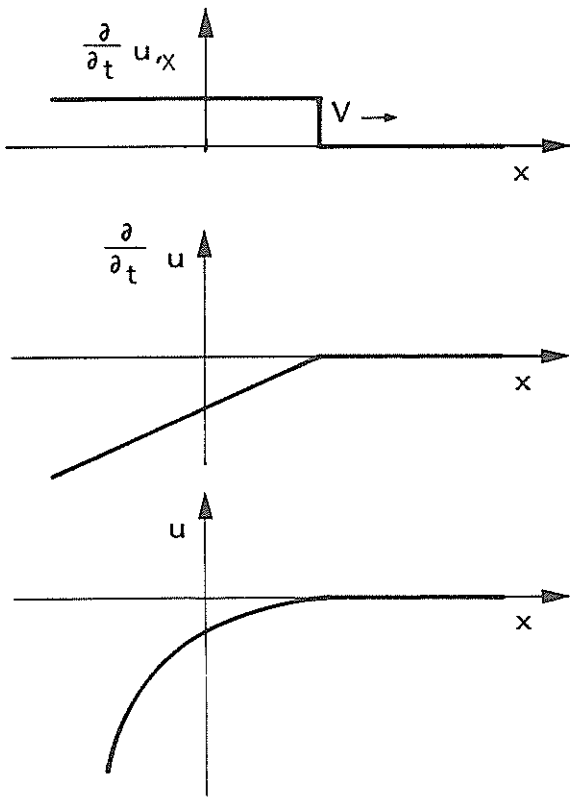

Figure 3.1 Displacement field at a moving yield line

Consider a straight yield line which moves down a plane surface with a constant velocity, leaving behind a plastically deformed region, Fig. 3.1. The rate of rotation and curvature on both sides of Γ are

$$\frac{\partial u^{+}_{,x}}{\partial t} = 0$$

$$\frac{\partial u^{-}_{,x}}{\partial t} = \dot{\theta} \qquad (3.18)$$

$$u^{+}_{,xx} = 0$$

$$u^{-}_{,xx} = \kappa = -\frac{1}{r}$$

Eq. (3.15) now reduces to

$$\dot{\theta} - \frac{v}{r} = 0 \tag{3.19}$$

Consequently, the moving hinge line imposes a constant curvature $\kappa = -\frac{1}{r}$ on the initially plane surface if the velocity field is related to the hinge velocity by Eq. (3.19). The interpretation of the above results for various other cases are shown in Fig. 3.2. A translation and a rotating hinge line transforms a plane surface into a cylindrical and a conical surface, respectively. A circular hinge line acting on a cylinder with radius R produces a toroidal surface with a small radius r and a large radius $\rho = r + R$.

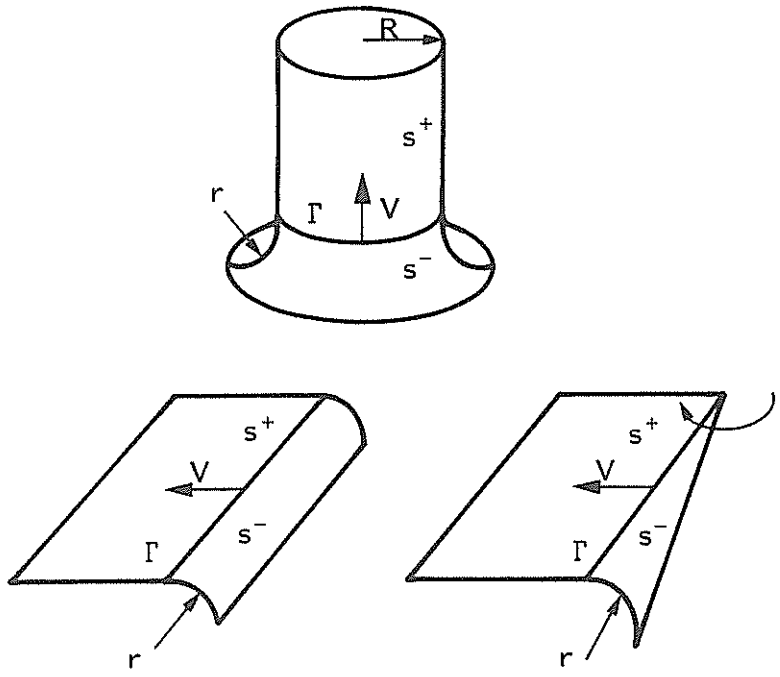

Figure 3.2 Kinematic continuity at various propragating hinge lines

4. CRUSHING MECHANICS OF STRUCTURAL ELEMENTS IN SHIPS

4.1 Ultimate Strength of Compression Panels

The initial buckling phase of deformation contributes to a minor extent to the energy absorption. However, the buckling mode may predict the type of plastic mechanism. In most cases the buckling pattern develops further into the plastic region and forms the energy absorbing mechanism. Thus, it is of great importance to study the initial buckling mode. Furthermore, the peak load, although being of a short duration, may yield the design load for the impact receiving structure.

It is common to distinguish between the following failure modes for a stiffened panel /40/.

Plate failure occurs in cases where the plate elements show a steep unloading characteristic after the maximum load, and the stiffeners are not able to carry the additional redistributed load. This failure mode is normally likely to occur only in very short panels, but loss of plating stiffness may have a strong influence on other failure modes.

Interframe flexural buckling of the stiffeners and associated plate flange occurs in a column-like mode. The collapse may be sensitive to the direction of buckling (towards or away from the stiffener outstand) involving significant interaction between overall and local modes.

Interframe tripping of stiffeners is likely to occur in short flexurally stiff girders and in stiffeners which are very short relative to their depth or which have low torsional rigidity. This collapse mode is normally avoided by using large safety margins.

Overall grillage buckling involves bending of longitudinal as well as transverse stiffeners.

The present classification can also be adopted for the buckling modes of stiffened cylindrical shells.

Bow structures are normally transversely framed resulting in plate elements of low aspect ratios. Accordingly, the buckling phenomenon is described subsequently with chief emphasis on plate failure.

4.1.1 Elastic Buckling

Elastic buckling stress formulae are often arranged in a generalized version of the plate buckling formula

$$\sigma_E = \frac{\pi^2 E}{12(1-\nu)^2} \left(\frac{h}{b}\right)^2 C_p \tag{4.1}$$

where h and b denote the thickness and width of the panel respectively. The coefficient C_p accounts for the boundary conditions and the plate aspect ratio. For long, simply supported plates $C_p = 4$. For short panels where the length a is much smaller than the width b a more convenient expression is

$$\sigma_E = \frac{\pi^2 E}{12(1-\nu^2)} \left(\frac{h}{a}\right)^2 \cdot C_p^{\,1} \tag{4.2}$$

These formulae may also be applied to curved panels and cylindrical sheets with radius of curvature R where the coefficients C_{Z1}, C_{Z2} are related to the Batdorf parameter

$$Z_1 = \frac{b^2}{Rh}\sqrt{1-\nu^2} \tag{4.3}$$

$$Z_2 = \frac{a^2}{Rh}\sqrt{1-\nu^2} \tag{4.4}$$

The coefficients may be obtained from Fig. 4.1 as a function of the Batdorf parameter.

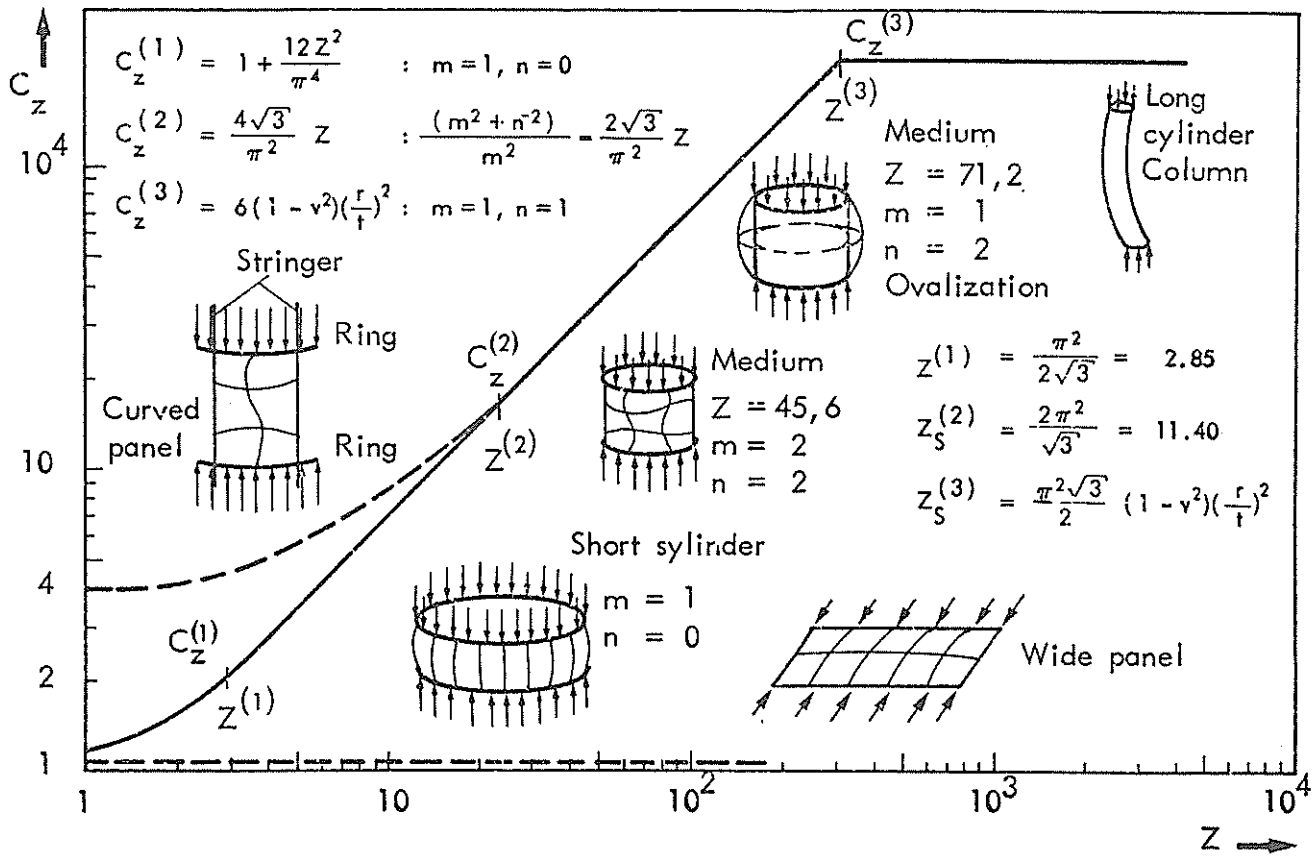

Fig. 4.1 Buckling coefficients for ring-stiffened cylinders.

Introducing the buckling coefficient for cylinders of medium length the classical cylinder buckling formula emerges

$$\sigma_E^{cyl} = \frac{E}{\sqrt{3(1-\nu^2)}} \frac{h}{R} \qquad (4.5)$$

For medium length, elliptical cylinders the buckling stress can be expressed in terms of Eq. (4.5) based on the radius of curvature at the ends of the minor axis and an augmentation factor which approaches unity for very thin shells

$$\sigma_E^{ell} = \sigma_E^{cyl} \cdot C_{ell} \qquad (4.6)$$

Similarly, the buckling stress for conical shells with circular cross-sections is found by substituting in Eq. (4.5) the smaller radius of the section in question and accounting for the semi-vertex angle ω

$$\sigma_E^{con} = \sigma_E^{cyl} \cos\omega \qquad (4.7)$$

It is distinguished between axisymmetric and unsymmetric buckling but the difference is very small.

Shape inperfections may significantly reduce the elastic buckling stress. This is especially true for cylindrical shells where the maximum stress may be only a fraction of the classical buckling stress. Thus, the critical stress should be reduced by a so-called "knock-down" factor /41/.

4.1.2 Inelastic Buckling

For ships and offshore structures plasticity effects more or less dominate in the buckling behaviour. It is well recognized that what is termed the ϕ method represents the most convenient technique for modifying the elastic buckling stress according to plasticity effects. Generally, the ultimate stress σ_u is related to the yield stress σ_y by

$$\sigma_u = \phi\sigma_y \qquad (4.8)$$

where the coefficient ϕ depends on the reduced slenderness ratio

$$\bar{\lambda} = \sqrt{\frac{\sigma_y}{\sigma_E}} \qquad (4.9)$$

Appropriate relationships for flat plates and curved panels are,e.g., found in design codes.

4.1.3 Ultimate Strength

It is well-known that long, slender plates can carry load substantially in excess of what is predicted by elastic theory provided that their unloaded edges are constrained to remain straight.

As a result of large lateral deflections membrane stresses develop in the transverse direction which tends to stabilize the plates. In this stage the distribution of stresses along the loaded edges is no longer uniform but increases towards the stiffeners.

There are basically two different semi-empirical approaches to predict the maximum strength. The effective width method establishes a relationship between the effective width of the plate b_e and the plate slenderness

$$\beta = \frac{b}{h}\sqrt{\frac{\sigma_y}{E}} \tag{4.10}$$

This method has found a wide application in marine structures and Faulkner /42/ proposed the following formula for simply supported rectangular plates

$$\frac{b_e}{b} = \frac{2}{\beta} - \frac{1}{\beta^2} \tag{4.11}$$

The maximum stress approach seeks a relationship of the form

$$\frac{\sigma_{max}}{\sigma_y} = \mu \left(\frac{\sigma_E}{\sigma_y}\right)^m \tag{4.12}$$

where the constants μ and m are adjusted to suit experimental results.

The method is mostly used in aircraft engineering and Gerard /13/ has proposed constants for various elements.

4.2 Basic Folding Mechanism

Consider the axial compression of a tube with a rectangular cross-section, Fig. 4.2a. One quarter of a model which is statically admissible is shown in Fig. 4.2b. In this model the imposed end shortening introduces the formation of a series of yield hinge lines which implies that a section of one of the sides has become a part of the other side. A theory for calculating the energy dissipation of such collapse modes was formulated by Wierzbicki and Abramowicz /43/. This theory will now be recapitulated.

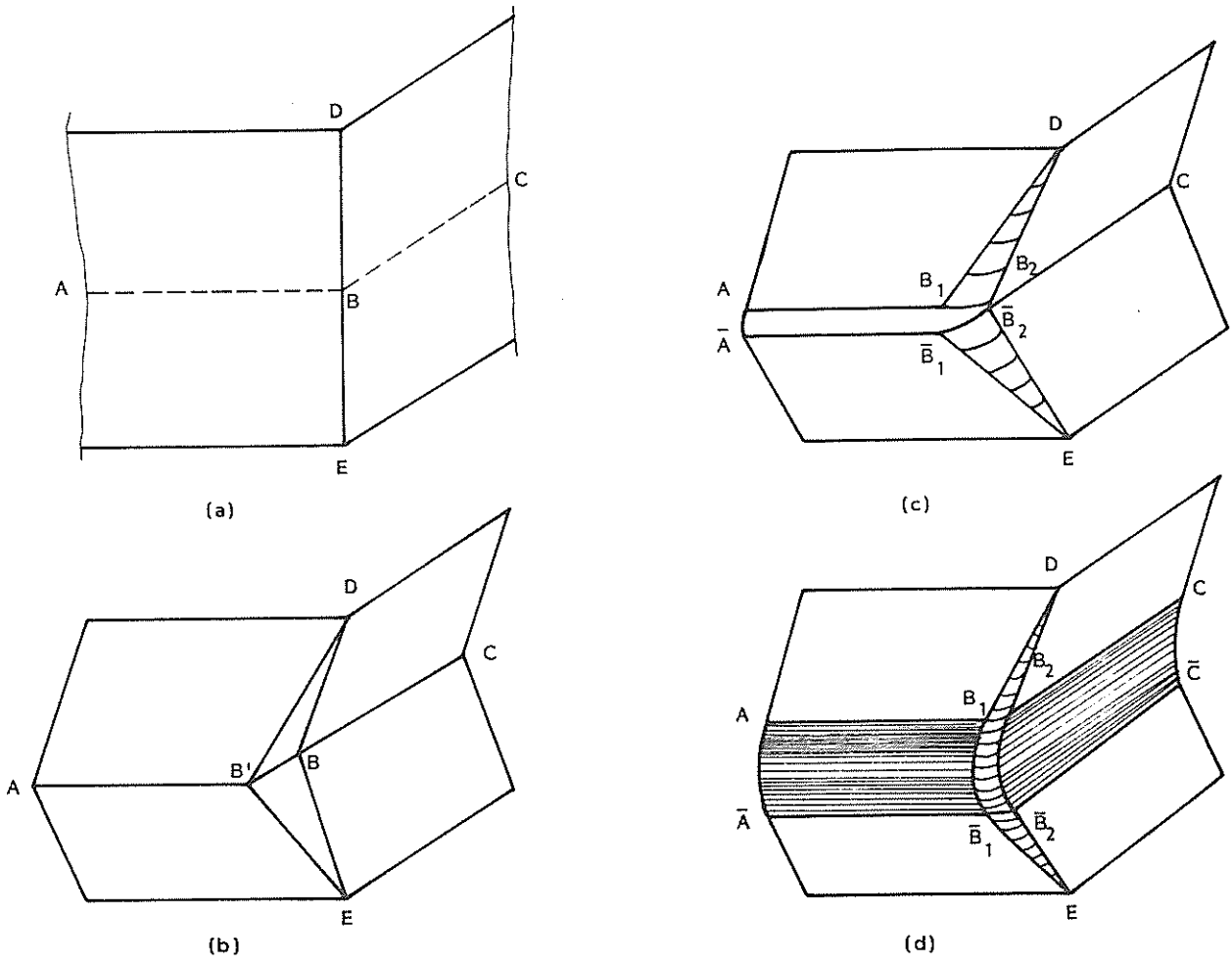

Figure 4.2 Construction of basic folding mechanism /43/

In the dynamic considerations it is assumed that the continuous deformation process is made feasible by the motion of a yield hinge line from its original position DB to a new position DB'. This deformation mode is kinemeticaly inadmissible since it implies a discontinuity in the slope across a moving hinge line. A consistent collapse mechanism is constructed by introducing two rotating hinge lines DB_1 and DB_2 along DB'.
The first hinge line imposes a constant curvature, the second removes curvature with the same amount. The resulting mode consists of two flat trapezoidal surfaces joined by a section of a conical surface as shown in Fig. 4.2c.

When two such modes are connected a stationary hinge line is formed at CB_2, where the slope discontinuity is admissible. However, this results in a material discontinuity along the remaining part of the line. The gap

increases linearly from B_2 to B_1 and is then held constant along B_1A. Obviously, this requires extension of the material perpendicular to the yield line.

The conditions of continuity can be met if the curvature at the stationary yield line is changed from infinite to a finite and constant value. In this way a section of a cylindrical surface is obtained between the trapezoidal elements. The region bounded by the four circular arcs constitutes a section of a toroidal surface. The resulting deformation mode shown in Fig. 4.2d is termed a basic folding mechanism.

The following modes of energy dissipation are identified

- bending about stationary yield hinge lines
- rolling about moving yield lines
- transverse extension and bending on the toroidal surface

4.2.1 Kinematic Relationships

In order to simplify calculations the global geometry is approximated by the folding mechanism shown in Fig. 4.3. The initial geometry of the compressed element is described by the height 2H, the average width C of the segments AB and BC and the angle $2\psi_o$ between two adjacent sides. The deformed geometry is described either by the crushing distance, δ, or the angle of rotation of the flat elements, α, or the horizontal displacement, δ_H of the point C. These quantities are mutually related by

$$\delta = 2H\,(1 - \cos\alpha) \tag{4.13}$$

and

$$\delta_H = H\sin\alpha \tag{4.14}$$

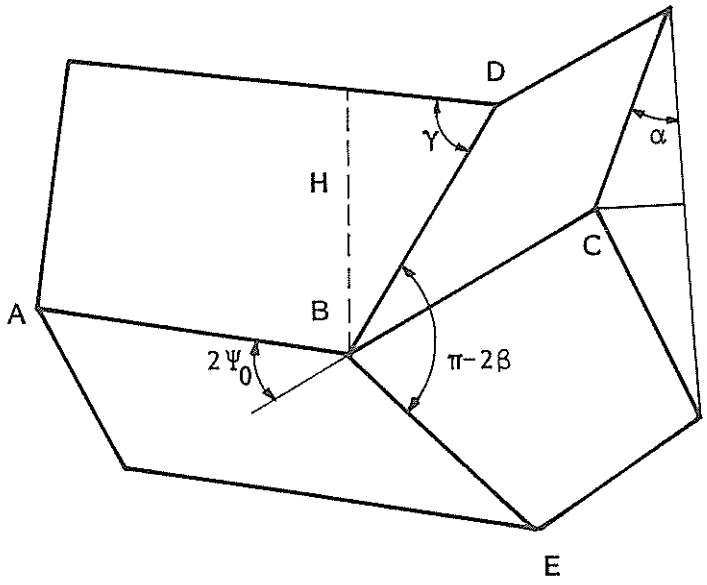

Figure 4.3 Global geometry of the basic folding mechanism

The following relationships exist between the three angles

$$\tan\gamma = \frac{\tan\Psi_o}{\sin\alpha} \tag{4.15}$$

and

$$\tan\phi_o = \frac{\tan\alpha}{\sin\psi_o} \tag{4.16}$$

The rate of axial shortening and the horizontal velocity of the point D is found by differentiation of Eqs. (4.13) - (4.14) with respect to time

$$\dot{\delta} = 2H \sin\alpha \, \dot{\alpha} \tag{4.17}$$

$$V_H = \dot{\delta}_H = H\cos\alpha \, \dot{\alpha} \tag{4.18}$$

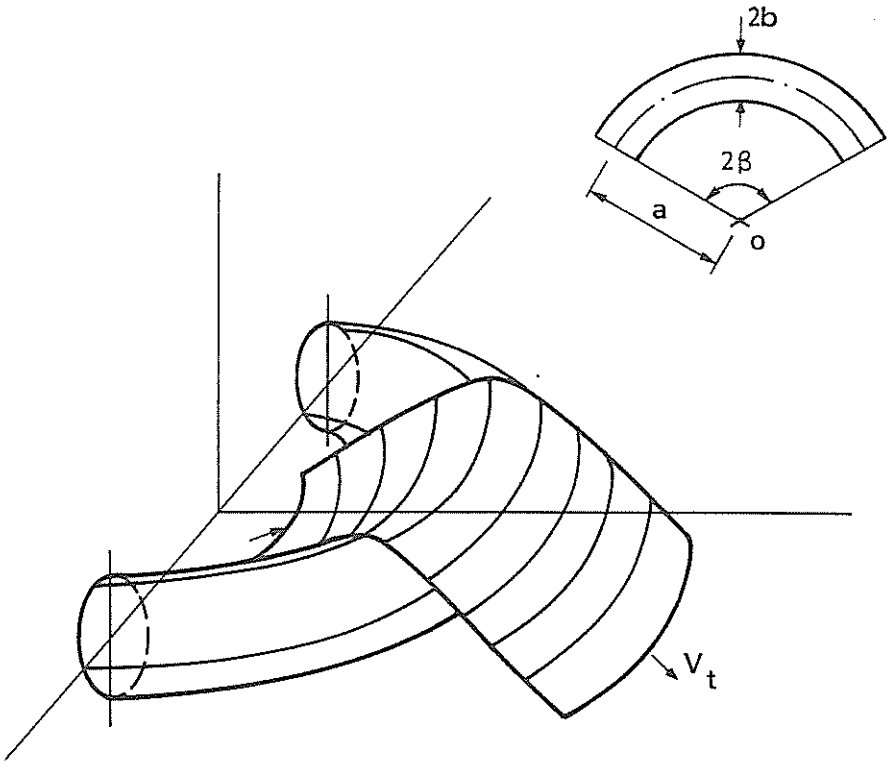

Figyre 4.4 Plastic flow of a metal sheet over a toroidal surface /43/

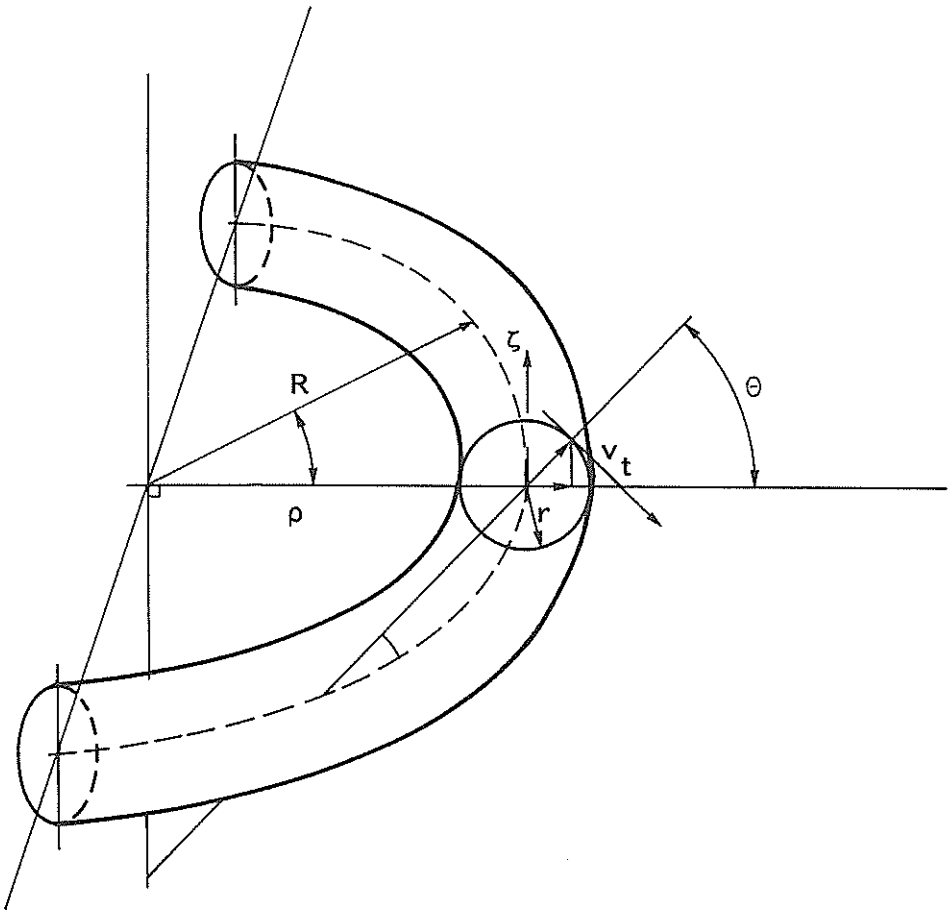

Figure 4.5 Geometrical description of the toroidal surface

For the local deformation field on the toroidal surface reference is made to Figs. 4.4 and 4.5. A local coordinate system (θ, ϕ, z) is introduced where θ and ϕ denote respectively the meridional and circumferential coordinate of the toroidal surface.

The motion of the shell is a radial flow of material points over the toroidal surface. The tangential velocity is the vector sum of the velocities of the points A and C in Fig. 4.3 given by

$$V_t = \dot{\theta} r = \frac{V_H}{\tan\psi_o} \tag{4.19}$$

Inextensibility in the meridional direction is assumed. A detailed derivation /44/ shows that there are only two nonvanishing strain rate components, i.e. rate of extension $\dot{\lambda}$ and rate of curvature $\dot{\kappa}$ both in the circumferential direction.

The rate of extension is given by

$$\dot{\lambda}_\theta = \frac{\dot{\rho}}{\rho} = \frac{\dot{\theta} r \sin\theta}{\rho} \tag{4.20}$$

where

$$\rho = R + r\cos\theta \tag{4.21}$$

denotes the current position of the point on the toroidal surface with respect to the symmetry azis. R and r represent the greater and smaller radius of the toroid, respectively.

The current radius of curvature in the circumferential direction is

$$r_\phi = \frac{\rho}{\cos\theta} \tag{4.22}$$

which yields the following expression for the rate of curvature

$$\dot{\kappa}_\phi = -\frac{\dot{r}_\phi}{r_\phi^2} = -\frac{\dot{\theta} R \sin\theta}{\rho^2} \tag{4.23}$$

4.2.2 Energy Dissipation

The rate of internal energy dissipation contains the contributions from the continuous and discontinuous velocity fields

$$\dot{E}_{int} = \int_F (M_\phi \dot{\kappa}_\phi + N_\phi \dot{\lambda}_\phi) dF + \int_L M_o \dot{\theta} dl \tag{4.24}$$

where the toroidal surface element is given by

$$dF = \rho d\phi r d\theta \tag{4.25}$$

The limits of integration are

$$\frac{\pi}{2} - \psi \leq \theta \leq \frac{\pi}{2} + \psi \tag{4.26}$$

and

$$-\phi_o < \phi < \phi_o \tag{4.27}$$

ϕ_o varies according to Eq. (4.16) while the angle ψ increases linearly with ϕ from ψ_o to $\pi/2$ according to

$$\psi = \psi_o + (1 - \frac{\psi_o}{\pi/2}) \phi \tag{4.28}$$

The flow of material over the toroidal surface is simultaneously subjected to extension as well as change of curvature in the circumferential direction. The yield condition for combined bending and tension for a rectangular cross-section takes the form

$$\frac{M_\phi}{M_o} + \left(\frac{N_\phi}{N_o}\right)^2 = 1 \tag{4.29}$$

where the plastic capacities for bending and axial force are given by

$$M_o = \frac{\sigma_o h^2}{4} \tag{4.30}$$

$$N_o = \sigma_o h \tag{4.31}$$

To simplify calculations the yield condition ((Eq. 4.29)) is approximated by a square interaction curve circumscribed on the parabola.

With these assumptions the energy dissipated on one half of the toroidal surface becomes

$$E_1 = \frac{1}{2} \int_{\phi_o}^{\phi_o} b \int_{\frac{\pi}{2}-\psi}^{\pi/2+\psi} \left(M_o \frac{\theta R \sin\theta}{\rho^2} + N_o \frac{\theta r \sin\theta}{\rho} \right) d\theta \, d\phi \qquad (4.32)$$

The details of integration of Eq. (4.32) can be found in /43/.

Here, it should be mentioned that the first term, associated with the change in circumferential curvature, is small and therefore is neglected. Consequently, the stress profile lies close to the line $N = N_o$ which warrants the assumption of the approximate yield curve.

The result of integrating Eq. (4.32) comes out to be

$$\dot{E}_1 = 2 N_o Hr \, f(\alpha, \psi_o) \, \dot{\alpha} \qquad (4.33)$$

where

$$f(\alpha, \psi_o) = \frac{\pi}{(\pi - 2\psi_o) tg\psi_o} \left\{ \sin\psi_o \sin \frac{\pi - 2\psi_o}{\pi} \phi_o + \cos\psi_o \left[1 - \cos \frac{\pi - 2\psi_o}{\pi} \right] \phi_o \right\} \cdot \cos\alpha \, \dot{\alpha} \qquad (4.34)$$

The angle ϕ_o is related to α and ψ_o by Eq. (4.16).

The work done on complete folding through the angle $\pi/2$ is found by integration of Eq. (4.33) and by replacing N_o by M_o

$$E_1 = 8 M_o \frac{Hr}{h} J_1(\psi_o) \qquad (4.35)$$

where

$$J_1(\psi_o) = \int_o^{\pi/2} f(\alpha, \psi_o) \, d\alpha \qquad (4.36)$$

The second integral in Eq. (4.24) represents the energy dissipated by the discontinuous velocity field on the horizontal and inclined hinges.

The length of each of the four horizontal hinge lines is C and the energy dissipated is

$$\dot{E}_2 = M_o C \dot{\alpha} \tag{4.37}$$

while the total work is given by

$$E_2 = M_o C \int_o^{\frac{\pi}{2}} d\alpha = \frac{\pi}{2} M_o C \tag{4.38}$$

The length of each inclined hinge, based on the approximate mechanism in Fig. 4.3, is

$$L = \frac{H}{\sin\gamma} \tag{4.39}$$

The discontinuity in the rate of rotation in the meridional direction

$$\dot{\theta} = \frac{V_t}{r} \tag{4.40}$$

is constant along L.

There are two inclined hinges, one imposing and one removing the curvature. The energy dissipation is expressed by

$$\dot{E}_3 = 2M_o L\dot{\theta} = 2M_o \frac{H^2}{r} \frac{1}{tg\psi_o} \frac{\cos\alpha}{\sin\gamma} \dot{\alpha} \tag{4.41}$$

and the total work is

$$E_3 = 2M_o \frac{H^2}{r} J_3(\psi_o) \tag{4.42}$$

where

$$J_3(\psi_o) = \frac{1}{tg\psi_o} \int_o^{\pi/2} \frac{\cos\alpha}{\sin\gamma} d\alpha$$

$$= \frac{1}{2} \left\{ \frac{\cos\psi_o}{\sin^2\psi_o} + \ln \frac{1 + \cos\psi_o}{\sin\psi_o} \right\} \tag{4.43}$$

The rate of external work is

$$\dot{E}_e = P\dot{\delta} = 2H\sin\alpha\,\dot{\alpha} \tag{4.44}$$

while the total plastic work required to fold the element completely can be related to the mean load by

$$E_e = P_{av} \cdot 2H \tag{4.45}$$

4.2.3 Average Crushing Load

The crushing force can now be found by summing up and equating the external and internal energy expressions. If the rates of energy dissipation are used the instantaneous load is obtained while the total energies yield the average crushing force. In both cases the resulting expressions contain two unknown parameters, namely the wave length H and the smaller toroid radius r. The general formula for the average load reads

$$\frac{P_{av}}{M_o} = A_1 \frac{r}{h} + A_2 \frac{C}{H} + A_3 \frac{H}{r} \tag{4.46}$$

In order to determine H and r the principle of minimum energy is used

$$\frac{\partial P_m}{\partial H} = 0, \quad \frac{\partial P_m}{\partial r} = 0 \tag{4.47}$$

The solution is

$$r = \sqrt[3]{A_2A_3/A_1^2}\ \sqrt[3]{Ch^2} \tag{4.48}$$

and

$$H = \sqrt[3]{A_2^2/A_1A_3}\ \sqrt[3]{C^2h} \tag{4.49}$$

Hence, the total load can be written

$$\frac{P_m}{M_o} = 3 \cdot \sqrt[3]{A_1A_2A_3}\ \sqrt[3]{\frac{C}{h}} \tag{4.50}$$

The result shows that all modes contribute equally to the total energy dissipation, irrespectively of the values of the coefficients A_1, A_2 and A_3.

If the instantaneous load is minimized rather than the mean load a variable wave length will result. This would contradict the assumptions made and would require an additional dissipation mechanism to account for the change in wave length.

It might be questioned whether the wave length will be determined in the elastic region under influence of boundary conditions and initial imperfections rather than by minimization of the total plastic work. However, predictions based on Eqs. (4.49) - (4.50) show good correlation with experiments as concerns mean crushing load and wave length /45/.

4.3 Extensional Collapse with a Stationary Hinge

4.3.1 Asymmetric Mode

In the basic folding mechanism discussed previously the hinge line is allowed to move relative to material points so that material from one panel continuously passes to the other panel and a shape distortion is produced without any in-plane distortion. However, in some cases the hinge line is fixed so that transfer of material points across the hinge line does not occur.

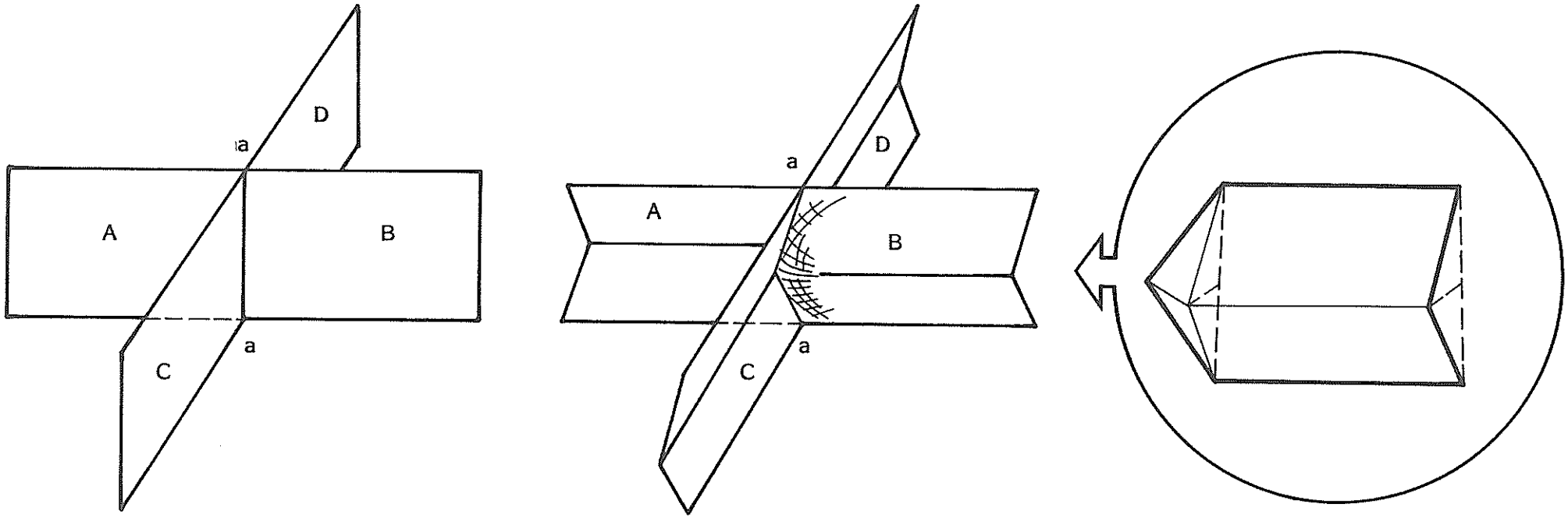

Figure 4.6 Collapse model of a cruciform joint

Consider the cruciform joint in Fig. 4.6 where the joint line a-a distorts in the reference plane of the flanges A and B. Obviously, three of the flanges can easily obtain an inextensible deformation mode while kinematical continuity at the joint line cannot be accommodated unless flange B is extended in the transverse direction. This mode is illustrated in Fig. 4.6b and has been observed in experiments.

The energy dissipation in flange B is now considered.

Compression tests with cruciforms show typically one single wave at the free edge of the flanges. Towards the joint line the wave length decreases and the plate assumes a doubly curved surface.

This complicated deformation pattern is approximated by the collapse model shown in Fig. 4.6c, where the plate surface is described by two rectangles identical to the undeformed configuration and two triangles which assure continuity at the joint line. The curvature is concentrated at the hinge lines.

Consider the current in-plane deformation state of one half of the flange B which originally was of a rectangular shape and assume that the plastic deformations are confined to the hatched triangle in Fig. 4.7.

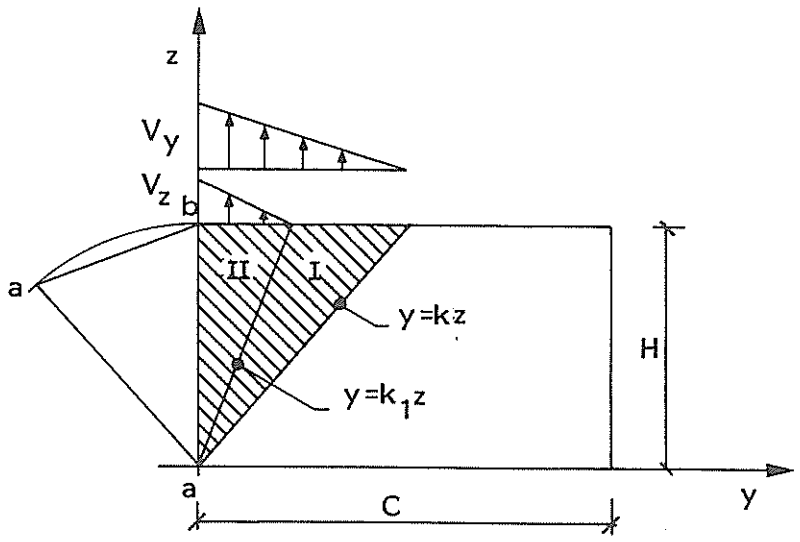

Figure 4.7 Current deformation state of rectangular elements

Material points currently located inside the triangle are subjected to a bi-linear velocity field in the y-direction only. When passing the hinge line a-b a bi-linear velocity field in the z-direction is added. Material points with y-coordinates equal to the current total displacement in y-direction lie on the boundary between the two regions.
The in-plane displacement of the midpoint is given by

$$v_o = - H \sqrt{(1 - \cos^4\alpha)} \tag{4.51}$$

$$w_o = - H \sin^2\alpha \tag{4.52}$$

With the linear variation of the displacement field the boundary line between the two regions is given by

$$y = k_1 z \tag{4.53}$$

where

$$k_1 = \left(\frac{1}{k} + \frac{1}{\sqrt{1 - \cos^4\alpha}} \right)^{-1} \tag{4.54}$$

Thus, the velocity field for the plastic region comes out to be:

$$V_y = V_{oy} \frac{z}{H} \left(1 - \frac{y}{kz}\right) \tag{4.55}$$

and

$$V_z = \max \left(V_{oz} \frac{z}{H} \left(1 - \frac{y}{k_1 z}\right), 0\right) \tag{4.56}$$

where

$$V_{oy} = \dot{u}_o \tag{4.57}$$

$$V_{oz} = \dot{v}_o \tag{4.58}$$

The plastic strain rate tensor is given by

$$\dot{\varepsilon}_{ij} = \frac{1}{2} \left(\frac{\partial V_i}{\partial X_j} + \frac{\partial V_j}{\partial X_i} \right) \tag{4.59}$$

In the Cartesian coorinate system the following components are obtained in Region I.

$$\dot{\varepsilon}_{yy} = -\frac{V_{oy}}{Hk} \tag{4.60}$$

$$\dot{\varepsilon}_{yz} = \dot{\varepsilon}_{zy} = \frac{V_{oy}}{H} \tag{4.61}$$

$$\dot{\varepsilon}_{xx} = \frac{V_{oy}}{Hk} \tag{4.62}$$

Correspondingly, in Region II

$$\dot{\varepsilon}_{yy} = -\frac{V_{oy}}{Hk} \tag{4.63}$$

$$\dot{\varepsilon}_{yz} = \varepsilon_{zy}\frac{1}{2}\left(\frac{V_{oy}}{H} - \frac{V_{oz}}{Hk_1}\right) \tag{4.64}$$

$$\dot{\varepsilon}_{zz} = \frac{V_{oz}}{H} \tag{4.65}$$

$$\dot{\varepsilon}_{xx} = \frac{V_{oy}}{Hk} - \frac{V_{oz}}{H} \tag{4.66}$$

The strain rate in the thickness direction, $\dot{\varepsilon}_{xx}$, results from the condition of incompressibility $\dot{\varepsilon}_{ii} = 0$.

The rate of energy dissipation is given by the expression

$$\dot{E} = \int_V \sigma_{ij}\dot{\varepsilon}_{ij}\,dV = \sigma_o \int_V \dot{\bar{\varepsilon}}\,dV \tag{4.67}$$

Applying the von Mises yield criterion, the effective strain rate is

$$\dot{\bar{\varepsilon}} = \sqrt{\frac{2}{3}\dot{e}_{ij}\dot{e}_{ij}} \tag{4.68}$$

Assuming k = 1 and substituting Eqs. (4.60) - (4.66) the following effective strain rate expression emerges

$$\dot{\bar{\varepsilon}} = \frac{V_{oy}}{H}\sqrt{\frac{5}{3}} \tag{4.69}$$

in region I and

$$\dot{\bar{\varepsilon}} = \frac{V_{oz}}{H}\sqrt{2(f^2 - f + 1 - \frac{1}{3}(f-1)\sqrt{1+f^2})} \tag{4.70}$$

in region II where f is defined by

$$f = \frac{\cos^2\alpha}{\sqrt{1-\cos^4\alpha}} \tag{4.71}$$

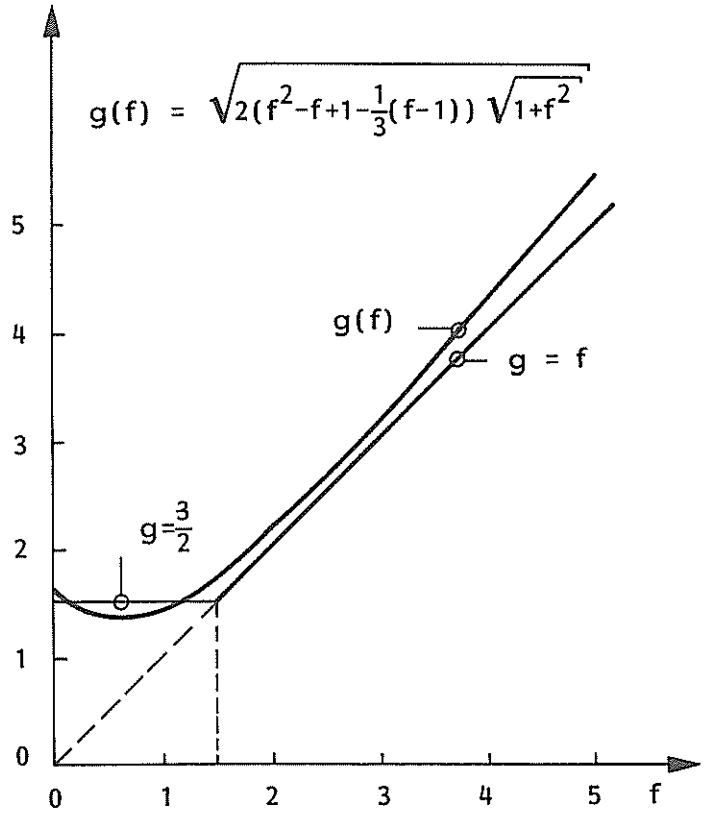

Figure 4.8 Linearization of the effective strain rate

The radical in Eq. (4.70) is plotted in Fig. 4.8. Evidently, a good approximation for Eq. (4.70) is offered by

$$\dot{\bar{\varepsilon}} = \frac{V_{oz}}{H} \cdot \max\left(f, \frac{3}{2}\right) \tag{4.72}$$

Thus, the rate of energy dissipation for Region I becomes

$$\dot{E}_4^I = \frac{1}{2}\sqrt{\frac{5}{3}}\,\sigma_o h H\, V_{oy} \cdot (1 - k_1) \tag{4.73}$$

and correspondingly for region II

$$\dot{E}_4^{II} = \frac{1}{2}\,\sigma_o H\, V_{oz} k_1 \max\,(f, \frac{3}{2}) \tag{4.74}$$

The angle in the expression for the velocities varies from $\alpha = 0$ at the beginning of the deformation process to $\alpha = \frac{\pi}{2}$ at the end.

Carrying out the integration in the above mentioned limits it can be shown that the total plastic work on the continuous deformation field is

$$E_4 = 0.8\,\sigma_o h\, H = 3.2\, M_o \frac{H^2}{h} \tag{4.75}$$

The expressions for energy dissipation along the stationary horizontal hinge lines are identical to those for an angle element.

The rate of plastic work in the stationary hinge line at the joint is

$$\dot{E}_5 = M_o H \cdot \dot{\alpha}^1 \tag{4.76}$$

where α^1 is related to α by

$$\sin\alpha^1 = \frac{1}{\sqrt{1 + \cos^2\alpha}} \qquad (\alpha > 0) \tag{4.77}$$

Accounting for the discontinuity in α^1 for $\alpha = 0$ the total work becomes

$$E_5 = \frac{\pi}{2} M_o H \tag{4.78}$$

4.3.2 Average Crushing Strength of a Cruciform. Asymmetric Mode

The total plastic work of the cruciform shown in Fig. 4.6 can now be calculated. The cruciform can be considered as an assemblage of one angular element (flanges A and C) deforming in the basic folding mechanism, one

flange, B, deforming in the extensional mode discussed, and one flange, D, with only stationary yield lines. Accordingly, the total energy dissipation contains the following contributions

$$E_i = \underbrace{2E_1 + 2E_2 + 2E_3}_{A} + \underbrace{2E_2}_{C} + \underbrace{2E_2 + 2E_4 + 2E_5}_{B} + \underbrace{2E_2}_{D}$$

$$= 2E_1 + 8E_2 + 2E_3 + 2E_4 + 2E_5 \qquad (4.79$$

The external work is related to the mean compression load by

$$E_e = 2HP_{av} \qquad (4.80)$$

Substituting the appropriate energy terms into Eq. (4.80) there comes out

$$\frac{P_{av}}{M_o} = A_1 \frac{r}{h} + A_2 \frac{C}{h}\frac{h}{H} + A_3 \frac{H}{h}\frac{h}{r} + A_4 \frac{H}{h} + \frac{\pi}{2} \qquad (4.81)$$

where

$$\begin{aligned} A_1 &= 4.64 \\ A_2 &= 2\pi \\ A_3 &= 2.3 \\ A_4 &= 3.2 \end{aligned} \qquad (4.82)$$

It is observed that two unknown parameters, the wave length H and the rolling radius r, appear in the expression for the mean load. A formal differentiation of Eq. (4.81) may be carried out yielding the following fourth order algebraic equations

$$\frac{H}{h} = \frac{A_1}{A_3}\left(\frac{r}{h}\right)^2 \qquad (4.83)$$

$$\left(\frac{r}{h}\right)^3 \left\{1 + \frac{r}{h}\frac{A_4}{A_3}\right\} = \frac{A_2 A_3}{A_1^2}\frac{C}{h} \qquad (4.84)$$

Eq. (4.84) can be solved numerically by repeated iteration

$$\left(\frac{r}{h}\right)_i = \left(\frac{A_2 A_3}{A_1^2}\frac{C}{h}\right)^{\frac{1}{3}} \left(1 + \left(\frac{r}{h}\right)_{i-1}\frac{A_4}{A_3}\right)^{\frac{1}{3}} \tag{4.85}$$

Eq. (4.85) converges rapidly. Alternatively the rolling radius can also be estimated by linearizing Eq. (4.84) and solving for r

$$\left(\frac{r}{h}\right)_o = \frac{A_3}{A_4}\, m \left(\frac{A_4}{A_1 A_3}\right)^{\frac{3}{4}} \left(A_1 A_2 A_3 \frac{C}{h}\right)^{\frac{1}{4}} - \frac{1}{4}\Bigg\} \tag{4.86}$$

Using Eq. (4.86) as a starting value sufficient accuracy is obtained with one iteration only, for normal values of A_i. Substituting Eqs.(4.83)-(4.84) into Eq. (4.85) and performing one iteration leads to

$$\frac{P_{av}}{M_o} = 3\left(A_1 A_2 A_3 \frac{C}{h}\right)^{\frac{1}{3}} \frac{1 + 2\frac{A_4}{A_3}\left(\frac{r}{h}\right)_o}{\left(1 + \frac{A_4}{A_3}\left(\frac{r}{h}\right)_o\right)^{\frac{1}{3}}} \tag{4.87}$$

when the small constant term is neglected.

The first term is recognized as the mean crushing load for an angle element. For $A_4 = 0$ the fraction correctly degenerates to unity. This term can be considered as an augmentation factor for a cruciform. The formula can be further simplified by introducing the approximation

$$\frac{1 + 2\frac{A_4}{A_3}\left(\frac{r}{h}\right)_o}{\left(1 + \frac{A_4}{A_3}\left(\frac{r}{h}\right)_o\right)^{\frac{1}{3}}} \sim \left(1 + 0.54\frac{A_4}{A_3}\left(\frac{r}{h}\right)_o\right)^{\frac{2}{3}} \tag{4.88}$$

Finally, by means of Eqs. (4.86) - (4.88) the mean crushing load turns into

$$\frac{P_{av}}{M_o} = 3\left(A_1 A_2 A_3 \frac{C}{h}\right)^{\frac{1}{3}} \left\{0.87 + 0.54\left(\frac{A_4}{A_1 A_3}\right)^{\frac{3}{4}} \left(A_1 A_2 A_3 \frac{C}{h}\right)^{\frac{1}{4}}\right\}^{\frac{2}{3}} \tag{4.89}$$

and by substituting the appropriate constants

$$\frac{P_{av}}{M_o} = 12.17 \left(\frac{C}{h}\right)^{\frac{1}{3}} \left\{ 0.87 + 0.63 \left(\frac{C}{h}\right)^{\frac{1}{4}} \right\}^{\frac{2}{3}} \qquad (4.90)$$

The considerations above are based on no rotational restraint along the compressed edges. If clamped supports are assumed the A_2 term is doubled and Eq. (4.90) turns into

$$\frac{P_{av}}{M_o} = 15.33 \left(\frac{C}{h}\right)^{\frac{1}{3}} \left\{ 0.87 + 0.74 \left(\frac{C}{h}\right)^{\frac{1}{4}} \right\}^{\frac{1}{3}} \qquad (4.91)$$

4.3.3 Symmetric Mode

In the deformation mode discussed the joint line distorts in a particular direction due to the asymmetric load distribution from the flanges. However, one alternative mode for the flanges to follow is a symmetric deformation pattern with respect to the joint so that this becomes stabilized against lateral displacement. The only way to accommodate the axial shortening of the cruciform is consequently by compressive yielding of the joint itself.

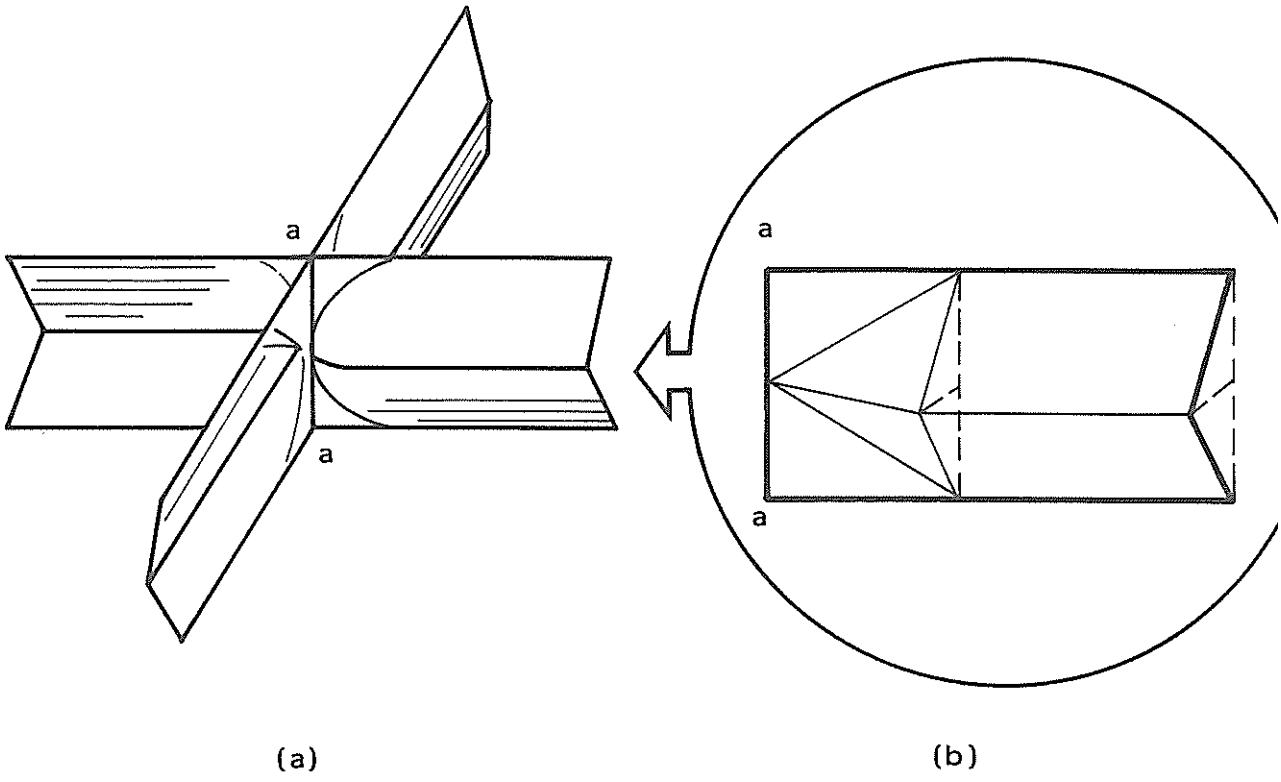

Figure 4.9 *Symmetric collapse model of a cruciform joint*

Again, the complicated deformation pattern suggested in Fig. 4.9 is approximated by a surface consisting of plane rectangles and triangles. The edge a-a remains straight during deformation while all curvature is concentrated at the hinge lines on the element boundaries.

The current in-plane deformation state for one half of the flange B is shown in Fig. 4.10. The shape distortion is assumed to take place in the rectangle $0<z<H$ and $0<y<kH$. The line $y=k(H-z)$ divides the area into two plastic regions which experience different velocity fields.

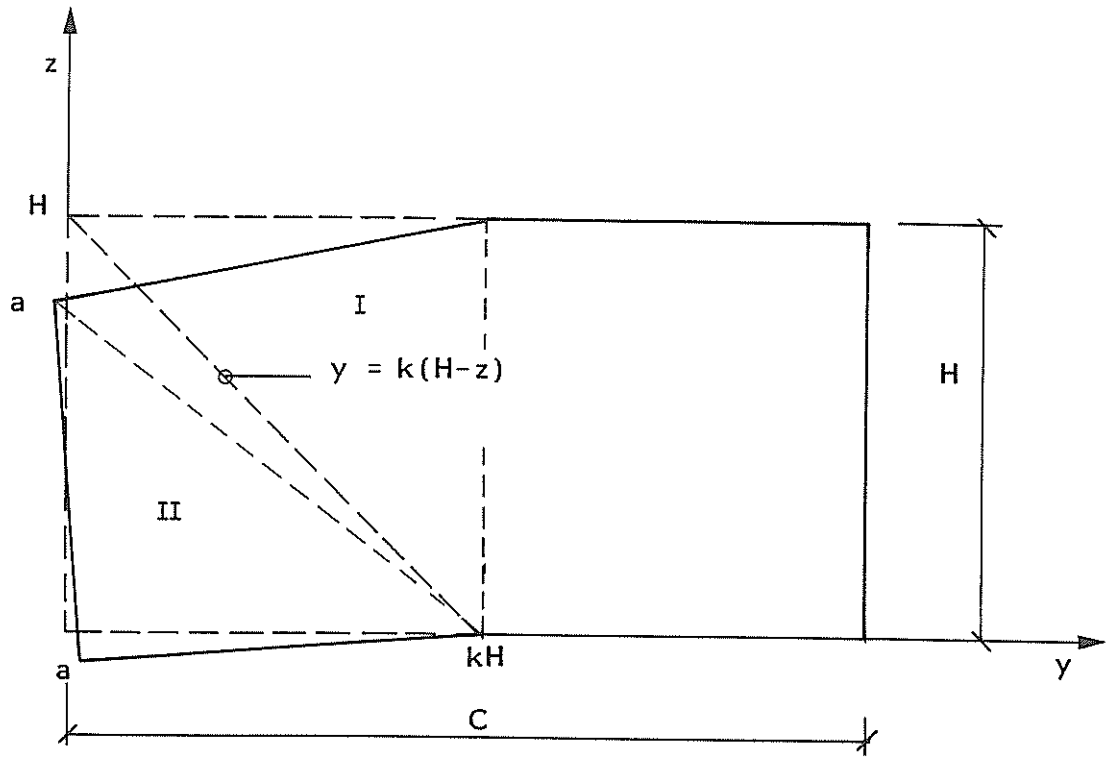

Figure 4.10 *Current deformation state of rectangular element folding in the symmetric mode*

Continuity requirements yield the following displacement components of the material point (0, H)

$$r_{Iy} = - H \left(\sqrt{k^2 + \frac{1}{4}\sin^2 2\alpha} - k \right) \tag{4.92}$$

$$r_{Iz} = - H \sin^2\alpha \tag{4.93}$$

Subtracting the rigid body part of the deformation field, region II is only subjected to compression in the z-direction equal to the shortening of the joint line

$$r_{IIz} = - H (1 - \cos\alpha) \tag{4.94}$$

As for the assymetric mode linear variations of the velocity fields are prescribed:

In region I

$$V_y = V_{Iy}\left(1 - \frac{y}{kH}\right) \tag{4.95}$$

$$V_z = V_{Iz}\left(1 - \frac{y}{kH}\right) \tag{4.96}$$

and in region II

$$V_y = 0 \tag{4.97}$$

$$V_z = V_{IIz}\frac{z}{H} \tag{4.98}$$

where

$$V_{Iy} = \dot{r}_{Iy} \tag{4.99}$$

$$V_{Iz} = \dot{r}_{Iz} \tag{4.100}$$

and

$$V_{IIz} = \dot{r}_{IIz} \tag{4.101}$$

Applying Eq. (4.59) the following strain rate components for region I occur

$$\dot{\varepsilon}_{yy} = -\frac{V_{Iy}}{Hk} \tag{4.102}$$

$$\dot{\varepsilon}_{yz} = \dot{\varepsilon}_{zy} = -\frac{1}{2}\frac{V_{Iz}}{Hk} \tag{4.103}$$

$$\dot{\varepsilon}_{zz} = 0 \tag{4.104}$$

$$\dot{\varepsilon}_{xx} = \frac{V_{Iy}}{Hk} \tag{4.105}$$

In region II the only non-vanishing components are

$$\dot{\varepsilon}_{zz} = \frac{V_{IIz}}{H} \tag{4.106}$$

$$\dot{\varepsilon}_{xx} = -\frac{V_{IIz}}{H} \tag{4.107}$$

The effective strain rate in region I and II is calculated by means of Eq. (4.69)

$$\dot{\bar{\varepsilon}}_I = \frac{\sin 2\alpha}{k\sqrt{3}\sqrt{1 - \frac{\cos^2 2\alpha}{4k^2 + 1}}}\,\dot{\alpha} \tag{4.108}$$

$$\dot{\bar{\varepsilon}}_{II} = \frac{2}{\sqrt{3}}\sin\alpha\,\dot{\alpha} \tag{4.109}$$

The total rate of energy dissipation is found by carrying out the integration of Eq. (4.68).

$$\dot{E}_6 = \sigma_o \int_V \dot{\bar{\varepsilon}}\, dV = \sigma_o khH^2\,(\dot{\varepsilon}_I + \dot{\varepsilon}_{II}) \tag{4.110}$$

Again the angle α varies between o and $\pi/2$ during deformation. Substituting Eqs. (4.108) - (4.109) into Eq. (4.110) and integrating the internal energy dissipation through complete folding comes out to be

$$E_6 = \frac{4}{\sqrt{3}} M_o \frac{H^2}{h}\left\{\sqrt{k^2 + \frac{1}{4}}\left(\frac{\pi}{2} - \arccos\frac{1}{\sqrt{k^2 + 1}}\right) + k\right\} \tag{4.111}$$

Theoretically, the total plastic work is minimum for $k = 0$. Physically, it is natural to assume that the collapse pattern is determined in the early stages of collapse and remains constant during further compression. Accordingly, the k value which minimizes the rate of energy dissipation for $\alpha = 0$ is of interest. This leads to

$$k = 0.573 \tag{4.112}$$

and

$$E_6 = 2.58\, M_o \frac{H^2}{h} \tag{4.113}$$

The rate of work and the total work along the horizontal stationary hinges are given by Eqs. (4.37) - (4.38).

Finally, plastic bending takes place at the inclined hinge separating the plastic regions and at the vertical hinge at $y = kH$.

The inclined hinge has a variable length and the angle changes from 0 to $\pi/2$. The slope discontinuity across the vertical hinge line is related to α by the equation

$$\sin\alpha_o = \left(1 + \frac{4k^2}{\sin^2 2\alpha}\right)^{-\frac{1}{2}} \tag{4.114}$$

α_o increases from zero to a maximum value and then decreases to zero again. The total change of angle will be close to $\pi/2$. Instead of carrying out the exact calculation the contribution from the inclined and vertical hinge is represented by

$$E_7 = \frac{\pi}{2} M_o (1 + k)H \approx \left(\frac{\pi}{2}\right)^2 H \tag{4.115}$$

Strictly, E_7 should be included in the minimization of Eq. (4.111). However, the influence would be of minor significance.

4.3.4 Average Crushing Strength of a Cruciform. Symmetric Mode

The collapse of a four flange cruciform which deforms in the symmetric mode can be modelled with eight elements of the type described above. The total energy balance for making a complete single fold of the length 2H reads

$$2HP_{av} = 8(E_6 + E_7 + E_2) \tag{4.116}$$

and by substitution of the relevant coefficients

$$\frac{P_{av}}{M_o} = 10.32\,\frac{H}{h} + 2\pi\,\frac{C}{H} + \pi^2 \tag{4.117}$$

Eq. (4.117) can be optimized with respect to the wave length H. The minimum exists for

$$H = \sqrt{\frac{2\pi}{10.32}}\,Ch \tag{4.118}$$

and is equal to

$$\frac{P_{av}}{M_o} = 16.10 \sqrt{\frac{C}{h}} + \pi^2 \qquad (4.119)$$

If the loaded edges are clamped against rotation the last term in Eq. (4.116) are doubled and the mean load becomes

$$\frac{P_{av}}{M_o} = 22.78 \sqrt{\frac{C}{h}} + \pi^2 \qquad (4.120)$$

In case of wide-flanged cruciforms the constant term can be neglected.

4.3.5 Comparison with Experiments

Several tests with small-scale soldered cruciforms made of copper sheet with thickness 0-35 mm have been reported by Hayduk and Wierzbicki/46/. Their results are plotted in Fig. 4.11.

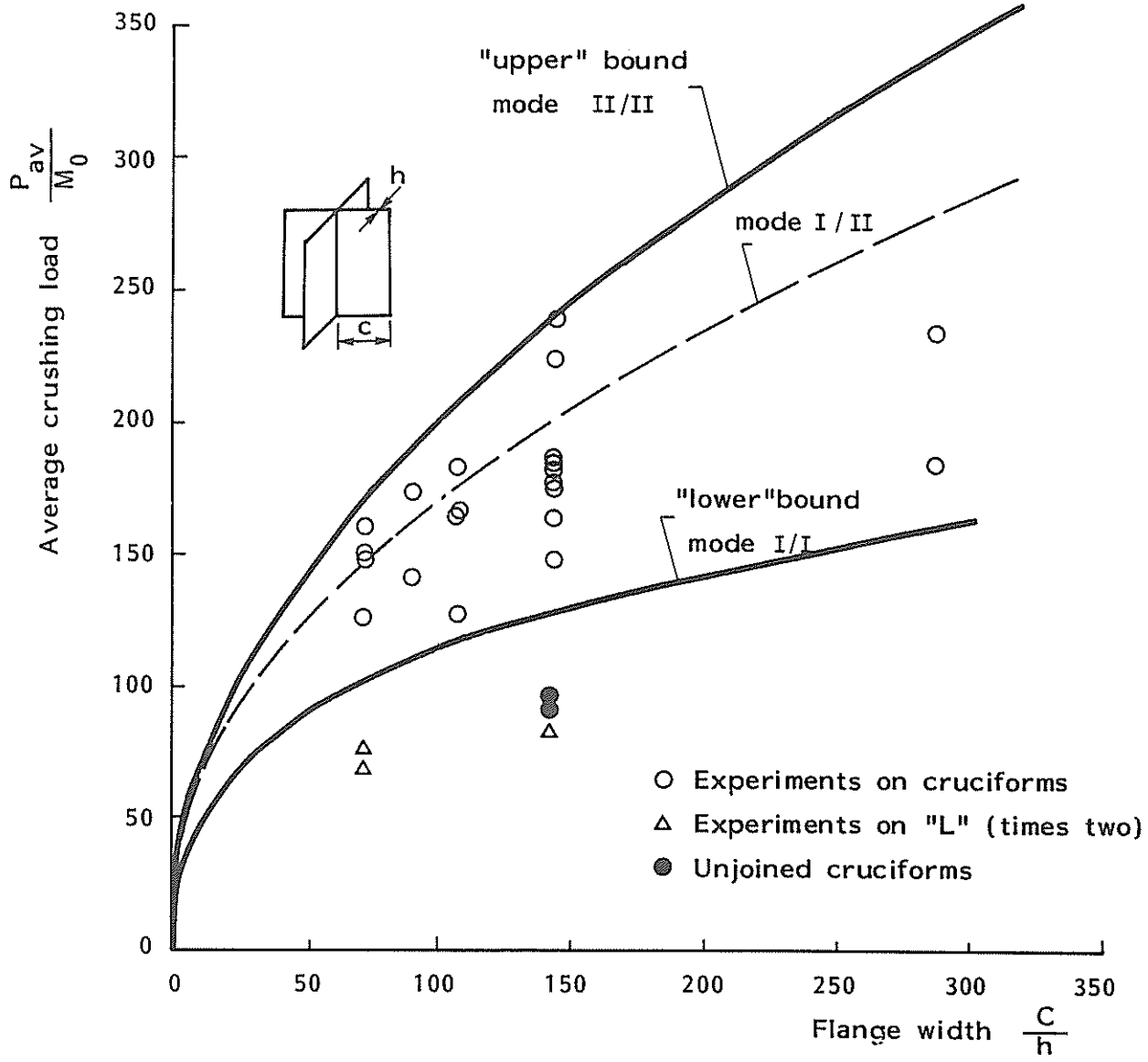

Figure 4.11 Mean crushing strength of a cruciform versus C/h

The theoretical predictions are based on a different deformation mode where the joint line distorts in the plane of symmetry, inclined by 45° to the neighbouring flanges. The upper bound solution is based on the assumption that two of the flanges are subjected to uniaxial extension and that the other two are subjected to uniaxial compression. The lower bound is obtained by the solution for an assemblage of two L-shaped elements, i.e. continuity requirements at the junction are not incorporated.

There is a considerable scatter of the experimental points and the authors concluded that no single, well defined collapse mechanism exists for cruciforms.

The collapse pattern suggested in Ref./46/ is not observed in the present experiments. This may be due to different material and fabrication technique as well as the much larger scale in the present test.

The theoretical predictions shown in Fig. 4.11 are based on clamped boundary conditions. Where several waves develop simply supported boundary conditions may as well be supposed, since two consecutive waves are likely to deflect asymmetrically. This is also a better representation of the conditions during our own tests.

The non-dimensional mean loads for the large scale steel cruciforms are plotted in Fig. 4.12 together with the theoretical load for the asymmetric mode Eq. (4.90) and the symmetric mode Eq. (4.119).

It is observed that the cruciform which collapses in the asymmetric mode (C/h = 100) has a considerably lower capacity than the other three.

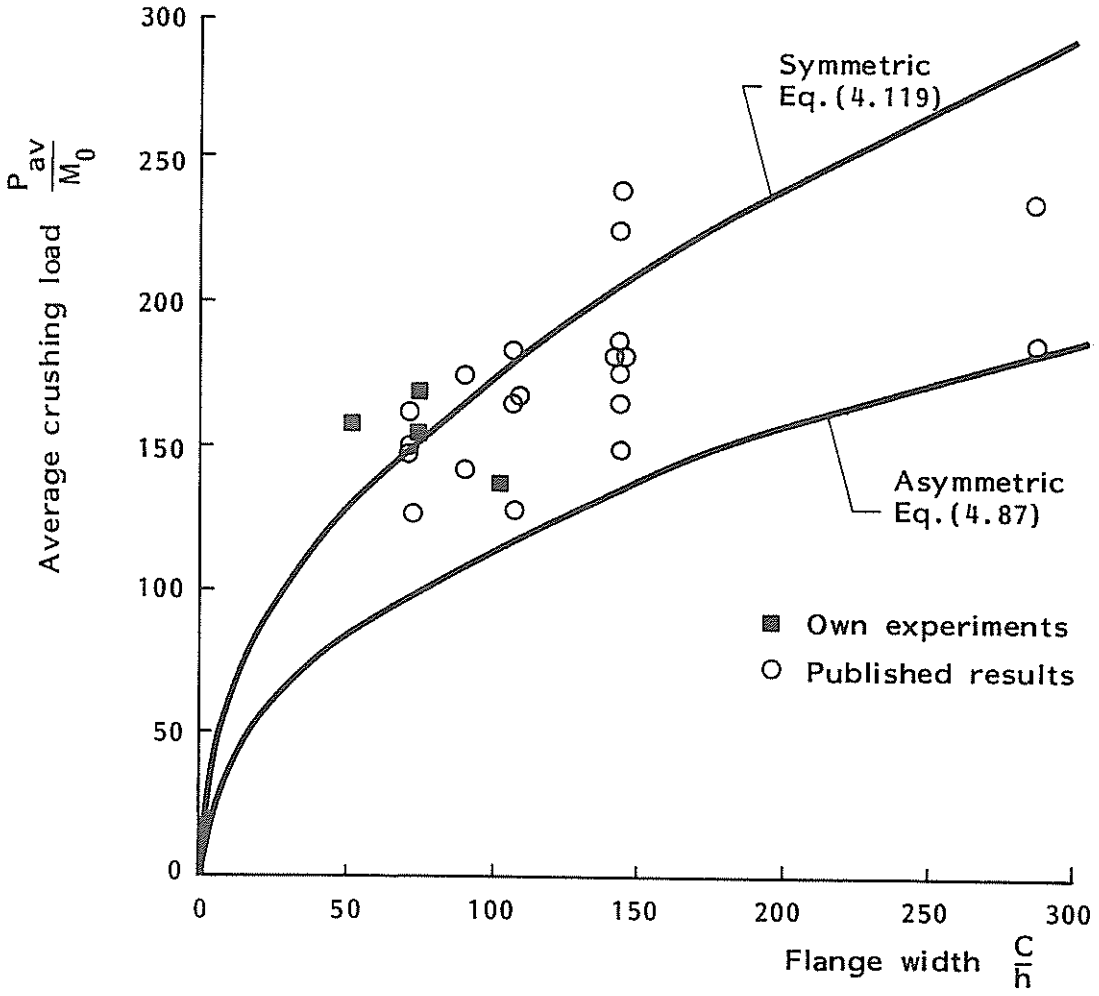

Figure 4.12 *Comparison between theoretical and experimental mean crushing strength of a cruciform*

It is interesting to notice that the theory underestimates the crushing strength in spite of the neglect of joint failures during compression. However, it was observed that the unloading succeeding failure is moderate which indicates that the fracture work itself is significant. Also, the limited compressibility of the cruciform soon brings about a load increase. Although the correlation is satisfactory, the number of tests is obviously insufficient to draw a final conclusion with respect to the quality of the theory.

4.4 Theoretical Crushing Strength of a T-section

A variety of deformation modes exists for T-sections. If it is assumed that the joint line distorts in one of the initial plate planes three different mechanisms are possible as illustrated in Fig. 4.13. Mechanism (a) may be

denoted the angle type mechanism, mechanism (b) the shape distortion mechanism and mechanism (c) the combined mechanism. Mechanism (a) consists of an angle element with an additional flange with only stationary hinges. With the notation of the preceding sections the energy balance equation for an element with clamped edges reads

$$2P_{av}H = 2E_1 + 2E_3 + 12E_2 \tag{4.121}$$

Carrying out the usual minimization, the mean crushing load comes out to be

$$\frac{P_{av}}{M_o} = 13.93 \left(\frac{C}{h}\right)^{\frac{1}{3}} \tag{4.122}$$

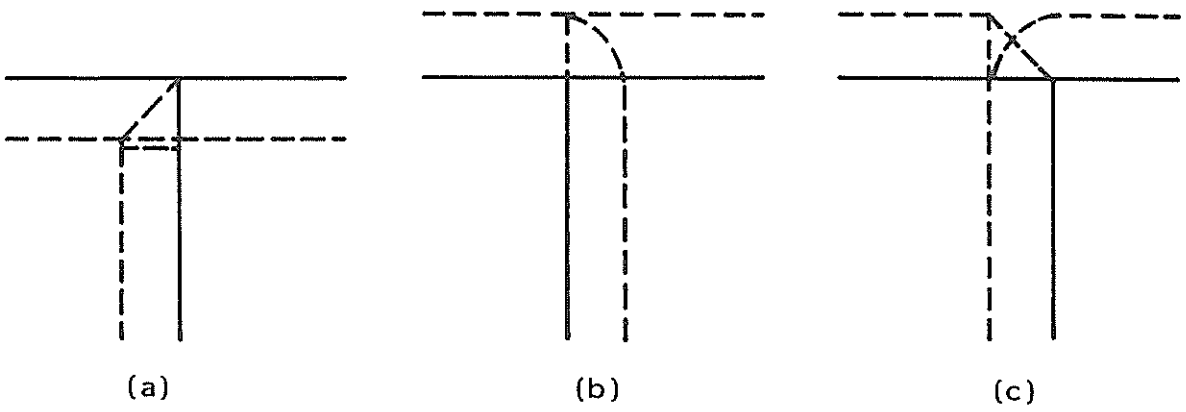

Figure 4.13 *Possible deformation modes of T-sections. Material line at midsection in deformed configuration is dotted*

Mechanism (b) is similar to the asymmetric mode for the cruciform except the flange with the angle type deformation. Hence, the energy balance can be written

$$2P_{av}H = 12E_2 + 2E_4 + 2E_5 \tag{4.123}$$

Neglecting the small constant term due to E_5 the mean load becomes

$$\frac{P_{av}}{M_o} = 10.98 \sqrt{\frac{C}{h}} \tag{4.124}$$

Mechanism (c) is constituted by an angle element together with a shape distorted flange. It contains all the previous energy dissipation terms

$$2P_{av}H = 2E_1 + 12E_2 + 2E_3 + 2E_4 + 2E_5 \tag{4.125}$$

Applying the minimization procedure described for the cruciform in Sec. 4.3.2 there comes out

$$\frac{P_{av}}{M_o} = 13.93 \left(\frac{C}{h}\right)^{\frac{1}{3}} \left\{ 0.87 + 0.69 \left(\frac{C}{h}\right)^{\frac{1}{4}} \right\}^{\frac{2}{3}} \tag{4.126}$$

The average crushing strength is plotted versus the slenderness parameter β in Fig. 4.14. It is seen that the average stress for mechanism (a) falls below the curve for the angle element, while the strength for the two other mechanisms is between the cruciform and the angle.

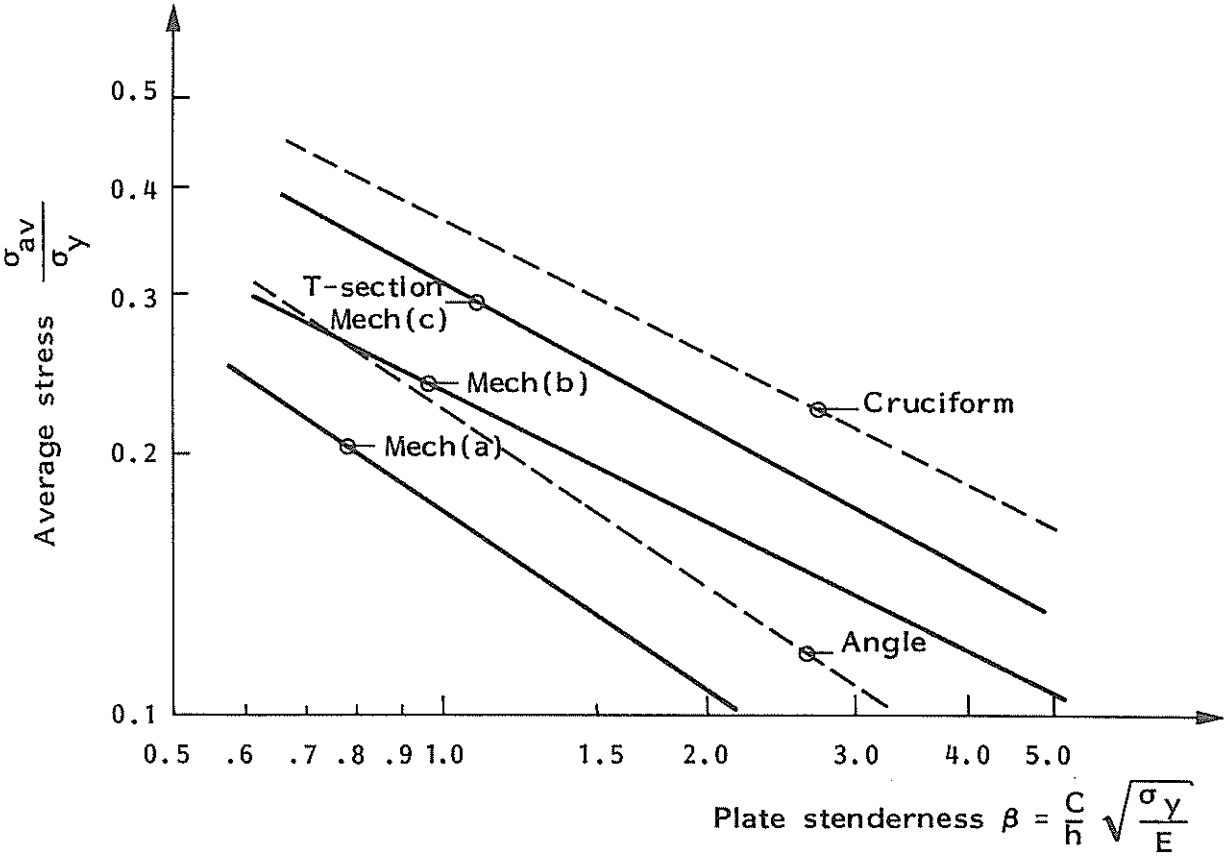

Figure 4.14 Average crushing strength of basic connections

For isolated, ideal elements mechanism (a) would be the natural deformation pattern. However, if initial imperfections or edge distortions are present, a deformation mode with greater energy dissipation is probable.

4.5 Folding Mechanism for an Oblique Angle

In this section the compression of wedge shaped rectangular sections is considered. The collapse model of one quarter section is illustrated in Fig. 4.15.

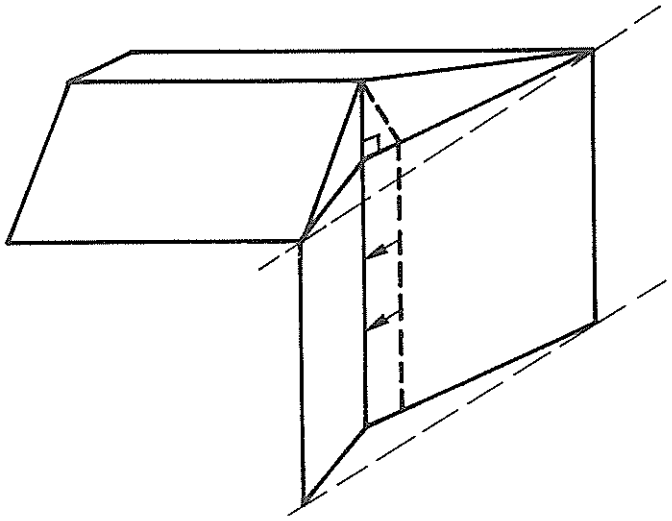

Figure 4.15 Collapse mechanism for an oblique angle

The model resembles the basic folding mechanism. The main difference is due to the fact that one of the midsection hinges is forced to travel so as to maintain continuity. The rolling radius is essentially the same as the large radius of the toroidal surface studied in Sec. 4.2. However, this parameter condensed during the elaborations and remains unknown. Probably, it could be determined by using more complete expressions to the expense of a considerably more complicated calculation. Alternatively, the radius will be determined by semi-empirical techniques.

First, the energy dissipation in a travelling hinge with variable radius is studied in more detail, see Fig. 4.16.

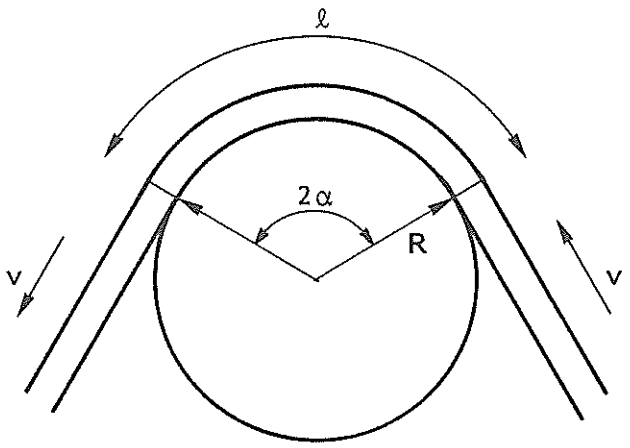

Figure 4.16 Travelling hinge with variable radius

There are two contributions to the energy dissipation. One part stems from the discontinuity in the rate of rotation where the material enters and leaves the hinge. The second part is due to the continuous change of curvature of the material in the yield zone.

The total energy dissipation can be expressed in terms of the radius of curvature R, the length of the yield zone $l = R\alpha$, and the velocity of the travelling hinge v.

$$\dot{E} = M_o \left\{ \frac{|v + \dot{l}| + |v - \dot{l}|}{R} + 2\alpha \frac{|\dot{R}|}{R} \right\} C \dot{\alpha} \qquad (4.127)$$

It is natural to assume the rolling radius R initially infinite and decreasing to a final value. On the other hand the yield zone should extend from zero.

Thus, if $\dot{l} < v$ Eq. (4.127) can be written

$$\dot{E} = 2M_o \left\{ \frac{v}{R} - \alpha \frac{\dot{R}}{R} \right\} C \dot{\alpha} \qquad (4.128)$$

On the other hand when $\dot{l} > v$

$$\dot{E} = 2 M_o C \dot{\alpha} \qquad (4.129)$$

which is identical to the expression for a stationary hinge.

Any functional relationship between the rolling radius R and α are subjected to the above mentioned constraints. Obviously

$$R = (\pi/2)^k R_o \alpha^{-k}, \quad 0 < k < 1 \tag{4.130}$$

yielding

$$1 = (\pi/2)^k R_o \alpha^{-k+1} \tag{4.131}$$

expresses the relationship principally correct.

Applying Eqs. (4.128) - (4.130)

$$\dot{E} = 2M_o \left\{ \frac{v}{R_o} \left(\frac{\alpha}{\pi/2}\right)^k + 1 \right\} C \dot{\alpha} \tag{4.132}$$

The second term is independent of the power k and is equivalent to the energy dissipation in a stationary hinge. The first term decreases with increasing k. Since the minimum energy is sought Eq. (4.132) is solved in the limit k = 1.

The velocity of the travelling hinge in Fig. 4.15 is found from the geometry

$$v = H tg\mu \cos\alpha \cdot \dot{\alpha} \tag{4.133}$$

where 2μ denotes the top angle of the wedge-shaped section.

When $k \to 1$ the length of the yield zone $l \to \pi/2\ R_o$ and Eq. (4.127) can be used to find the total energy dissipation

$$E = M_o \left\{ \left(2 - \frac{4}{\pi}\right) \frac{H tg\mu}{R_o} + \pi \right\} C \tag{4.134}$$

It still remains to determine the final value of the rolling radius. The experiments with bow models indicate that the total plastic strain in the hinges becomes approximately equal to the strain at the point of ultimate strength in uniaxial tensile test, ε_u,

$$\varepsilon_u = \frac{h}{2R_o} \tag{4.135}$$

Accordingly, Eq. (4.134) can be written

$$E = M_o \{ 1{,}45\ \varepsilon_u \frac{H}{h} \operatorname{tg}\mu + \pi \} C \tag{4.136}$$

The deviation above is approximate in the sense that the real collapse geometry of the two waves is not symmetric. This also affects the energy dissipation in the travelling hinges and on the toroidal surface. However, an accurate calculation would be considerably more complicated.

The first term in Eq. (4.136) yields an additional energy contribution compared with the angle element. The mean load of this component is independent of the free parameters H and r so that the total average load reads

$$\frac{P_m}{M_o} = 3 (A_1 A_2 A_3 \frac{c}{h})^{\frac{1}{3}} + A_8 \frac{c}{h} \tag{4.137}$$

where

$$A_8 = 0.73\ \operatorname{tg}\mu\varepsilon_u \tag{4.138}$$

It appears that the term due to rolling of the side becomes increasingly important with increasing flange width. On the other hand it may be questioned whether the entire side actually is affected by the deformation process at the corner.

The experiments show that the rolling process is not initiated automatically, but may be imposed if the load is applied through a wide rigid plate.

Unfortunately experiments have not been carried out which are fitted to support this theory.

4.6 Folding Mechanisms for Circular Shells

The postbuckling behaviour of circular tubes may take on two forms, one with the shell in axisymmetric convolutions, the other in which asymmetric folds are developed. The latter mode is the general collapse mode for thin tubes but is not encountered in thick tubes or in tubes with closely spaced ringstiffeners similar to bulbous bows. Accordingly, the asymmetric mode is

not dealt with in the present study. Reference is made to /47,48/. A particular case of axisymmetric deformation is the tube inversion /49.50/. This is a possible mechanism for unstiffened rotationally symmetric shells but often requires a properly shaped die. Except for the spherical tip of the bulb the internal stiffening system prevents the development of such mechanisms.

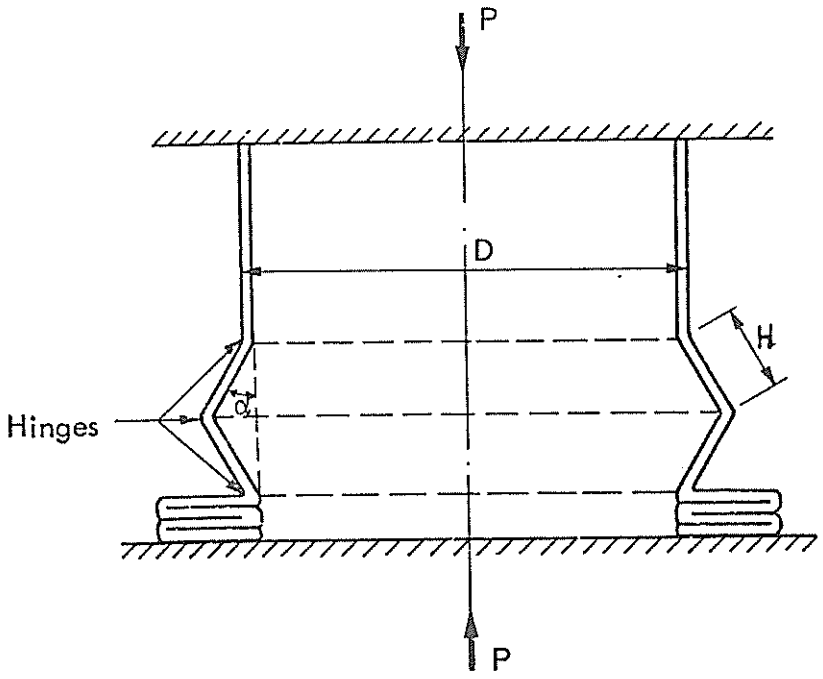

Fig. 4.17 Axisymmetric collapse model for a circular tube. /51/

The axisymmetric mode for an unstiffened tube has been studied by Alexander /51/. The collapse model is shown in Fig. 4.17. Elastic strains are neglected and a rigid-plastic material without strain hardening is assumed.

There are two contributions to the internal energy dissipation, namely the work associated with bending at the stationary yield lines and stretching in the circumferential direction, respectively.

The rate of work in the three hinges is given by

$$\dot{E}_8 = 4M_0\pi(D + H\sin\alpha)\dot{\alpha} \qquad (4.139)$$

where M_0 is the plastic moment per unit circumferential length of the hinge, D is the shell diameter, H is the buckling half wave and α is the current

rotation angle. It is natural to assume that the material is deformed under substantially plane strain conditions so that the flow stress in the plastic moment expression takes the form

$$\sigma_p = \frac{2}{\sqrt{3}} \sigma_o \tag{4.140}$$

where σ_o is the flow stress in uniaxial testing.

The rate of work related to stretching of the material in the circumferential direction can be expressed.

$$\dot{E}_g = 2\pi\sigma_o H^2 h \cos\alpha \, \dot{\alpha} \tag{4.141}$$

The external rate of work is

$$\dot{E}_e = P \cdot 2H \sin\alpha \, \dot{\alpha} \tag{4.142}$$

The instantaneous crushing force is determined by equating the internal and external rate of energy dissipation

$$P = \frac{\pi\sigma_o h^2}{\sqrt{3}\sin\alpha} \left(\frac{D}{H} + \sin\alpha + \sqrt{3}\frac{H}{h} \cos\alpha\right) \tag{4.143}$$

The load is sketched versus axial deformation in Fig. 4.18 For $\alpha \to 0$, $P \to \infty$.

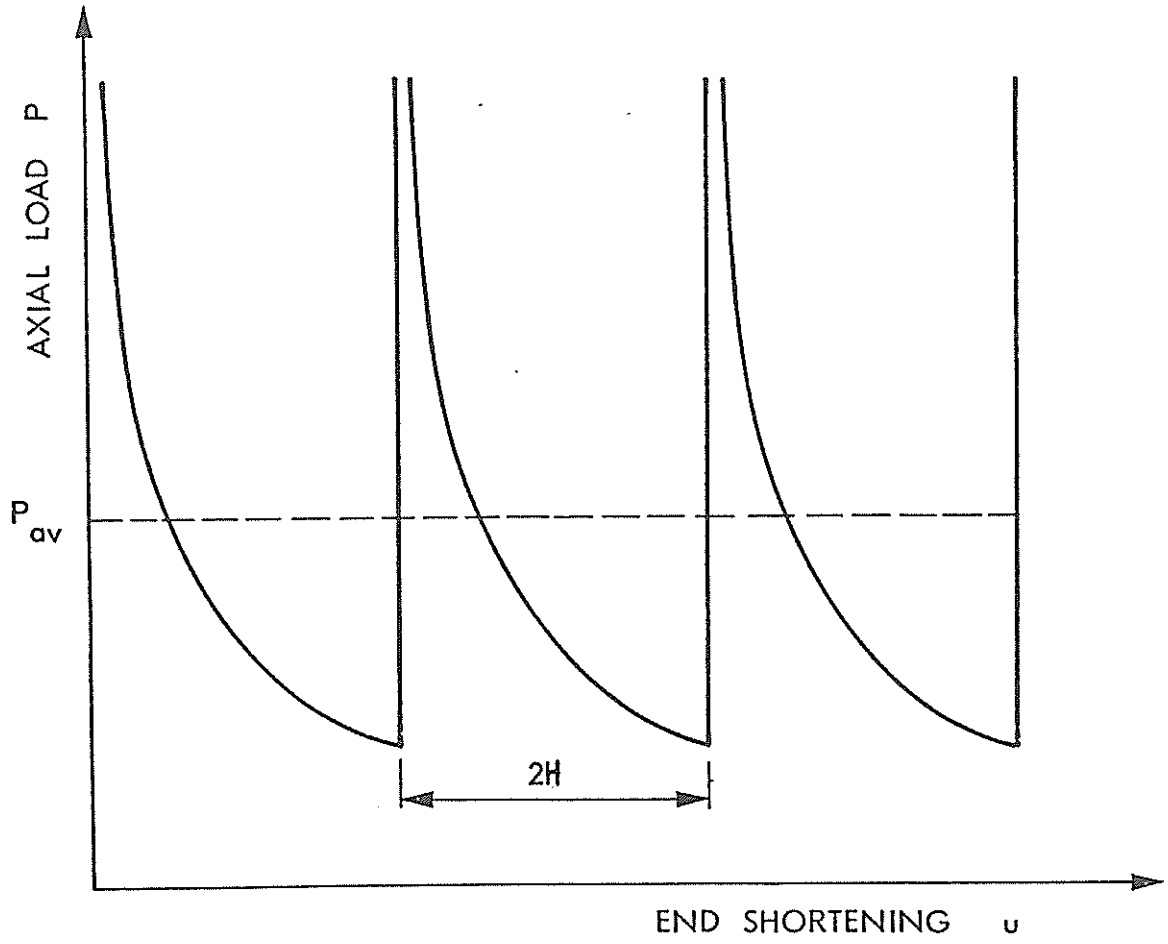

Fig. 4.18 Load deformation relationship predicted by theory.

However, in practice, the load level is limited by the initial buckling strength of the cylinder wall.

For the present purpose it is more convenient to operate with the average crushing load. Integrating the various energy terms there comes out

$$P_{av} = \frac{\pi \sigma_o h^2}{\sqrt{3}} \left(\frac{\pi}{2} \frac{D}{H} + 1 + \sqrt{3} \frac{H}{h} \right) \qquad (4.144)$$

The expression may be differentiated with respect to H to obtain the minimum load

$$D_{av} = \frac{\pi \sigma_o h^2}{\sqrt{3}} \left(3.3 \sqrt{\frac{D}{h}} + 1\right) \qquad (4.145)$$

for $H = 0.953 \sqrt{Dh}$

The load function in Eq. (4.145) is not very sensitive to variation in H. Hence, if the shell is provided with ring stiffeners it is likely that the

wave length within reasonable intervals will be equal to the stiffener spacing. It is interesting to notice that the wave length based on plastic analysis is rather close to the elastic buckling length, $H = 1.22\sqrt{Dh}$.

For elliptical cross-sections with relative small eccentricities the same approach applies provided that an equivalent diameter is introduced which yields a perimeter equal to that of the ellipse.

For large eccentricities or when the structure can be considered as an assemblage of two sections of a circular cylinder with a slope discontinuity at the intersections, the energy dissipated by membrane stretching is reduced. The contribution should only be taken proportional with the fraction of the total central angle of the shell sections to the angle of revolution.

4.7 Ultimate Strength Versus Mean Compressive Strength of Basic Elements

The results obtained for the collapse mechanisms are not directly comparable to the maximum strength formulas since the former is correlated to the flow stress σ_0 rather than the compressive yield stress σ_y.

In most tests the average loads are compared to predictions based upon ultimate stress. Tensile tests show that this is in the range of 1.3-1.5 times the yield stress. Introducing

$$\sigma_u = 1.4\,\sigma_y \tag{4.146}$$

the average load formulas can be expressed in the format of the maximum strength, Eq. (4.12). For the angle element the average stress becomes

$$\frac{\sigma_{av}}{\sigma_y} = 0.22\left(\frac{1}{\beta}\right)^{0.67} \tag{4.147}$$

and for the cruciform

$$\frac{\sigma_{av}}{\sigma_y} = 0.37\left(\frac{1}{\beta}\right)^{0.50} \tag{4.148}$$

where $\beta = \frac{b}{h}\sqrt{\frac{\sigma_y}{E}}$ (4.149)

The average loads are compared with maximum strength predictions due to Gerard /13/ in Fig. 4.19.

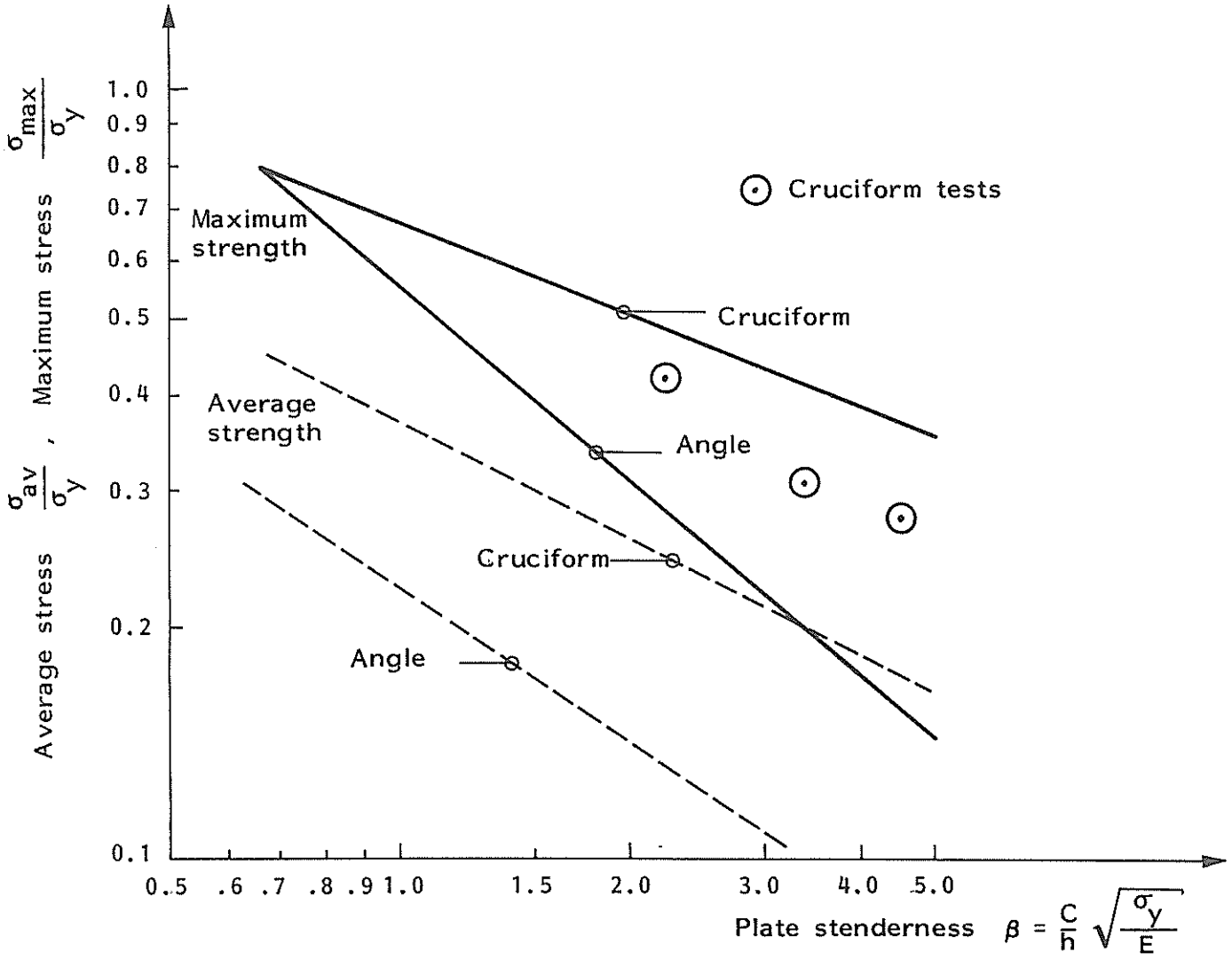

Figure 4.19 *Average crushing strength versus maximum strength of basic elements*

It is interesting to notice that the maximum strength is roughly two times greater than the average compressive strength over a wide interval.

It should be pointed out that the formulas for ultimate strength are valid for plates where the length of the unloaded edges exceeds the width of the loaded edges so that one fully elastic buckling wave is accommodated. For

transversely framed bow structures this restriction is often not complied with so the formulas should be used with care.

The width of the tested cruciform elements exceeded or was equal to the length. As could be expected the recorded maximum strength is smaller than what is predicted by the semi-empirical approach. The best fit is obtained for the square flanged specimen.

4.8 Dynamic Effects

4.8.1 Average Strain Rates in the Basic Folding Mechanism

In Sec. 4.2 it is shown that the crushing process of a rectangular cross-section can be modelled by some characteristic deformation modes, such as bending about stationary and travelling hinge lines and extension and bending on a toroidal surface.

In order to evaluate the effect of the speed of deformation on the energy absorption the strain rates must be determined. Unfortunately, the strain rates cannot be directly calculated from the model, but must be estimated approximately.

In a rigid plastic model the curvature of a stationary hinge is infinite, but remains finite when strain-hardening and strain rate sensitivity are taken into account.

Consider the bending of an initially flat strip of unit width about a hinge to the final radius r_s. In the rigid-viscoplastic model, the curvature is assumed to change continuously with an average curvature rate

$$\dot{\kappa}^s_{av} = \frac{\frac{1}{r_s}}{\Delta t} \tag{4.150}$$

where the duration of the process is equal to the time required to complete a fold of length 2H when the rate of axial shortening is

$$\Delta t = \frac{2H}{V} \tag{4.151}$$

Thus, Eq. (4.150) becomes

$$\dot{\kappa}^{s}_{av} = \frac{V}{2Hr_s} \tag{4.152}$$

On the travelling hinges the rate of rotation is related to the tangential velocity V_t and the small radius of the toroidal surface r,

$$\dot{\alpha}_r = \frac{V_t}{r} \tag{4.153}$$

The discontinuity in the rate of rotation where the material enters the circular arc implies infinite rate of curvature. In the rigid- viscoplastic model the process is assumed to have a finite extension ξ so that the mean rate of curvature becomes

$$\dot{\kappa}^{r}_{av} = \frac{V_t}{r_\xi} \tag{4.154}$$

Here, the deformation zone ξ is unknown. A useful approximation is to assume a constant relationship between V_t and ξ

$$\frac{V_t}{\xi} = \frac{V}{2H} \tag{4.155}$$

This is a valid assumption since initially the tangential velocity is very large and so is the rolling radius r and the deformation zone ξ. Later on V_t as well as ξ diminish.

This yields

$$\dot{\kappa}^{r}_{av} = \frac{V}{2Hr} \tag{4.156}$$

The strain rate varies linearly over the shell thickness. A good mean value is obtained by

$$\dot{\varepsilon}_{av} = \dot{\kappa}_{av} \frac{h}{4} \tag{4.157}$$

yielding

$$\dot{\varepsilon}^{s}_{av} = \frac{V}{8H}\,\frac{h}{r_s} \tag{4.158}$$

$$\dot{\varepsilon}^{r}_{av} = \frac{V}{8H}\,\frac{h}{r} \tag{4.159}$$

Thus the same strain rates are encountered provided that the rolling radius r, and the final radius of curvature r_s of the stationary hinge are equal. In the following this is assumed. According to Ref. /52/ experiments have shown that h/r is likely to fall in the range 1/5-1. Thus with h/r = 1

$$\dot{\varepsilon}_{av} = \frac{V}{8H} \tag{4.160}$$

The strain rate on the toroidal surface is given in /43/.

$$\dot{\varepsilon}^{t}_{av} = \frac{V_t \sin\Theta}{a + b\cos\Theta} \tag{4.161}$$

Hence

$$\dot{\varepsilon}^{t}_{av} = \frac{1}{2\psi}\int_{\frac{\pi}{2}-\psi}^{\frac{\pi}{2}+\psi} \dot{\varepsilon}^{t}\, d\theta = \frac{V_t}{a}\,\frac{\sin\psi}{\psi} \tag{4.162}$$

ψ varies from 0 to ψ_0 where $2\psi_0$ defines the angle between two adjacent panels. The trigonometric term is approximately equal to unity.

The large radius of the toroidal surface is an undetermined parameter unless it is assumed much larger than the small radius r. However, it is observed that if a constant relationship

$$\frac{V_t}{a} = \frac{V_t}{4r} = \frac{V}{8H} \tag{4.163}$$

is introduced a similar expression for the mean strain rate on the toroidal surface is arrived at

$$\dot{\varepsilon}_{av} \sim \frac{V}{8H} \tag{4.164}$$

The present analysis is very crude. Yet, the derived formulas are believed to be predict at least the order of magnitude of the average strain rates.

An important result is that the strain rates for various mechanisms of energy dissipation are approximately equal.

Thus their relative contributions to the total crushing load are independent of the speed.

4.8.2 Material Strain Rate Sensitivity

The yield point and flow stress of steel are affected by the temperature as well as the rate of the strain applied to the material. Fig. 4.20 /53/ shows the influence of the strain rate on the tensile stress-strain relationship of mild steel tested at room temperature. Some important features are observed.

- The strain at ultimate stress and the fracture elongation do not depend on the strain rate except for extremely low speeds (due to strain-aging)
- The (lower) yield stress increases considerably more with the strain rate than does the ultimate stress.

For gross plastic deformation the total energy absorption capability is of interest.

Fig. 4.21 /54/ shows a rearrangment of the results presented in Ref. /53/. The total work up to fracture and the average flow stress are plotted versus the strain rate.

It is seen that there is a noticable increase in the average flow stress for high strain rates.

Various formulas have been proposed for correlating stress and strain rate.

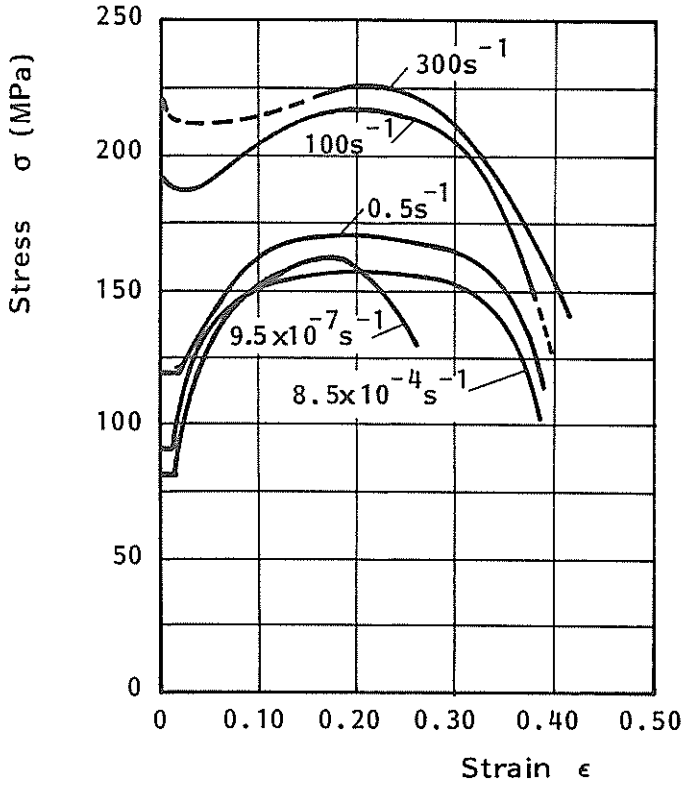

Figure 4.20 Stress-strain curves for various rates of strain /53/

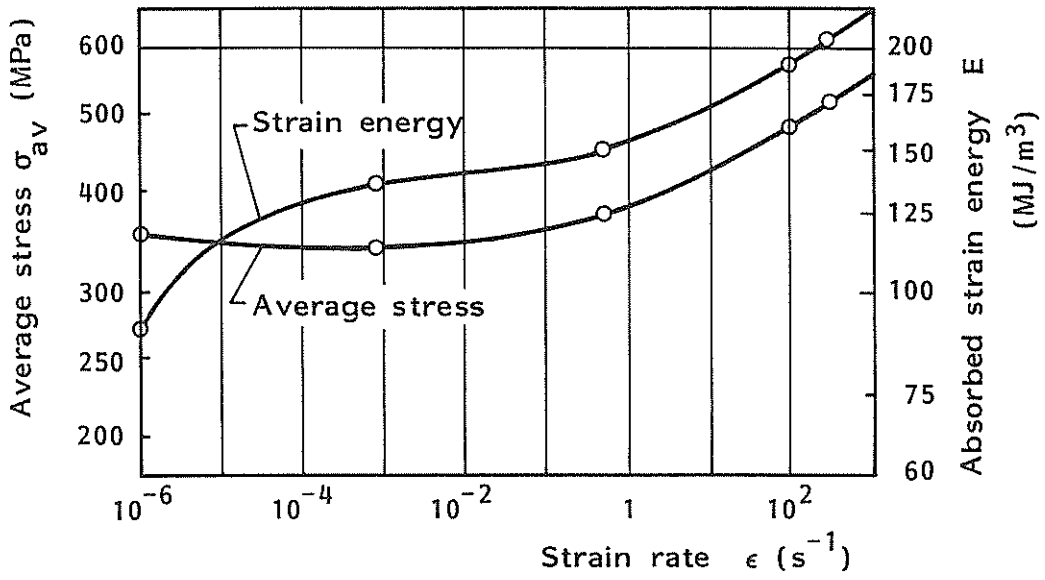

Figure 4.21 Total strain energy and average stress for various rates of strain /54/

For the dynamic upper yield stress Cowper and Symonds /55/ propose

$$\frac{\sigma_y^1}{\sigma_y} = 1 + \left(\frac{\dot{\varepsilon}}{\dot{\varepsilon}_0}\right)^{\frac{1}{n}} \tag{4.165}$$

where $\dot{\varepsilon}_0$ and n are material constants determined to get the best fit of experimental data. Fig. 4.20 was used to obtain $\dot{\varepsilon}_0 = 40$ and $n = 5$ for mild steel.

A similar but weaker dependency on the strain rate has been suggested for the average flow stress /56/

$$\frac{\sigma_0^1}{\sigma_0} = 1 + \left(\frac{q\dot{\varepsilon}}{\dot{\varepsilon}_0}\right)^{\frac{1}{n}} \tag{4.166}$$

where q is an empirical constant (0.01 for mild steel). Other forms that have been applied are

$$\frac{\sigma_0^1}{\sigma_0} = 1 + c \ln \frac{\dot{\varepsilon}}{\dot{\varepsilon}_0} \tag{4.167}$$

and

$$\frac{\sigma_0^1}{\sigma_0} = \left(\frac{\dot{\varepsilon}}{\dot{\varepsilon}_0}\right)^n \tag{4.168}$$

One disadvantage of the formulas above is that they do not approach unity for small strain rates. Hence, a good fit of experimental data can only be obtained for a limited range of strain rates. However, Eq. (4.168) is a very useful tool for correlating a model with a prototype when two tests are run at different speeds V_0 and V_1. Applying Eqs. (4.160) and (4.164) the ratio of the mean loads is

$$\frac{P_{av_1}}{P_{av_0}} = \frac{\sigma_1^1}{\sigma_0^1} = \left(\frac{V_1}{V_0}\right)^n \tag{4.169}$$

Thus the strain rate influence depends only on one single material parameter n, which may be determined experimentally.

4.8.3 Inertia Effects

In the classical theory of elasticity the stability of an elastic body is derived under the assumption of static equilibrium between internal and external forces. For dynamically applied loads the inertia forces of the element may become significant.

It is normal to distinguish between impact loads and rapidly applied loads. In the former case the effects must be considered in terms of stess wave propagation within the body so that at any instant the stress and strain distribution will be inhomogeneous. For a rapidly applied load the time required to reach the critical load is much greater than the time required for a pressure wave to travel from one end of the element to the other. Thus in-plane inertia effects are neglected and only the motion normal to the middle surface needs to be considered.

The complexity of the governing equations of motion is such that numerous simplifications have to be made in order to achieve any tractable analysis. Hence, the dynamic influence will be discussed in rather qualitative terms based on studies of simple, idealized cases.

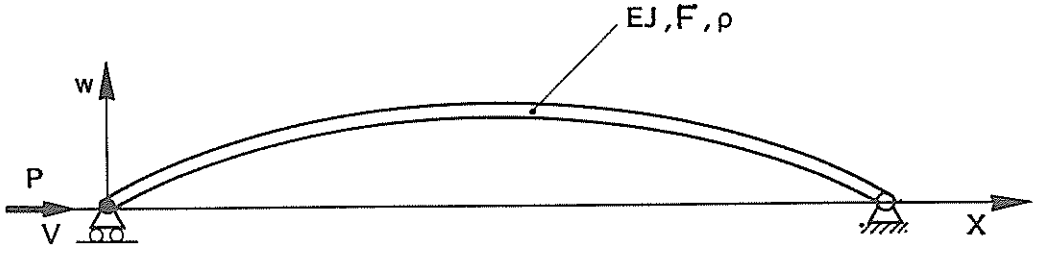

Figure 4.22 Dynamically loaded column

Consider the strut in Fig. 4.22. The motion of an elastic element is governed by the equations /57/

$$EJ\left(\frac{\partial^4 w}{\partial x^4} - \frac{\partial^4 w_o}{\partial x^4}\right) + \frac{\partial}{\partial x} P \frac{\partial w}{\partial x} + \rho F \frac{\partial^2 w}{\partial t^2} = 0 \qquad (4.170)$$

$$P + FE\left\{\frac{\partial u}{\partial x} + \frac{1}{2}\left\{\frac{\partial w^2}{\partial x^2} - \frac{\partial w_o^2}{\partial x^2}\right\}\right\} = 0 \qquad (4.171)$$

$$\frac{\partial P}{\partial x} + \rho F \frac{\partial^2 u}{\partial t^2} = 0 \qquad (4.172)$$

where the properties of the element are described by the bending rigidity EJ, the cross-sectional area F and the mass density ρ. The displacement components on the axial and lateral direction are designated u and w respectively. w_o is initial deflection.

Eq. (4.170) is the equation of lateral motion neglecting rotary inertia, shear and Poisson's effect. Eq. (4.171) is the axial strain-displacement relation and Eq. (4.172) expresses longitudinal equilibrium.

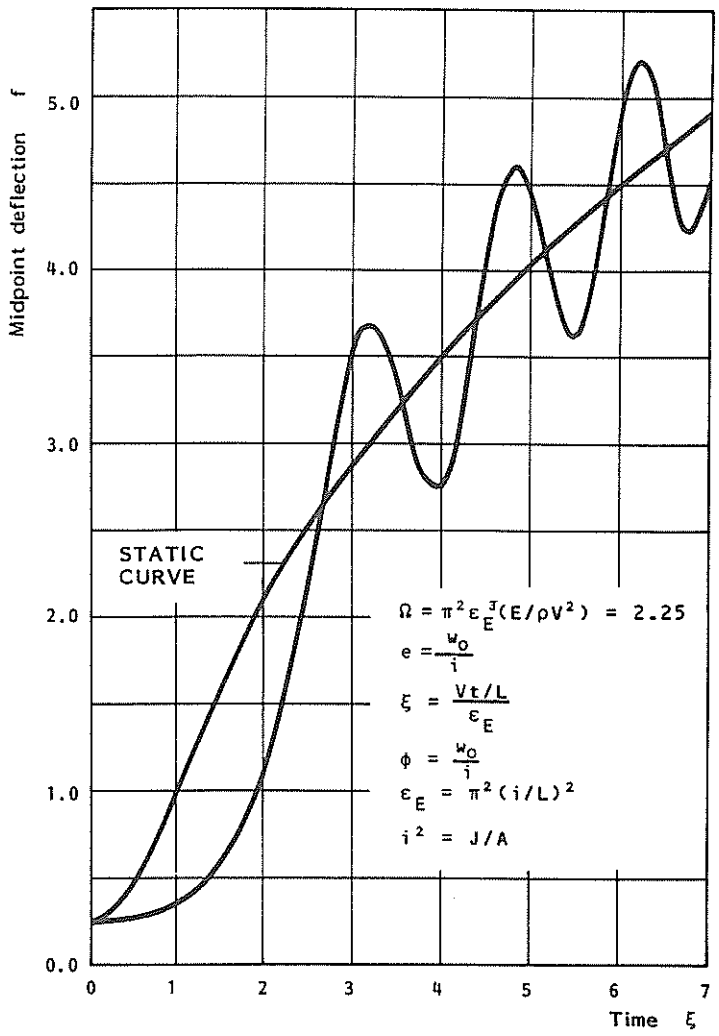

Figure 4.23 Deflections of mid-point of column, /58/

Hoffet.al/57,58/have solved Eqs. (4.170) and (4.171) by numerical means neglecting axial inertia forces. As illustrated in Fig. 4.23, initially, there is a time lag between the static and dynamic solution caused by lateral inertia forces which increases with the rate of loading. Subsequently the dynamic response oscillates about the static curve. The maximum load attained by the column is plotted in Fig. 4.24 versus the socalled dynamic similarity number. It shows that very large overload factors can occur if the initial deflection and the dynamic similarity number are small.

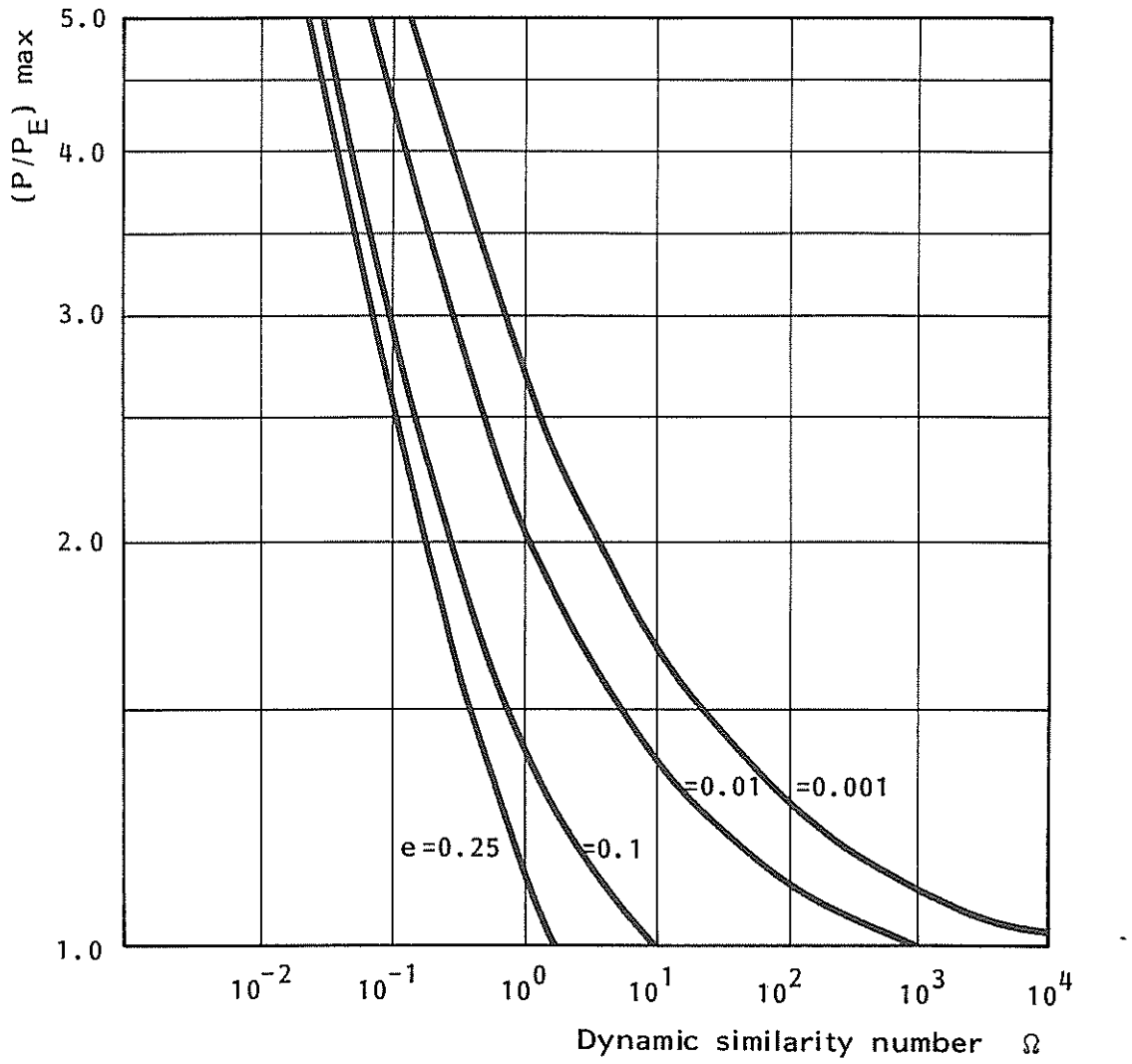

Figure 4.24 Dynamic augmentation of buckling load /57/

Ekstrøm /59/ has extended this approach to rectangular orthotropic plates.

Consider a longitudinal impact at a speed of 2.0 m/s on a transversely stiffened plate field (a = 0.6 m) for which the Euler stress is supposed to be σ_E = 150 N/mm^2. This yields a dynamic similarity number Ω = 0.024. The dynamic augmentation factor depends on the imperfection parameter $e = w_o/i$, where i = 5.1 mm is the radius of gyration. Inspection of Fig. 4.24 indicates that considerable magnification of the buckling load is possible for moderate initial imperfection.

The solution to the axial equilibrium condition Eq. (4.71) gives the speed of wave propagation

$$V_C = \sqrt{\frac{E}{\rho_o}} \tag{4.173}$$

The propagation of stress is related to the speed of impact V by

$$\sigma = \frac{V}{V_C} E \tag{4.174}$$

A usual hypothesis is that on impact the stress front propagates along the specimen, and when it has traversed a length equal to the static instability wave length corresponding to the stress level, buckling occurs. The static Euler load for a rod with length ℓ and radius of gyration i is

$$\sigma = \varepsilon_E E = \pi^2 \left(\frac{i}{\ell}\right)^2 E \tag{4.175}$$

By elimination of σ the slenderness there is obtained

$$\bar{\lambda} = \frac{\ell}{i} = \pi \sqrt{\frac{V_C}{V}} \tag{4.176}$$

Thus, the wave length decreases with increasing velocity. This tendency is confirmed by experiments which also show that the deformations are concentrated towards the frontal end of the rod.

Eq. (4.106) can alternatively be expressed by the reduced slenderness ratio

$$\bar{\lambda} = \frac{\lambda}{\lambda_y} = \sqrt{\frac{V_C}{V} \frac{\sigma_y}{E}} \tag{4.177}$$

Consider impact against a mild steel specimen with a speed v = 2.0 m/s. Assuming σ_y = 250 N/mm^2 one finds a slenderness ratio $\bar{\lambda}$ = 1.75.

This corresponds to a Euler stress equal to σ_E= 81 N/mm^2. Obviously, this is in the range of actual buckling stresses for transversely framed deck structures, indicating that situations may arise where the buckling wave length may be smaller than the frame spacing. However, for the present calculations this effect is considered of minor importance and is neglected.

4.8.4 Fracture

The initiation of plate fracture is greatly affected by plate thickness and does not lend itself to scaling. Thus small scale model tests may strongly overestimate the energy dissipated in actual ship structures, especially where membrane effects predominate.

Furthermore, plate fracture is also influenced by strain rate and temperature.

An attempt to incorporate the fracture criteria in crushing force predictions is presented in Ref. /10/. Three point bending tests were carried out with I-beams in order to obtain data for nominal strain at the instant of plate fracture. The specimens were made of materials with different thicknesses covering the range from model size to thick plates usually employed in ship structures. Some of the specimens were provided with a notch simulating a crack likely to exist in actual ship plates.

The tests revealed almost no notch influence on the ductility of thin plates. On the other hand, the notched specimen of 20 mm plate thickness appears to have a typical brittle fracture behaviour. As seen in Table 4.1 the nominal fracture strain is more than halved compared with the unnotched specimen. The authors compensate for this effect by reducing proportionally the deformations at the instant of fracture.

Plate Thickness	With Notch	Unnotched
20 mm	0.05	0.12
6 mm	0.18	0.23
2.3 mm	0.19 - 0.25	

Table 4.1 Nominal Strain at Fracture /10/

A fracture mechanics approach to this problem has been presented in Ref. /23/. Based upon crack opening displacement (COD)-values and critical crack lengths estimates of the fracture strain could be derived. The strong thickness dependency was also confirmed by theoretical means. Evidently, there is a need for further research in this area.

In the present investigation fracture considerations are not included in application of the theoretical crushing models to full scale collisions.

The main reason for this is that the data foundation is still very incomplete. Furthermore, the strains are not explicitly derived in the calculation models. However, contrary to sideway collisions membrane effects are much less predominant in longitudinal impacts. The neglect of reduced ductility may also be compensated by other effects, such as lower compressibility of actual ships.

5. MEAN CRUSHING RESISTANCE OF INTEGRATED STRUCTURES

5.1 Structures Composed of Basic Elements

5.1.1 Compatibility of Folding Modes

So farisolated basic elements deforming in a regular way have been studied. However, in composite structures the problem of mode compatibility may arise. According to Wierzbicki /14/, the following modes of two adjacent corners are not compatible if:

i) The deformations are antisymmetric with the same wave length.

ii) The deformation is not symmetric (the wave lengths are different).

iii) The deformations are out-of-phase.

iv) Any combination of the above cases.

An approximate calculation model for the energy dissipation associated with a transition of folding mode has been made in Ref. /14/. This was inspired by the observations made during the test with the box-shaped model, see Sec. 7. In his theoretical model Wierzbicki introduced cuts between any two corners, each representing a transition zone with associated energy.

However, in the remaining tests such transition zones were generally not observed. This is presumably due to the lower width to thickness ratio of the flanges, In the present model mode incompatibility is overcome by adjustment of the deformations at the corner itself.

Most of the joints in a complex structure will be of a T-section type. In sec. 4.4 different mechanisms for T-sections are dealt with. It is seen that mechanism C possesses the desired property of including a possible mode transition. Hence, T-sections found in composite structures are assumed to deform in mechanism C.

As to angle elements inextensional deformation is always theoretically possible as shown in /60/ regardless of the deformation modes of the two flanges. However, in practice shape distortions are frequently encountered due to the way of fabrication. Sharp angles and welds generally disturb the activation of the rolling process. Since mode incompatibility already has

been assumed at each T-section and since the number of angles is small compared with the number of T-sections no allowance is made for any shape distortion of the flanges of an angle.

Buckling mode transition is implicitely assumed for cruciforms deforming symmetrically and no further energy should be added.

5.1.2 Average Strength

The foregoing analysis will be used for predicting the crushing resistance of a complex structure like a ship bow. The procedure is as follows:

Similar to the method suggested by Gerard, conceptual cuts are introduced so that the bow cross-section is reduced to an assembly of fundamental elements such as angles, T-sections and cruciforms. In accordance with the concept of the kinematic method of plasticity the contributions to the internal energy dissipation from each element are added up and equated to the work done by the external load over the specified distance. For the purpose of simplicity it is assumed that all elements fold with a common wave length. This leads to a minimization problem of the same type as encountered for the cruciform in the asymmetric mode of deformation.

The internal energy dissipation can formally be written

$$E_I = \sum_A E_i + \sum_T E_i + \sum_C E_i \qquad (5.1)$$

All terms are related to the plastic moment capacity of a plate strip of unit width which is generally different from one panel to another. While the variation of plate thickness is accounted for in the summation process, the yield stress is assumed constant. Any variation of the latter can be accommodated by adjusting the plate thickness.

In angle elements the following energy dissipation takes place

$$E_I^A = \sum_A (2E_{1i} + 8E_{2i} + 2E_{3i}) \qquad (5.2)$$

As stated in sec. 5.1 the combined mode of deformation is assumed for T-sections

$$E_I = \sum_T (2E_{1i} + 12E_{2i} + 2E_{3i} + 2E_{4i} + 2E_{5i}) \tag{5.3}$$

Finally, the following terms are associated with symmetric collapse of cruciforms

$$E_i^C = \sum_C (8E_{2i} + 8E_{6i} + 8E_{7i}) \tag{5.4}$$

Noting that the summation of the E_2 terms is nothing but summing over all flanges n_f, the total energy dissipation becomes

$$\begin{aligned} E_I = {} & \sum_{A+T} 2E_{1i} + \sum_{n_f} 4E_{2i} + \sum_{A+T} 2E_{3i} + \sum_{T} 2E_{4i} \\ & + \sum_{T} 2E_{5i} + \sum_{C} 8E_{6i} + \sum_{C} 8E_{7i} \end{aligned} \tag{5.5}$$

Introducing the appropriate expressions from sec. 4 there comes out

$$\begin{aligned} E_I = {} & 2\sum_{A+T} 4.64\, \sigma_o \frac{h_i^2}{4} \frac{h_r}{h_i} + 4 \sum_{n_f} \frac{\pi}{2} \sigma_o \frac{h_i^2}{4} \cdot C_i \\ & + 2\sum_{A+T} 2.36\, \sigma_o \frac{h_i^2}{4} \frac{H^2}{r} + 2\sum_{T} 3.2\, \sigma_o \frac{h_i^2}{4} \frac{H^2}{h_i^2} + \sum_{T} \frac{\pi}{2} \sigma_o \frac{h_i^2}{4} \cdot H \\ & + 8 \sum_{C} 2.58\, \sigma_o \frac{h_i^2}{4} \frac{H^2}{h_i} + \sum_{C} \left(\frac{\pi}{2}\right)^2 \sigma_o \frac{h_i^2}{4} \cdot H \end{aligned} \tag{5.6}$$

Equating the internal work to the external work

$$E_e = 2P_{av} \cdot H \tag{5.7}$$

and simplifying, the average load during the compression of one fold is obtained

$$\begin{aligned} \frac{P_{av}}{\sigma_o} = {} & 1.16 \sum_{A+T} h_i \cdot r + \frac{\pi}{4} \sum_{n_f} h_i^2 C_i \cdot \frac{1}{H} + 0.575 \sum_{A+T} h_i^2 \cdot \frac{H}{r} \\ & + \left(0.8 \sum_{T} h_i + 2.58 \sum_{C} h_i \right) H + \frac{\pi}{16} \sum_{T} h_i^2 + \frac{\pi^2}{32} \sum_{C} h_i^2 \end{aligned} \tag{5.8}$$

This formula is basically of the same kind as Eq. (4.81). Correspondingly, the minimum with respect to the wave length and rolling radius exists. The principal solution is given by Eq. (4.89) which takes the form

$$P_{av} = 3\,\sigma_o\, B_1^{\frac{1}{3}} \left(0.87 + 0.54\,(B_2 B_1)^{\frac{1}{4}}\right)^{\frac{2}{3}} \tag{5.9}$$

where

$$B_1 = 0.524 \left(\sum_{A+T} h_i \cdot \sum_{n_f} h_i^2\, c_i \cdot \sum_{A+T} h_i^2 \right) \left\{ 0.54 \cdot (B_2 B_1)^{\frac{1}{4}} \right\}^{\frac{2}{3}} \tag{5.10}$$

and

$$B_2 = 57.9 \left[\frac{\sum_{C} h_i + 0.31 \sum_{T} h_i}{\sum_{A+T} h_i \sum_{A+T} h_i^2} \right]^3 \tag{5.11}$$

The two small constant terms in Eq. (3.8) have been neglected above.

Eqs. (5.10) and (5.11) may alternatively be expressed in terms of average thicknesses

$$B_1 = 0.524 \left(n_1^2\, h_1\, h_2^2\, h_3^2\, L \right) \tag{5.12}$$

$$B_2 = 57.9 \left[\frac{n_2\, h_4}{h_1^2\, h_1\, h_2^2} \right]^3 \tag{5.13}$$

where by definition

$$h_1 = \frac{1}{n_1} \sum_{A+T} h_i$$

$$h_2 = \left(\frac{1}{n_1} \sum_{A+T} h_i^2 \right)^{\frac{1}{2}} \tag{5.14}$$

$$h_3 = \left(\frac{1}{L} \sum_{A+T} h_i^2 c_i \right)$$

$$h_4 = \frac{1}{n_2} \left(\sum_{A+T} h_i + 0.31 \sum_{T} h_i \right)$$

$$n_2 = n_c + 0.31 n_T$$

Here n_1 denotes the number of angles and T-sections, n_2 the weighted number of cruciforms and T-sections, while L is the total length of all flanges in the cross-section.

In particular, for a uniform thickness $h_i = h$, Eq. (3.9) simplifies

$$P_{av} = 2.42\ \sigma_o\ n_1^{\frac{2}{3}}\ h^{\frac{5}{3}}\ L^{\frac{1}{3}} \left[0.87 + 1.27\ \frac{n_2}{n_1} \left(\frac{L}{n_2 h} \right)^{\frac{1}{4}} \right]^{\frac{2}{3}} \qquad (5.15)$$

It is interesting to notice that the crushing strength depends on the thickness to the power of 1.65 - 1.5 and on the total length of flanges to the power of 0.33 - 0.50, depending on the n_2/n_1 ratio. The first extremity belongs to a structure composed of angles only, the second of a structure built up of cruciforms.

5.1.3 Contribution from a Curved Skin

For structures which contain a curved outer shell, such as bulbous bows, membrane tension or compression forces will arise depending on the direction of distortion. From Eq. (4.143) it is seen that the contribution to the average load is proporational with the wave length H. Thus their influence can be retained in the foregoing analysis if the factor h_4 Eq. (5.14) is modified according to:

$$h_4 = \frac{1}{n_2} \left(\sum_{A+T} h_i + 0.31 \sum_{T} h_i + 1.22\ k_s h_s \right) \qquad (5.16)$$

where the thickness of the skin plate is denoted by h_s. k_s is a factor which takes care of any incompleteness of revolution of the shell sections as discussed in Sec. 4.6.

5.1.4 Correction for Compressibility

The shell thickness as well as the finite radius of curvature of the hinges impose constraints on the compressibility of actual structures compared with the thin shell theory. This is easily observed in the experiments. The effect can be approximately accounted for by introducing an effective crush distance

$$\delta_{eff} = H - k\,(2R_0 + h) \tag{5.17}$$

where the radius of curvature of the yield lines in the termination state is given by

$$R_o = \frac{h}{2\varepsilon_u} \tag{5.18}$$

ε_u denotes the strain at ultimate strength as measured in uniaxial tensile tests. For transversly framed structures k = 1 and when longitudinal frame elements are present k = 2.

5.1.5 Comparison with other Formulas

In the method proposed by Wierzbicki the following relationship was proposed

$$P_{av} = 1.5\,\sigma_o\, g^{0.5}\, h^{1.5}\, L^{0.5} \tag{5.19}$$

where g is the number of cuts and flanges inspired by Gerard's method /13/. Generally, the dependency on the thickness is somewhat weaker, while it is stronger as to the length of flanges. But Eqs. (5.15) and (5.19) are equivalent when the number of cruciforms is large.

Gerard's approach for determining the maximum load of composite structures takes the form

$$P_{max} = \mu g\, \sigma_y\, F \left[\frac{gh^2}{F} \sqrt{\frac{E}{\sigma_y}} \right]^m \tag{5.20}$$

where F denotes the total cross-sectional area. Letting $E/\sigma_y = 840$

Eq. (5.20) can be recast in the form

$$P_{max} = 9.8\,\sigma_y\, h^{1.85}\, L^{0.15}\, g^{0.85} \tag{5.21}$$

for structures composed of "angles" (distorted edges) and

$$P_{max} = 2.6\,\sigma_y\, h^{1.4}\, L^{0.6}\, g^{0.4} \tag{5.22}$$

for structures composed of T-sections and cruciforms (unloaded edges). It is very interesting to find that the exponents in these formulas

"circumscribe" the intervals for the powers of Eq. (5.15). In that respect the tendency of this expression seems to be confirmed.

5.2 Stern Section

Fig 5.1 shows the idealization of a typical stern section of a supply vessel fitted with a stern roller. The model contains an outer shell plate bent to a constant radius of curvature at the end, a framing system constituted by T-section ring stiffeners and bulkheads stiffened by vertical, flat slabs.

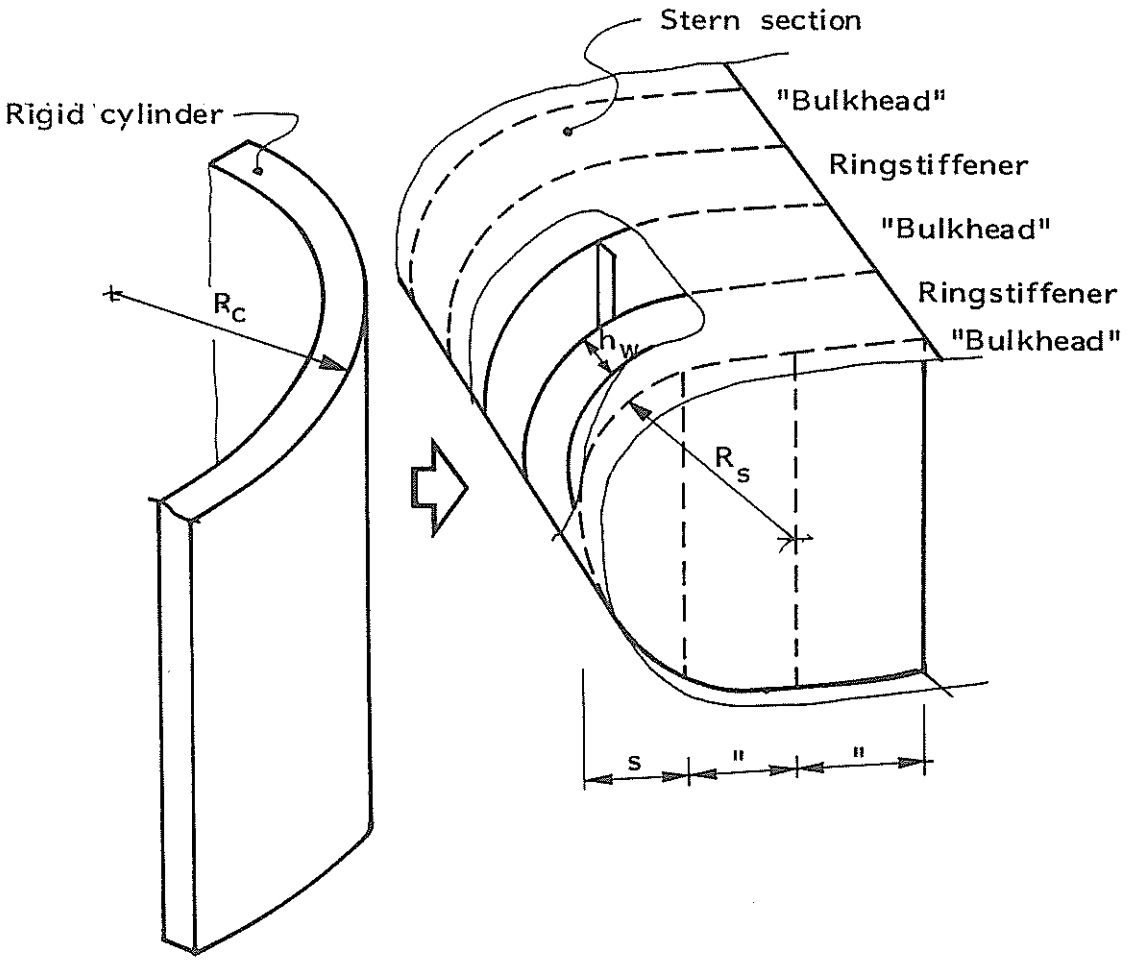

Figure 5.1 *Idealization of stern-concrete shaft impact*

The load is applied through a rigid, circular curved panel with the axis normal to the axis of the curved end of the stem. The indenter represents the supporting structure of a platform.

The real deformation process is very complex and several simplifying assumptions are introduced in the theoretical analysis which is based on the kinematic methods of plasticity

- The material is rigid-perfectly plastic
- The indenting body is infinitely stiff
- Continuity is maintained during deformation
- The theory is valid for moderate deformations, say 2/3 of a frame spacing
- The shell plate deforms isometrically, i.e. no change of length
- The bulkheads and ringstiffeners are subjected to gross shape distortion

The outer shell plate contributes to the energy dissipation by transformation of the surface with curvatures $(\frac{1}{R_c}, 0)$ to a new surface with curvatures $(0, \frac{1}{R_s})$. The transformation is supposed to take place at a pair of moving hinge lines located at the intersection between the surfaces of the indenter and the stern. The first hinge line is supposed to change the curvature in the meridional direction from $\frac{1}{R_s}$ to $\frac{1}{r}$ where r denotes the rolling radius. The second hinge lines remove this curvature but imposes a new curvature $\frac{1}{R_c}$ in the circumferential direction.

The retention of a finite rolling radius reduces the rate of external work. Hence, the unknown rolling radius r can be determined by minimization yielding the following load component

$$P_{shell} = 4 \pi M_o \sqrt{R_s R_c} \left(\frac{3}{R_s} + \frac{1}{R_c} \right) \qquad (5.23)$$

where M_o denotes the plastic moment capacity of the shell.

It is seen that the load does not depend on the depth of indentation. This is due to the linear relationship between the notional contact area, F_c, or the area circumscribed by the outer hinge line, and maximum indentation δ_o,

$$F_c = 2\pi \sqrt{R_s R_c \delta_o} \tag{5.24}$$

Eq. (5.24) is approximately correct for moderate deformations.

The second contribution to the energy dissipation stems from the deformation of the ring stiffeners. It is assumed that the web distorts by pure shear yielding. However, the slenderness of the web implies that buckling occurs in the compressive direction. Accordingly, this component is reglected by taking one half of the theoretical shear work only.

Any energy dissipation in the top flange is not accounted for.

The load component derived is

$$P_{ring} = \frac{1}{\sqrt{3}} N_o h_w \frac{\arccos\left(1 - \frac{\delta_o}{R_s}\right)}{\sqrt{\frac{\delta_o}{R_s}\left(2 - \frac{\delta_o}{R_s}\right)}} \tag{5.25}$$

where N_o, h_w are the plastic tension capacity of a unit platestrip and the web height, respectively.

The bulkheads are subjected to compression in way of the impact load and to tension in the transverse direction. Depending on the relative strength of the shell plate and the bulkhead there are two candidate deformation modes provided that continuity is retained.

In the first case the bulkhead plating remains inextensional and impose the necessary shortening of the shell plate along their intersection.

However, if the shell plate is thick, as in the present case, compression is not allowed. Thus it expands transversely during collapse in order to preserve length with a consequent elongation of the bulkheads which are attached to it.

In the load direction the bulkhead is assumed to buckle in a single wave between the edge and first vertical stiffener. The lateral deflection produces a second transverse extension component.

The two components are calculated separately and added.

The dissipation in other mechanisms such as bending about stationary yield lines are small and neglected.

The resulting expression for the load contains a scale dependent factor and a function of the non-dimensional indentation parameter δ_o/R_s.

$$P_{bulk} = N_o r\, f(\delta_o/R_s) \tag{5.26}$$

The total load is assembled from all the deforming structural components.

$$P = P_{shell} + \Sigma P_{ring} + \Sigma P_{bulk} \tag{5.27}$$

where the local indentation δ_o for each panel varies according to the position relative to initial contact.

A principle sketch of the load-displacement relationship is shown in Fig. 5.2. First contact occurs at a bulkhead and the initial load stems from deformation of the shell plate and bulkhead. Every time new strength members come into contact and start to crush there is a sudden jump in the curve.

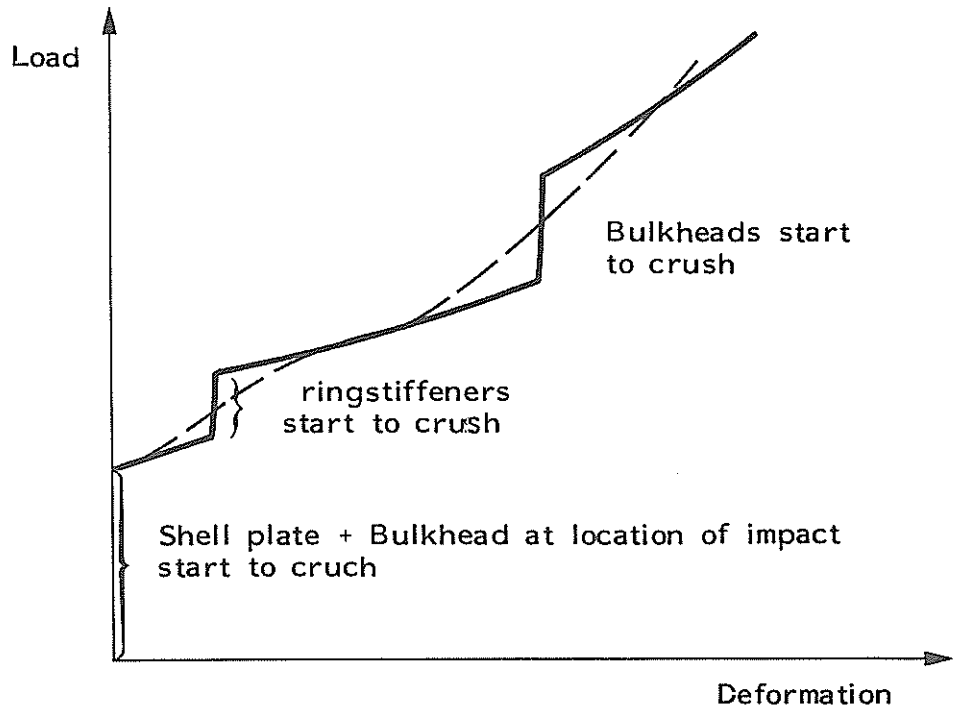

Figure 5.2 Load displacement curve for stern section

In practice there will be a smooth transition as indicated in Figure 5.2.

It is emphasized that the curve overestimates the load considerably at small indentations where elastic effects are important.

5.3 Bow-Bracing Impact

The analysis of bow/bracing impacts comprises two items

- Load at initial failure
- Loads during sustained indentation

The first item is very important as concerns the direction of energy dissipation. Depending on the relative strength the ship, the bracing or both may start to deform at the instant of impact. However, the task of determining the response history is complicated by the fact that the mutual load distribution and relative strength change during the deformation process. The location of impact is also an important parameter in this context. Consider the situation illustrated in Fig. 5.3 Initial contact is assumed to occur midway between two stringers or breast hooks.

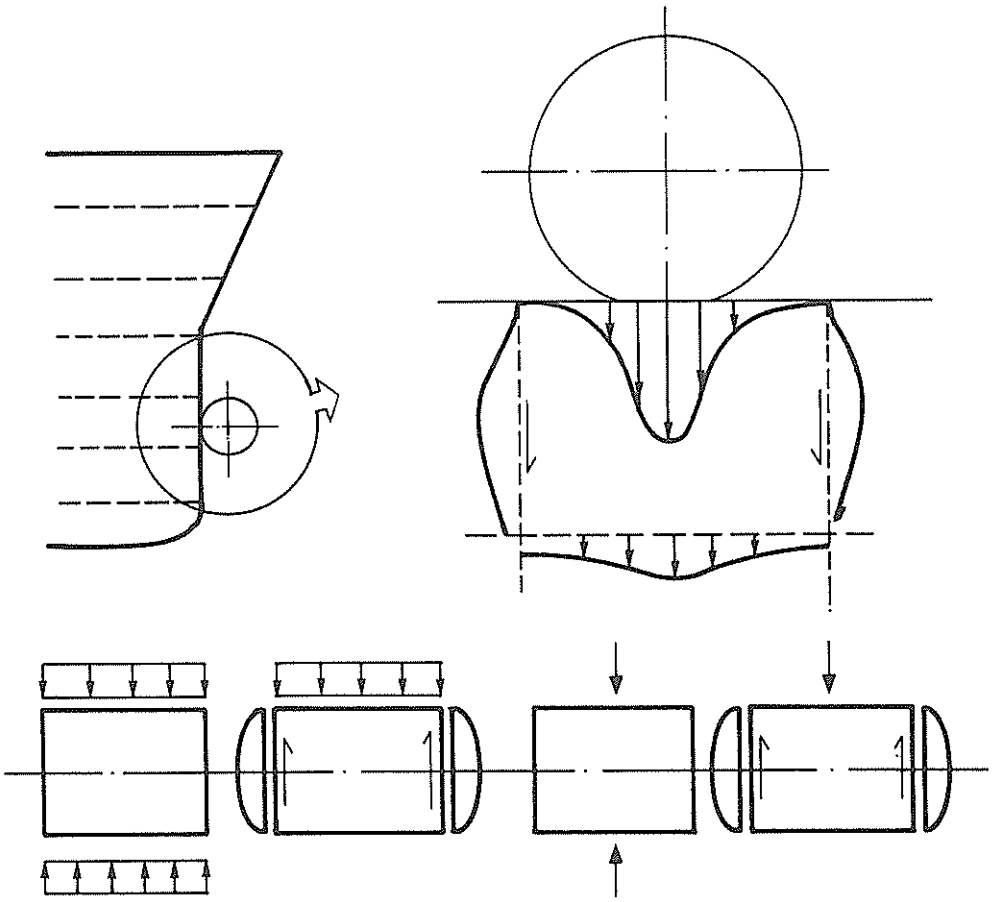

Figure 5.3 Idealization of bow/bracing impact, simplified load distributions and edge conditions

The stem may fail immediately or, if it resists the load initially, the tube starts to deform while the contact area as well as the load increase.

The resulting stress distribution is non-uniform as indicated in Fig. 5.3. The load is supported partly by shear forces along the side edges and partly by compression on the opposite edge. At later stages the contact area splits into two separate parts each with a similar load distribution. The shear deformations tend to equalize the axial stresse.

After initial failure of the plate it is likely that an increasing amount of the forces is carried by the side edges while the mid-plane stresses decrease. Maximum load is encountered when the plate ruptures or the stiffener fails.

Unfortunately there is no ready solution to this buckling problem. However, buckling formulas exist /61,62/ for the following extreme support conditions:

i) The load is entirely supported by shear forces along the side edges

ii) The load is supported by compressive forces on the opposite edge symmetric to the load distribution

It is natural to assume that the real behaviour is close to the first condition in the case of a concentrated load but approaches the second condition when the force is distributed over a larger area.

Calculations conducted for the bow models described in Sec. 7.5 show that the higher buckling load is obtained for the second condition. The total capacity increases by approximately 30% from a concentrated to a distributed load.

Subsequent to failure large plastic deformations develop. Probably an intermediate phase of unloading occurs, but the load increases again as membrane forces develop in the skin plates.

Further collapse may take on different forms.

First of all stringers in direct contact with the bracing are likely to deform. Depending on their strength, stringers surrounding the contact may collapse consecutively, thus mobilizing a large portion of the bow structure. On the other hand, with strong stringers cracks may occur in the plating close to the stringers and the bracing starts cutting into the bow.

In both cases the maximum elongation of the plate is limited by the ductility of the material. In the theoretical calculations the fracture strain is subject to assumption.

In the present study the theoretical calculation model developed for broad side impacts is applied. The justification for this is the close analogy between the case of a column/ship side inpact and the bow/bracing impact. From the structural point of view the stringers correspond to the frames of the hull girder, the stem profile to the ship side, the skin plates to the

deck/bottom and the frames represent the longitudinals. Thus it is a simple task to generate a model which can be used by the computer program.
A detailed description of the calculation model can be found in Ref. /63/.

Especially for small indentations the computer results should be interpreted carefully. The influence of the stem profile is not properly accounted for. Furthermore, the bracing may distort locally as discussed, while a rigid column is presupposed in the program.

6. COLLAPSE MODELS FOR PLATFORM BRACING

6.1 General

For impact against a bracing element the deformation modes of the platform can conveniently be split into the following components:

a. Local deformation of tube wall at the point of impact.
b. Beam deformation of bracing element.
c. Overall deformation of platform.

The first two modes involve considerable plastic energy absorption while the global response is mainly elastic, possibly with some dynamic effects involved. Normally the contribution to energy absorption from overall deformation can be neglected and is not dealt with in the present study.

The transition between the different deformation modes is difficult to define in practice. The response of a tube to lateral load can be described as follows:

In the initial stages of deformation the response is governed by bending effects which are affected by and interacts with the local denting under the load. In this stage the bending capacity will also be reduced if local buckling of the tube wall occurs on the compression side towards the ends. As the beam undergoes finite deflections the load carrying capacity may increase considerably due to the development of membrane tension forces. This depends on the ability of the adjacent structure to keep the tubular joints fixed in space.

Provided that the adjacent structure does not fail, the energy absorption capability is restricted either by excessive straining of the tube or joint failure.

It is very difficult to account for all the behavioural effects simultaneously by analytical means. A useful approach is to study local deformation and beam deformation separately and to construct the interaction curve on the basis of this information.

6.2 Local Deformation of Tube Wall at Point of Impact

The extent and form of local damage in the wall of a bracing element depends on the nature of impact. A head-on collision gives a more concentrated force than a sideway impact and results in a larger amount of local energy absorption of given mass and velocity of the vessel. Due to this complexity it is impossible to present one single analytical model for establishing local energy absorption. Several types of models have to be considered related to different collision situations.

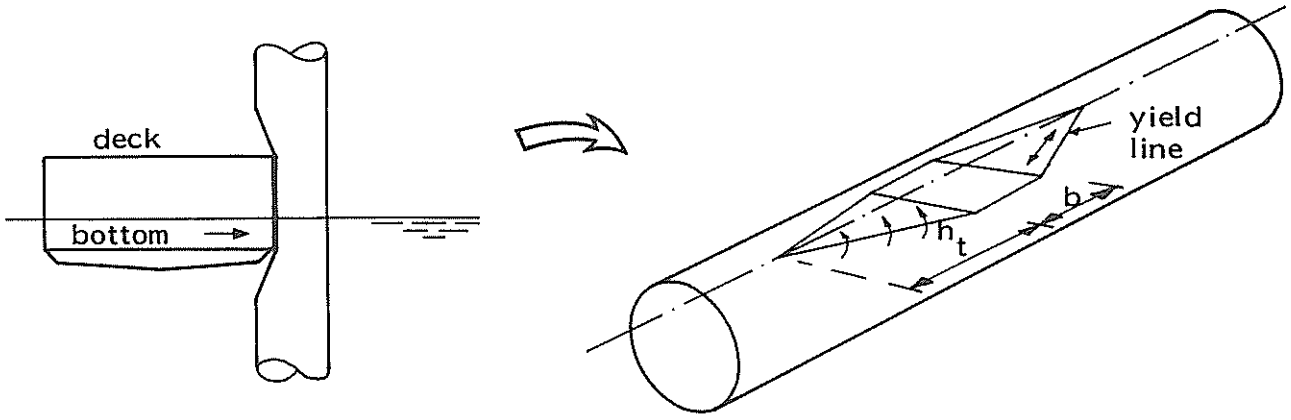

Fig. 6.1. Plastic Mechanism for Sideway Impact by Supply Vessel

For sideway impact a simple yield line model is presented in Ref. /64/, see also Fig. 6.1. The deformed surface is bounded by a series of yield lines and the following plastic effects are included:

a. Rotation of surface at yield lines
b. Flattening of surface between yield lines
c. Tension work due to elongation of generators

The theoretical model which is presented in a non-dimensional format in Fig. 6.2, gives fairly good agreement with experimental results for small and medium indentations. The model can form the basis for possible design curves when further verification against experiments has been performed.

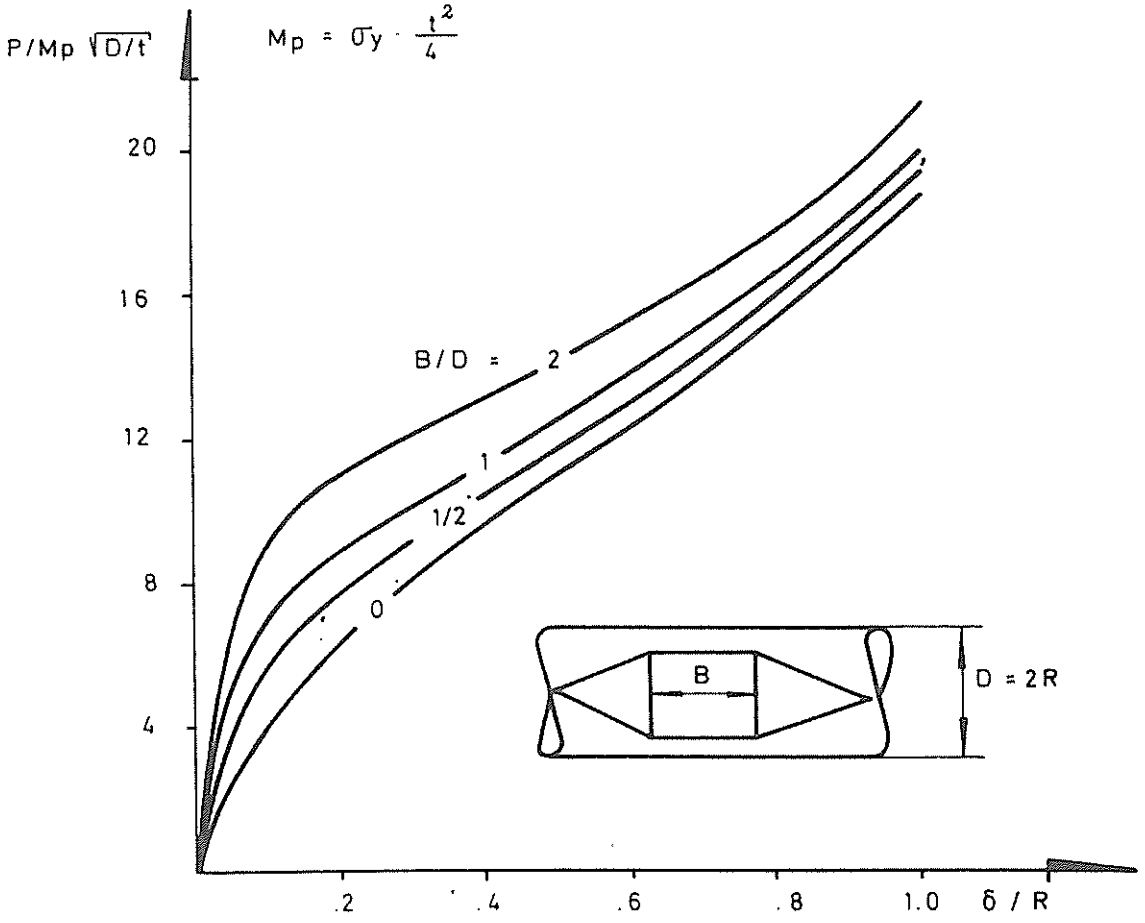

Figure 6.2 Non-dimensional load-indentation relationships for steel tubes.

6.3 Analytical Techniques for Beam Deformation

The rigid-plastic methods of analysis /35,65,66/ provide simple analytical results, often with acceptable accuracy and are appropriate for design situations. The simplest approach to the beam type of deformation is the three hinge mechanism, Fig. 6.3.

In the case of axially restrained ends the load carrying capacity of the beam increases considerably as the beam undergoes finite deflections due to the development of membrane tension forces. For a centrally loaded tubular beam the load-deflection relation is given by /67/.

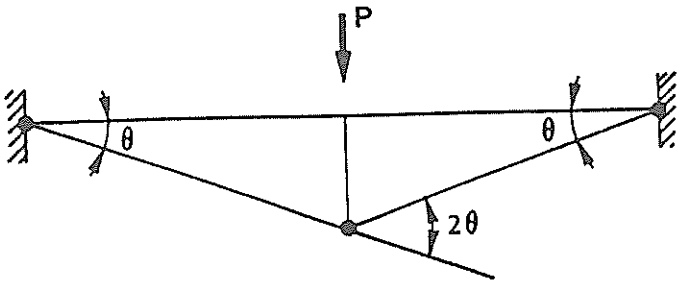

Fig. 6.3. Collapse Mechanism for Bracing Element

$$\frac{P}{P_0} = \sqrt{1 - \left(\frac{w}{D}\right)^2} + \frac{w}{D} \arcsin \frac{w}{D}; \qquad \frac{w}{D} \leq 1 \tag{6.1}$$

$$\frac{P}{P_0} = \frac{\pi}{2}\frac{w}{D}; \qquad \frac{w}{D} > 1 \tag{6.2}$$

where w is the central deflection at the point of impact and D is the tube diameter. P_0 is the plastic collapse load of a circular tube with wall thickness h in pure bending:

$$P_0 = \frac{8M_0}{\ell} = \frac{8\sigma_0 D^2 h}{\ell} \tag{6.3}$$

The above expressions are based on the assumption that the ends have full axial restraint. In a real frame system like a jacket the bracing element sustains a certain degree of elastic support from the adjacent elements. Such elastic restrictions can be included by extending Hodge's method /35/ for the case of tubular members.

It is a major requirement for the validity of the present simple theory that no buckling of the tube wall takes place so that the full plastic capacity of the cross section is retained during deformation. Thus, restrictions must be set on maximum D/h-ratio for which the rigid-plastic theory can be used. Sherman /68,69/ on the basis of tests on steel tubes in bending concluded that for members with D/h of 35 or less the full plastic moment is activated and sustained during deformation.

The API rules /70/ prescribe $D/H < 900/\sigma_0$ (σ_0 is yield stress in N/mm^2) to maintain full capacity through plastic deformation. In the range $9000/\sigma_0 < D/h < 15200/\sigma_0$ only a limited plastic rotation capacity can be presumed.

The limits to membrane straining is a matter of uncertainty. The collapse mechanism yields no assessment of the strain level. In fact, the strains in the yield hinges are infinite. Presently the fracture criterion is related to an overall elongation to equal 0.10 /71/.

6.4 Computational Techniques for Bracing Elements

In an effort to come up with an efficient tool for collision analysis of bracing elements a simple finite element beam program IMPACT /72/ has been modified to take care of local effects such as moment capacity reductions due to indentation and local buckling of tube wall.

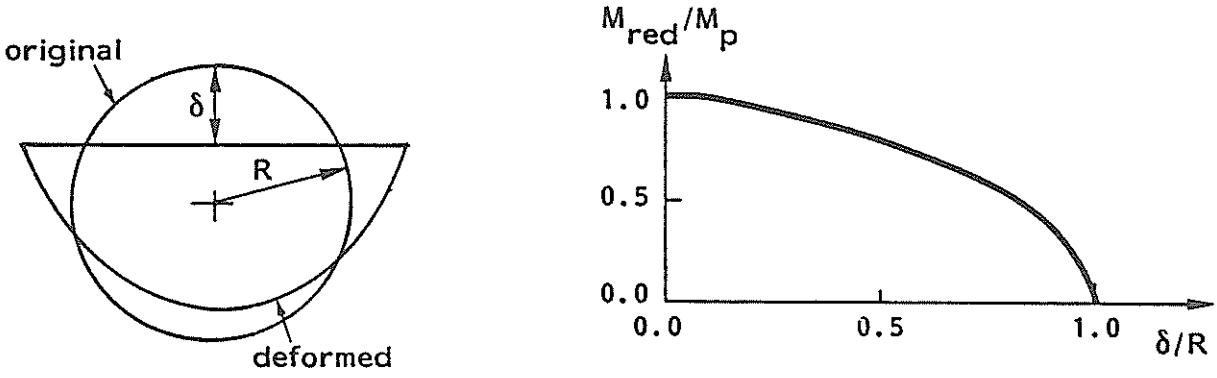

Fig. 6.4. Deformation Model at Point of Impact for Calculating Reduced Moment Capacity

The deformation model at the point of impact is shown in Fig. 6.4. It is assumed that the indented area is flat and that the remaining part of the cross section has a constant radius of curvature. The shape of the cross section can now be determined for any indentation by requiring the area to be constant and the reduced plastic section modulus comes out from simple integration over the deformed cross section.

The beam elements at the point of impact are modified continuously during deformation so as to satisfy this reduced plastic moment capacity.

In order to calculate the amount of indentation at different load levels, the technique described in Sect. 6.2 is applied. The program system now consists of three integrated parts:

a. A finite element beam program with elasto-plastic material behaviour and large deflection effects incorporated

b. A yield line program for predicting local indentation.

c. A program for calculating reduced moment capacity due to local deformation at point of impact.

The load is applied in increments with equilibrium iterations within each load step. A further description of the numerical technique is found in Ref. /71/.

The above program accounts for strain hardening effects which may have a significant influence on the load/deformation characteristics in the plastic range. In order to model the real behaviour of tubular joints spring elements can be introduced at the element ends with any characteristics for horizontal movement and rotation. As failure criterion in the element, the maximum strain is used in such a way that the limit on accumulated plastic strain is given as input. The magnitude of this maximum strain is usually in the order of 15-20%, see Fig. 6.5.

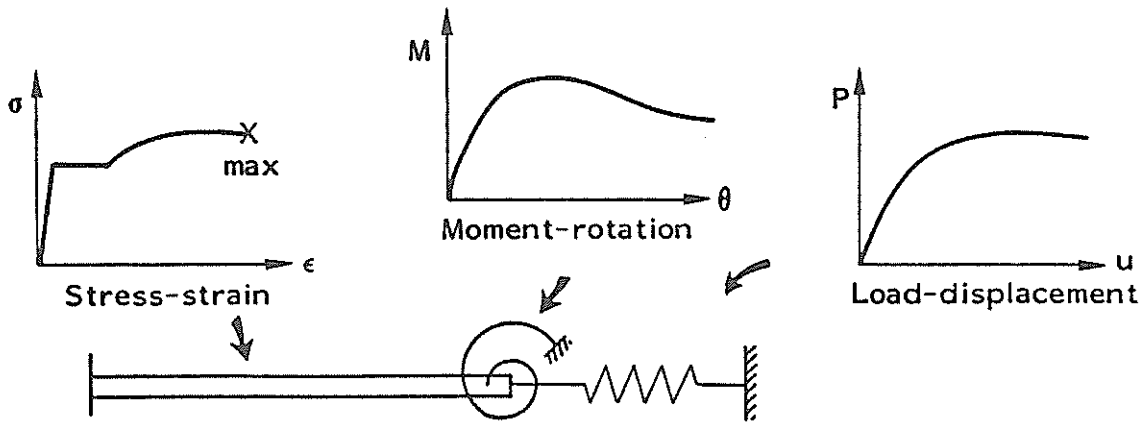

Fig. 6.5. Stress-Strain and Spring Characteristics

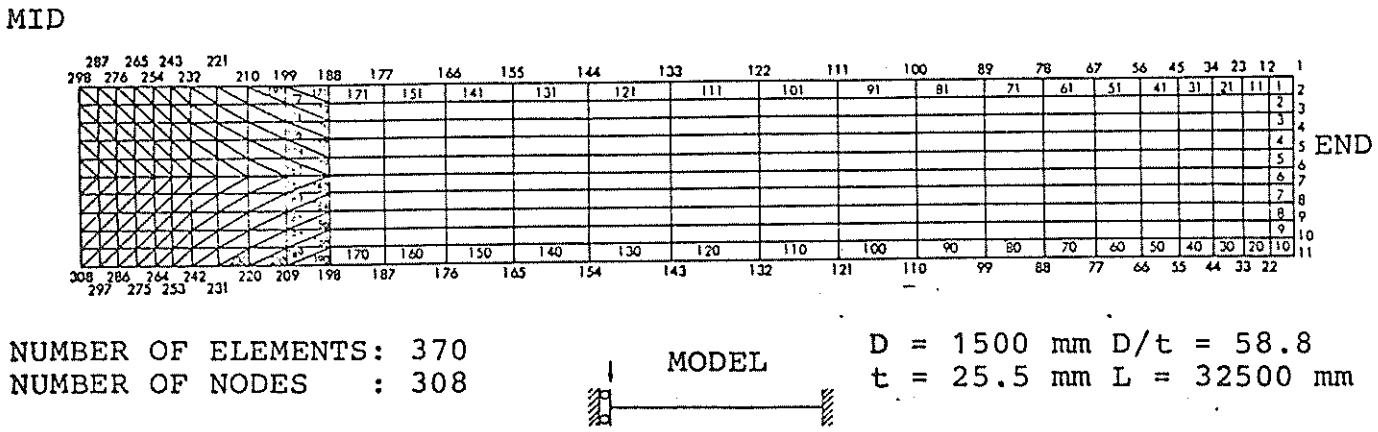

Fig. 6.6. Finite Element Shell Model of Bracing Element

6.5 Finite Element Shell Analysis

In order to simulate the real deformation pattern in the tubular member a full shell analysis must be performed in which material as well as geometric nonlinearities are incorporated. Fig. 6.6 shows the finite element model of a bracing element analysed by the computer program TUBBUC /73/. In the central region close to the point of impact a fine mesh of triangular thin shell elements is used while the tube wall outside the local indentation area is represented by a coarser mesh of rectangular elements. The total number of elements is 370.

Strain hardening is accounted for by combining what is termed the sublayer technique with the flow theory of plasticity. Geometric nonlinearity is modelled by the updated Lagrangian formulation in which element strains are referred to local element axes.

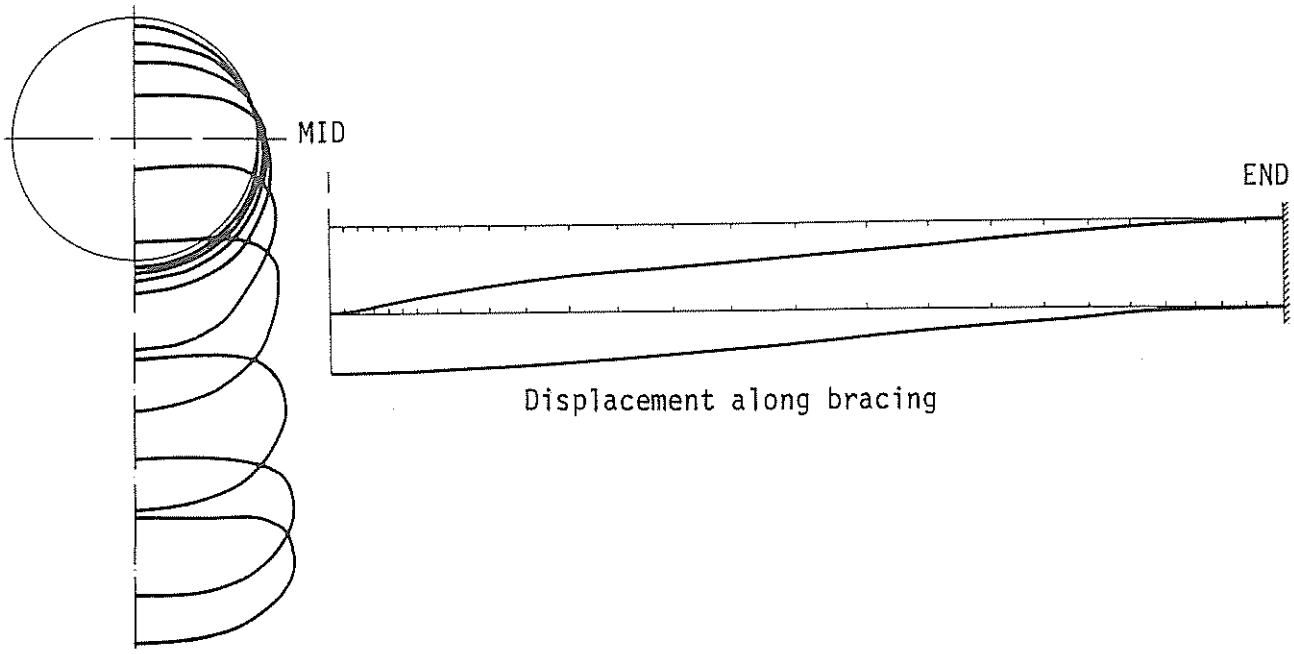

Fig. 6.7 Deformation Patterns from Shell Analysis.

The displacement patterns along the bracing and deformation of midsection are shown in Fig. 6.7 as calculated by TUBBUC and the corresponding load/displacement curve is illustrated in Fig. 6.8. The stiffening effect of membrane forces is clearly demonstrated.

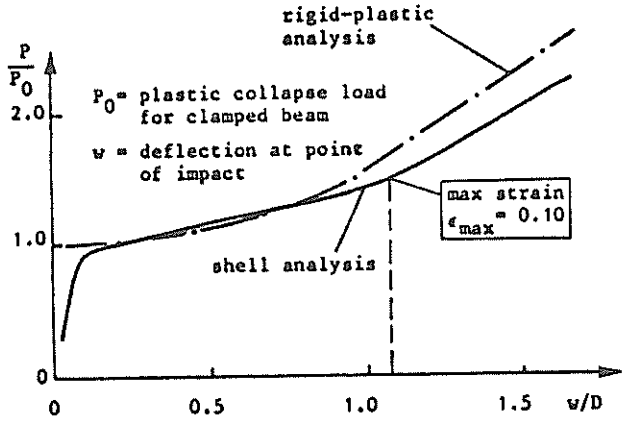

Fig. 6.8 Load-Displacement Relation for Bracing Element. Finite Element Shell Analysis.

It is clear that the above technique is time consuming and costly. For design purposes a simpler numerical tool should be available. However, modification of the computational method also reduces the accuracy of the predictions. The shell program can be used to study special effects in the member performance e.g. stress distribution close to the point of impact and local instability phenomena.

6.6 Tubular Joint Capacity

The introduction of translational and rotational springs in the beam model of Sec. 6.4 (Fig. 6.5) requires separate studies to be performed on the deformation characteristics of tubular joints. Most of the work carried out on tubular joints concerns fatigue life or ultimate load capacity. In the study of energy absorption capability the load-deformation relationship of the joint may also be of interest.

In the linear elastic regime of deformation the restraints from the joint on the bracing element can be calculated by a finite element shell program for different load cases such as axial tension, axial compression, inplane hending and out-of-plane bending. However, in the nonlinear range numerical shell calculations are complicated and most of the information is to be taken from laboratory tests.

Failure criteria for tubular joints should be given as deformation limits for the springs. Typically, a joint subjected to bending may fail by buckling of the chord wall on the compression side resulting in a reduction in joint stiffness and strength. On the tension side fracture through the chord wall is the most probable mode of failure. It is clear that the combination of membrane forces and moments at the ends of the tubular elements should be checked against empirical data on tubular joint capacity. The simplest alternative is to use springs for which the load-deformation characteristic is given as input, either in the form of an ideal elasto-plastic type of relation or a general nonlinear curve including unloading in the plastic regime.

Valuable information on the nonlinear behaviour of unstiffened tubular joints has been presented by Yura et al. /74/. Capacity formulas based on experimental data are also given in design codes /4,70/.

7. EXPERIMENTS ON MODELS OF SHIP STRUCTURES

7.1 Test Arrangement

The experimental set up is shown in Fig. 7.1. The hydraulic actuator (1) is mounted on the transverse beam of the rig.The model (3) is compressed between the two parallel plates.

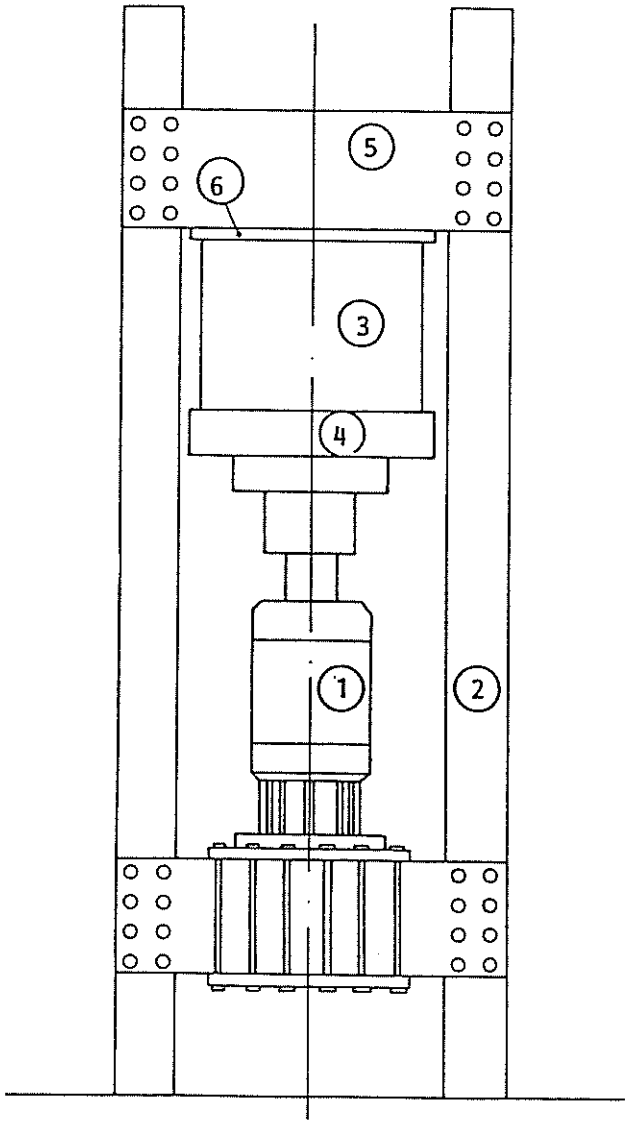

Figure 7.1 Experimental set-up.

The load is applied as controlled axial displacement with a rate of deformation equal to 0.15 mm/sec for the static tests and 10 mm/sec for the dynamic test.

The only measurements gathered are the load versus movement of the top plate as given by the actuator.

7.2 Ship Bows

7.2.1 Test Results

The series of bow collision tests contains six specimens. The main dimensions and structural arrangement are given in Fig. 7.2.

The first model is box-shaped and has transverse frames. The second model is similar except for the wedge shape.

The next three models are also wedge-shaped but an internal deck is introduced and the frame system is varied. One model is provided with a longitudinal centre bulkhead, one has longitudinal stringers at a quarter height and one is longitudinally stiffened.

The last test piece which is the most advanced one, is a simplified model of the upper part of a supply vessel bow. The scale is approximately 1:5. The model has transverse frames and a centre girder is located in the upper deck and the mid-deck.

In the front a stem profile and two breast hooks are found.

The models are fabricated from 2 mm thick mild steel plates of ordinary commercial quality with a static yield stress σ_y = 22 N/mm^2 and ultimate stress σ_u = 310 N/mm^2. Transverse frames, stiffeners and stringers are made of 3 mm flat slabs with σ_y = 260 N/mm^2 and σ_u = 390 N/mm2.

The elements are assembled by continuous double fillet welds except in the front section where availability permits a single weld only. The TIG welding technique is applied. After welding the specimens are stress relieved by heating to 550·C.

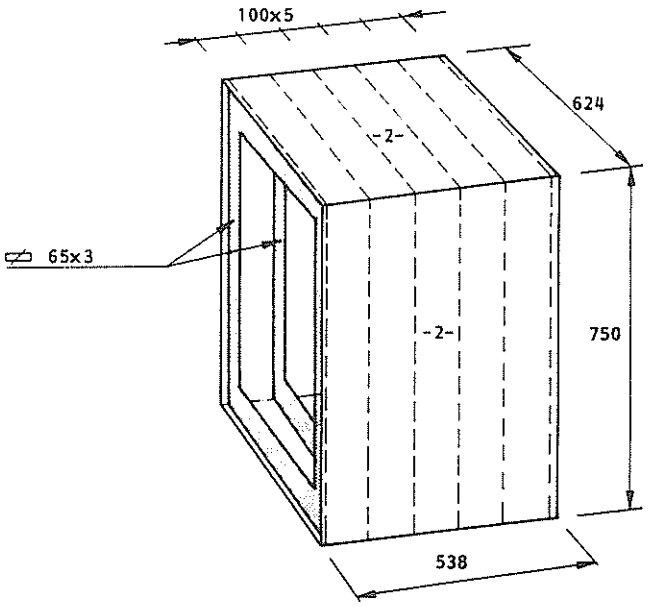

Model 1

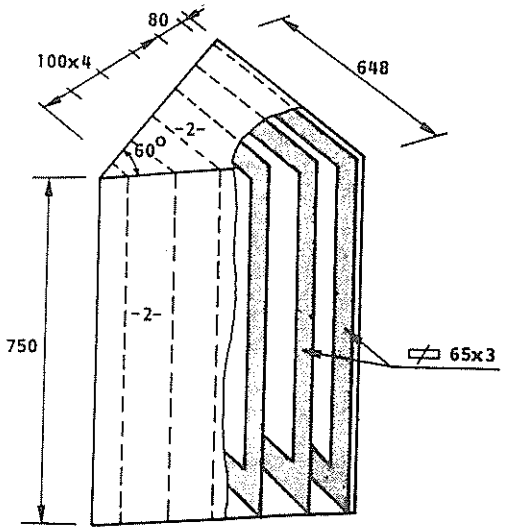

Model 2

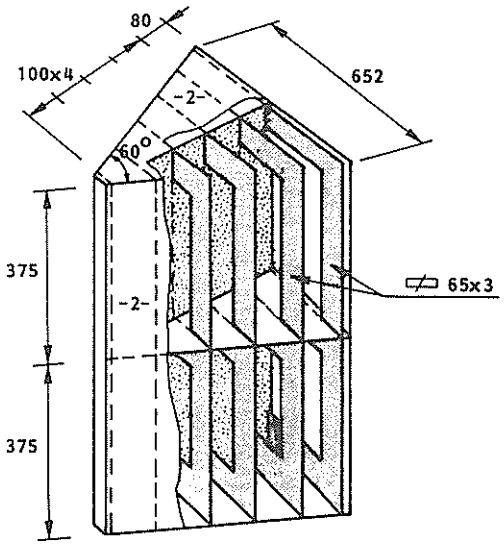

Model 3

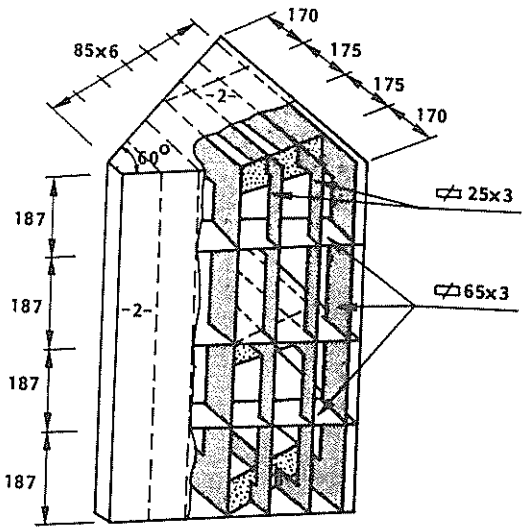

Model 4

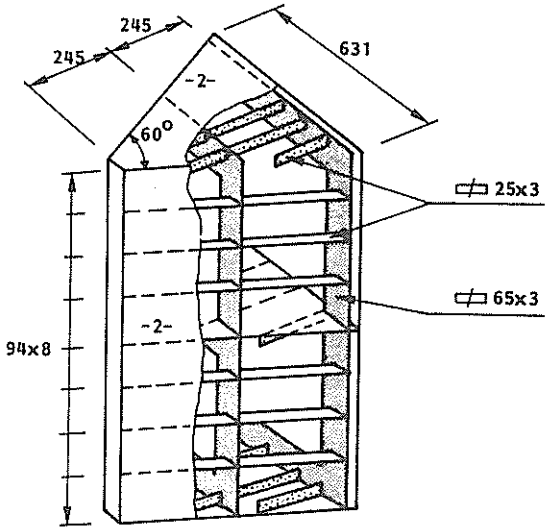

Model 5

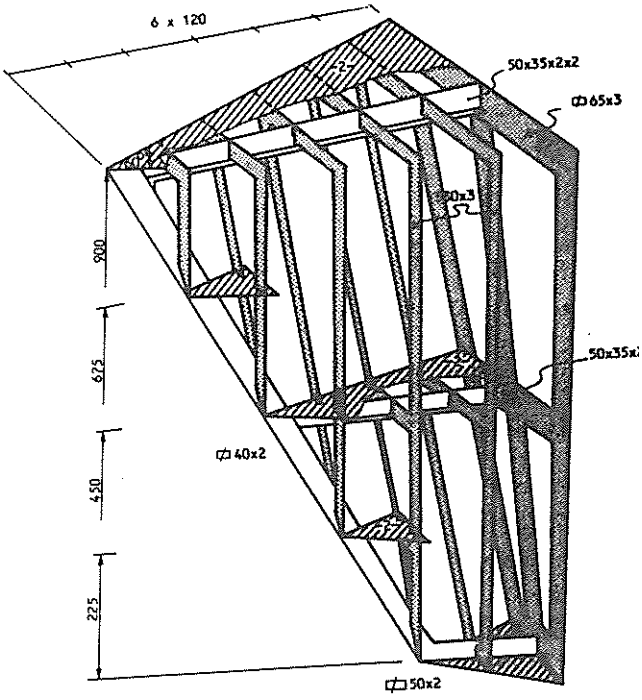

Model 6

Figure 7.2 Bow models

The experimental results are conveniently presented in diagrams of compressive load versus end shortening, see Figs. 7.3 -7.8. Details about each test can be found in Appendix. Here, the results are commented upon in general terms.

The shape of the load-displacement diagrams can be explained by the development of plastic hinges in the structures. Initially the models behave elastically and load rises steeply until some plate field start to buckle between the two first frames. This causes a redistribution of load which occasionally leads to an increased capacity until all panels have collapsed.

After the peak load is reached the axial load drops to a minimum during continuing plastic deformation. When the two first frames overlap the load rises as the next region buckles and then declines again. This oscillation of the axial load continues until all regions have collapsed.

Due to growing shape disturbances and distortions of boundaries the consecutive buckling loads are lower than the initial buckling. As a result of uneven material density the regions of collapse generally progress at different rates in the various panels. This has also an equalizing effect on the load-curve.

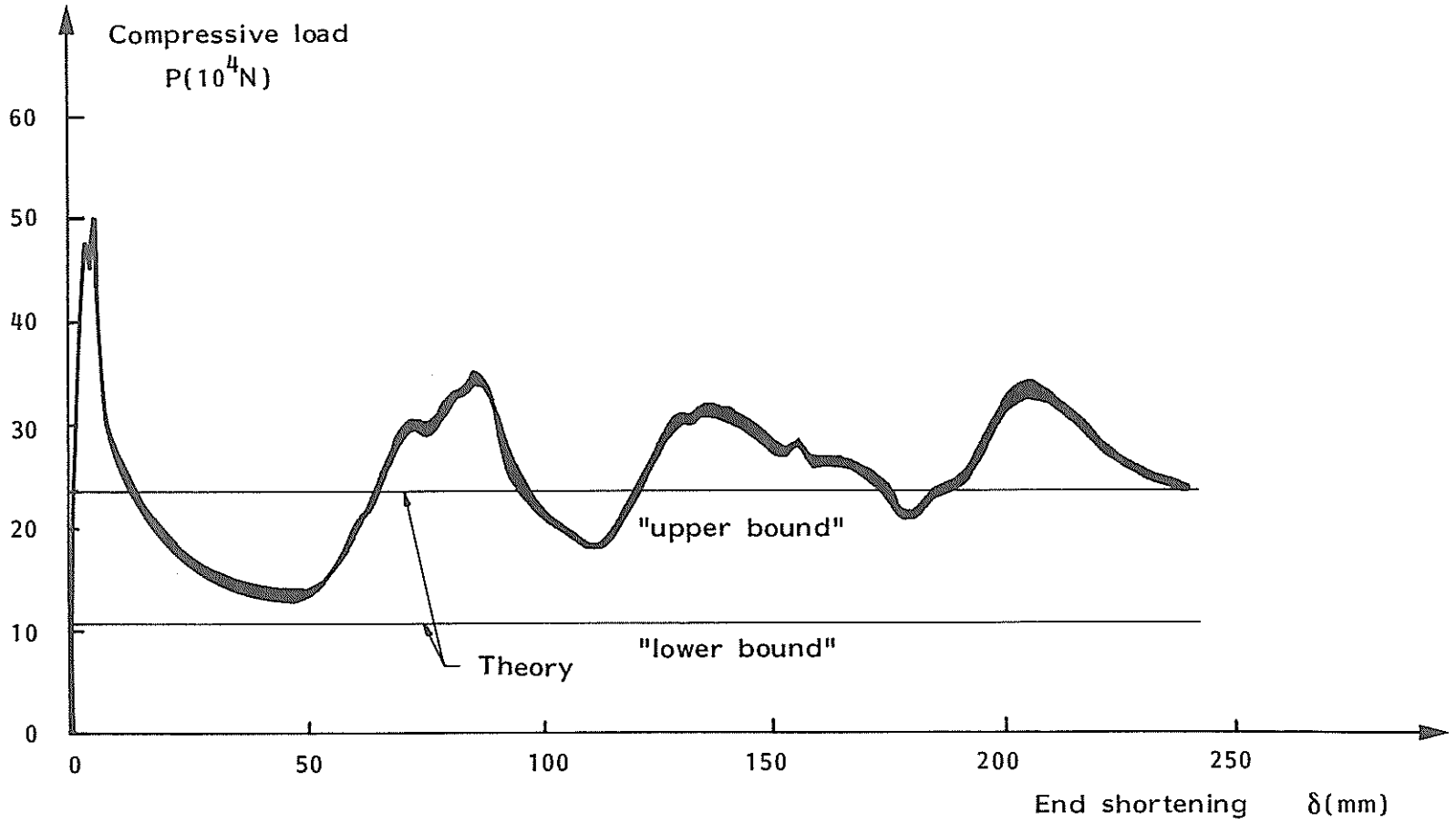

Figure 7.3 Load displacement curve for box-shaped model (Model no. 1)

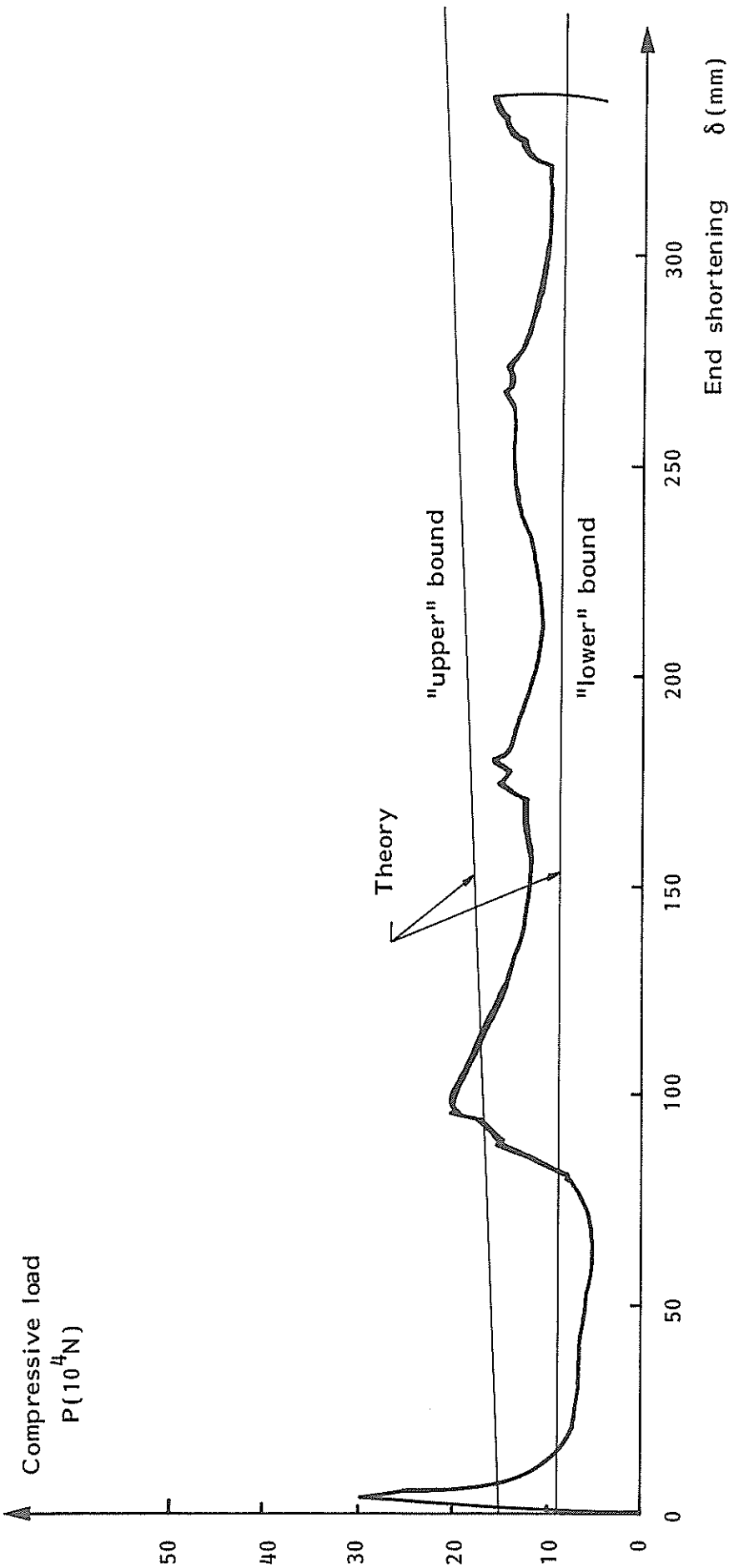

Figure 7.4 Load displacement curve for bow model with transverse frames (Model no. 2)

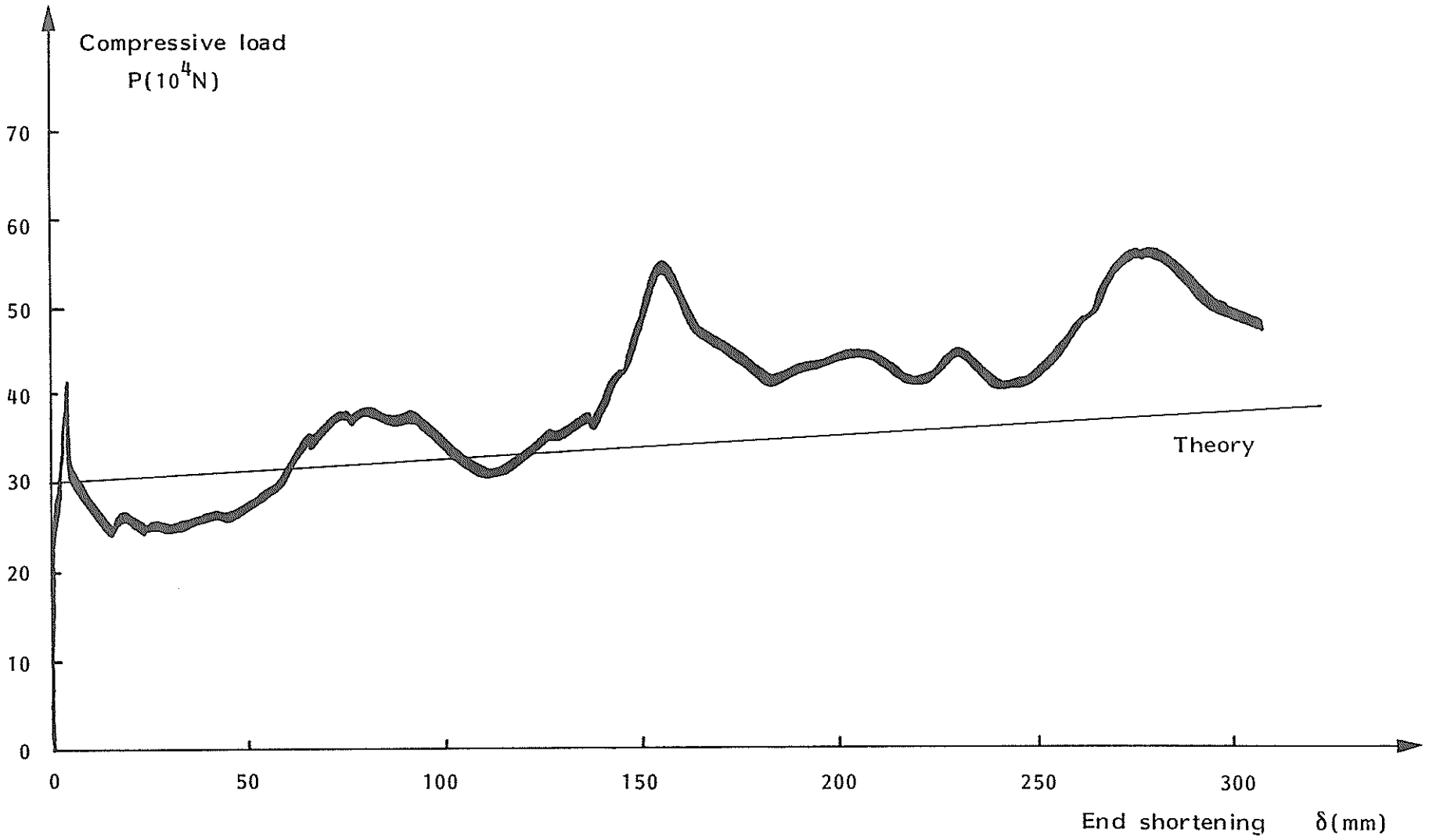

Figure 7.5 *Load displacement curve for bow model with transverse frames, deck and a longitudinal bulkhead (Model no. 3)*

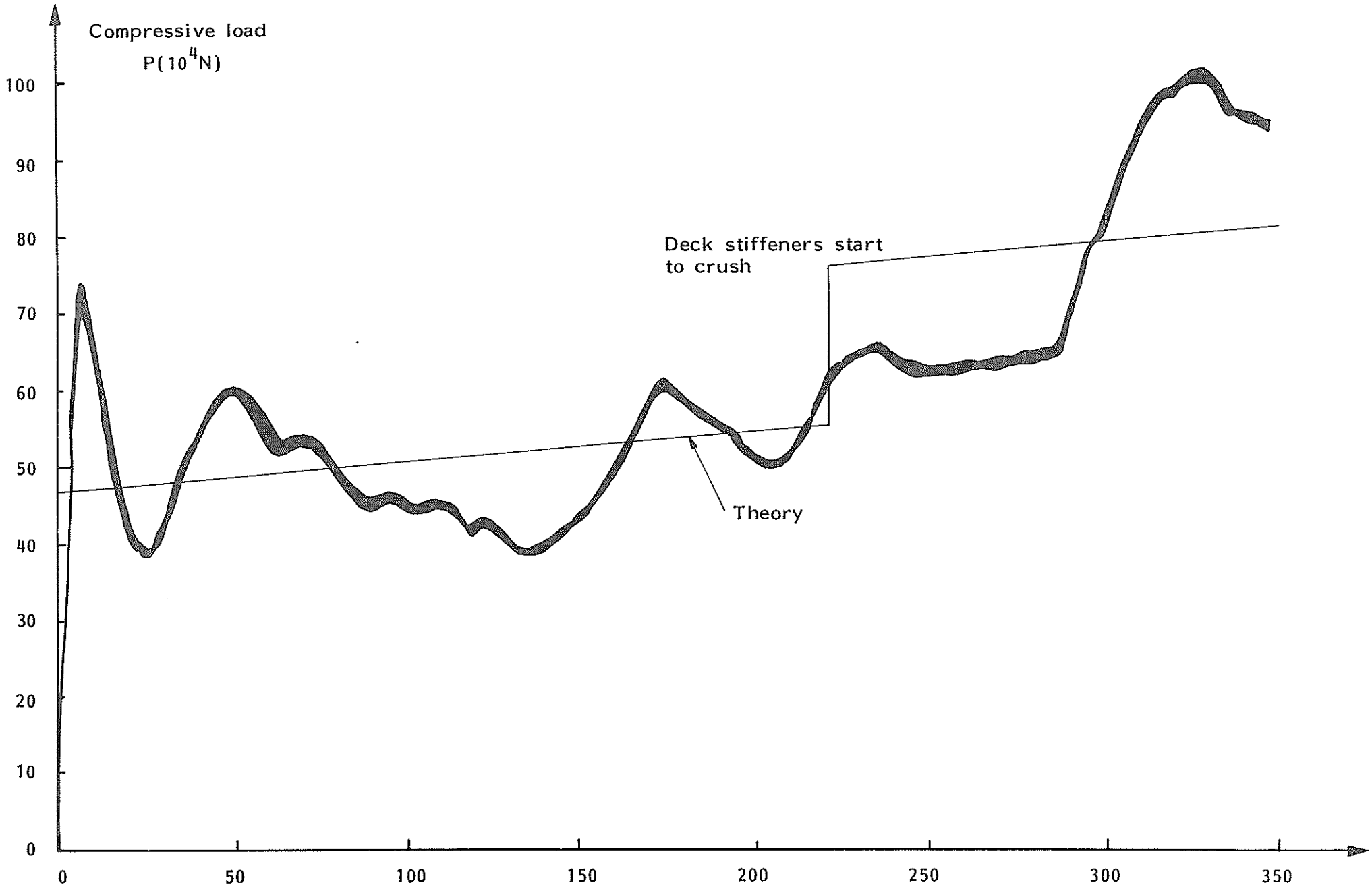

Figure 7.6 Load displacement curve for bow model with mixed framing (Model no. 4)

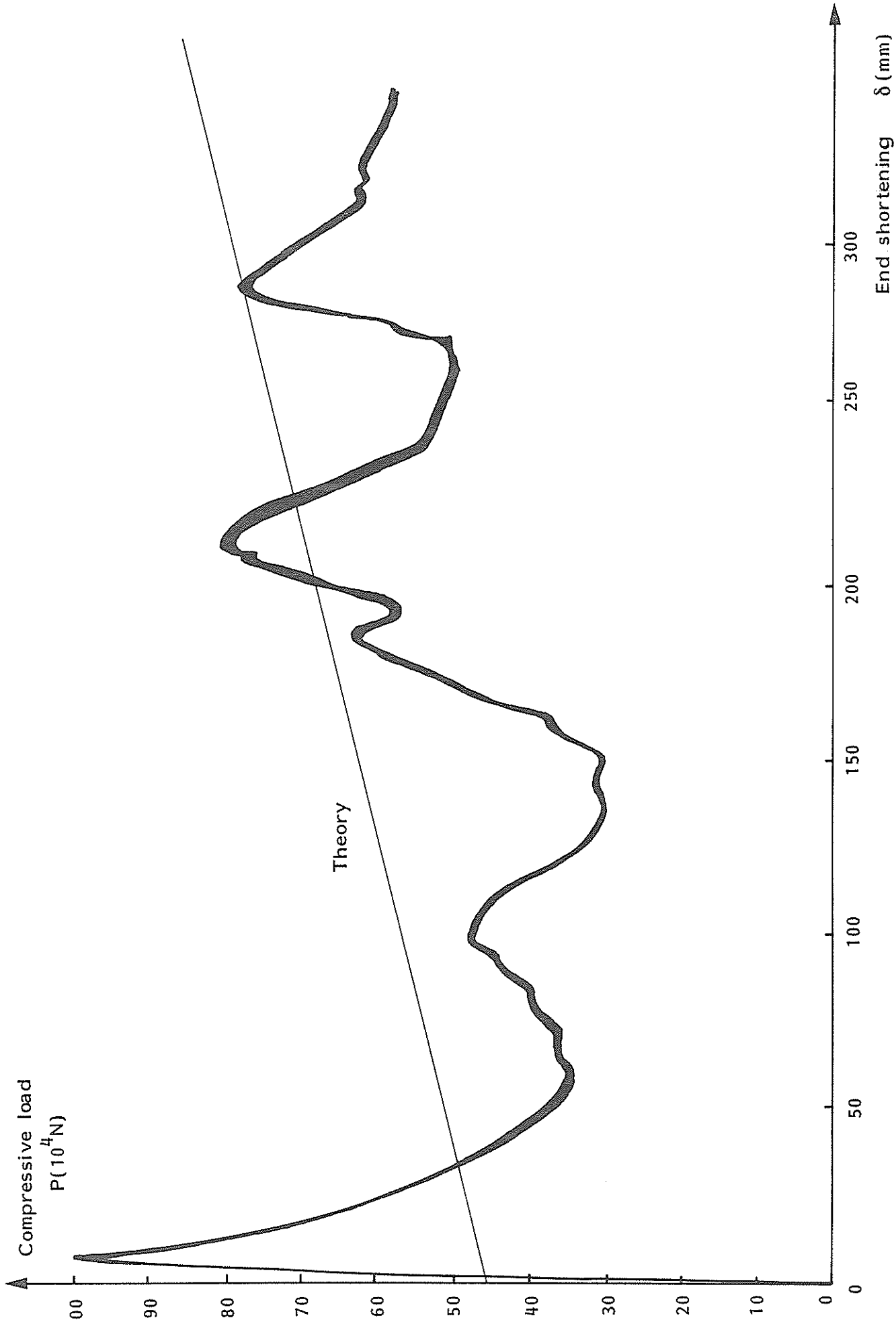

Figure 7.7 Load displacement curve for bow model with longitudinal stiffeners (Model no. 5)

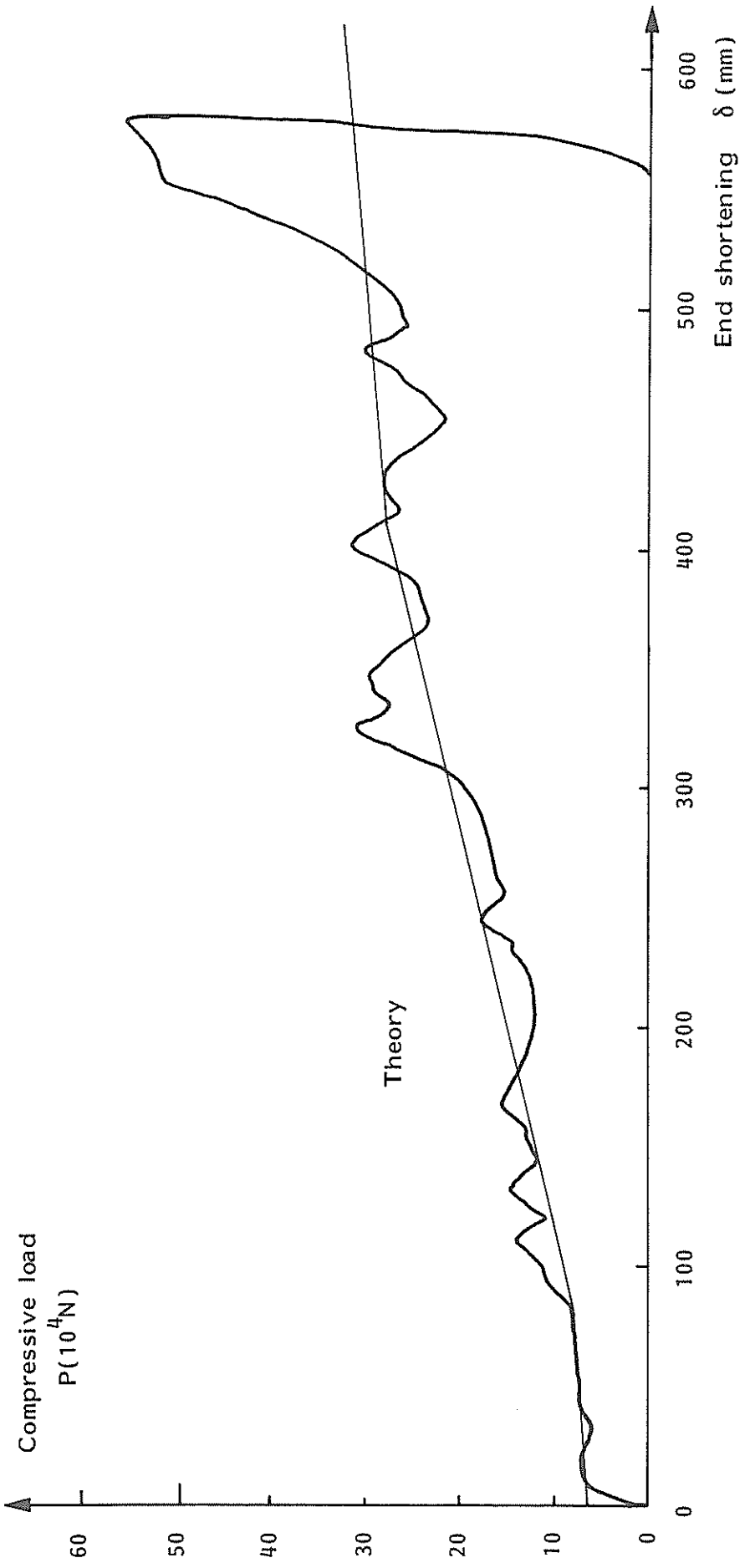

Figure 7.8 Load displacement curve for raked bow model (Model no. 6)

7.2.2 Comparison with Theory

Generally, much of the features of the collapse mechanisms described in Sec. 2 are recognized in the tests, but irregularities are found which complicates the analysis process.

The test results are compared with theoretical predictions based upon the methods outlined in Sec. 2 and 3. The theoretical curves relate to the mean collapse load for each panel between adjacent transverse frames.

For the first two models two estimates are given. First one assumes that every corner deforms in the mode of the basic folding mechanism. This can be considered as a lower bound. The "upper bound" prediction is derived for a specimen which fails in outward symmetric folds similar to one half of the symmetric collapse mode for a cruciform.

For the box-shaped model it can be seen that the lower bound underestimates the average load significantly while the upper bound is close to the measured value. This is not merely due to the occurrence of several outward symmetric buckles as opposed to inextensional angle deformations, but stems also from the creation of mode transition zones. It is possible to account for such transitions zones (confer Ref. /14/), but this is omitted here since they are only encountered in extremely wide panels.

As to the bow model with transverse frames the lower bound approach predicts the average load correctly for the first region which deforms very regularly. At later stages "irregularities" are produced which raises the load level. Apparently the mean of the two theoretical curves complies well with the results.

For the third bow model the theory agrees excellently with the experiment in the first half of the deformation. In the second half the load is underestimated for reasons stated above.

A peculiarity of the load assessment for the mixed framed model Fig. 7.6 is the sudden jump when the deck stiffeners start to crush. The transition is of course more smooth in practice.

For the longitudinally stiffened model the theory yields a load considerably in excess of the measured ones. The discrepancy is due to the

assumption of local plate failure throughout the deformation while this failure mode is succeeded by general panel instability in the test.

As concerns the raked bow model the theory again correlates very satisfactorily with the test curve.

The results of the comparative study are summarized in Table 7.1 which contains data for initial buckling load along with the average load for the entire compression.

		Model 1	Model 2	Model 3	Model 4	Model 5	Model 6
Initial buckling	Exp.	48	30	42	72	97	-
	Theory	43	36	63	72	85	-
Average load	Exp.	22	12.5	39	59	51	22
	Theory	10.4/23		34	62	63	21

Table 7.1 Analytical and Experimental Values for Peak Load and Average Load

The peak load values are included only for the sake of curiosity since the boundary conditions are modelled very poorly. Nevertheless the theoretical figures agree surprisingly well with the experimental results for several of the models. The low experimental load for model 3 is probably due to uncomplete welding ahead of the first frame.

A further basis for verification of the theory is provided by several tests carried out in Japan as mentioned in Sec. 1. The comparison is performed in Figs. 7.9 - 7.13. The ultimate stress is assumed $\sigma_u = 310$ N/mm^2 throughout.

Fig. 7.9 relates to a study of collision with a nuclear powered ship /9/. Among the six stem models the two models with transverse frames are well suited for the present investigation. The results presented show that the response of T-1 is predicted fairly well. However, the theory breaks down for model T-2 owing to the high plate thickness and small frame spacing of the model. This leads to an unrealistically high compressibility factor. If this term could be reduced by one half a much better agreement would result.

Various stem models have been tested for the purpose of evaluation of ship to bridge piers collisions /11/. Fig. 7.10 shows the principal dimension of

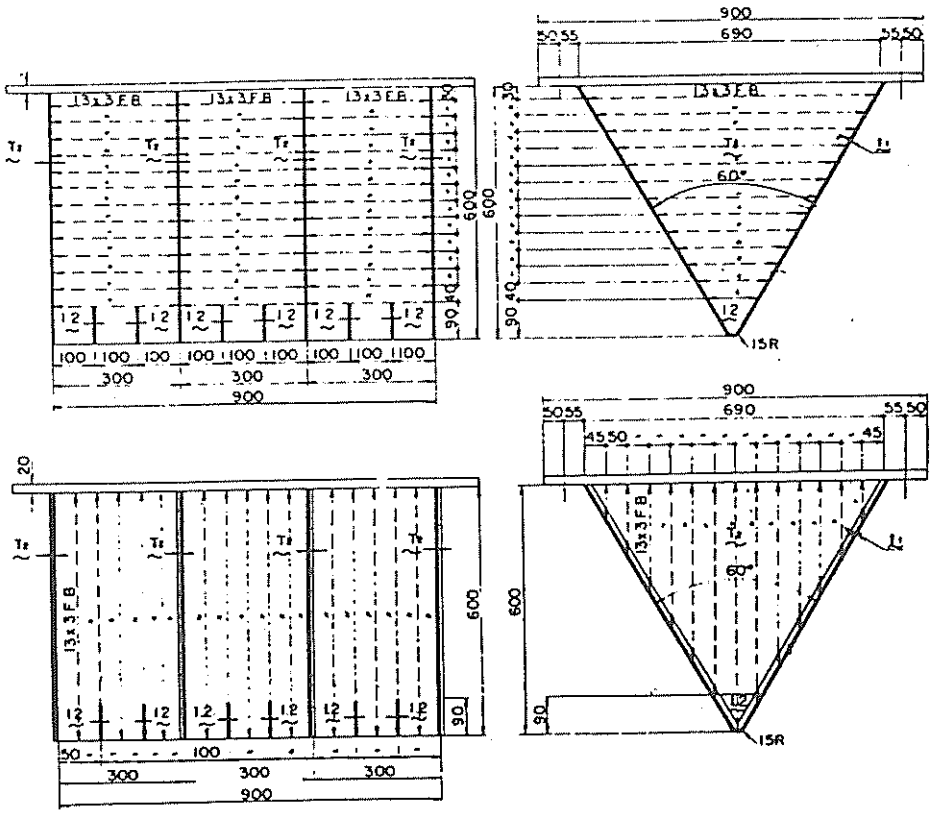

STEM MODEL	THICKNESS OF SHELL PLATE T_1 mm	THICKNESS OF DECK PLATE T_2 mm
T-1	1.6	1.2
T-2	2.3	3.2
L-1	1.6	1.2
L-2	2.3	3.2
L-3	2.3	2.3
L-4	3.2	3.2

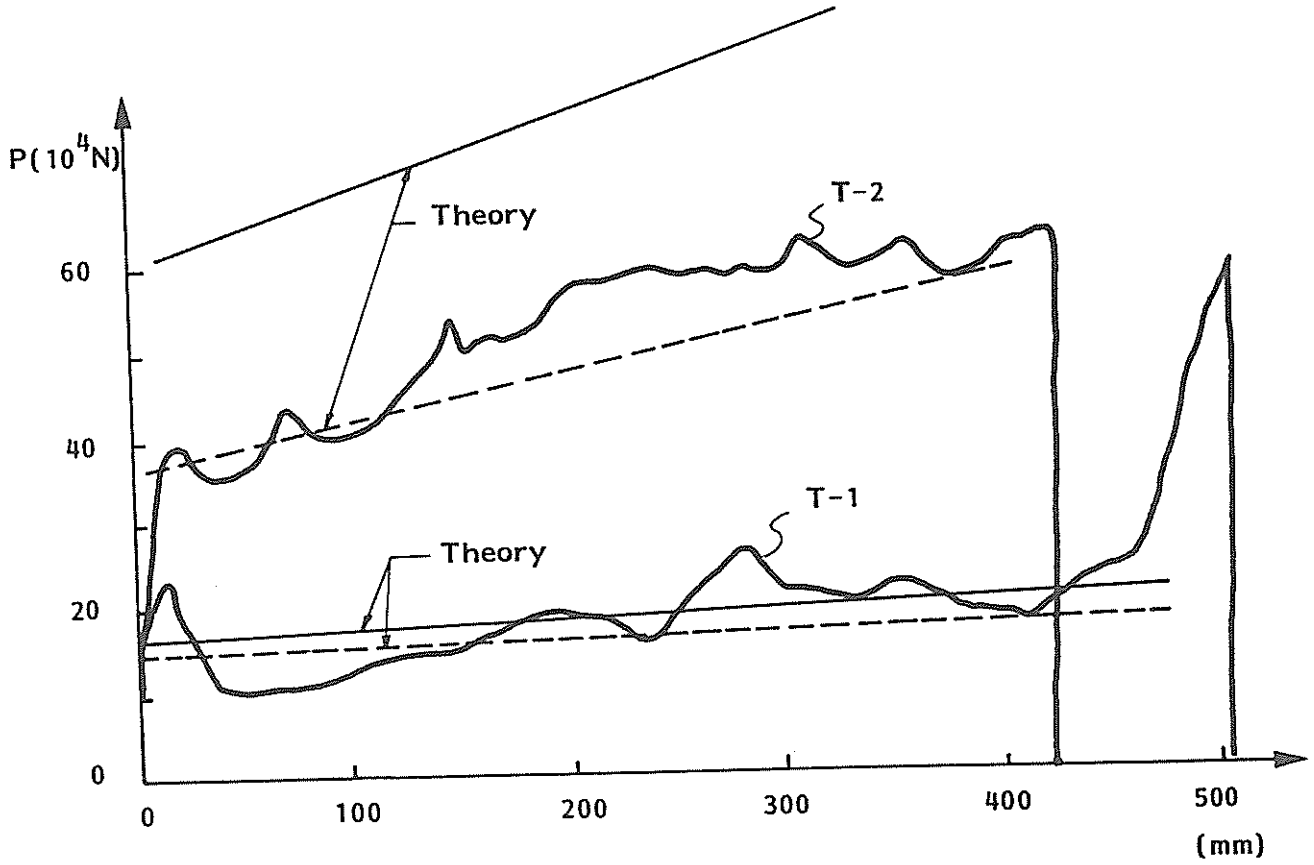

Figure 7.9 Comparison between present theory and experiments carried out in Japan / 9 /.

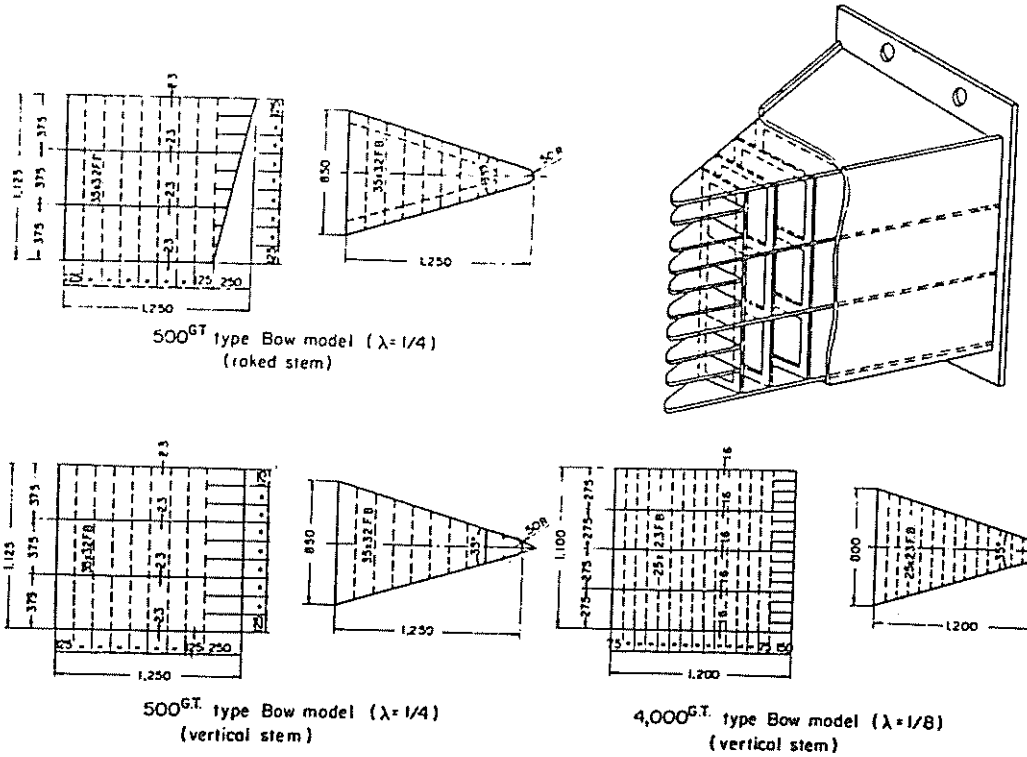

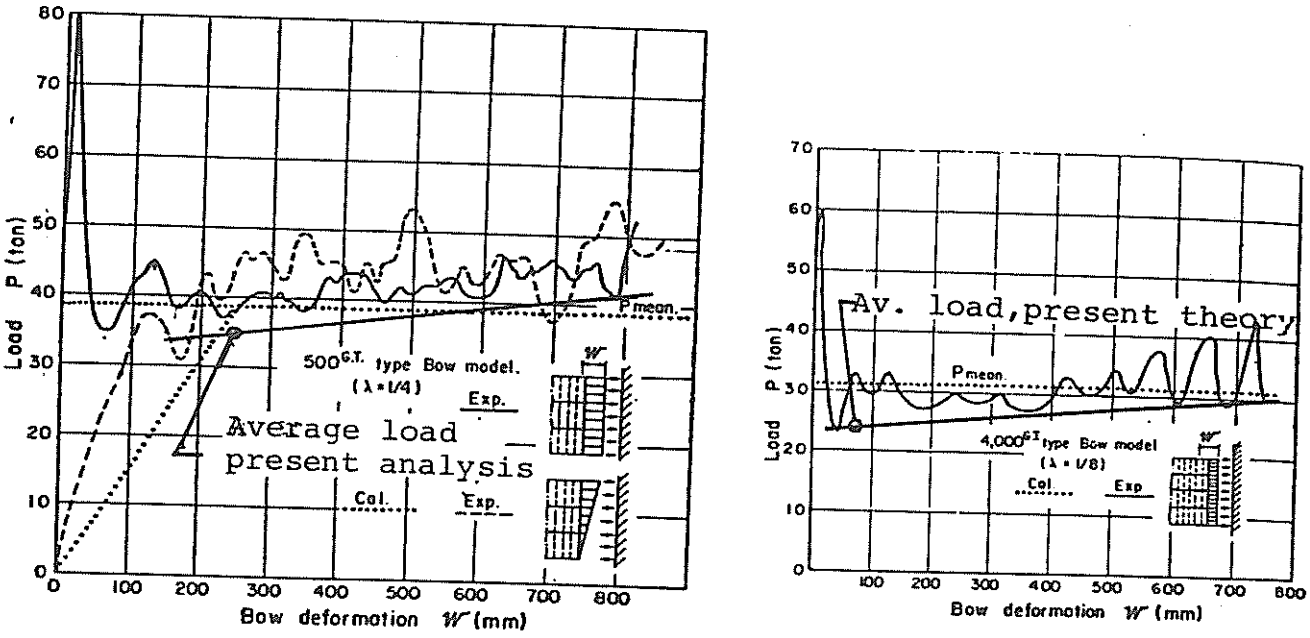

Figure 7.10 Comparison betweem theory and experiments on bow models/11/.

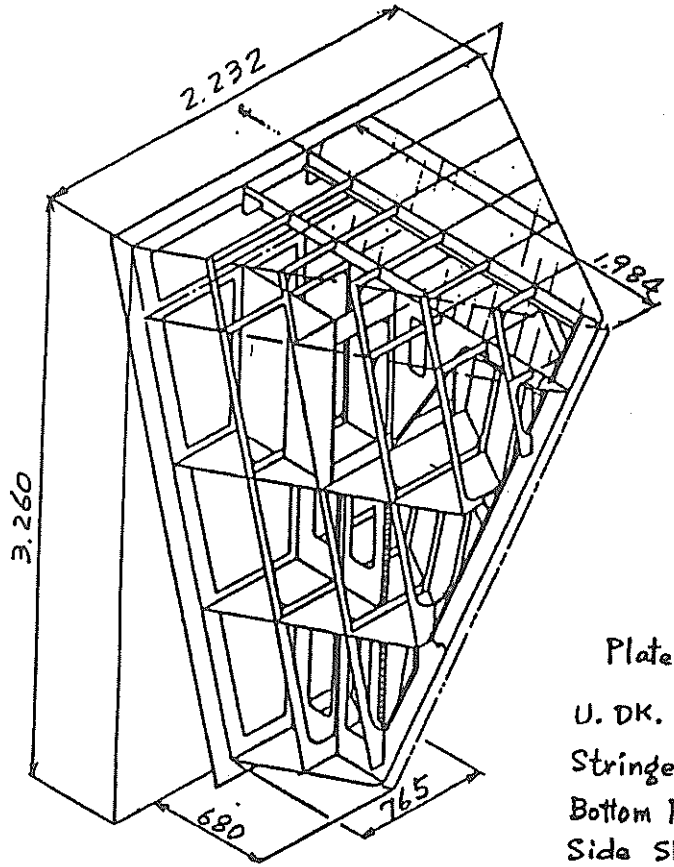

Plate Thickness

U. DK. 1.8 , 2.0
Stringer 1.8
Bottom Plate 4.5
Side Shell Plate 2.3
Inner Structure 1.8, 2.0, 2.3

A. Normal Bow

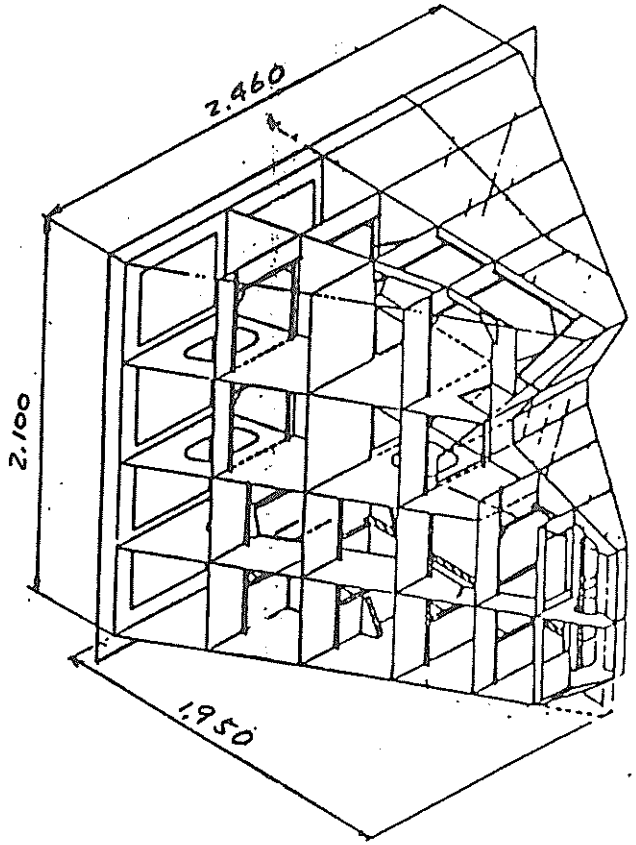

Plate Thickness

U. DK. 2.3
Stringer 1.8
Bottom Plate 3.2
Side Shell Plate 3.2
Inner Structure 1.8
2.0
2.3

B. Bulbous Bow

Figure 7.11 Structural models in Japanese tests/10/.

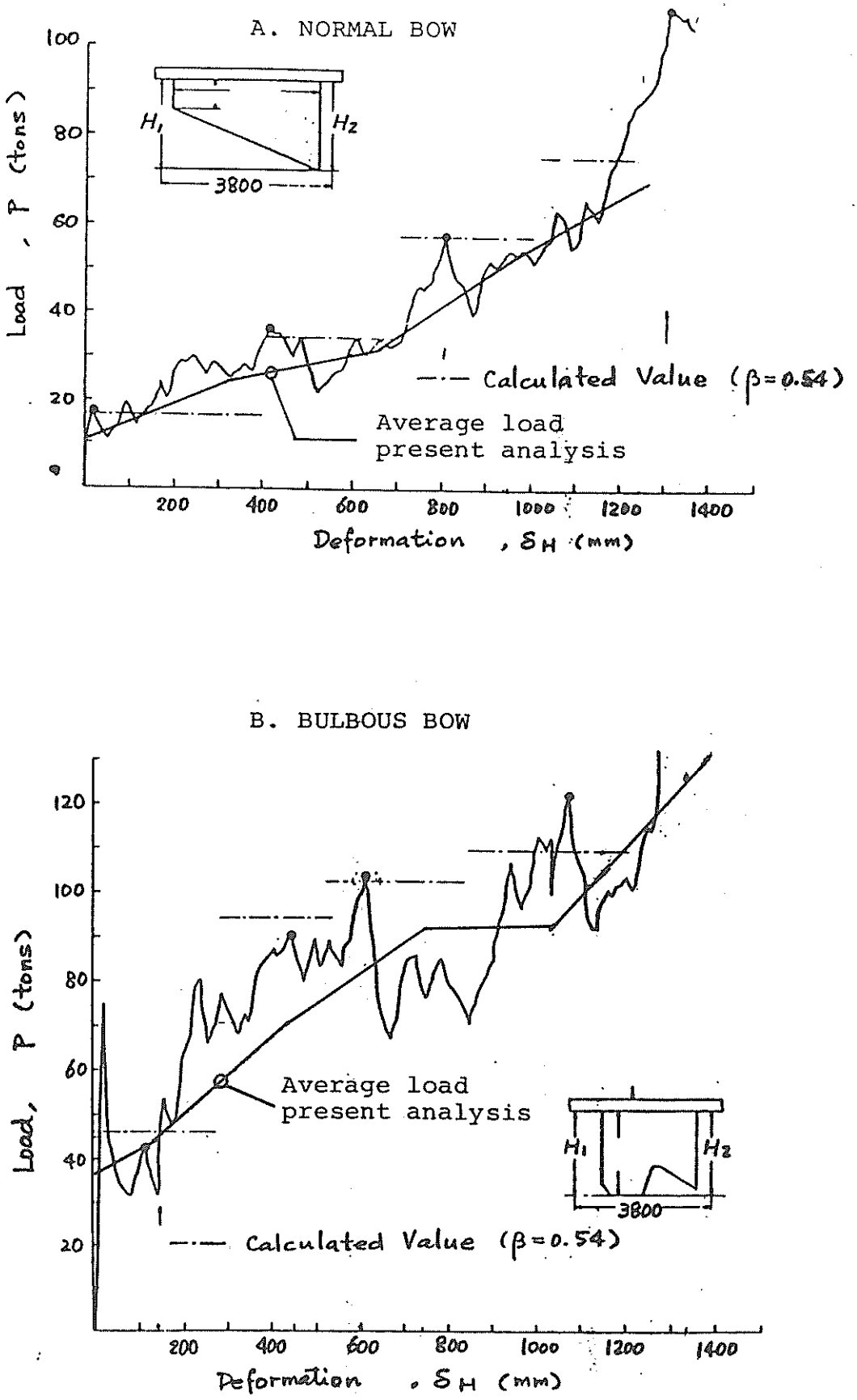

Figure 7.12 Comparison between theory and experiments on bow models/10/.

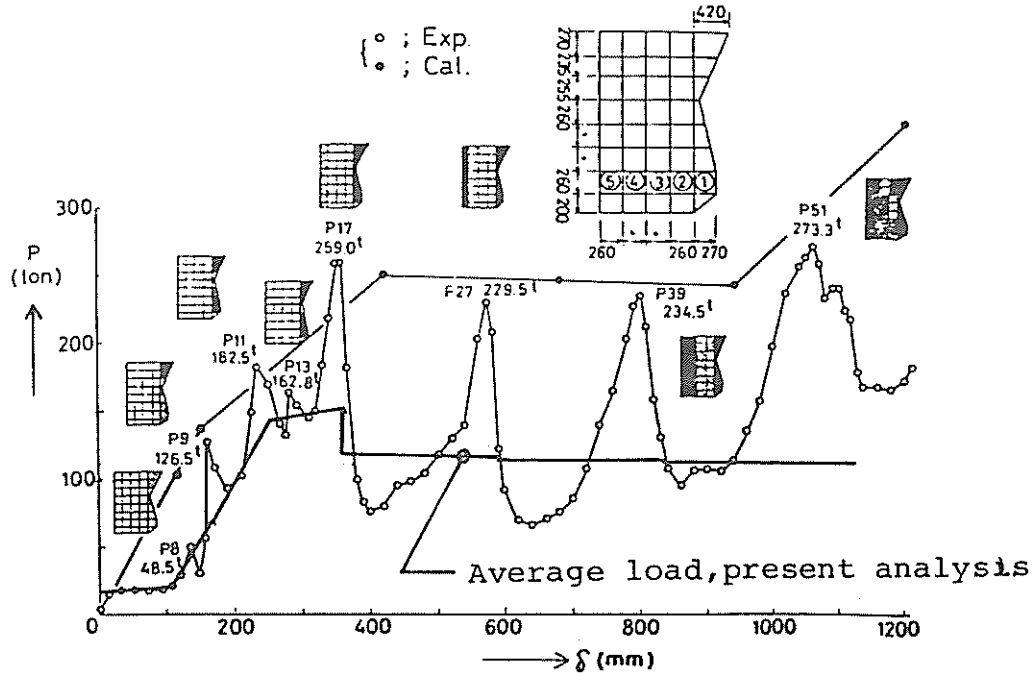

Gigure 7.13 Comparison between theory and experiment with a container ship model/12/.

the model. The predicted values are slightly in short of the experimental results, but this may possibly be attributed to the assumption with respect to the ultimate stress.

Considerably more sophisticated are the models used in some recent tests /10/. As shown in Fig. 7.11 the level of detailing is very high. Again the correlation between theory and experiments in Fig. 7.12 is remarkably good.

The final curve belongs to the stem of a container ship, Fig. 7.13 /12/. The method predicts correctly the slight decrease of the mean load when the indicated failure sequence is taken into account.

The conclusion to this comparison is that the theory yields credible force predictions for composite structures provided that the number of plate intersections is not too small. For structures with predominantly longitudinal stiffeners the load is overestimated. In lack of adequate methods a careful use of the method may provide reasonable estimates.

It is emphasized that the present theory adresses average compressive load only. In most cases this is relevant because the local peaks will not exceed the average load very much as buckling of individual panels does not occur simultaneously. However, for certain bow structures characterized by few longitudinal strength members and almost constant cross-sectional area, such as the container carrier, each frame section may have a pronounced simultaneous collapse. In this case a separate assessment of maximum load is required.

7.3 Bulbous Bows

7.3.1 Circular Cross-Sections

As an introductory study a series of 9 circular ringstiffened tubes is tested in axial compression. Four specimens, denoted by MA1-MA4, are machined from 12 mm thick seamless tubes that are stress relieved before being machined. These cylinders are almost ideal in the sense that residual stresses and shape imperfections are small.

The five fabricated cylinders denoted by FA1-FA5 are rolled from a 2 mm plate, and then closed by a longitudinal butt weld. The ring stiffeners are machined from 25 mm seamless tubes and attached to the shell by intermittent fillet welds. After welding the cylinders are stress released by heating to 550°-600°.

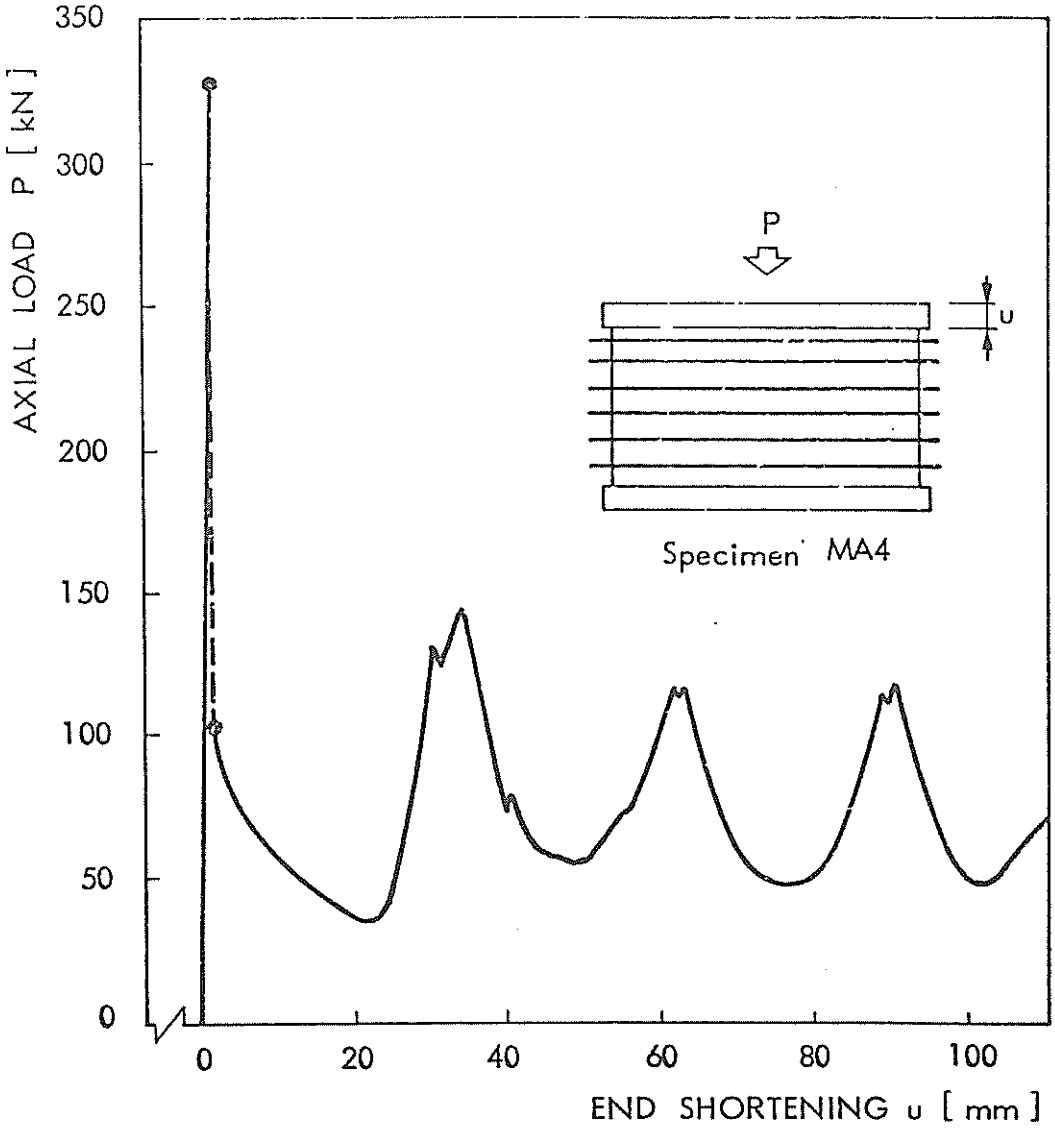

Fig. 7.14 Load-displacement curve for specimen MA4.

The diameter is 400 mm for all cylinders. Data for thickness, stiffener spacing, yield stress and ultimate stress are given in Table 7.1

Test specimen	MA1	MA2	MA3	MA4	FA1	FA2	FA3	FA4	FA5
Wall thickness h mm	0.97	1.22	0.99	0.98	2.03	2.06	2.06	2.04	2.05
Stiffener spacking ℓ mm	23.0	37.0	33.5	33.5	47.0	57.0	67.0	97.0	117.0
Yield stress σ_y [N/mm^2]	267	267	267	267	236	236	236	228	228
Ultimate stress σ_u [N/mm^2]	374	374	374	374	300	300	300	300	300

Table 7.1. Data for Test Specimens

The load displacement curve for specimen MA4 is shown in Fig. 7.14. The shape of the curve can be explained by considerations similar to those for the bow models.

An illustration of the successive development of plastic mechanisms is found in Appendix.

For the machined specimens it is found that the initial capacity exceeds the theoretical elasto-plastic buckling stress. One major reason for this result is that the machined specimens are almost ideal specimens as far as shape imperfections and residual stresses are concerned.

Owing to the low D/t-ratio the fabricated models have little sensitivity for shape imperfections. Thus the buckling stress is often considerably higher than predicted also for these specimens.

Of major concern in the present study is the average load during compression. The theoretical solutions are compared with the experimental values in Table 7.2.

Test specimen	MA1	MA2	MA3	MA4	FA1	FA2	FA2	FA4	FA5
Experiments [kN]	68.1	103.2	80.5	62.5	158.2	147.8	143.6	139.9	147.7
Theory [kN]	54.5	73.0	52.2	51.3	130.7	125.0	121.3	115.3	113.1
Theory/Exper.	0.80	0.71	0.65	0.82	0.83	0.85	0.84	0.82	0.77

Table 7.2. Analytical and Experimental Values for Average Load P_{av}

The tests confirm that the average load is influenced only slightly by the stiffener spacing. However, Table 7.2 indicates some discrepancy between analytic predictions and test results. In all cases the experimental values lie above the analytical predictions. Several factors can explain this discrepancy.

First, the deformation patterns in the tests differ somewhat from the configurations assumed in the mechanism models. For the machined models the ring stiffeners are rather weak so that they undergo twisting. The deformed stiffeners prevent the development of an ideal mechanism in the shell wall. This effect is very pronounced for MA2, MA3.

The second effect of importance is that in the theoretical models the plastic hinges are supposed to be stationary. However, during the tests it is easily observed that the location of plastic zones changes during deformation. Such a motion of plastic hinges gives an extra contribution to plastic energy absorption and thereby raises the average load P_{av}. The theoretical models do not account for this effect.

7.3.2 Stiffened Elliptic Cross-Section

The present test series include four specimens with principal dimensions as shown in Fig. 7.15. The cross-sectional shape is identical for three of the models but the stiffening system is varied.

Transverse frames constitute the principal stiffening system for the first model but longitudinal stringers are also found.

In the next model a deck and a bulkhead is introduced.

The third specimen is stiffened primarily by L-profiles in the longitudinal direction. The deck and bulkhead is retained.

The fourth model is a combination of the two first specimens in the sense that the first half contains the deck and bulkhead, while these panels are omitted in the second half. Furthermore the cross-section is a part of an elliptical cone so that the front section coincides with the shape of the three other models.

The particulars of fabrication, material properties etc. are identical to those for the bow models.

The load-displacement characteristics for the test specimens are presented in Figs. 7.16 - 7.19. Below, the tests are commented upon briefly. For further details reference is given to Appendix.

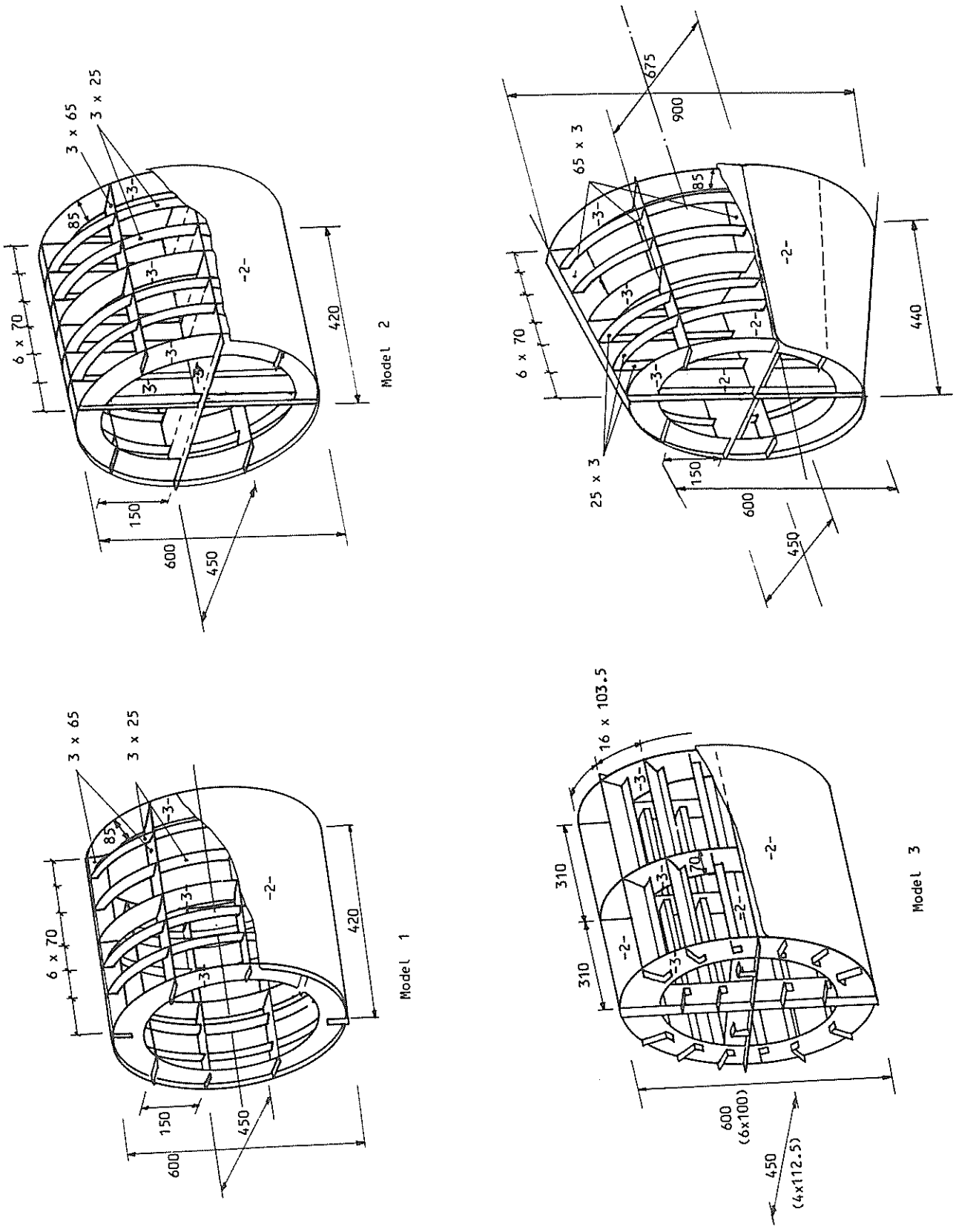

Figure 7.15 Bulbous bow models.

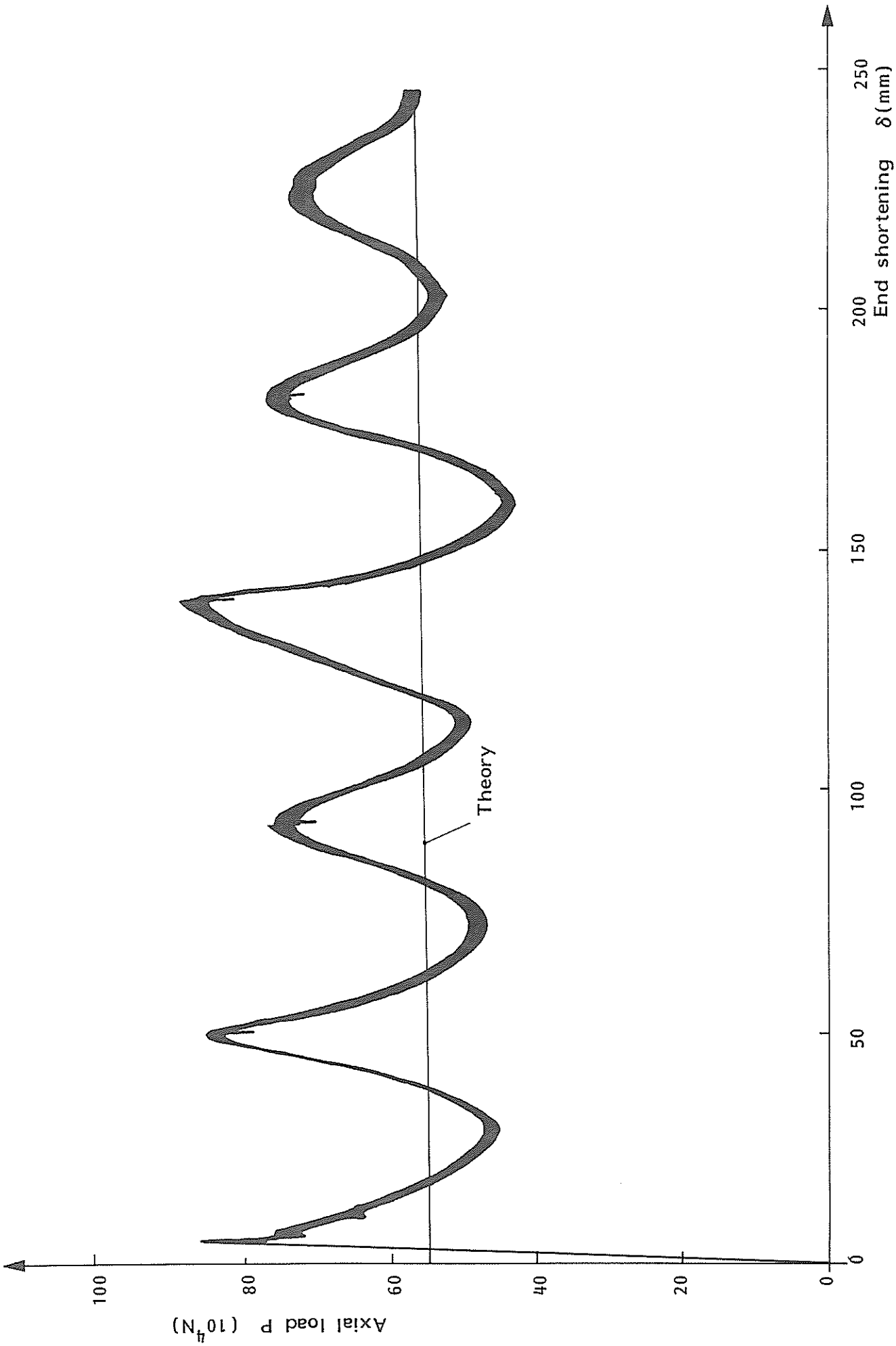

Figure 7.16 Load-displacement curve for elliptical cylinder

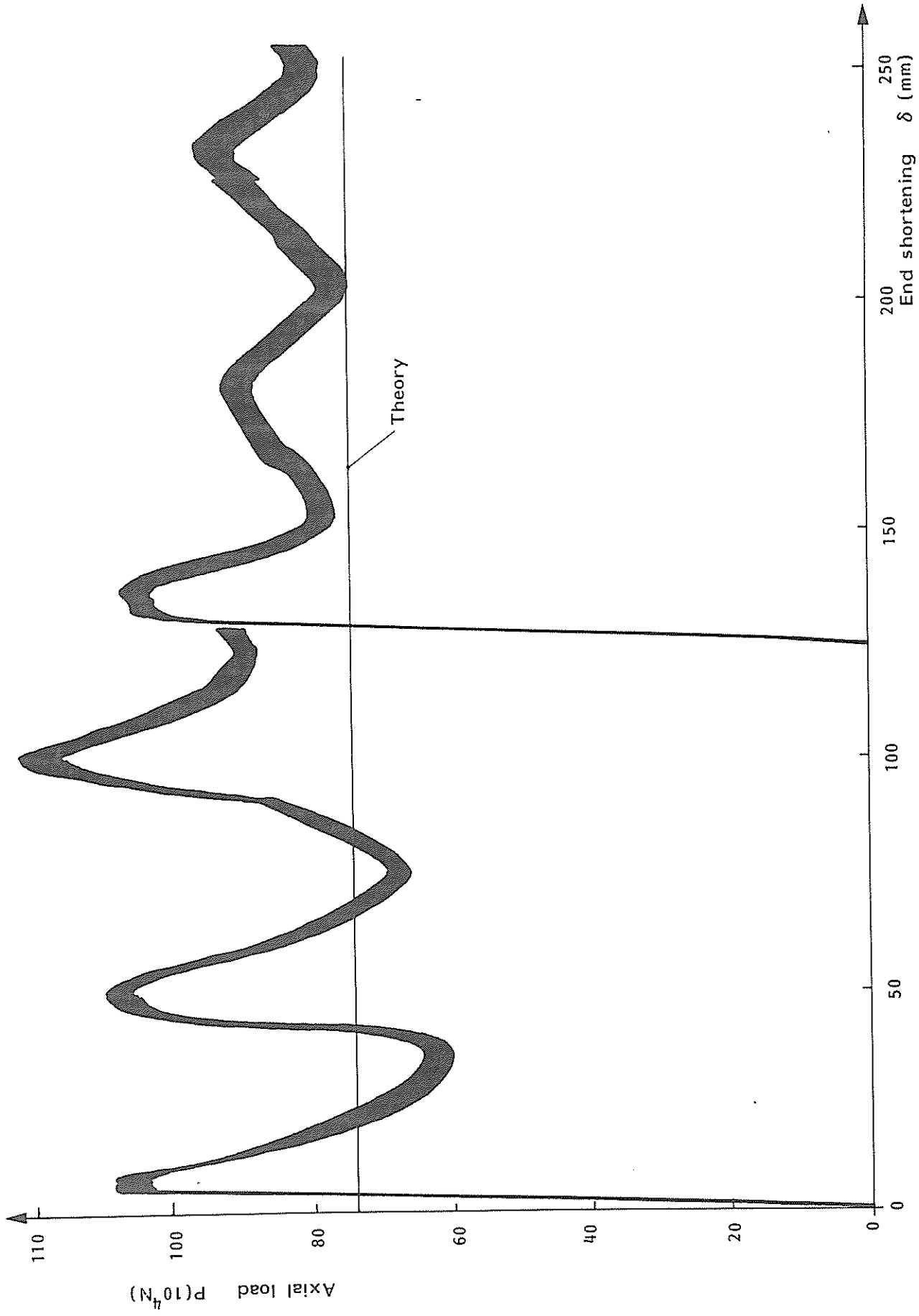

Figure 7.17 Load displacement curve for elliptical cylinder with deck and bulkhead

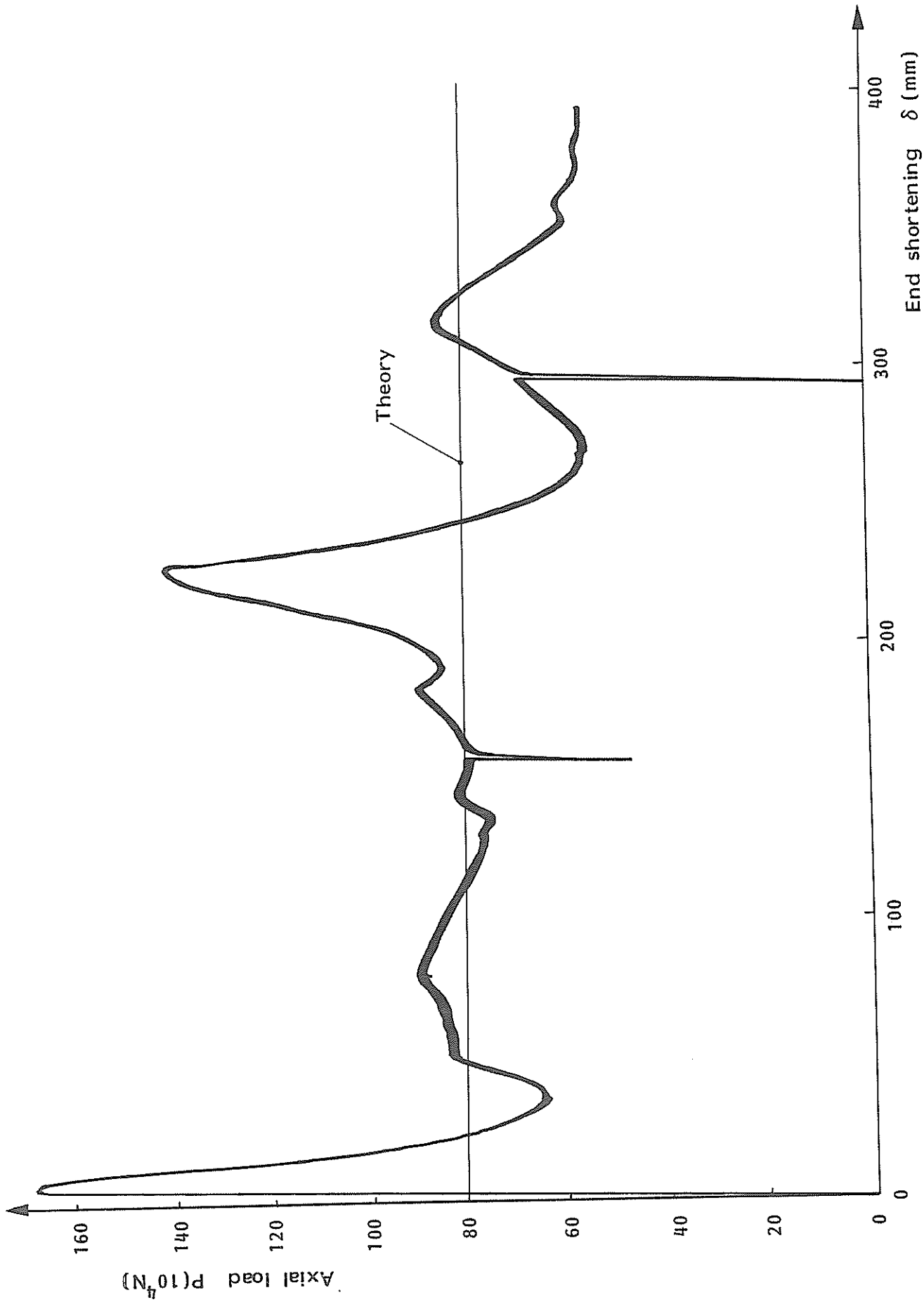

Figure 7.18 Load-displacement curve for elliptical cylinder with longitudinal stiffeners

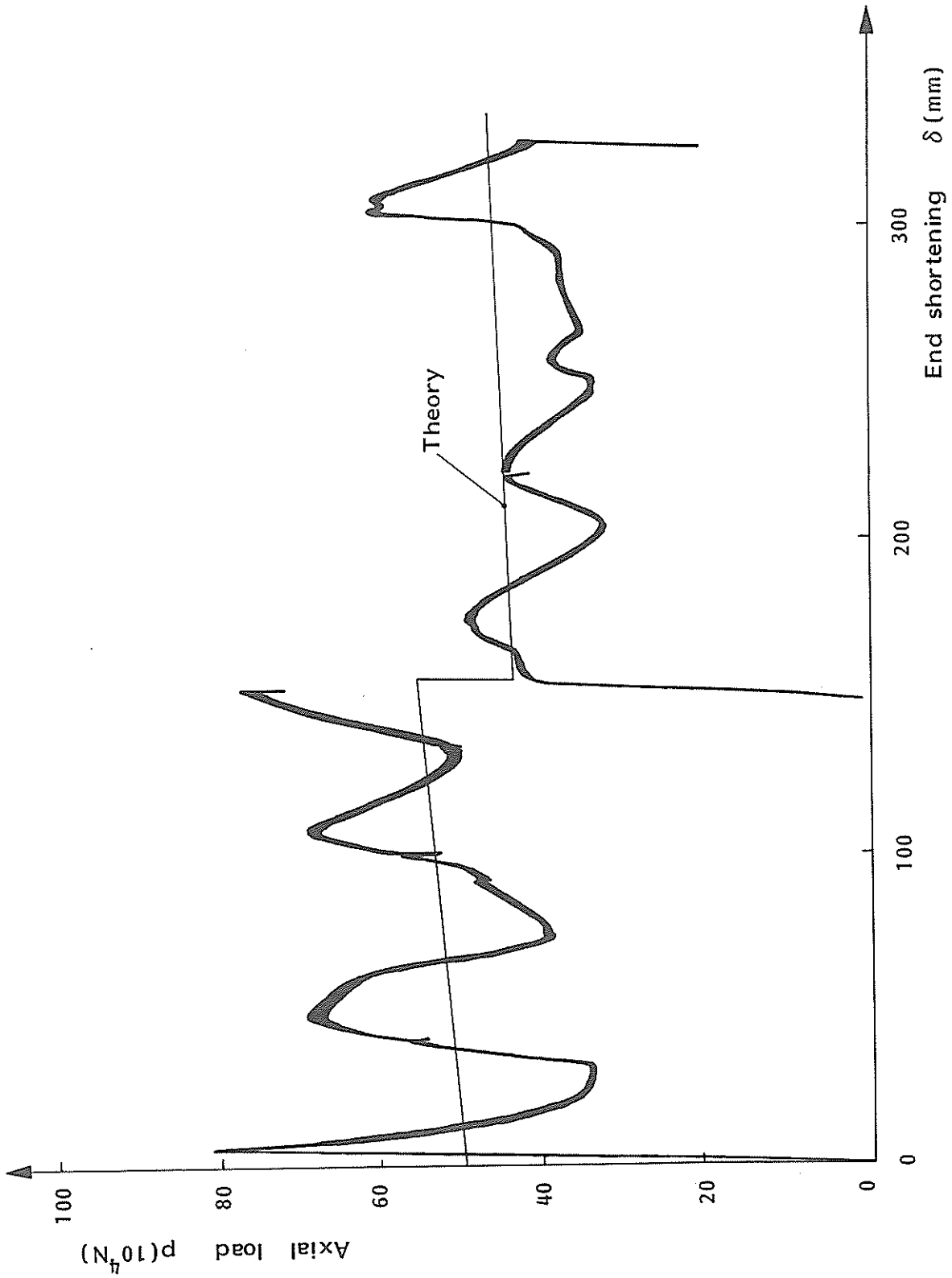

Figure 7.19 Load displacement curve for conical model

The load displacement curve for the first model, Fig. 7.16, shows a remarkable regularity. Each peak is associated with the formation of a new fold. Due to strong frames and low slenderness the subsequent peak loads do not decline very much compared with the initial buckling load. This is especially true for the field adjacent to the mid-frame.

Fig. 7.17 demonstrates the effect of the support on the load-curve. In the first phase the internal elements are unsupported at one end and the load oscillates considerably. In the second phase a complete support is provided. The result is an almost constant load although the average load remains approximately unchanged. The difference is mainly caused by increasing distortion of boundaries due to a non-uniform compressibility of the cross-section.

The longitudinally stiffened model shows a distinct double peak response caused by initial buckling. In the first several local folds are created at an almost constant load level. In the second field overall panel instability interacts with local buckling, thereby reducing the average load.

The load curve for the conical model, Fig. 7.19, is split into two phases. The first phase belongs to compression of the front section during which the internal elements are supported at the aft end. The increase of the average load caused by increasing cross-section is apparent.

In the second phase the absence of deck and bulkhead reduces the total load consideraly. However, the reduction of average load overcompensates for the reduction of cross-sectional area. The reason for this is that there is a tendency of skin reversal, which after all is prevented by transverse frames. This effect limits the completeness of folding.

The load diagrams contain a plot of the predicted average load. The results of the comparative study are also summarized in Table 7.3.

		Model	Model 2	Model 3	Model 4
Initial buckling	Experiment	83	109	165	82
	Theory	81	120	142	84
Average load	Experiment	58	84	80	46
	Theory	55	75	79	48

Table. 7.3 Comparison between Experiments and Theory. Unit: [10^4N]

The calculated elasto-plastic buckling loads are based upon the smaller buckling stress for the skin plates. It is interesting to see that the experimental values are very high in spite of a very poor adjustment of edge conditions.

The shortage of the predicted load for model no. 2 is due to the lack of support of the internal elements in the test which makes the assumption of a uniform stress at the instant of buckling too optimistic.

The high buckling load of model no. 3 is presumably due to a reserve capacity from the increased yield stress of the stiffners.

Generally, the agreement between the measurement and predicted average loads is satisfactory. It is observed that this holds true also for model no. 3 with longitudinal stiffners, while a considerable discrepancy was obtained for the bow model with I-profiles. This is explained by the fact that the bulb model suffers local collapse to a great extent while overall instability predominates the collapse behaviour of the bow model.

It should be mentioned that the compressibility reduction factor is based upon one wave length between two frames. In reality three and two waves occurred in the bulb test. If the true wave length is used the theoretical load will be raised somewhat.

7.3.3 Analysis of an Actual Grounding Incident

The pallet carrier M/S Fjord grounded in 1983 on Byneset close to Trondheim harbour. The ground on the spot is characterized by a steep cliff down to several metres of depth. Thus the ship was stopped by a virtually rigid barrier with a great similarity to the boundary conditions in the present experiments. The replaced region is indicated in Fig. 7.20 showing that only the bulbous section of the bow was damaged.

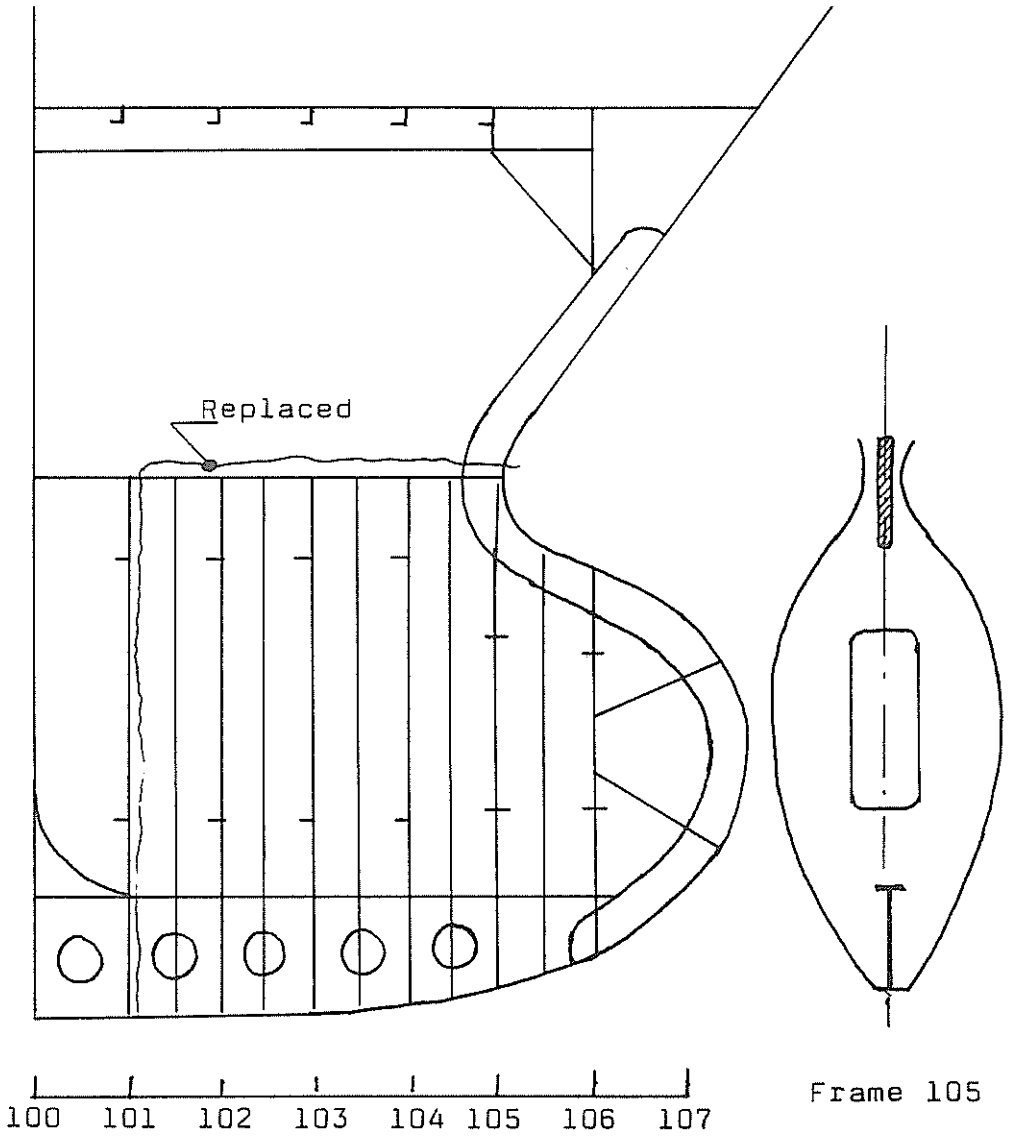

Fig. 7.20 Damaged bow section

The actual region of completely compressed elements was approximately bounded by the imaginary continuation of the stem profile. In the present calculations the damage is assumed to be equally distributed over the height. In average the depth of indentation is limited to frame 103.

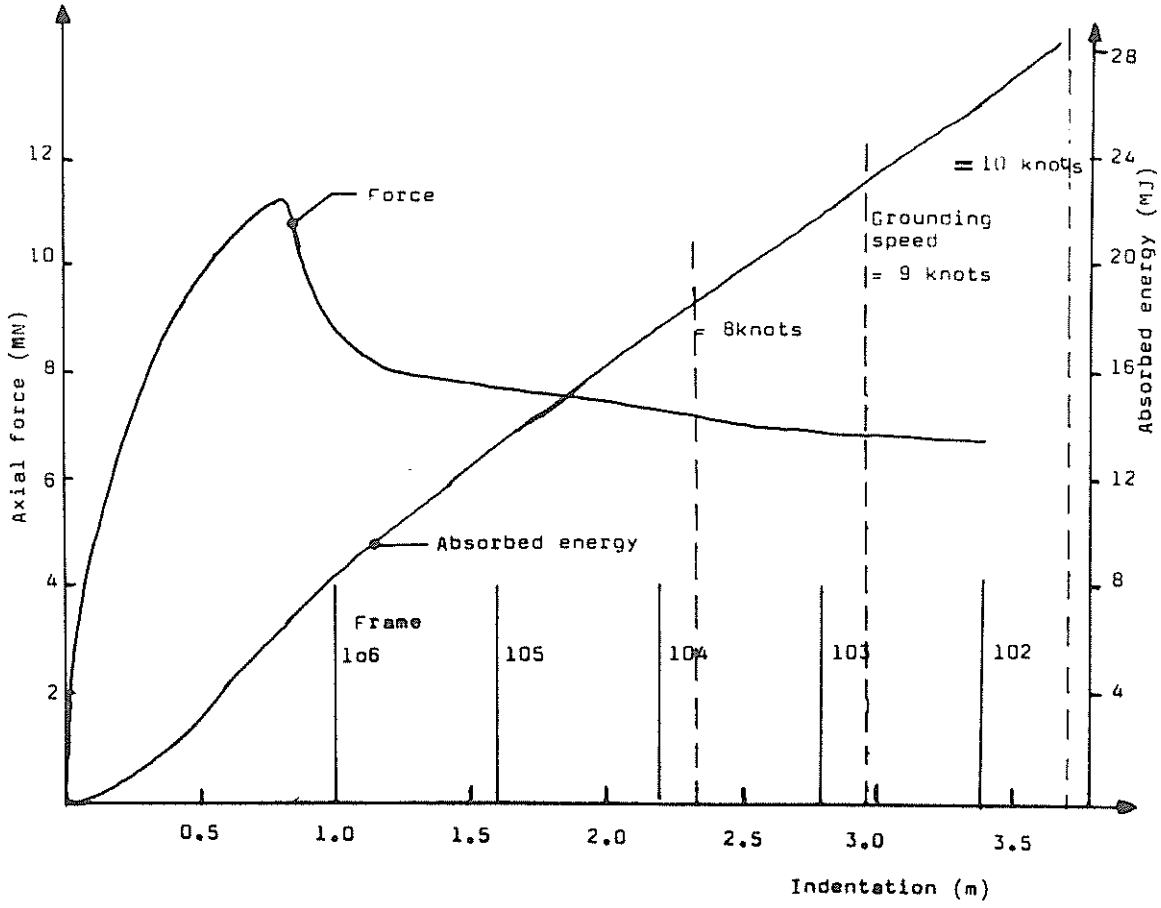

Fig. 7.21 Axial load and energy absorption versus indentation

In Fig. 7.21 the load and absorbed energy are plotted versus indentation. Also shown is the equivalent speed of the vessel in the accident loading condition provided that the kinetic energy is exclusively absorbed by plastic deformation of the hull. It appears that the damage assumption corresponds to a grounding velocity close to 9 knots.

This result agrees excellently with the statement of the captain who estimated the speed to be in the range of 8-10 knots and most likely 9 knots.

Of course, the present case yields a very simple control of the theoretical model and the sources of uncertainty are numerous. Nevertheless, the agreement is encouraging as concerns application of the method to full scale incidents.

7.4 Stern Section

7.4.1 Test Results

Fig. 7.22 shows the dimensions of the models used. Two specimens are constructed; one for a static test, the other for a dynamic test. The models are fabricated as identical as possible.Corresponding elements are taken adjacent to each other from the model material and the same welding procedures are applied.

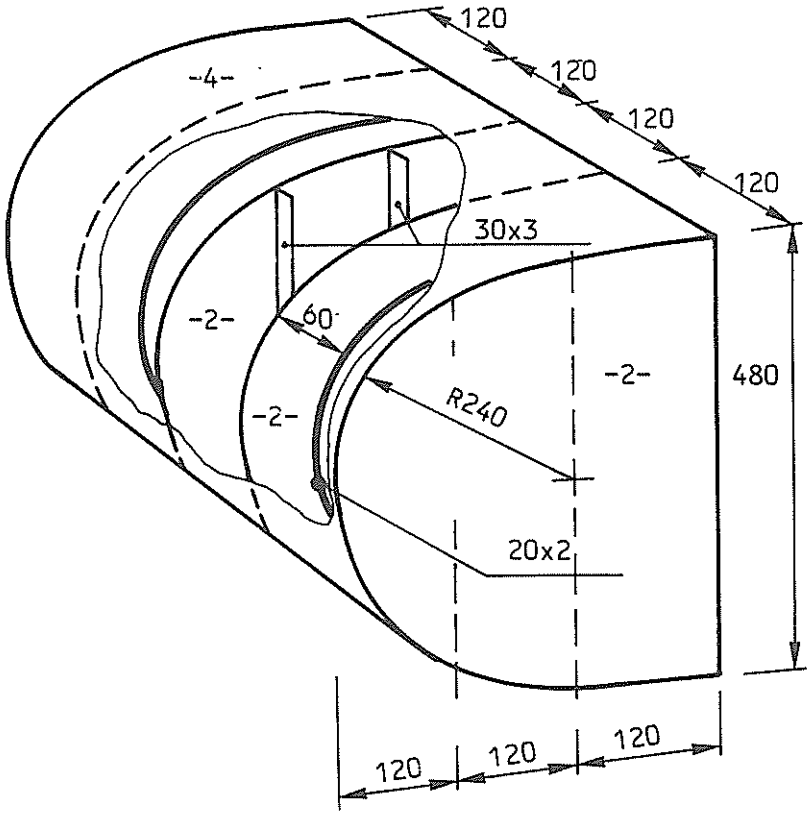

Figure 7.22 Model of a stern section

The indenter is a rigid section of a curved cylindrical shell with a radius of curvature of 1 m. The axis is oriented prependicular to the axis of the curved end of the stern section and initial contact occurs at the center bulkhead.

Both tests are executed at a constant rate of deformation amounting to 0.15 mm/s in the static test and 70 mm/s in the dynamic test.

The load-deformation diagrams for the tests are presented in Fig. 7.23. The shape of the curves appears to be quite similar, but the dynamic test yields a higher load level. This is also indicated by the dynamic augmentation factor which is presently defined as the fraction of dynamic load to static load.

The geometry of the impacting bodies causes a steady increase of the contact area and the load. The local gradients are due to activation of other ringstiffeners or bulkheads. The maximum load is attained when cracks start to develop at the skin/frame intersections. However, at this stage the test has been run far beyond the validity range for the impact model.

A further description of test observations is presented in Appendix.

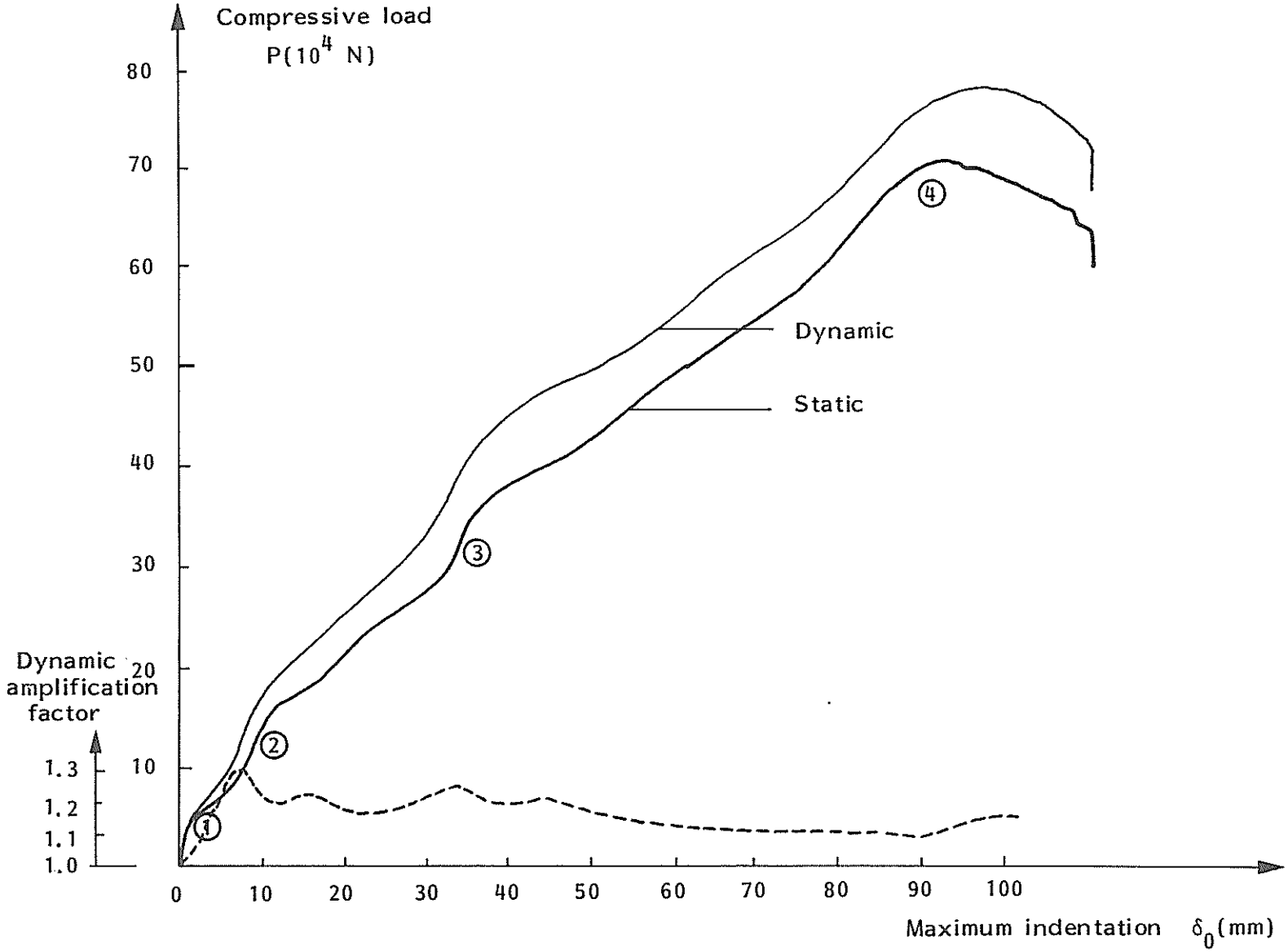

Figure 7.23 Load versus indentation for stern models

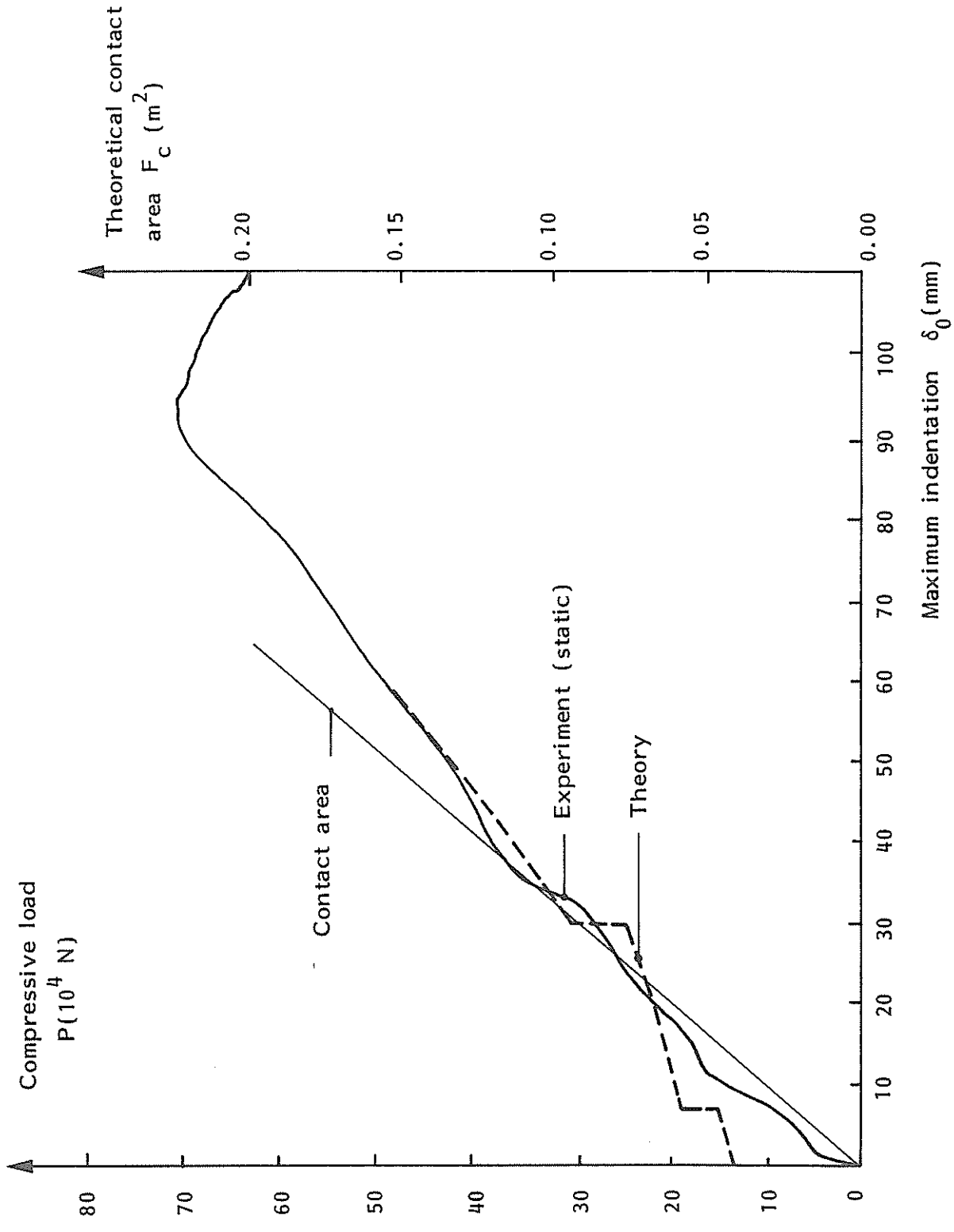

Figure 7.24 Comparison between theory and test for stern model

7.4.2 Comparison with Theory

The predicted load-deformation curve, based upon the theory outlined in Sec. 5.2 is compared with the results from the static test in Fig. 7.24. The correllation is satisfactory except for small indentations where elastic strain contributions predominate.

The jumps in the theoretical curve relate to activation of ringstiffeners and bulkheads. In practice there will be a smooth transition.

The predicted values are somewhat too high for large indentations since the theory assumes a continuous unbounded model, whereas the contact zone expands past the side bulkheads.

Also plotted is the theoretical contact area which increases linearly with deformation.

As to the dynamic amplification factor it is postulated that this is caused predominantly by the strain rate sensitivity. Two different methods can be used to estimate this effect.

The average strain rate for the basic folding mechanism is derived in sec. 4.8.1. Assuming Eq. 4.160 valid also for the present problem the strain rates comes out to be $3 \cdot 10^{-4}$ s^{-1} in the static case and 0.15 $\bar{s}^{1}$ in the dynamic case. Thus the average flow stress σ_0^1/σ_0 given by Eq. 4.166 becomes 1.038 and 1.130 yielding a dynamic to static amplification ratio equal to 1.09. Eq. (4.165) may be used to predict a peak augmentation factor of 1.22.

These figures are considerably lower than the measured ones, especially in the first stages of collapse.

An alternative approach is to apply Eq. (4.168) where the material constant n is determined experimentally. Let the average amplification facator as measured for the test specimens be 1.20. This yields n = 0.03.

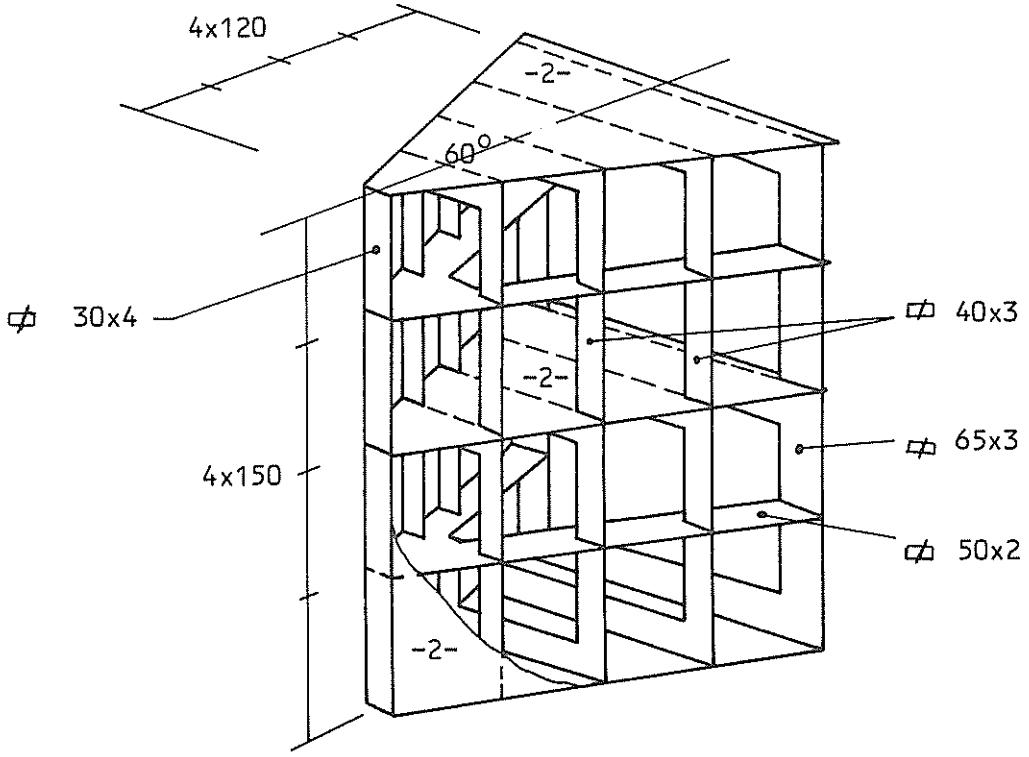

Model 1

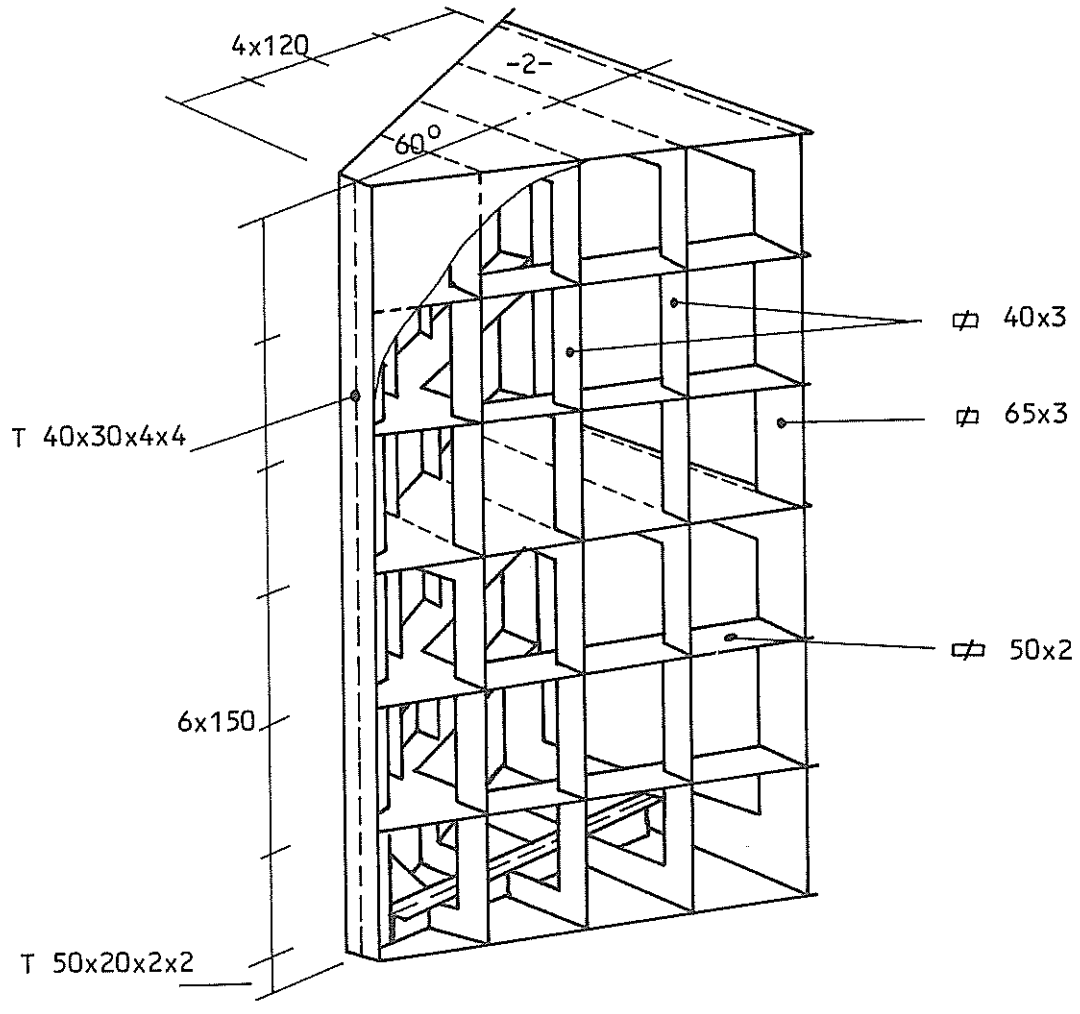

Model 2

Figure 7.25 Models for bow-bracing impact.

7.5 Bow - Bracing Impact

7.5.1 Test Results

In this section tests simulating impacts between the bow of a supply vessel and a platform bracing are described. The structural arrangement of the models shown in Fig. 7.25, is similar with respect to dimensions of the shin, decks, stringers and frames. Model No. 2 is an extended version of Model No. 1 by introducing two additional stringers. Furthermore, the stem plate is restrengthened by a web plate so that a T-profile emerges. Each end is supported by a longitudinal girder.

The thickness of the stem plates is twice the thickness of the remaining longitudinal elements. The stem is assembled by a continuous, double fillet weld.

The specimens are intended to model the icestrengthened zone of a supply vessel bow. Model No. 1 is considered to be representative of a medium strength stem, while Model No. 2 reproduces the principal features of a strong stem.

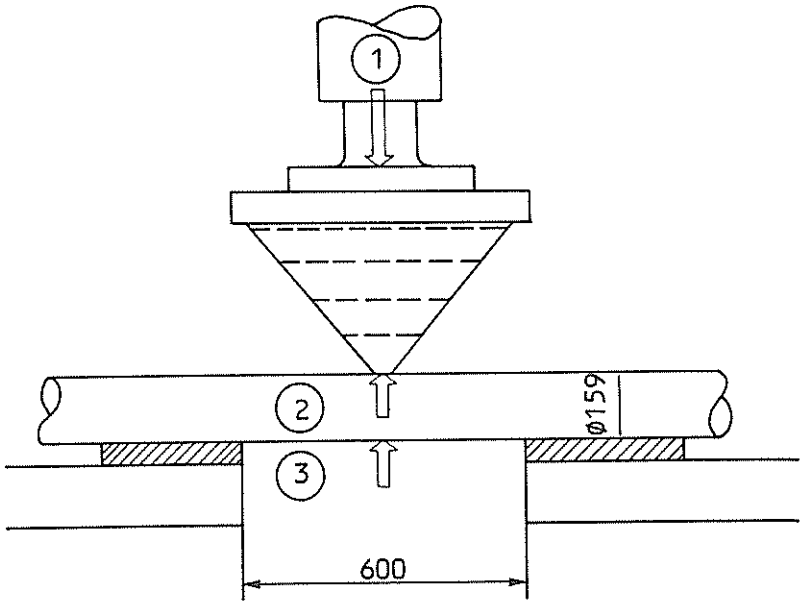

Figure 7.26 Test arrangement

The test arrangement is shown in Fig. 7.26. The tube simulating the struck bracing has a very small span in order to avoid beam collapse. The ends are simply supported and soft supports are provided by pieces of rubber.

Evidently the beam behaviour of the tube is not simulated very well. The local response is more realistic, which is the effect of major importance in this investigation.

Two different tubes are available both with an outer diameter D = 159 mm. The smaller tube has wall thickness t = 5.0 mm and yield point σ_y = 270 N/mm^2. The corresponding specifications for the second tube are t = 6.5 mm and σ_y = 380 N/mm^2.

Model No. 1 hits the tube midway between the centre deck and the stringer while initial contact for Model No. 2 occurs at mid-deck level. Displacements are recorded continuously at three positions; by the motion of the hydraulic piston itself, one displacement transducer attached to the tube directly under the stem tip and one at the lower generator. Thus the total deformation can be separated into one part related to penetration of the bow and one part associated with local denting of the tube.

The experimental results are presented in Figs. 7.27-7.29. A detailed description of the test can be found in Appendix.

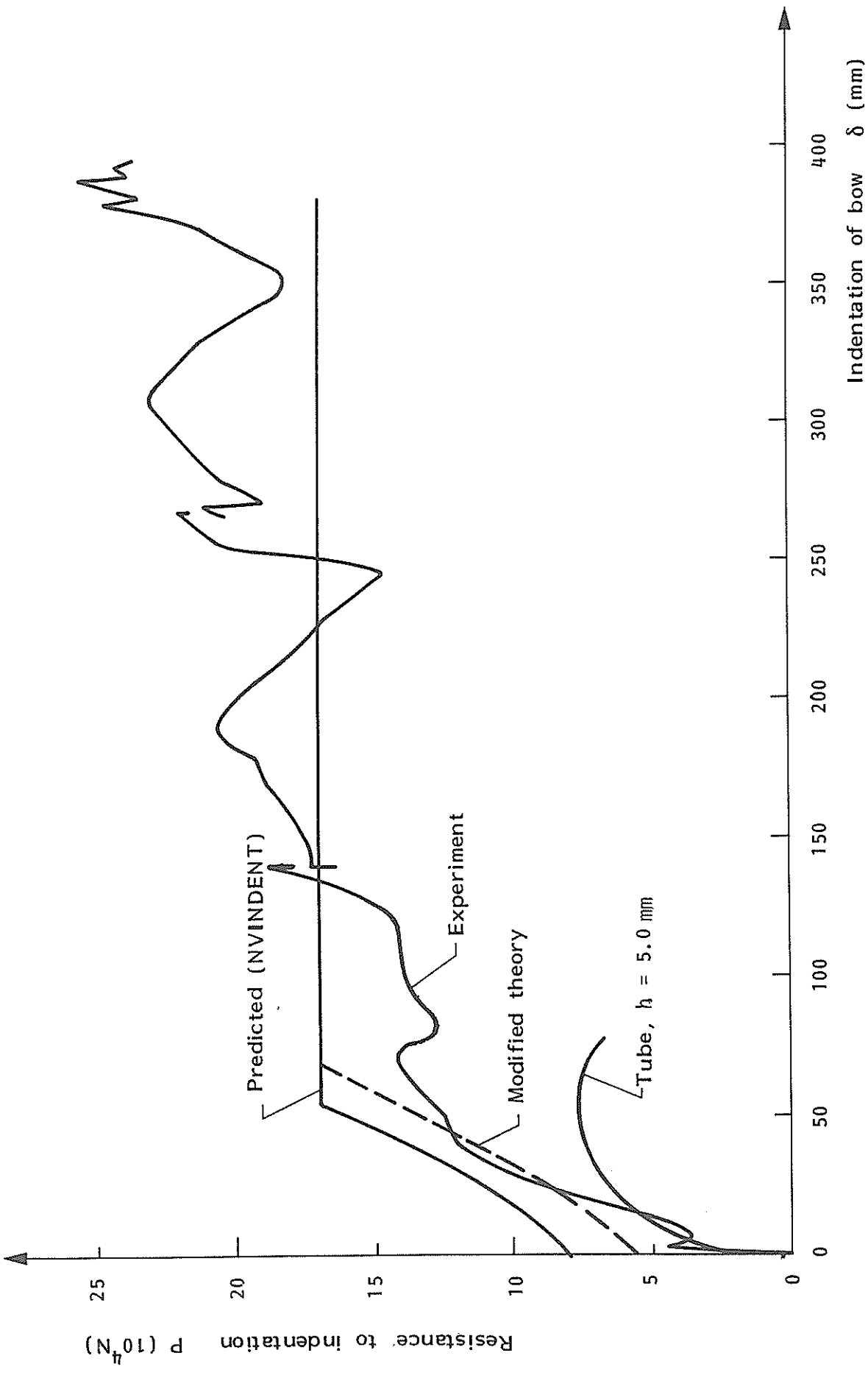

Figure 7.27 Load versus bracing indentation for medium strength stem

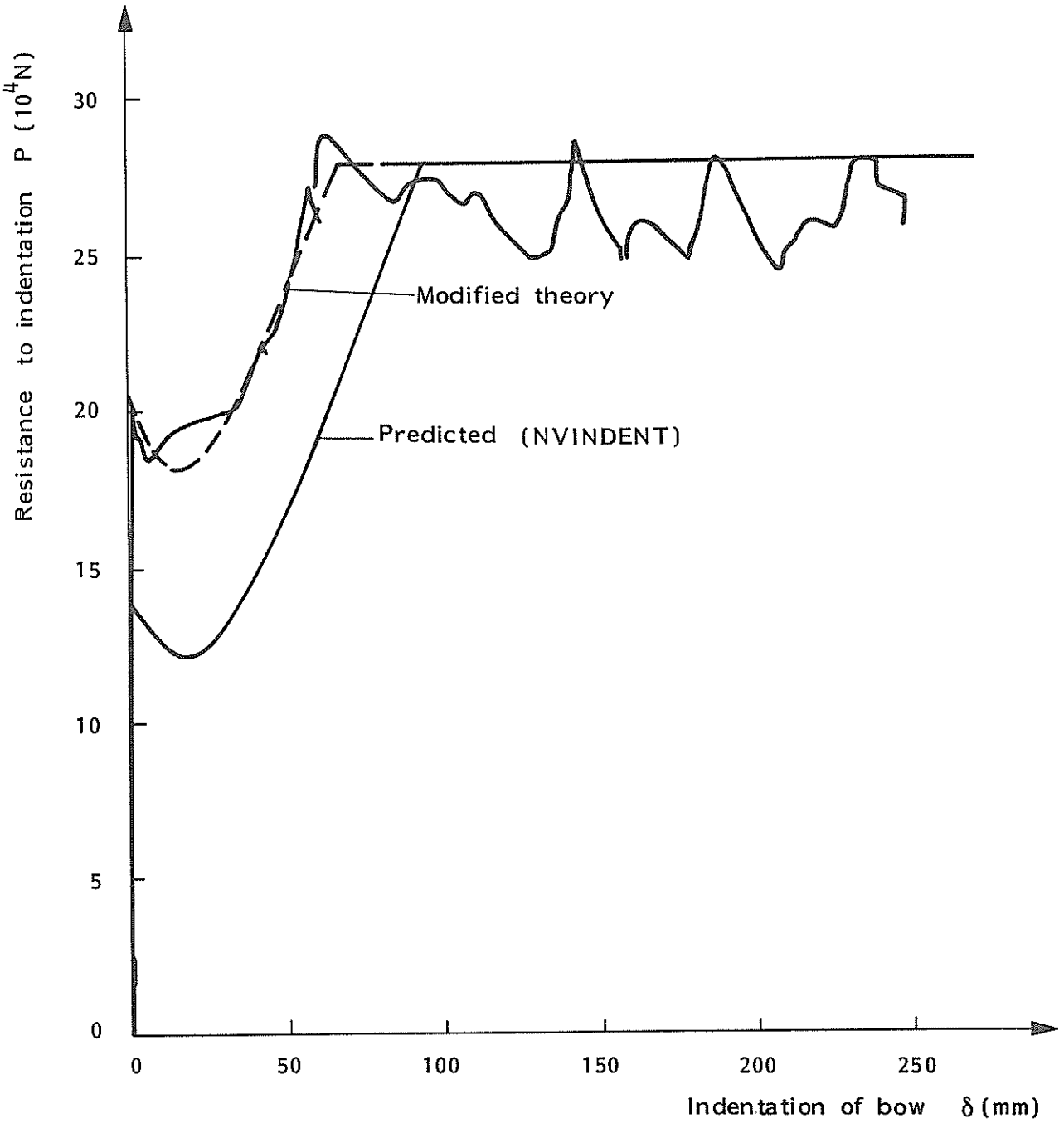

Figure 7.28 Load versus bracing indentation for strong stem

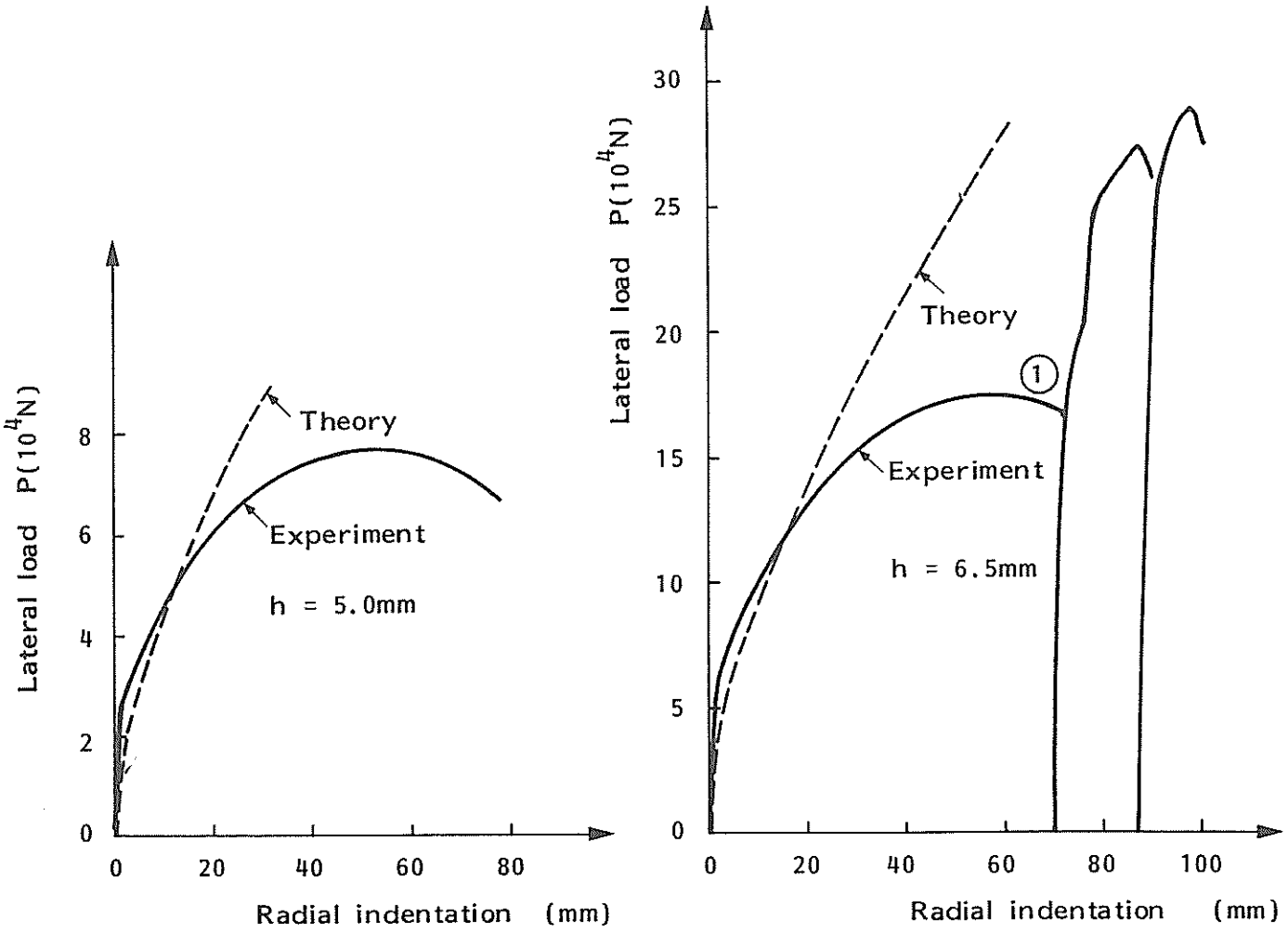

Figure 7.29 Load versus radial indentation of test tubes

Some important features can be learned from the first test. First of all initial failure depends on the mutual state of deformation of the colliding bodies. In the first run the tube suffers all the deformations. The bow remains virtually undamaged even though the total load exceeds the failure load experienced in the second run. This is due to the increase of the contact area as well as the motion of it towards the plate edges as the tube deforms.

Thus there may be a dramatic change in the mutual response for small variations of relative stiffness.

Initial failure of the bow depends strongly on the local configuration and location of contact. Thus introducing a stem web and changing the initial contact to a stringer bring about a five time increase of the buckling load. The post failure loads do not differ very much. The average load should be approximately constant with local peaks caused by consecutive buckling of panels and/or penetration of transverse frames. The slight increase experienced with Model No. 1 is probably due to roll up of the deck.

7.5.2 Comparison with Theory

The failure loads are compared with theoretical predictions based upon the approach outlined in Sec. 5.3. The total buckling resistance for a concentrated load which is supported by shear along the axial edges comes out to be 54 kN as compared with the measured failure load of 44 kN for the medium strength model.

The second estimate yields the buckling load of four panels adjacent to the point of contact. A uniform stress field is assumed which is motivated by the capability of the stem profile to distribute the load. The prediction contains also a contribution from buckling of the centre deck. The agreement between the measured value 202 kN and the theoretical figure 205 kN is excellent.

The load during large displacement is calculated with the computer program NVINDENT /2/. It appears that the mean load is assessed fairly well except for small indentations. This is mainly due to different assumptions with regard to initial buckling and post-buckling conditions.

However, the shape of the theoretical curve complies reasonably well. An improved load prediction is obtained by constructing a curve which is merely a parallel shift of the computed curve to the theoretical buckling load.

8. RECOMMENDED ANALYSIS PROCEDURE AND DESIGN CURVES

8.1 Bow Impacts

The method outlined in Sec. 5.1 is used to assess load-deformation curves for bow collisions against a concrete column. This is substantiated by the satisfactory correlation obtained between experiments and theory. The vessel in consideration is a supply vessel of 5000 tons displacement which constitutes the basis for the recommended design curves in Ref. /6/. The structural arrangement is shown in Figs. 8.1a, d. The composition of basic structural elements in the calculation model is based on the frame drawings.

The material used in the bow is mild steel with σ_y = 240 N/mm^2. The theory is correlated against the ultimate stress. For the class of material in question the DnV rules prescribe a tensile strength in the range of σ_u = 400 - 490 N/mm^2. Accordingly σ_u = 450 N/mm^2 is used in the theoretical calculations. No allowance is made for any dynamic effect (e.g. strain rate).

Owing to the finite curvature of a platform leg the deformations progress is faster in the centre than at the sides. This is accounted for in a simplified manner in that the total load is expressed as a linear combination of those frames which are intersected by the leg contour at a given indentation. Here, equal weights are used.

The results are compared with the present recommended design curve according to Veritas in Fig. 8.2. The curves deviate little especially for small indentations. This is somewhat surprising taking into account the very different approach underlying the pair of curves.

The present load prediction exceeds the curve proposed by Wierzbicki et al. in Ref. /14/. It is not straightforward to see what causes this difference. Possibly some of it is due to different assumptions as concerns the ultimate stress σ_u.

Load-indentation relationships for two other supply vessels are also plotted in the diagram. For moderate indentations these curves lie significantly below the prediction for the "design vessel", mainly due to smaller deck areas in the foreship. For large indentations, however, the ice-strengthened bow section starts to crush and the load grows rapidly.

Thus, the present design curve does not represent any upper bound for high energy collisions involving ice-strengthened stems.

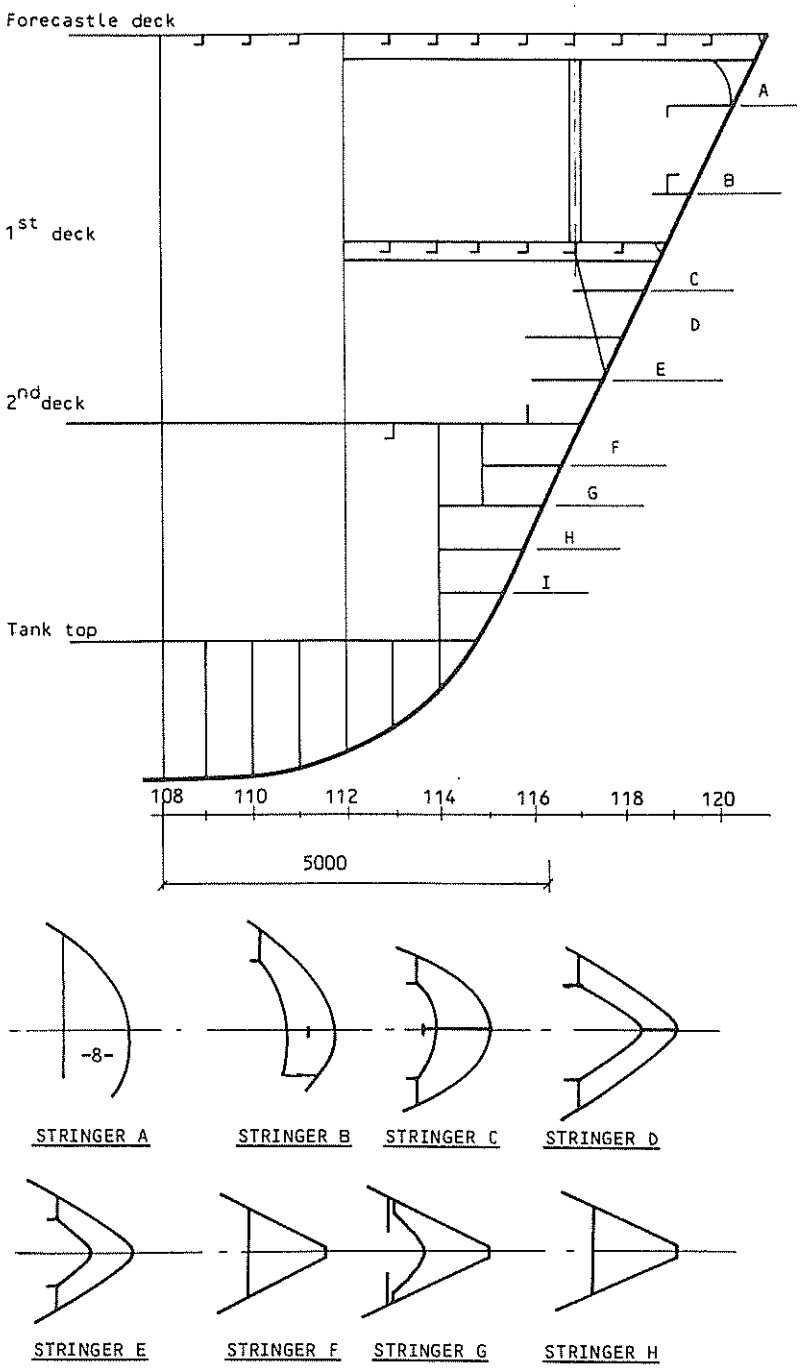

Figure 8.1a Supply vessel of 5000 tons displacement

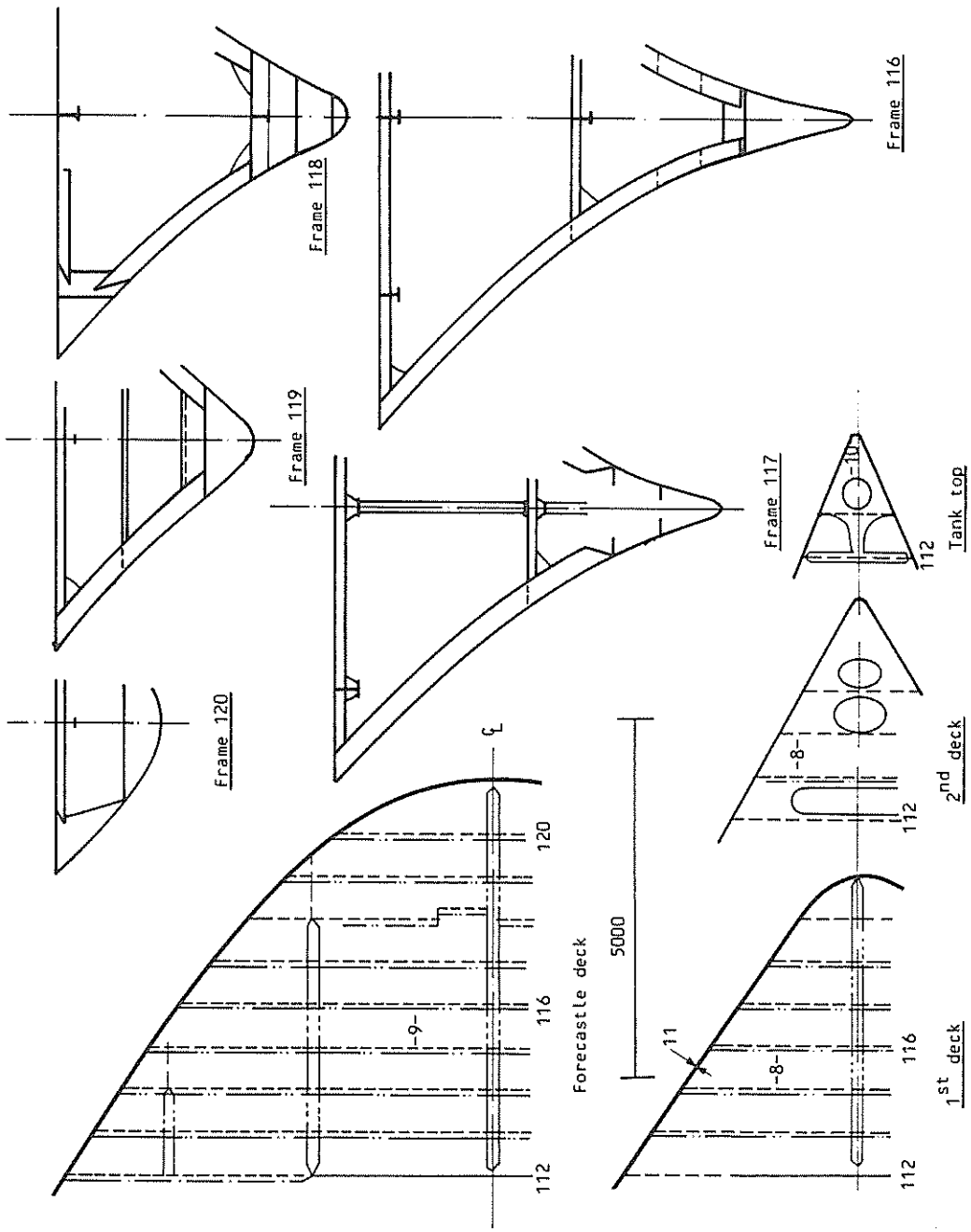
Frame 118
Frame 116
Frame 119
Frame 120
Frame 117
Tank top
2nd deck
1st deck
Forecastle deck
5000
120
116
112
-9-
-8-
-10-
11
℄

Figure 8.1.*b*

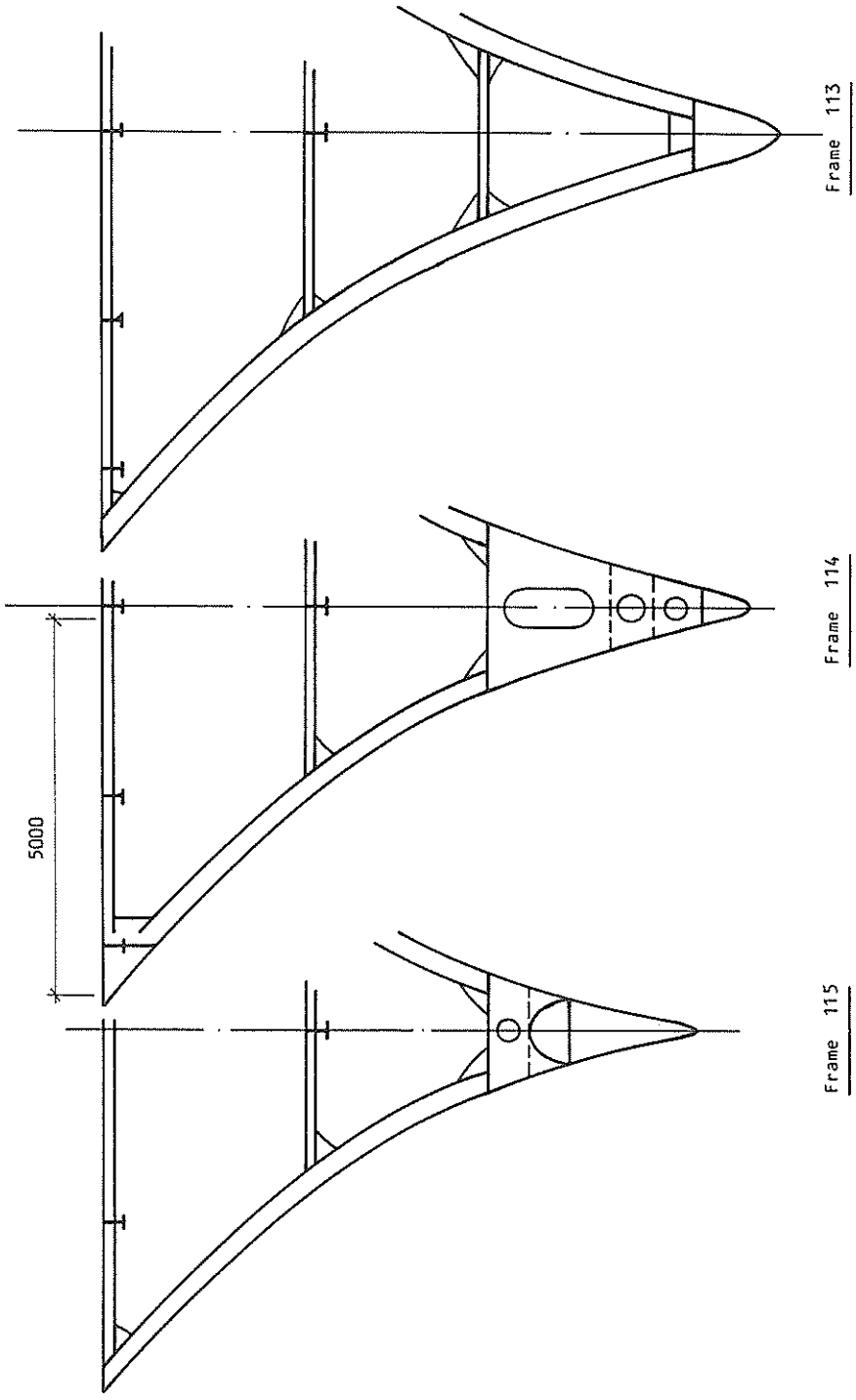

Figure 8.1.c

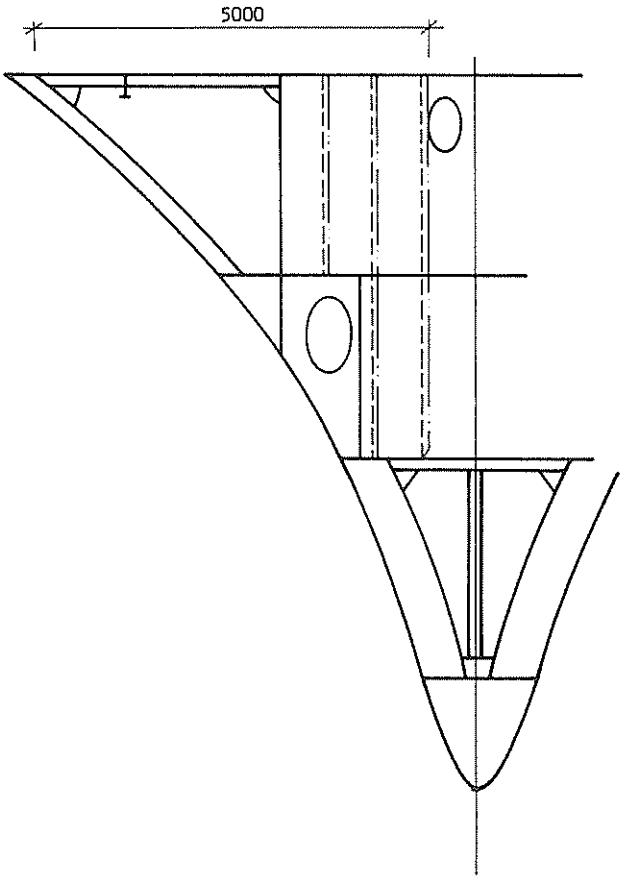

Frame 112

Figure 8.1.*d*

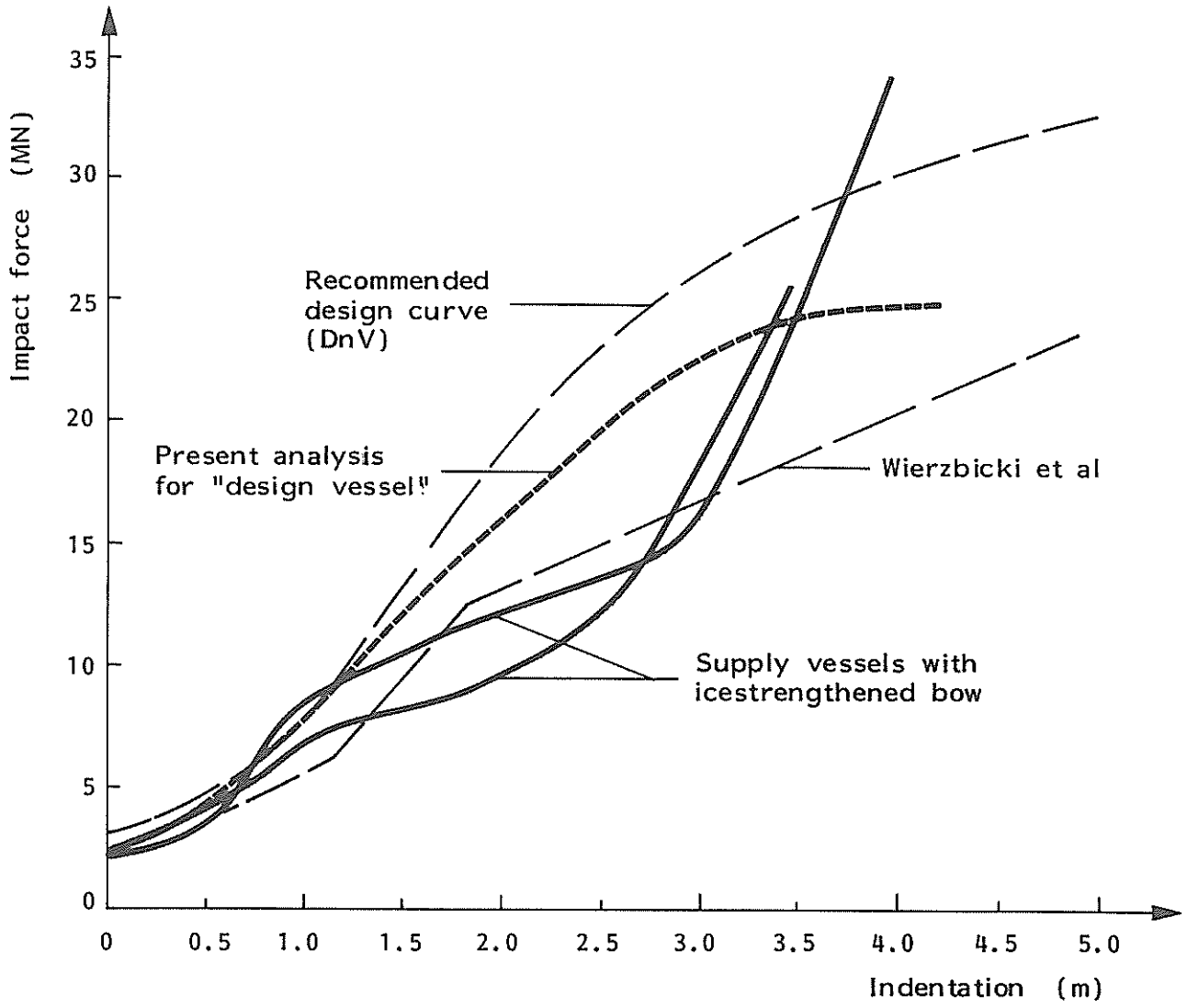

Figure 8.2 Load indentation curves for bow impact

8.2 Stern Impacts

Fig. 8.3 shows the principal dimensions and structural arrangement of a supply vessel fitted with a stern roller. Potential impacts may be classified according to the location of initial contact

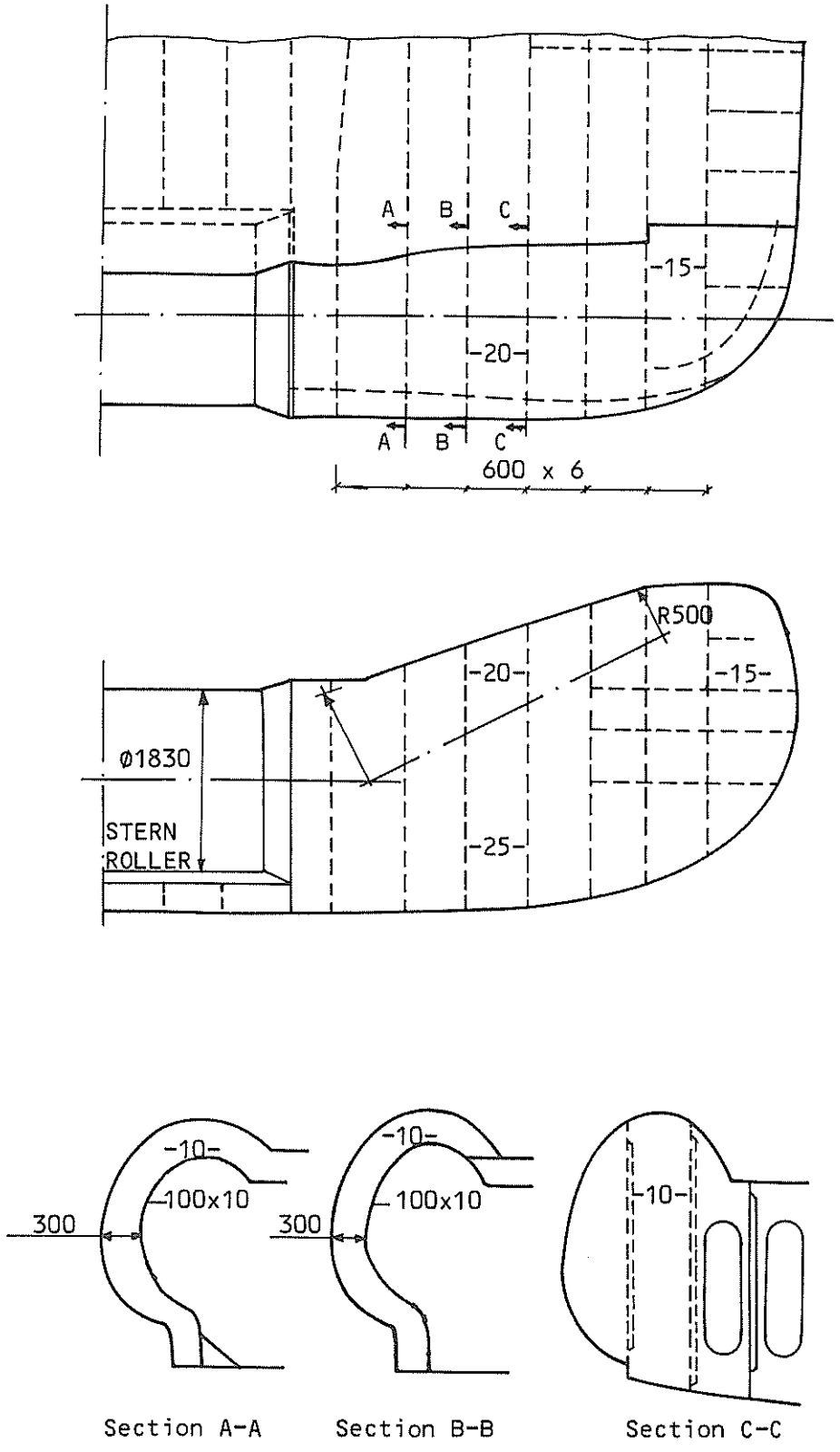

Figure 8.3 Structural arrangement of a supply vessel with stern roller.

i) Stern roller
ii) Curved end section
iii) Stern corner

The present study is limited to operational impacts with the curved end section only. According to Ref. /6/ the velocity defined for operational impacts is 0.5 m/s and the resulting load effect should not cause permanent deformations to the platform. This means that the ship is supposed to absorb the major part of the energy. Since the kinetic energy is only 1/16 of the accidental impact energy the damage to the ship structure will be relatively small and the analysis procedure outlined in Sec. 5.2 can be utilized.

The complexity of the structural arrangement necessitates a few simplifications. The end section is modelled analogously to the test pieces described in sec. 7.4 with a constant radius of curvature R = 1200 mm. Initial contact occurs at the bulkhead (section C-C).

Strain rate effects are accounted for. A fundamental assumption is that the material constant n found in sec. 7.3.2, can be considered valid also for the ship plate material. This yields a dynamic amplification factor of 1.22.

In the early stages where elastic effects are important the curve is partly drawn on the basis of "engineering judgement".

For concrete columns operational impacts may be critical with respect to local punching shear strength. Hence the average load intensity defined as the ratio between the load and total contact area is also assessed.

Some comments should be attached to calculation of contact area which is taken as the hypothetical area bounded by the intersection line between the shaft and the stern in undeformed configuration.

This is slightly conservative as far as the size of the contact area is concerned as this will be larger due to deformation of the ship structure.

Current design practice is to account for uneven load distribution by reducing the theoretial contact area by a certain factor. However, this is not fully consistent and probably conservative.

The reason for this is that the indentation progresses in stages. As new strength members become activated a local peak load is created at the spot. Consequently, the highly stressed regions may as well be located close to the edge of the contact area as in the centre where the deformation process has ceased. Thus, applying the total force over a reduced area in the centre of the contact zone may be unfavourable with respect to assessment of punching shear strength of the shaft.

Instead, load intensity estimates should be based on more thorough considerations of actual load distributions.

In Fig. 8.4 load diagrams are presented for two column diameters typical for a concrete column and a steel leg respectively.

The load predictions are compared with present design curve as recommended by Veritas /6/, Fig. 8.5. It is emphasized that the present curves apply to minor impacts only while the design curves apply to major impacts. The stern geometries are also different. However, it seems that the design curves may underpredict the load level for moderate indentations.

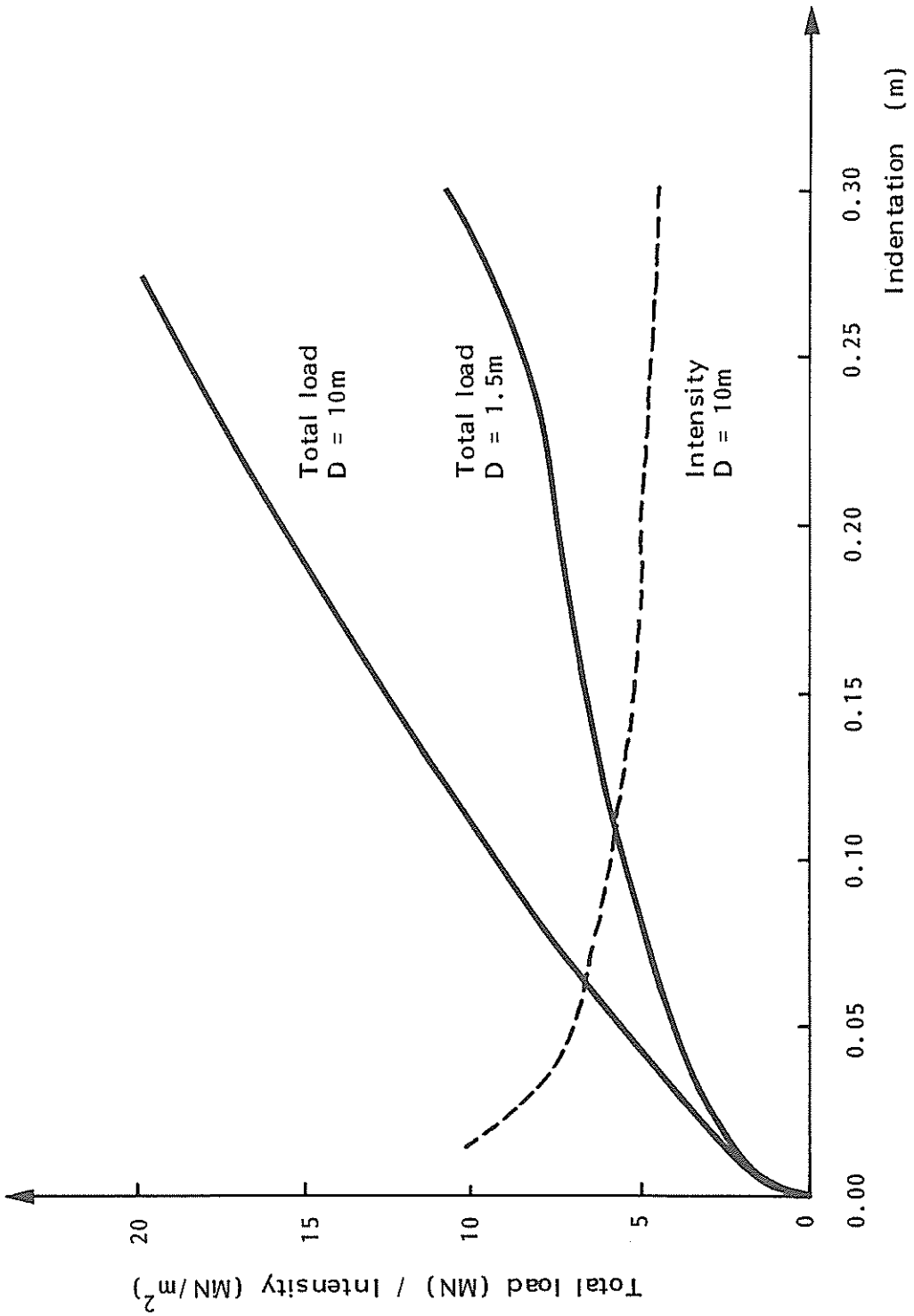

Figure 8.4 Recommended load deformation curves for minor stern impacts from supply vessels

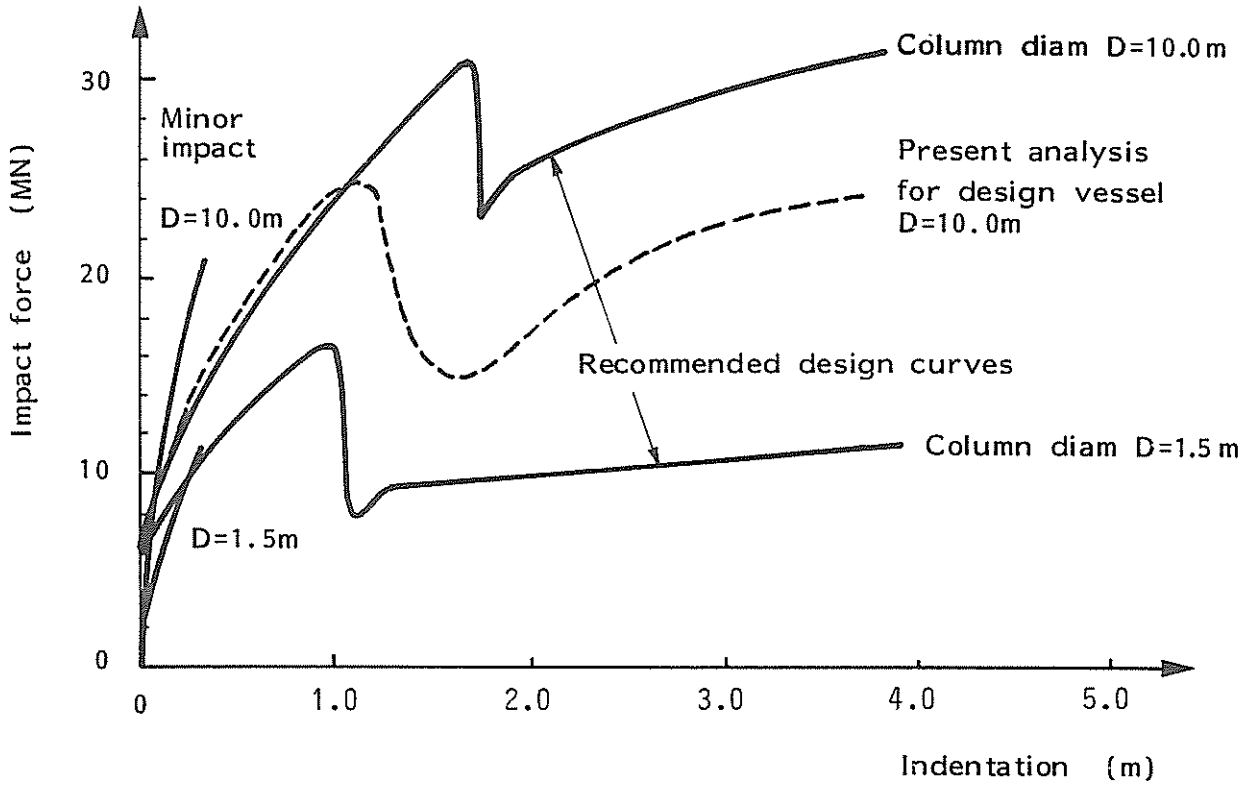

Figure 8.5 *Comparison between present load predictions and recommended design curves*

A load-indentation relationship for high-energy collisions is assessed for the stern of the supply vessel shown in Ref. /6/ applying the technique described in sec. 5.1. The indenting object is assumed to be a rigid colum with diameter D = 10 m.

The shape of the indenter implies a growth of the contact area with increasing indentation at a given cross-section. The step-wise increase of the load is calculated, and the total load derived by summation over all involved cross-sections. A plot of the resulting curve is shown in Fig. 5.5. It is noticed that the present analysis yields a significantly lower load level.

8.3 Bow/Bracing Impacts

In Fig. 8.6 the structural arrangement of the lower section of an ice-strengthened foreship of a supply vessel is shown. The principal stiffening system consists of horizontal breast hooks and stringers. The vertical stem in the front is a massive T-profile which serves to distribute concentrated loads to adjacent elements.

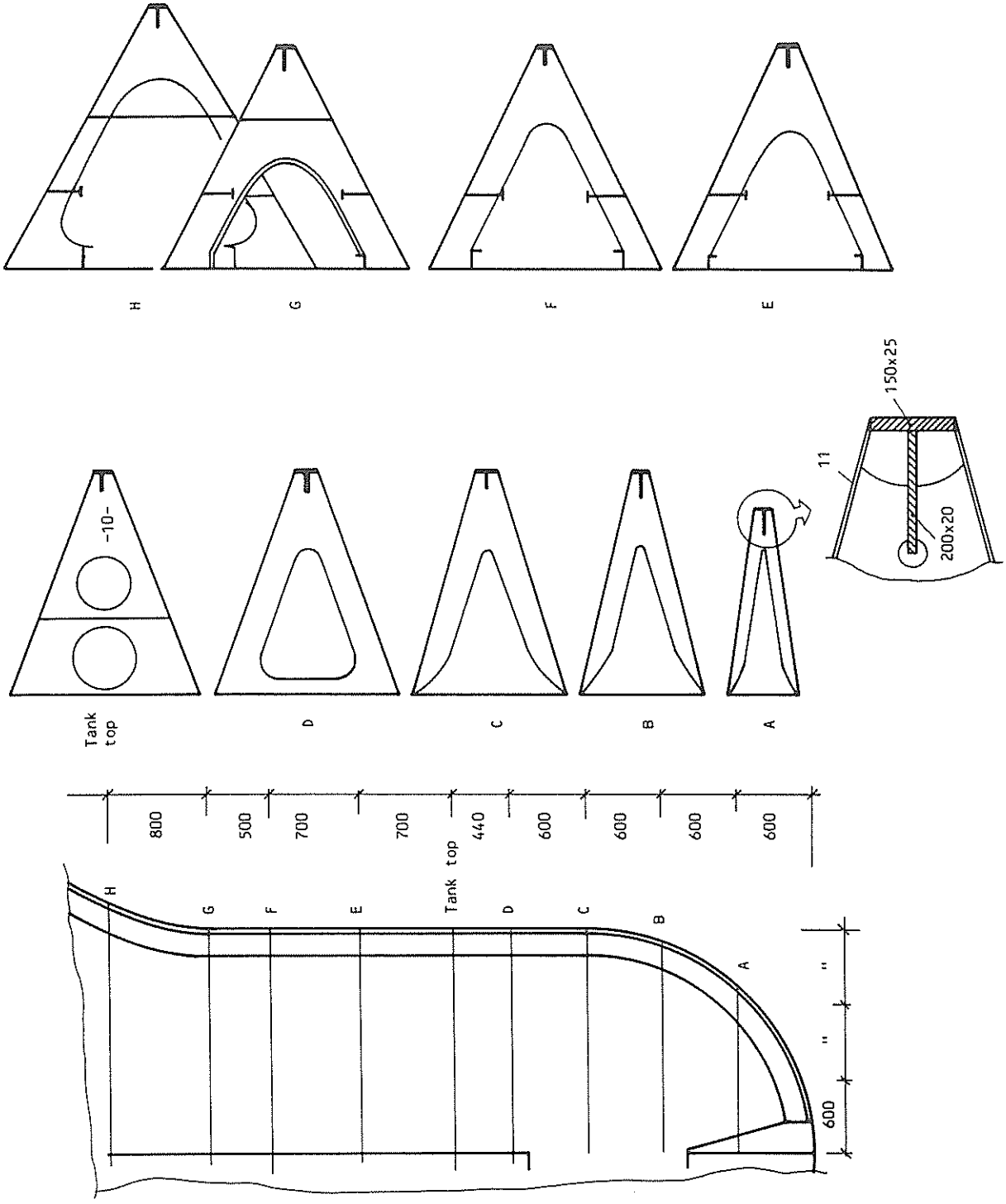

Figure 8.6 *Ice-strengthened foreship of a supply vessel*

The present structure is considered to be a very strong stem. Normally the stem web is omitted. The diameter of a typical bracing is D = 0.75 m. Thus the collision potential comprises interframe impacts as well as contacts directly on one or two stringers/breast hooks. Three cases have been investigated applying the theoretical approach outlined in sec. 5.3; namely impact

i)	On stringer	D = 0.74 m
ii)	Between stringers	D = 0.75 m
iii)	Between stringers	D = 1.00 m

For simplicity purposes the stringer spacing is assumed constant and equal to 0.75 m.

This implies that in case ii) no stringer comes into contact with the bracing (neglecting local deformation of bracing). On the other hand two stringers will be hit by the bracing in case iii). In these cases a stem without the stem web is considered.

The results of the analyses are presented in Fig. 8.7.

The higher buckling load occurs when the bow is hit directly on a stiffener and the bracing is forced to flatten locally so that four side panels are mobilized. The smaller buckling load is related to interstringer contact when the bracing is strong enough to resist local indentation. Probably, initial failure is bounded by these extremities. As anticipated the resistance during gross indentation is much higher when the bracing diameter exceeds the stringer spacing.

The conclusion to the present investigation is incorporated in the recommended design curve shown in Fig. 8.7. The curve "circumscribes" the results of the various impact cases and is considered to be a conservative estimate of the resistance to penetration of the bow structure.

The load-deflection characteristic of a typical bracing is indicated in Fig. 8.8. Comparing this curve with the bow resistance the tube is generally susceptible to local as well as beam deformation. However, provided that the ends are restrained against axial displacement membrane forces may be activated so that the bow may suffer damage towards the end of the impact period.

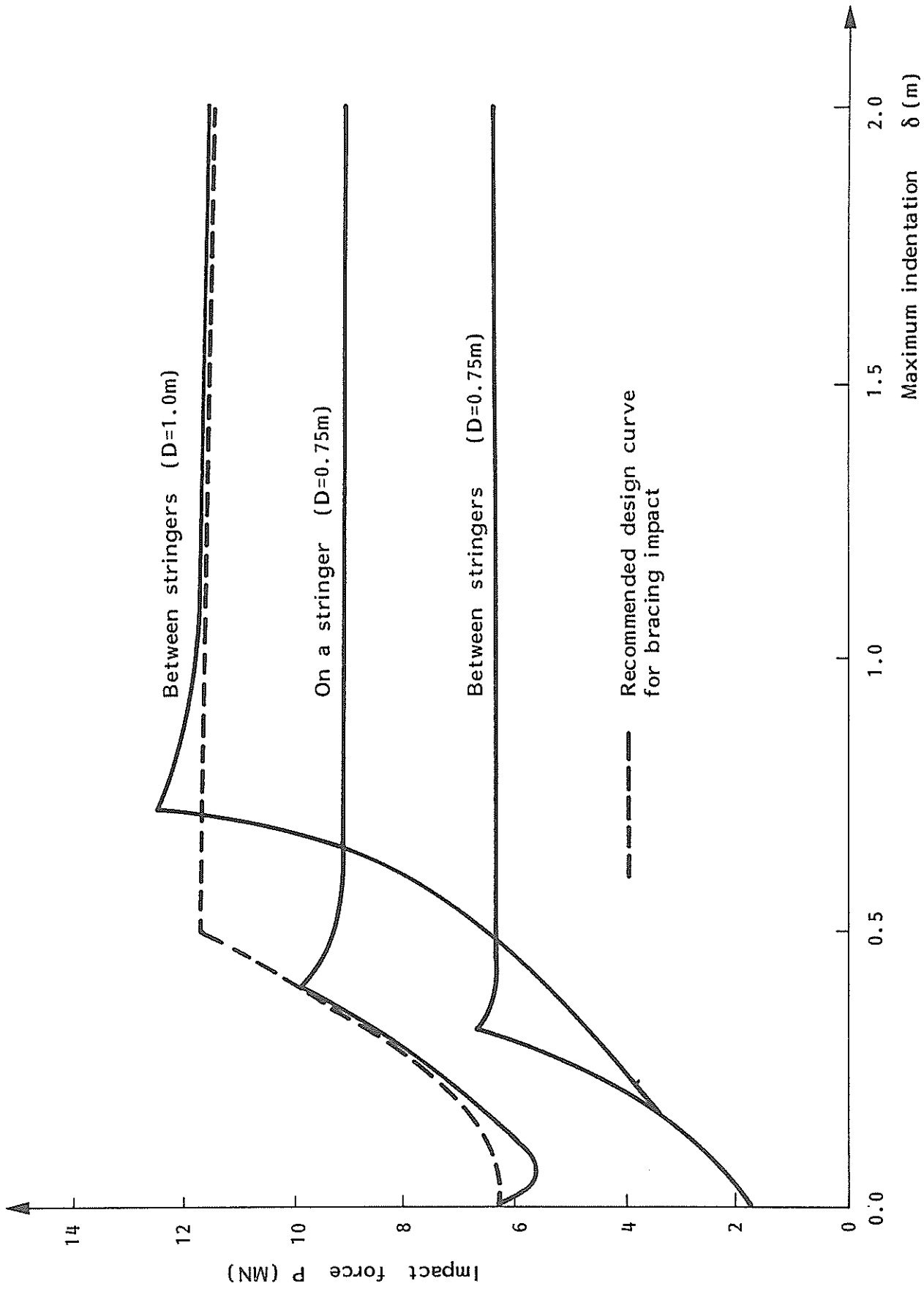

Figure 8.7 Load deformation curves for bow-bracing impact

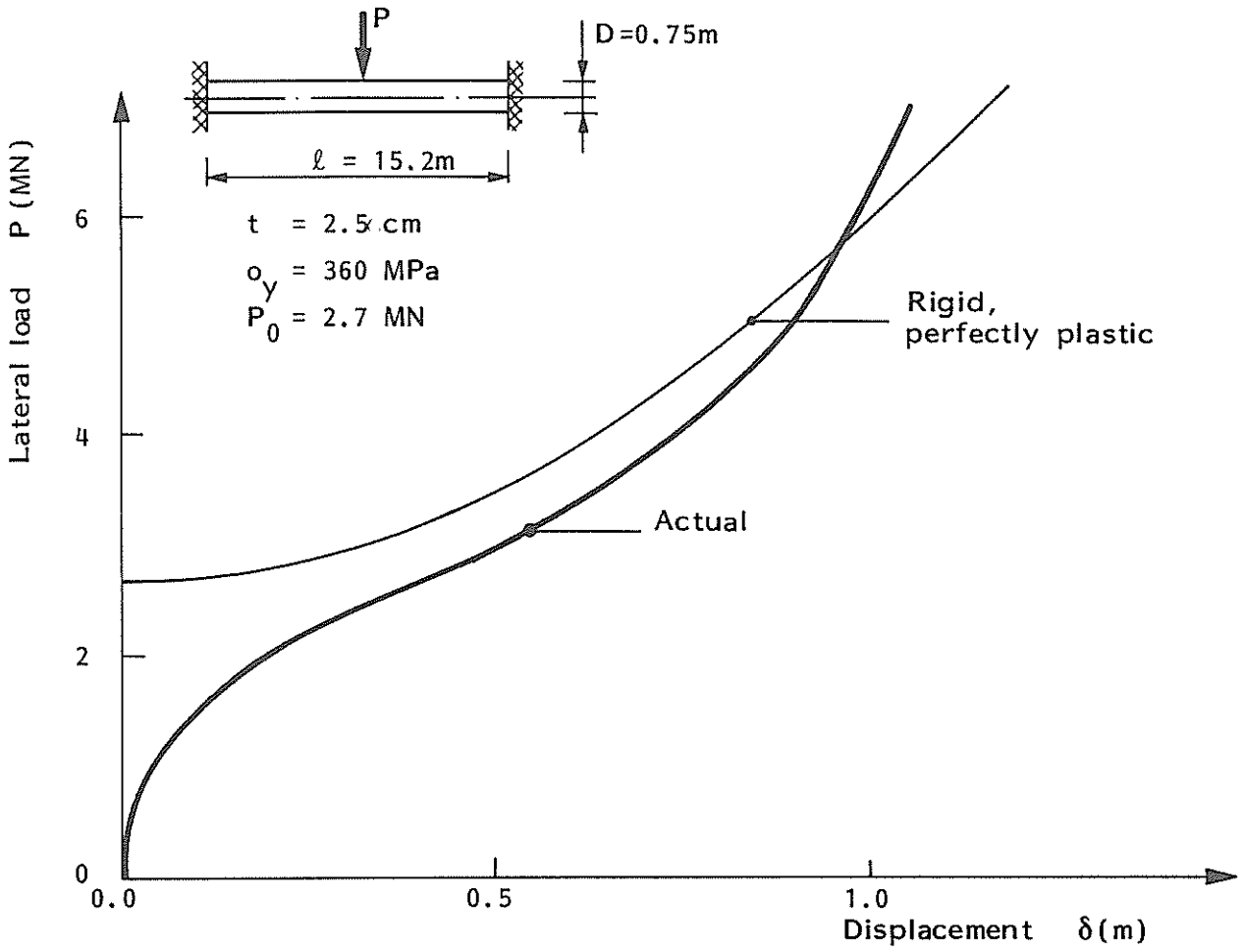

Figure 8.8 Load displacement characteristic for a typical bracing

9. EXPERIMENTS ON MODELS OF PLATFORM BRACING

9.1 Test Specimens

Characteristic cross-sectional dimensions of bracing elements in the water plane of jackets and semisubmersibles are:

$1.0 < D < 2.0$ m
$20 < D/h < 100$
$10 < L/D < 30$

Geometric and material data for the models are given in Table 9.1.
The range of variation is:

$63 < D < 125$ mm
$22 < D/h < 61$
$10 < L/D < 20$
$204 < \sigma_o < 328$ /N/mm^2

where σ_o denotes yield stress according to uniaxial tensile tests.

SPECI-MEN	OUTER DIAMETER D (mm)	WALL THICK NESS h (mm)	D/h	LENGTH L (mm)	L/D	YIELD STRESS σ_o (N/mm^2)	STATIC OR DYNAMIC	HORIZ. CONDIT.
IAI	125	2.0	61	1244	10	204	Static	Free
IAII	125	2.0	61	1245	10	211	"	"
IAIII	125	2.0	61	1244	10	207	"	Fixed
IBI	125	2.5	50	1244	10	251	"	Free
IBII	125	2.5	50	1245	10	230	"	Fixed
IBIII	125	2.5	50	1245	10	268	"	Free
ICI	125	3.0	41	1245	10	260	"	
ICII	125	3.1	40	1240	10	328	Dynamic	
ICIII	125	3.0	41	1246	10	256	Static	Fixed
IDI	114	3.2	35	1240	11	318	"	"
IDII	114	3.2	35	1240	11	318	Dynamic	"
IEI	88	3.0	30	1240	14	294	Static	"
IEII	88	3.0	30	1240	14	294	Dynamic	"
IFI	63	2.9	22	1240	20	442	Static	"
IFII	63	2.9	22	1240	20	442	Dynamic	"

Table 9.1 Data for Bracing Models

9.2 Test Rig

The experimental set-up is shown in Fig. 9.1.

The hydraulic actuator is mounted on the upper transverse beam of the rig. The test specimen is fixed to each column in the way that a steel plate is welded to the ends of the tube and this plate is then bolted to a special arrangement which allows for various boundary conditions.

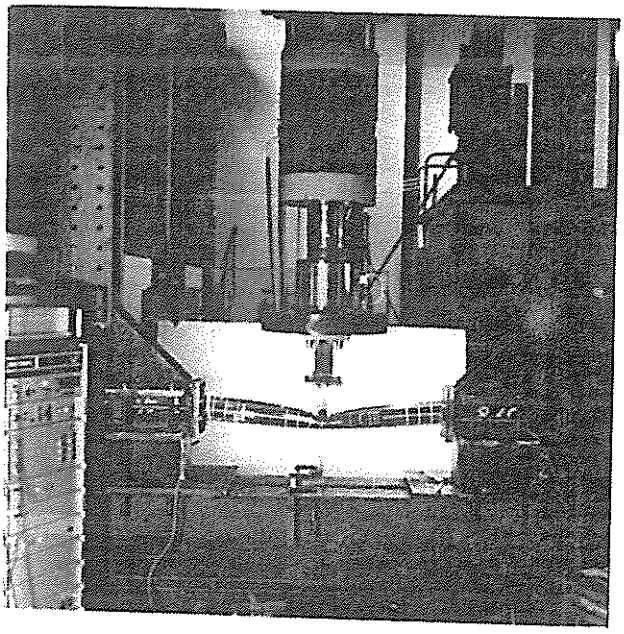

Fig. 9.1 Experimental Set-up

A better indication of the end conditions is given in Fig. 9.2. The rollers make it possible to simulate free horizontal movement as well as full membrane restraint. In both cases the tube end is rotationally clamped, which is assumed to be close to the real situation for a bracing element.

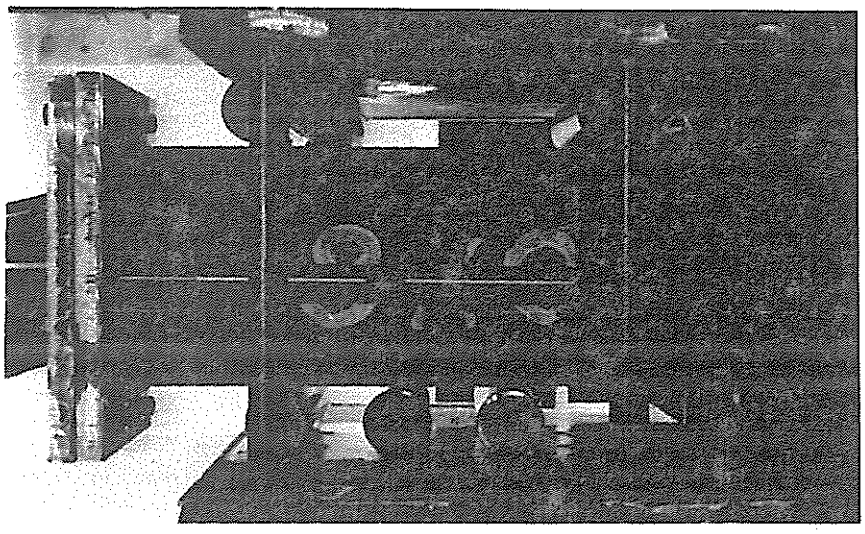

Fig. 9.2 End of Test Specimen

Displacement control of the hydraulic actuator is applied with a displacement rate of 0.15 mm per second for the static tests and 54 mm per second for dynamic testing which by scaling gives a real speed of 1.0-2.0 m per second. A rectangular indenter is used with a width (along bracing element) equal to 50 mm.

Strain gauges are placed close to the indenter where local deformation is expected and at the tube ends. Displacement transducers are mounted on each end to measure the horizontal movement and under the tube at the central section to register the vertical displacement of this point, which is to be compared with the movement of the top point given by the actuator.

9.3 Static Tests

First, attention is given to the effect of membrane forces by considering the two specimens IAI and IAIII with equal geometric and material properties. Specimen IAI has horizontally free end conditions while IAIII is clamped against axial movement. Deformed configurations at different levels of loading are shown in Figs. 9.3 and 9.4 for IAI and IAIII, respectively. For specimen IAI it is seen that at maximum load carrying capacity the global deformation is small as compared with the local indentation (Fig. 9.3b). The effect of membrane forces is demonstrated by the difference in load carrying capacity. It is also seen that the stretching effect in specimen IAIII gives a much more overall ovalization of the tube than the very local cross-sectional deformation at point of impact for specimen IAI.

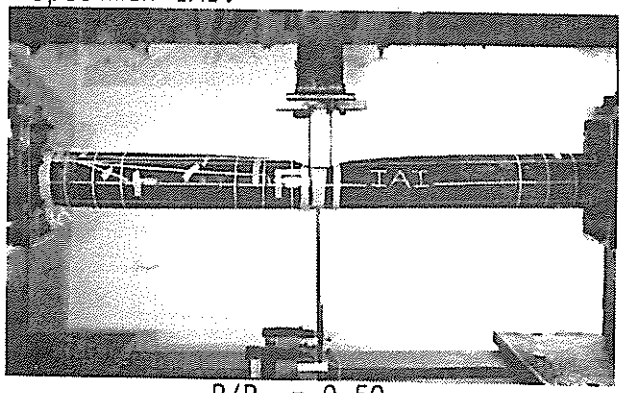

$P/P_0 = 0.50$

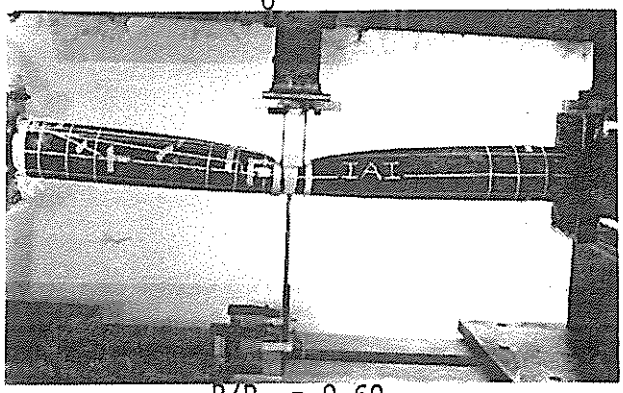

$P/P_0 = 0.69$

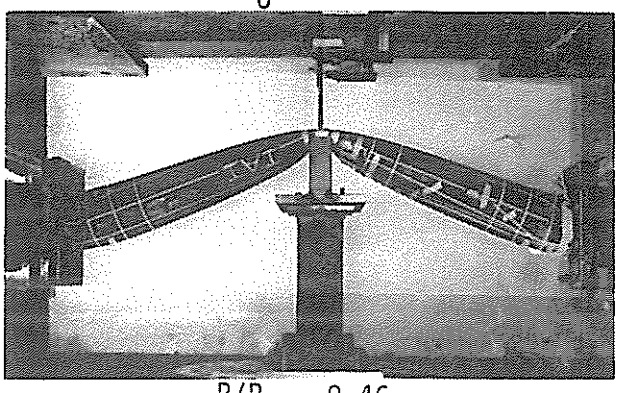

$P/P_0 = 0.46$

Fig. 9.3 Deformation of horizontally free specimen IAI.

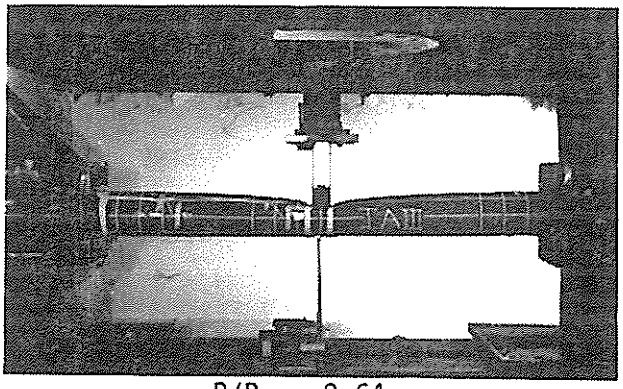

$P/P_0 = 0.64$

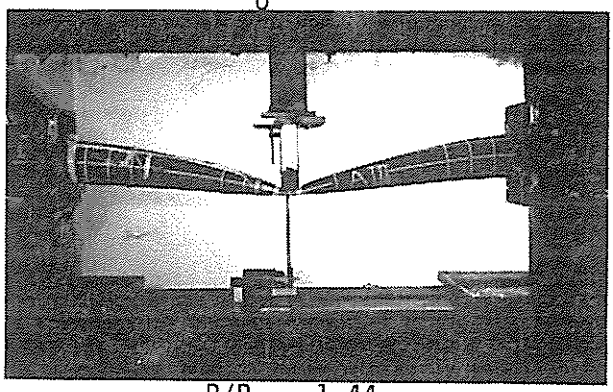

$P/P_0 = 1.44$

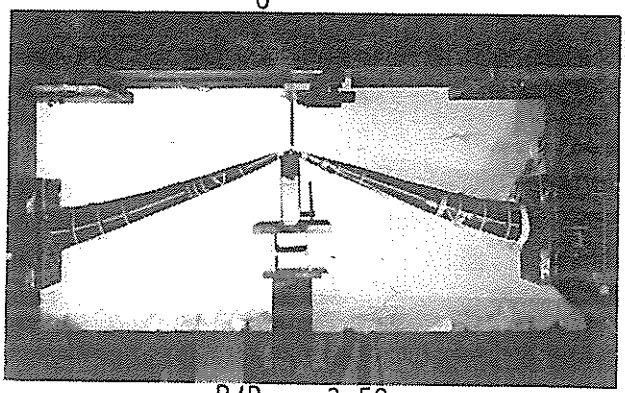

$P/P_0 = 3.50$

Fig. 9.4 Deformation of horizontally fixed specimen IAIII.

Fig. 9.5 shows the permanent deformation of IAI and IAII after collapse. The axial elongation of specimen IAIII is clearly demonstrated by the difference in length between the two models.

The maximum indentation for the two specimens is close to 250 mm (2D).

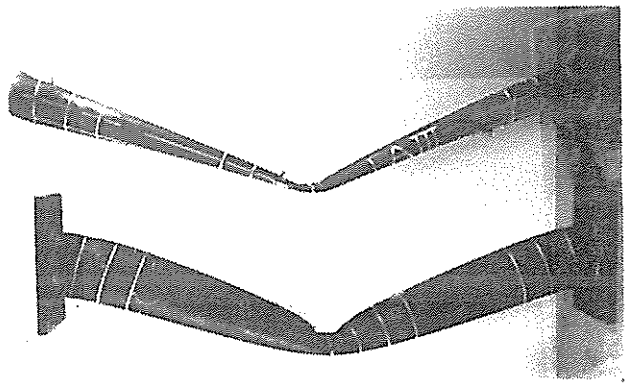

Fig. 9.5 Permanent Deformation of Specimens IAI and IAIII

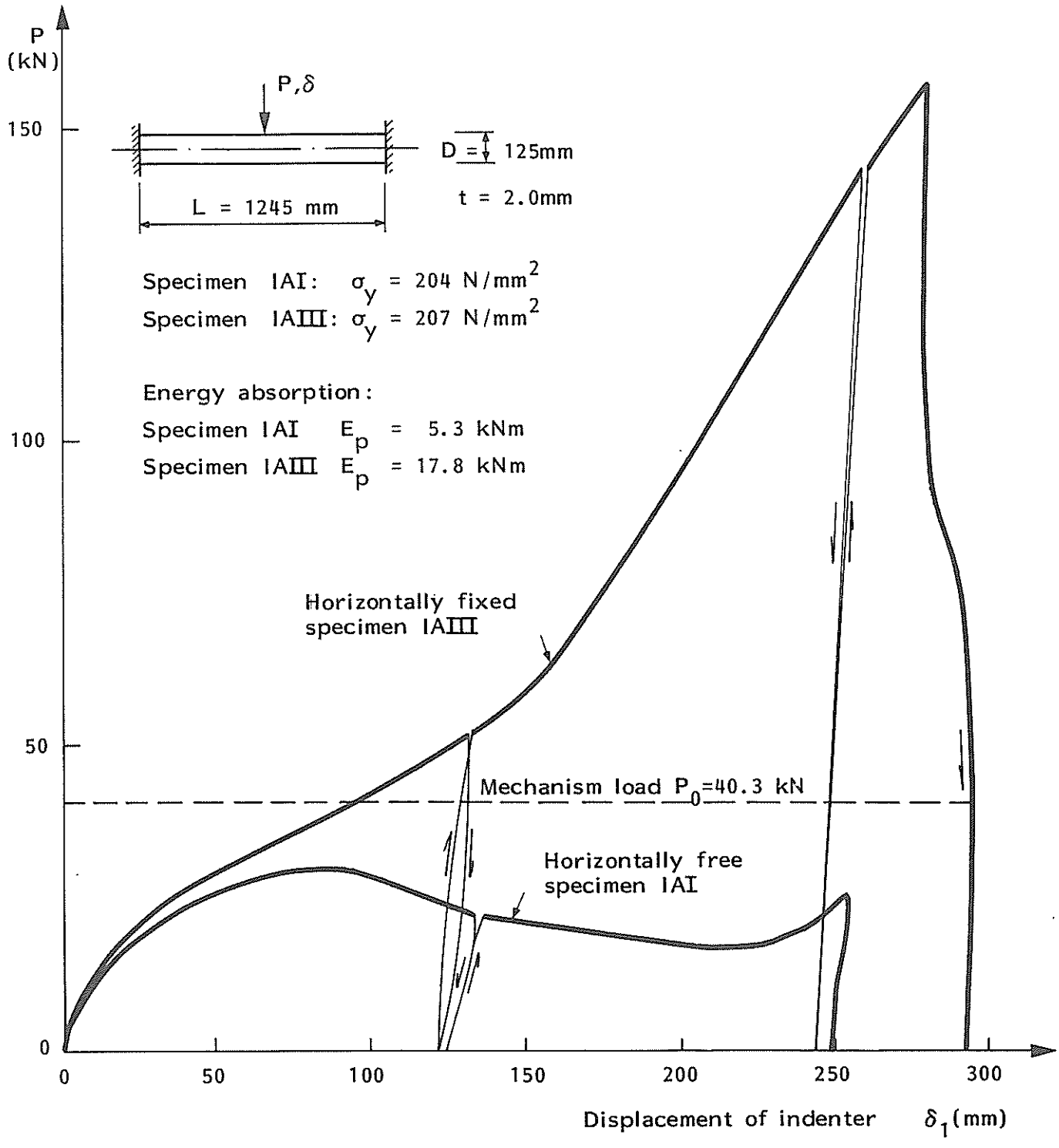

Figure 9.6 Load-displacement curves for indenter. Specimens IAI and IAIII.

The relationships between load and displacement of indenter are given by the curves in Fig. 9.6. It is seen that the horizontally free specimen IAI reaches a maximum load of 0.73 P_0 at an indentation of about 85 mm (δ/D = 0.68) where P_0 is the mechanism load as given by Eq. (6.3):

$$P_0 = \frac{8M_0}{L} = \frac{8D^2h\sigma_0}{L} = 40 \text{ kN} \qquad (9.1)$$

h and L denote tube wall thickness and span, respectively. By further deformation of IAI the lateral load reduces to 0.40 P_0 (16 kN). The reason for this behaviour is twofold. First, due to the flattening of the central cross section the plastic section modulus is reduced. Second, local crippling of the tube wall is observed on the compression side of the ends (Fig. 9.7), an effect which also reduces the moment capacity.

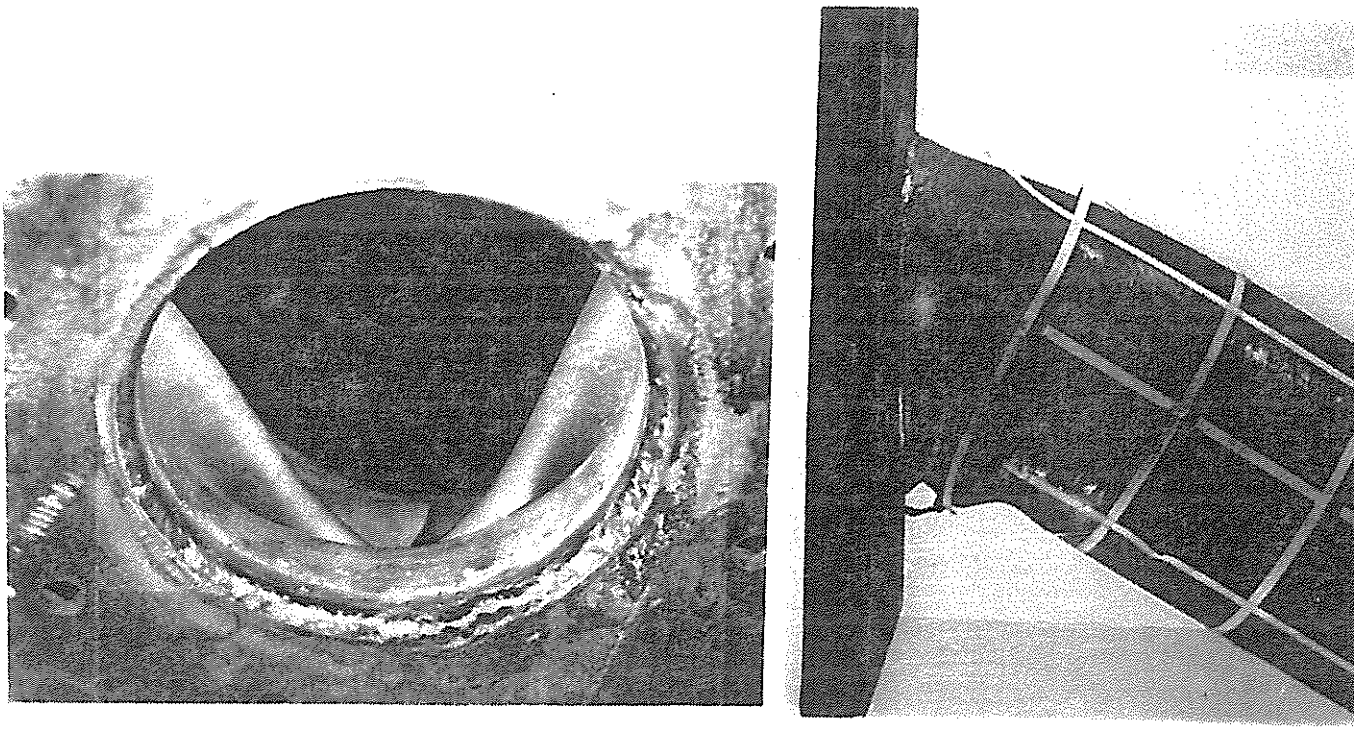

Fig. 9.7 Local Crippling of Tube Wall at End of Horizontally Free Specimen IAI

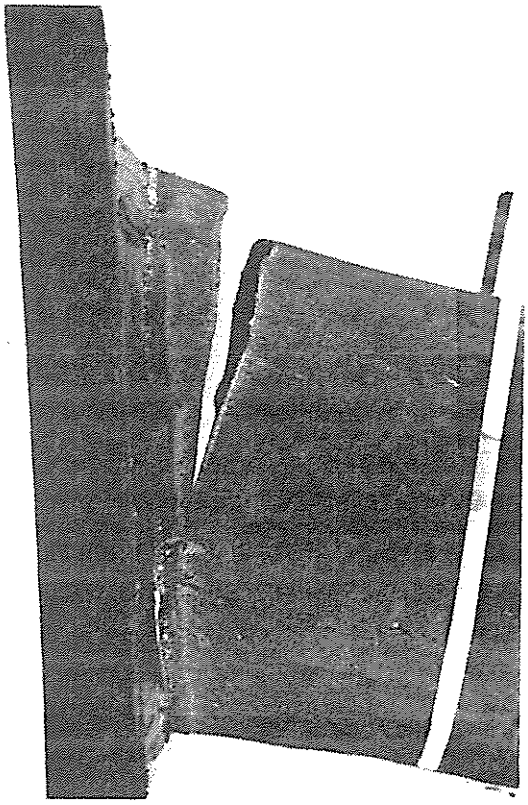

Fig. 9.8 Fracture at End of Horizontally Fixed Specimen IAIII

In the final stage of deformation it is seen from Fig. 9.6 that the lateral load on specimen IAI rises as the first buckle at the ends closes and before the next buckle develops.

The load-displacement curve in Fig. 9.6 for specimen IAIII with membrane action is quite different. The load increases continuously and reaches an ultimate value of 4 P_0 (157 kN) before collapse. The energy absorbed is 17.8 kNm for IAIII versus 5.3 kNm for specimen IAI. The type of collapse of model IAIII is different from the horizontally free case.

Due to the membrane action the ends of specimen IAIII are in tension all over the cross section and no crippling occurs. Instead, the tube fails by fracture of the material close to the welds as shown in Fig. 9.8.

Although the present tests do not simulate the real behaviour of tubular joints some indications are obtained as far as type of collapse is concerned.

9.4 Dynamic Tests

Consider the specimens IDI and IDII which are tested statically and dynamically, respectively with the deformation rates mentioned in Sect. 9.2. The load-displacement curves are shown in Fig. 9.9 where series 1 of curves is given for the indentation on the upper side of the specimens and the series 2 is related to the displacement transducer on the opposite side of the central cross section.

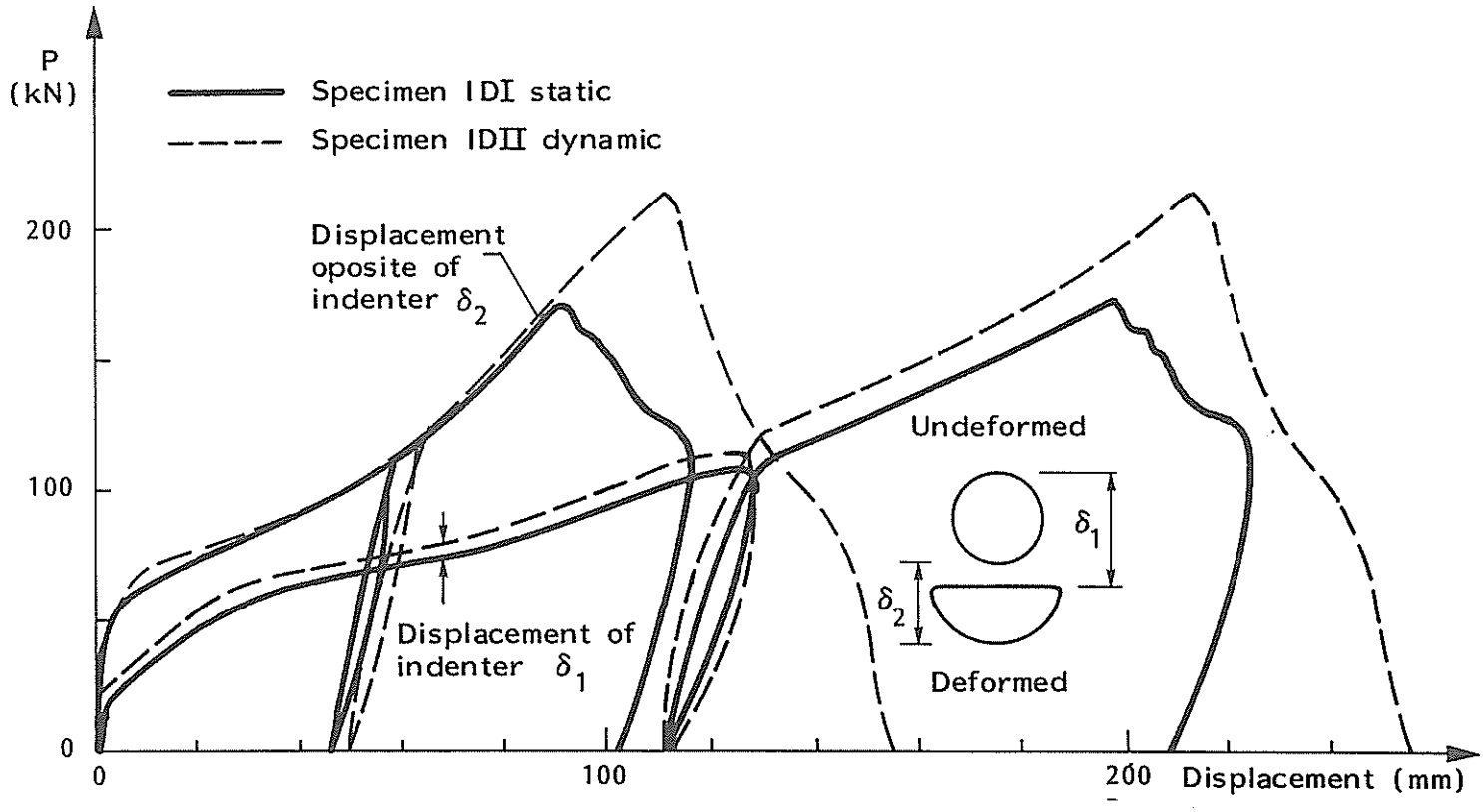

Fig. 9.9 Static and Dynamic Load-Displacement Curves

Fig. 9.9 shows that the load-indentation curve (series 1) is raised by about 10 percent due to the dynamic loading, while very little influence is obtained on the opposite side of the cross section (series 2). This phenomenon indicates that the dynamic loading primarily affects the local deformation at point of impacts where the strain rates reach high magnitudes, and that the increase in load carrying capacity is caused by a rise in the material stress-strain curve as discussed in Sect. 2.8. However, it should be emphasized that this conclusion is representative only for the present range of impact velocity. Inertia forces may change the dynamic influence for higher velocities.

9.5 Comparison between Test Results and Theory

One special problem arises when relating the test results to theoretical load-displacement curves, namely the choice of reference displacement. The analytical rigid-plastic technique of Sect. 6.3 and the modified elasto-plastic computer program of Sect. 6.4 both refer to lateral deflection w as the centre line displacement while mid-section deflection is measured on top and bottom of the tube.

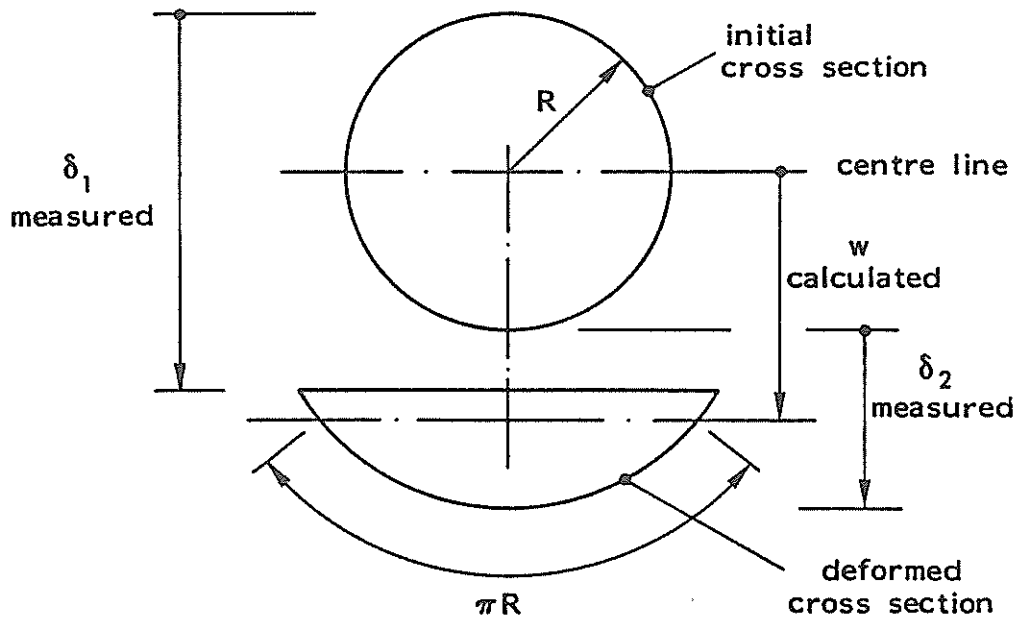

Fig. 9.10 Calculation of centre line deflection.

In order to make test results and theoretical solutions compatible the measured top and bottom displacements δ_1 and δ_2 are transformed into centre deflection w via the model in Fig. 9.10. The deformed cross section at point of impact is approximated by a horizontal part and a circular part with increased radius of curvature, similar to the model used in Fig. 6.4 for calculating reduced section modulus. Incorporating the

requirement of constant circumference during deformation of the cross section w can be calculated and now denotes physically the displacement of points on centre line.

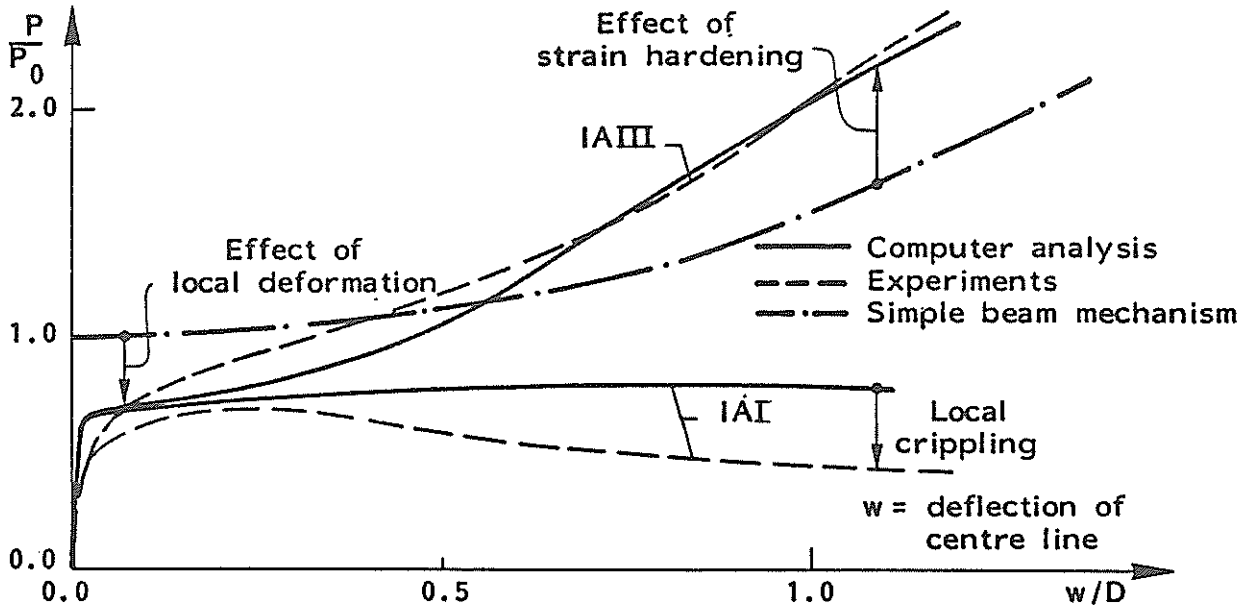

Fig. 9.11 Load-deflection characteristics for specimens IAII and IAII

Fig. 9.11 shows the transformed test results and the theoretical load-deflection curves. It is seen that the modified beam computer program IMPACT with strain hardening included fairly well follows the experimental deflection for the horizontally fixed specimen IAIII. Some discrepancy arises through the development of local dent in the first phase of deformation. Also for horizontally free specimen IAI the maximum load is well predicted by the program. However, since full rotational rigidity is assumed at the tube ends, the unloading due to local crippling does not come ouf of the numerical analysis. For specimen IAI it is also clear that the simple mechanism model neglecting local deformation of cross section gives too high load carrying capacity.

The part of energy absorption due to global beam deformation is found as the area under the load-deflection curces in Fig. 9.11. Further, the energy absorbed by local dent plastification must be calculated separately and added to the global contribution to obtain the total energy absorption capability as given by Fig. 9.6. In the computer program IMPACT the calculation of local energy absorption is carried out by the local indentation program part b of Sect. 6.4.

10. CONCLUSIONS AND SUGGESTIONS FOR FURTHER WORK

For the purpose of ship impact analysis the ship structure can be considered as an assembly of basic elements, e.g. angles, T-sections and cruciforms. A major part of the work is devoted to studies of the energy absorption behaviour of such basic elements undergoing very large deformation. The analysis is based on the kinematic methods of plasticity along with construction of yield line mechanisms, where due account is taken to possible kinematic constraints imposed by adjacent members when the element acts as an integral part of a composite structure.
The correlation between theory and results from own tests and data published in the literature is in general satisfactory. For isolated angle elements, where the collapse mechanism is particularly simple and unambiguous, the agreement is excellent. Conversely, several potential collapse modes exist for a cruciform, for which the theoretical predictions are more unreliable.

For an integrated structure the average crushing load at a given cross-section is found by summing the energy dissipated in all individual elements. Theoretical predictions match favourably results from experiments with scale models of ship structures. Satisfactory correlation is also obtained with data from a number of similar model tests carried out in Japan. This points to the validity of the approach and justifies application of the theory to actual ship structures.

It is emphasized that the present theory addresses the average crushing load, only. Normally, this yields a reasonable prediction for the instantaneous load level due to the low degree of simultaneousness of local element failure. However, for certain bow structures characterized by few longitudinal strength members and relatively constant cross-section like the Japanese container ship model, the whole frame section may collapse almost simultaneously. This produces typically a "saw-toothed" load curve and a separate assessment of the peaks is necessary.

Care should be exercised when analyzing structures with heavy longitudinal stiffening. If overall grillage buckling is the likely mode of collapse the present theory tends to overestimate the load level since the interframe collapse mode is associated with a higher rate of energy dissipation.

Although the approach used in this report is quite different from Gerard's method the load predictions differ remarkably little. As the latter method seeks a maximum stress relationship significant overestimation of the load would be expected. The reason that this does not actually occur is that the unloaded edges are generally assumed free to distort, the case of which has the lower buckling load. For several elements in a ship cross-section straight edges would comply better with physical boundary conditions.

Theoretical predictions of load-deformation relationships are presented for impacts between various supply vessels and the leg of a concrete platform (D=10m). The reference vessel is the 5000 tons displacement supply vessel underlying the design curves recommended by VERITAS. From the comparison it is concluded that the present design curve overestimates the load somewhat. Exception is made for very large collisions where excessive forces may results from activation of ice-strengthened bow sections.

By introducing some minor modifications the procedure used for bow collisions has also been found applicable for load assessment of major stern impacts. The boat in consideration is the 5000 tons supply vessel with a transom stern. It is found that current design recommendations are fairly conservative for such stern configurations.

Impacts from supply vessels fitted with a stern roller are subjected to a separate study. The location of impact is assumed next to the roller. The structure on the spot is characterized by curved panels with twice of the normal plate thickness and dense framing. The theory which is developed and supported by experiments is limited to minor impacts only. It is concluded that the load is likely to exceed the force for a transom stern at small indentations and thus may be an active requirement for local designing of concrete legs.

Two tests have been run simulating collision between a bracing and an ice-strengthened stem. The theoretical analysis which partly makes use of the methodology developed for broad side impacts, shows that typical brace members are not strong enough to resist the collision force. A design curve enveloping various impact cases is proposed. However, it is emphasized that this part of the work should merely be understood as an introductory study.

Theoretical methods to calculate the energy absorption capability of steel

tubular members used in braced offshore structures have been presented. It is shown that rigid plastic methods of analysis along with three-hinge beam mechanism provide good understanding of the physical behaviour and yield approximate prediction of the load. However, for a realistic assessment it is clear that the weakening effect of local indentation on the global strength must be taken into consideration.

A case study applying a refined non-linear finite element shell program showed that the deformation process can be simulated with a high degree of credibility. However, the analysis is time-consuming and costly and for this reason the main part of the numerical studies has been performed with a simple finite element beam program where the moment capacity reduction due to local indentation has been incorporated. By this the experimental load-deflection characteristics could be followed quite accurately. The tests included horizontally free members as well as elements with full axial restraints. The development of membrane forces affected the deformation characteristics and type of collapse. In the cases with free horizontal movements the elements failed by local crippling of the tube wall on the compression side of the ends. For the axially restrained members total collapse was caused by fracture close to the welds.

Dynamic tests with a velocity corresponding to 1.0 - 2.0 m/s in full scale indicated an increase in load carrying capacity of about 10% as compared with static tests. Most of this reserve was due to strain rate effects in the region of local indentation.

It is suggested that further work should concentrate upon developing and refining basic folding mechanisms capable of modelling the collapse behaviour of strength members in a ship section. Of particular interest is compression of skew angle elements representing deck-side intersections of bows. Analytic work in this area should be accompanied by experiments. Test specimens should preferably be of large scale with realistic material properties and welds in order to gain improved knowledge of the influence from material thickness on the energy absorption capability. In this context a rational criterion for plate rupture should be established, a topic which has been only briefly dealt with in this report.

For longitudinally stiffened panels the present approach constitutes an upper bound to the energy absorption capability. A beam-column type mode of failure would represent a lower bound. A collapse mechanism describing

this failure mode should be developed. The conditions for which failure path an actual structure is to follow should be studied.

A limited number of stern impacts has been considered. Other cases with large damage potential should be identified and analyzed, such as impacts against a stern roller and minor impacts against a transom stern where inertia forces may become important. Especially, improved knowledge as to peak forces, variation and size of contact area and distribution of impact load over this area should be aimed at.

The deformation behaviour of tubular members subjected to large lateral loads should be studied under realistic end conditions. High priority should be given to establishing simple methods to assess adequate rotational - and translational spring characteristics for a joint which can be used in finite element programs as well as in simple analytic models.

Failure of the member is crucial with respect to the energy absorption capability. It is suggested that further effort be put into analyzing various failure modes and developing failure criteria. Such failure modes may be fracture on the tension side or local buckling on the compression side in the member itself or in the chord wall.

REFERENCES

/ 1/ Kjeøy, H. and Straube, P.:
"Impacts and Collisions Offshore.
Project Summary of Phase I and II"
VERITAS Report No. 83-0375, 1983

/ 2/ Hysing, T.:
"Analysis of Penetration of Hull"
VERITAS Report No. 78-0433, 1978

/ 3/ Kjeøy, H. and Amdahl, J.:
"Ship Impact Forces in Collision with Platform Legs"
VERITAS Report No. 79-0691, 1979

/ 4/ "Rules for the Design Construction and Inspection of Offshore Structures"
Det norske VERITAS 1977 (Reprint 1982)

/ 5/ Technical Note TNA 101
"Design against Accidental Loads"
Technical Note Fixed Offshore Installations
Det norske VERITAS, 1981

/ 6/ Technical Note TNA 202
"Impact Loads from Boats"
Technical Note Fixed Offshore Installations
Det norske VERITAS, 1981

/ 7/ Minorsky, V.V.:
"An Analysis of Ship Collisions with Reference to Nuclear Power Plants", Journ. of Ship Research, Vol. 3, 1959, pp. 1-4

/ 8/ Woisin, G.:
"Die Kollisionsversuche der GKSS"
Jahrbuch der Schiffbautechnischen Gesellschaft, 70.8, Hamburg 1976

/ 9/ Akita, Y., Ando, I., Fujita, Y. and Kitamura, K.:
"Studies on Collision-Protective Structures in Nuclear Powered Ships", Nuclear Engineering and Design, Vol. 19, 1972, pp. 365-401.

/10/ Hagiwara, K., Takanabe, H. and Kawano, H.:
"A Proposed Method of Predicting Ship Collision Damage",
Ship Strength Laboratory, Nagasaki Techn. Inst., Nagasaki, Japan, 1982.

/11/ Nagasawa, H., Arita, K., Tani, M. and Oka, S.:
"A Study on the Collapse of Ship Structure in Collision with Bridge Piers", Nav. Arch. and Ocean Eng., Soc. Nav. Arch., Japan, Vol. 19., 1981.

/12/ Ohnishi, T., Kawakami, H., Yasukawa, W. and Nagasawa, H.:
"On the Ultimate Strength of Bow Construction",
SNAME Japan, Vol. 151, July 1982.

/13/ Gerard, G.:
"The Crippling Strength of Compression Elements",
Am. Inst. of Aeronautics and Astronautics, May 1957.

/14/ Wierzbicki, T., Abramowicz, W. and Oliveira, J. de:
"Crushing Analysis of Ship Structures with Particular Reference to Bow Collisions",
VERITAS Rep. No. 82-0709, 1982.

/15/ Van Mater, P.R., Gianotti, J.G., McNatt, T.R., and Edinberg, D.L.:
"Vessel Collision Damage Resistance"
Report No. CG-D-21-80, Gianotti & Ass. Inc., Annapolis, MD 21401, 1980

/16/ Van Mater, P.R. and Giannotti, J.G.:
"Critical Evaluation of Low-Energy Ship Collision Damage Theories and Design Methodologies - Volume I - Evaluation and Recommendations",
Ship Structure Committee Report SSC-284, 1979

/17/ Van Mater, P.R. and Giannotti, J.G.:
"Critical Evaluation of Low-Energy Ship Collision - Damage Theories and Design Methodologies - Volume II - Literature Search and Review",
Ship Structure Committee Report SSC-285, 1979

/26/ Mahmood, H.F. and Poluszny, A.:
"Design of Thin-walled Columns for Crash Energy Management - Their Strength and Mode of Collapse",
SAE Paper No. 811302, Proc., 4th Int. Conf. on Vehicle Structural Mechanics, Detroit Nov., 1981

/27/ Minorsky, V.U.:
"Bow Loading Values (Bulbous Bow)".
George G. Sharp Inc., New York 1977

/28/ Minorsky, V.U.:
"Evaluation of Ship-Bridge Pier Impact and of Islands as Protection",
Ship Collisions with Bridges and Offshore Structures,
IABSE Colloquium, Copenhagen 1983

/29/ DeRuntz, J.A. and Hodge, P.G.:
"Crushing of a Tube Between Rigid Plates"
Journ. of Applied Mechanics, pp. 391-395, 1963

/30/ Reid, S.A., Reddy, T.Y.:
"Effect of Strain Hardening on the Lateral Compression of Tubes between Rigid Platens",
Int. Journal of Solids and Structures, Vol. 14, pp. 213-225, 1978

/31/ Watson, A.R., Reid, S.R., Johnson, W. and Thomas, S.G.:
"Large Deformations of Thin-Walled Circular Tubes Under Transverse Loading",
Int. Journ. of Mechanical Sciences, I-III, Vol. 18, 1976

/32/ Morris, A.J. and Calladine, C.R.:
"Simple Upper Bound Calculations for the Indentation of Cylindrical Shells",
Int. Journ. of Mechanical Sciences, pp. 331-343, Vol. 13, 1971

/33/ Oliveira, J.G.de:
"Simple Methods of Estimating the Energy Absorption Capability of Steel Tubular Members Used in Offshore Structures",
Report SK/R50, Div. of Marine Structures, NTH, 1979

/34/ Amdahl, J.:
"Impact Capacity of Steel Platforms and Tests on Large Deformations of Tubes under Transverse Loading",
VERITAS Report No. 80-0036. 1980

/35/ Hodge, P.G.:
"Post-Yield Behaviour of a Beam with Partial End Fixity".
Int. Journ. of Mechanical Sciences, pp. 385-388, Vol. 16, 1974

/36/ Oliveira, J.G.de:
"The Behaviour of Steel Offshore Structures under Accidental Collisions",
OTC 4136, 1981

/37/ Oliveira, J.G.de, Wierzbicki, T. and Abramowicz, W.:
"Plastic Behaviour of Tubular Members under Lateral Concentrated Loading",
VERITAS Report No. 82-0708, 1982

/38/ Rashed, S.M.H.:
"Behaviour to Ultimate Strength of Tubular Offshore Structures by the Idealized Structural Unit Method",
Report SK/R51, Div. of Marine Structures, NTH, Trondheim, 1980.

/39/ Hopkins, H.G.:
"On the Plastic Theory of Plates",
Proc., Royal Society, London, Series A, Vol. 241, 1957

/40/ Smith, C.S.:
"Grillage Strength and Primary Hull Strength",
1st WEGEMT Course on Advanced Ship Design Techniques,
Univ. Newcastle-upon-Typne, 1978.

/41/ Det norske Veritas:
"Rules for the Design, Constructions and Inspection of Offshore Structures, 1977."

/42/ Faulkner, D.:
"A Review of Effective Plating for Use in the Analysis of Stiffened Plating in Bending and Compression",
Journ. Ship Research, Vol. 19, 1975.

/43/ Wierzbicki, T. and Abramowicz, W.:
"On the Crushing Mechanics of Thin-Walled Structures",
Mass. Inst. of Techn., Dept. of Ocean Engineering,
Rep. No. 82-4, 1982.

/44/ Stolarski, H.:
"Dynamics of Strongly Deforming Rigid Plastic Structures",
Lecture Notes prepared for CISM Course on "Dynamic of Plastic Structures", Udine, Italy, October 1979

/45/ Åkerstrøm, T., Jernstrøm, C. and Wierzbicki, T.:
"Shape Optimization of Sheet Metal Structures against Crash",
SAE Paper 811314, 4. Int. Conf. on Vehicle Structural Mechanics,
Detroit, November 1981

/46/ Hayduk, R.J. and Wierzbicki, T.:
"Extensional Collapse Mode of Structural Members in Crash Loading",
NASA-Langley, 1982.

/47/ Pugsley, A.G.:
"On the Crumpling of Thin Tubular Struts",
Quart. Journ. Mechs. Appl. Maths., Vol. 32, 1979

/48/ Johnson, W., Soden, P.D. and Al-Hassani, S.T.S.:
"Inextensional Collapse of Thin-Walled Tubes under Axial Compression",
Journ. of Strain Analysis, Vol. 12, No. 4, 1977

/49/ Al-Hassani, S.T.S., Johnsen, W. and Lowe, W.T.:
"Characteristics of Inversion of Tubes Under Axial Loading",
J. Mech. Eng. Sci., No. 14, 1972

/50/ Oliveira, J.G. de and Wierzbicki, T.:
"Crushing Analysis of Rotationally Symmetric Plastic Shells",
Journ. of Strain Analysis, Vol. 17, No. 4, 1982

/51/ Alexander, J.M.:
"An Approximate Analysis of the Collapse of Thin Cylindrical Shells Under Axial Load",
Quart. Journ. Mechs. Applied Maths., Vol. 13, 1960

/52/ Wierzbicki, T. and Abramowicz, W.:
"Crushing of Thin-Walled Strain Rate Sensitive Structures",
paper presented at Euromech Colloquium No. 121, August 1979.

/53/ Manjoine, M. J.:
"Influence of Rate of Strain and Temperature on Yield Stresses of Mild Steel",
Journal of Appl. Mechanics, pp. A/211-218, Dec. 1944.

/54/ Woisin, G.:
"Die Kollisionsversuche mit Platten hauptsächlich aus Schiffbaustahl bei zur Stossrichtung parallelen Ebenen entsprechend Z.B. Schiffsdecks",
Schiffstechnik Bd 15, Heft 79, 1968.

/55/ Cowper, G.R. and Symonds, P.S.:
"Strain Hardening and Strain Rate Effects in the Impact Loading of Cantilever Beams",
Brown University, Techn. Report No. 28, 1957

/56/ Toni, M. and Funahashi, A.:
"Energy Absorption by the Plastic Deformation of Body Structural Members",
SAE Paper No. 780368, SAE, Inc., 1978.

/57/ Hoff, N.J., Narda, S.V. and Erickson, B.:
"The Maximum Load Supported by An Elastic Column in A Rapid Compression Test",
Proc. of the First U.S. National Congress of Applied Mechanics,
ASME, New York, 1952

/58/ Hoff, N.J.:
"The Dynamics of the Buckling of Elastic Columns",
Journ. of Applied Mechanics, Vol. 18, No. 1, p. 68, March 1951

/59/ Ekstrøm, R.:
"Dynamic Buckling of a Rectangular Orthotropic Plate",
AIAA Journal, Vol. 11, No. 12, December 1973

/60/ Amdahl, J.:
"Compression Tests with Small-Scale Bow Models. Preliminary Report".
VERITAS Report No. 82-0264, 1982

/61/ Column Research Committee III.3 (eds.),
"Handbook of Structural Stability",
Corona Publishing Company, Tokyo, 1971.

/62/ Wilkesmann, F.W.:
"Stegblechbeulung bei Längsrandbelastung",
Der Stahlbau, Heft 10, Oktober, 1960.

/63/ Hysing, T.:
"Analysis of Penetration of Hull",
VERITAS Report No. 78-0433, 1978.

/64/ Furnes, O. and Amdahl, J.:
"Ship Collisions with Offshore Platforms",
Intermaritec, Hamburg, 1980

/65/ Jones, N.:
"Plastic Behaviour of Ship Structures",
Transactions Society of Naval Architects and Marine Engineers,
Vol. 84, 1976, pp. 115-145.

/66/ Guedes Soares, C. and Søreide, T.H.:
"Large Plastic Deformation of Laterally Loaded Circular Tubes",
Division of Marine Structures,
The Norwegian Institute of Technology, Trondheim, 1982

/67/ Søreide, T.H.:
"Ultimate Load Analysis of Marine Structures",
Tapir Publishing Company, Trondheim 1981

/68/ Sherman, D.R. and Glass, A.M.:
"Ultimate Bending Capacity of Circular Tubes"
OTC 2119, pp 901-910, 1974.

/69/ Sherman, D.R.:
"Tests of Circular Steel Tubes in Bending",
ASCE J. Struct. Div., Vol. 102, No. ST11, 1976, pp. 2181-2195

/70/ American Petroleum Institute:
Recommended Practice for Planning, Designing and Constructing
Fixed Offshore Platforms, API RP 2A, 1979

/71/ Foss, G.:
"Ship Impact in Jacket Type Structures"
VERITAS Report No. 81-0728, 1981

/72/ Søreide, T.H.:
"IMPACT - A Computer Program for Non-linear Geometric and Material Analysis of Beams and Columns",
Division of Marine Structures, The Norwegian Institute of Technology, Trondheim, 1981

/73/ Remseth, S.N., Holthe, K., Bergan, P.G. and Holand, I.:
"Tube Buckling Analysis by the Finite Element Method",
Finite Elements in Nonlinear Mechanics, Tapir Publishing Company, Trondheim, 1977

/74/ Yura, J.A., Zettlemoyer, N. and Edwards, I.F.:
"Ultimate Capacity Equations for Tubular Joints",
OTC 3690, 1980

APPENDIX

This appendix contains documentation of collision tests with models of bow structures, stern section and bow/bracing encounter.

CONTENTS

DESCRIPTION OF TESTS

PHOTOS

APPENDIX - TEST DESCRIPTION

1. BOX-SHAPED MODEL

The load-displacement curve is shown in Fig. 1 . The first peak load 1 , is associated with buckling of one of the side panels. This is shown in Plate 1a. At this stage the adjacent deck and bottom panels are still intact and the corner sections have remained straight. Buckling of a panel implies a reduction in its load-carrying capacity thus promoting a redistribution of the load to the uncollapsed panels. The second peak 2 , is associated with buckling of these panels. Now the structure deforms by developing plastic mechanisms as shown by Plate 1b at stage 3 . It is observed that the edges on both sides of the side panel start to move in. At stage 4 the first field is compressed completely, plate 1c.

Buckling of the second frame spacing takes place from 4 to 5 , Plate 1d. The panels are influenced to various degree of the deformation pattern of the preceeding field. Thus buckling of the panel does not take place simultaneously but is extended in time. In fact, the side panel opposite to the photographed one buckles in the third field at stage 6 , before the compression of the second field is finished.

This effect becomes even more pronounced at later stages of deformation. Plate 1d shows the situation in the side panel at 7 , when the second field has folded. There is a growing inward deflection in the corner zones. Due to initial distortions the plating in the middle tends to deflect in the opposite direction delaying the collapse of the field. During this process the frames distort visibly at the corners. The panel collapses as the last one in the third field 8 , once the growing corner buckles meet in the middle. This leads immediately to a drop in the load level. The low degree of simultaneousness of buckling results in a more smooth and uniform load curve as compared to the preceding fields.

The panels in the fourth field buckle more simultaneously yielding a higher peak load.

The frames become more and more distorted as seen in Plate 1e at end of test. This is caused by the deformations in the corner zones. Due to welds and dense material the folding in the corners completes early, enforcing local collapse in the next field.

Plate 1f gives a close view of the corner deformations. The first fold with both sides bending inwards, and the third fold with one side bending inwards and the other outwards, behave very ideal in the sense that lengths are preserved involving little circumferential stretching. The similarity with the angle mechanism is recognized.

On the other hand, both panels go predominantly out in the second field. This collapse mode involves a more complex mechanism.

It is interesting to notice that the collapse of the corner in the fourth field has triggered a different buckling pattern locally, with two waves between the frames. The collapse pattern is further demonstrated by Plate 1g showing a vertical section through two of the side panels.

Finally, consider Plate 1h. It is seen that in the second and third field the fold changes to opposite mode of deflection. It is evident that the transition implies shape distortion and elongation of the material in the transverse direction with a corresponding increase of the energy absorption.

2. BOW MODEL

The load-displacement curve appears in Fig. 2. Initial buckling occurs almost simultaneously at 1 , except the bottom panel, which buckles at 2 . The first field deforms very regularly with both side panels going outwards while deck and bottom go inwards. The initial buckling and subsequent deformations are illustrated by Plate 2a, b. The buckling mode of the side panels is exactly as anticipated from inspection of welding distortions. It is noticed that the side buckles into two equal waves in the middle while the wave bends forward towards the corner to meet with the deck fold. At this stage an inward deflection is imposed on the subsequent plate field.

The first field continues to fold the side meets with the load beam at 3 , Plate 2c. By further deformation a new fold is created in the upper half of the field and the load rises again.

Plate 2c also shows that the end field has buckled. However, further collapse is prevented by redistribution of the load to the corners, deck and bottom.

At 4 the deck and bottom buckle in the second field with two waves between the frames. The collapse pattern influences the side panels considerably so that they come outwards at 5 as seen on Plate 2d. This is contrary to the prospects held out by the previous deformations.

Due to the limited width of the load beam it tends to be pushed into the mid section of the bow while the triangular panels and the transverse frames are deformed heavily. At 6 the third field in the deck and bottom buckles. On the other hand the side panels remain relatively unaffected until 7, Plate 2e. At this stage the load beam is replaced by a flat plate in order to increase the contact area. Thereafter the third field collapses completely, until the fourth field starts to buckle at 9 . This is accompanied by a steep increase of the load.

Plate 2f shows the model at the end of test. The buckling pattern is further illustrated by the plane section in Plate 2g and the vertical section in Plate 2h. The different mechanisms in the first and subsequent fields in the side are demonstrated. This is among all due to the limited width of the load beam which is pushed into the mid section. The severe distortions of the frames are also visible.

3. BOW MODEL WITH DECK AND BULKHEAD

At a load level of 270 kN, see Fig. 3, the shape of the load curve suggests that local buckling takes place. However, no buckle is visible on the skin plates, indicating that the centre/bulkhead fails. This cannot be confirmed visually since inspection is not permitted in front of the second frame.

Increasing the load further the maximum buckling load 400 kN on is obtained at stage 1. A purely asymmetrical buckling mode is triggered, Plate 3b. The side buckles outwards above the inner deck and inwards below the deck. On the other side the collapse mode is opposite.

The assymetrical buckling mode is a consequence of the edge conditions at the mid deck.

The smaller stiffness of the side plates makes their collapse precede the failure of the deck and bottom plates. The mode of deflection is inwards for both panels. The deflections do not cover the whole plate but is concentrated towards the front edge. This has also a marked influence on the shape of the side buckle, which has a pronounced forward "bend" towards the edges. The mid-deck bends upwards on the right hand to comply with the mode shape of the side.

The deflections increase gradually, Fig. 3, while the load stabilizes at a level of 25 tons. At stage 2 the side buckles meet with the load plate and further deflection in this mode is restricted. Thus a secondary outward buckle is created in the upper half wave.

The fold is gradually compressed during increasing load level, Plate 3c. Parts of the load increase is also due to compression of inward buckles against transverse frames. Plate 3d demonstrates the mode of deflection at the corner between the side and bottom plating.

During this stage secondary buckles are created at the aft end of the first spacing in deck and bottom.

At stage 3 the side buckles in the second spacing above the mid deck. Shortly afterwards, outward buckles are formed at the foremost frame in the same spacing in deck and bottom.

The situation at stage 4 is illustrated by Plate 3e. Both sides deflect outwards over the entire height.

The next load increase is mainly caused by heavy compression of internal panels. The "density" of material is greater in the bulkhead/mid deck intersection. Accordingly the deformations progress faster in this area. Buckling is initiated in bulkhead and decks followed by deck, bottom and finally by the sides. For the third spacing this takes place from 5 to 6 .

Plate 3f visualize the situation at 6 . The previous fold is not yet fully compressed. In the following deformations progress simultaneously in both the second and third spacing.

The particular deformation pattern at the mid deck level is demonstrated by Plate 3g. One part of the side is subjected to reversed bending in order to comply with the deflection of the mid deck. The adjacent lower part of the side is stretched considerably in order to maintain continuity. Eventually it is strained beyond the ductility limit and fracture occurs.

Buckling of internal panels in the fourth spacing commences at stage 7 . The side panels still have a considerable way to go before they meet with the loading plate. The load increases until it reaches the maximum value of 530 kN. Then a secondary outward buckle is created in the third as well as a new fold one in the fourth spacing and the mode of deflection from the previous field is repeated.

The end state of the model is shown in Plate 3h.

The deformations at the corners and plate intersections show several of the features of the basic folding mechanisms discussed in sec. 2, see Plate 3h, i, j, k.

4. BOW MODEL WITH MIXED FRAMING

Initial buckling occurs in the sides at a load of 715 kN, Fig. 4. The collapse promotes redistribution of load to the decks, bottom and stringers which then fail. The collapse pattern of the sides is demonstrated by Plate 4b. The panels deflect outwards except those above mid-deck on each side. These modes are perfectly in accordance with the shape of the initial distortions caused by fabrication.

The stringers buckle away from the mid-deck while the decks and bottom all deflect towards stiffeners in the first stages of collapse.

The load declines to a minimum until the side hits the load plate and a secondary collapse is initiated in the upper half of the folds, Plate 4c. This event is accompanied by a load increase.

The local maximum at stage 2 is caused by collapse of the panels in the second field; first triggered in the decks and bottom then followed by the sides.

Several stringers are not capable of carrying the load and suffer local buckling. Further collapse is avoided due to load redistribution to adjacent cross-sections.

The subsequent sequence of collapse is not straight forward. The various panels do not fail simultaneously. Owing to greater material density decks and bottom are the first to fail. Several failures are just as well caused by distortion of boundaries as by load increase. Hence initiation of collapse needs not be accompanied by a significant load peak.

The load increase from stage 3 to stage 4 seems to be caused by collapse of one of the sides in the third field together with decks and bottom in the fourth field. Plate 4f shows that the side is distorted considerably beyond the third field.

The next load peak, stage 5 is associated with secondary collapse of the sides in the third field as well as initial collapse of the fifth field in decks and bottom.

From stage 6 the load rises steeply due to reduced compressibility in the vertical panels. Side panels fail at short intervals without being fully compressed, see Plate 4g, h at the end of test.

Further details about the compressed state is provided by Plate 4i, j, k. A nice example of an inextensional, outward symmetric collapse mode is observed in Plate 4i.

It is seen that the collapse mode mostly changes at plate intersections in deck/bottom while most side buckles go outward.

It is also apparent that the deformation zone grows faster around the centre bulkhead due to the limited compressibility of this area.

5. BOW MODEL WITH LONGITUDINAL STIFFENERS

The structural response is linear until the maximum load of 970 kN is reached, Fig. 5. The mode of collapse is local buckling of the side plating between longitudinals followed by tripping of the longitudinals. The buckling of the plates involves significant plastic effects.

From Plate 5b it is observed that failure occurs mostly towards the stiffeners. From the crude measurements of the initial deflections it is not possible to explain the different buckling modes. The welding imperfections go inwards between stiffeners. However, the influence from adjacent fields probably makes the failure sequence decisive.

First buckling is succeeded by a steep unloading curve, due to initiation of global collapse of the side plates with stiffeners. The deformations are especially concentrated towards the free edges of the panels while the zones around the midframe and mid-deck are significantly less affected. One of the side panels has a particular behaviour in the sense that the overall collapse is limited to the foremost part of the panel. Plate 5c belongs to stage 2 in the load diagram.

The collapse of decks and bottom progresses so as to comply with the deformations of the side plates.

A close view the deck corner is shown in Plate 5d. The mode of collapse resembles the basic folding mechanism discussed in Sec. 2.1. of DnV Report No. 83-0331. Longitudinals subjected to compression eventually trip but occasionally remain straight for large rotations.

The load rises slightly again as internal elements are squeezed together and parts of sides meets with the local plate. The side suffers a secondary collapse at stage 3 as illustrated by Plate 5e, and the load drops again. The continuing compression of the first field induces bending action with local buckles in the second field. As to further collapse of these panels the situation is more complex compared the buckling of the first field. The boundaries at the transverse frame is affected by previous deformations to

various degree. When the remaining undistorted parts of the first field come into contact with the load plate, 4 , compression forces are transferred directly into the sides. This is accompanied by a considerable load increase although the level of first buckling is not reached, 5. The collapse mode is composed of deformations on both sides of the frame, Plate 5f.

However, the panels have not yet reached the ultimate state. A secondary buckle is created at stage 6 . This is preceded by local buckling. The final deformations are visualized in Plate 5g at the end of test.

Plate 5h-j show the final deformations of the models. Zones of extensive local plastification are mixed up with more undisturbed areas bounded by folds and wrinkles. The skew orientation of the stem is distinct. This is due to the unsymmetry in the initial deflection modes.

The inside view demonstrates the large rotations of the longitudinals. Several longitudinals have tripped but some have remained straight until fracture. On the compression side local buckling has determined the plastic deformation mode.

6. RAKED BOW MODEL

The first peak 1 in the load-diagram is due to local buckling, Fig. 6. Due to the small contact area several folds are created in the first field as illustrated by Plate 6b. Overall interframe buckling does not occur until the second field, Plate 6c. The regular angle deformation at the deck corner is noticed.

The load-curve is remarkably smooth and increases roughly speaking proportional with the indentation. The various fields collapse consecutively. Plate 6d-f serve to illustrate the progress of indentation and relate to stage 2 - 4 respectively.

The course of deformation shows generally the same features observed in the previous tests. At the deck-side intersections assymmetric and symmetric inextensional collapse modes are frequently encountered, see Plate 6g.

At stage 5 the decks are almost fully compressed and the load starts to rise steeply. Plate 6h shows the model at the termination of the test.

A vertical - and a horizontal section are shown in Plate 6i,j. It appears that the folds are much more compressed in the decks compared with the sides due to higher material density.

Plate 6k illustrates the complex deformations at the intersection between the mid-deck and the longitudinal girder.

7. STERN IMPACTS

The following comments are related to the static test.

The local curve, Fig. 7, is remarkably smooth but some jumps are observed. Initially, elastic and elasto-plastic effects predominate the response until buckling of the centre bulkhead occurs at 1 . Thereafter the contact area increases until the ringstiffeners on each side of the centre bulkhead become activated. This causes a pronounced increase of the load. By further deformation the same phenomenon takes place at 2 as the side bulkheads start to deform. At this stage the validity of the model strictly ceases, but it is decided to run the test further.

The model undergoes gross deformations with a steady increase of the load until several fractures develop at the point of maximum load. By further deformation the load declines rapidly.

The deformation modes are shown in Plate 7.

Plate 7b,c originating from stage 2 and 3 in the deformation history, demonstrates how the curved stern section transforms into a new curved panel adopting the curvature of the indenter.

Plate 7d gives an internal view of the model at stage 3 . The shear buckles of the ringstiffeners as well as the first buckle of the centre bulkhead are visible. Plate 7e,f describe the situation just before stage 4 . The model is distorted heavily but continuity is still maintained. The different restraint from the bulkheads and the ring-stiffeners on the deformation of the shell plate is distinct.

The test is finished at a total indentation of δ_o = 185 mm which is far beyond the validity range for the impact model.

The final deformed configuration is visualized in Plate 7g.

The deformation pattern is further demonstrated by the transverse sectional cut in Plate 7h.

8. BOW/BRACING IMPACT. MEDIUM STRENGTH BOW

Initially, the thinner tube is used to simulate the bracing. The location of contact is midway between the centre deck and adjacent stringer, as illustrated by Plate 8b.

During the first loading sequence the tube suffers the major part of the deformations while the bow remains virtually undamaged.

In the next run the damaged tube is replaced by the thicker tube. This time the bow fails by local buckling at the point of contact, Plate 8c, at a load level of approximately 40 kN (stage 1 in the load diagram, Fig. 8).

Failure is succeeded by an intermediate phase of unloading but the load regains shortly afterwards as membrane forces become activated in the skin and stem plate, confer Plate 8d from stage 2 .

The subsequent deformations in the skin plates proceed asymmetrically as demonstrated by Plate 8e, f (stage 3).

At this stage the load is reduced slightly due to fracture of the stem plate. The cracks grow continuously into the skin plates adjacent to the centre deck. At the stringers crack initiation is not experienced since the surrounding structure is not capable of supporting membrane forces. Instead, the end-deck is pulled towards the contact zone, see Plate 8g, related to stage 4 . The associated load peak is caused by the resistance to penetration of the first transverse frame, Plate 8h.

By further penetration the load grows slowly. This is mainly caused by increasing roll up of the deck while the crack work probably yields a constant load contribution. Each load peak is associated with penetration of a transverse frame.

Plate 8j, k shows an external and internal view of the deformations as the test is terminated.

9. BOW/BRACING IMPACT. STRONG BOW

In this test the thicker tube is positioned beneath the mid-deck as shown in Plate 9b. A first run is conducted with a tube span of 100 mm.

The tube starts to deform without penetrating the stem. However, as the tube ovalizes the contact area splits into two regions which move away from the deck zone. Thus very local buckles are triggered in the adjacent skin plates at a load of 160 kN, see Plate 9c. The stem is not deformed further due to internal load-redistribution. Since the resistance of the tube to beam deformation is exhausted at the same load level the span is reduced to 360 mm.

A practical collapse of the bow does not occur until stage 1 in the load-diagram, Fig. 9, at a load of 200 kN.

Subsequent to failure unloading occurs, but the loads starts rising again as membrane forces develop in the skin plates. The shape of the folds are illustrated by Plate 9d,e taken at stage 2 and 3 respectively.

Plate 9f,g visualizes the extent of deformations at stage 4 . The total indentation equals 60 mm but from the internal view it appears that the stem web has not tripped yet due to its low slenderness.

To avoid beam collapse the span of the tube is reduced further to 210 mm before continuing the test. The subsequent load peak is probably caused by failure of the stem web on the compression side. Now the tube penetrates the bow at an almost constant load level. The local peaks are associated collapse of side panels or internal elements. The deformation zone expands steadily thus activating more and more panels. This is demonstrated by Plate 9h,i,j,k originating from stage 5 , 6 , 7 and 8 respectively. It is observed that roll up is not avoided at late stages of deformation.

10. ELLIPTICAL CYLINDER

Initially the model behaves elastically until the shell becomes instable at stage 1 in the load-displacement diagram, Fig. 10. The sequence of collapse is first buckling of the panels adjacent to the top and bottom generator where the panel width is greater, followed by the centre regions and finally by the stringers. The mode of collapse is axisymmetrical as demonstrated by Plate 10b.

The course of the load deformation curve can be explained by arguments parallel to those of bow model test. Each peak is associated with the formation of a fold around the circumference. Due to shape disturbances from collapsed regions as well as initial distortions the peak loads vary somewhat. The strong midframe reduces this effect and here a peak load of the same level as the first peak load is obtained. The regularity of the load curve is striking. The average load during compression of one field deviates at maximum 8% from the total average load.

The consecutive development of plastic mechanisms is demonstrated by Plate 16c, d from stage 2 and 3 respectively.

The deformed termination state, stage 4 , is illustrated by the external view, Plate 10e, and the longitudinal cut Plate 10f. Most waves go outwards but inward folds are occasionally found in the skin. It is observed that the stringers fold regularly. Normally the fold direction is asymmetric in two consecutive fields.

The deformation pattern at the junction between the skin and stringers resembles those occurring in the bow models. The configuration is largely determined by the collapse mode of the stringers in the sense that the stringers and one part of the skin plate tend to create a regular angle-type mechanism. The adjacent skin plate undergoes considerable membrane stretching in order to maintain continuity.

The tension work would be kept to a minimum if the shell deflects inwards. However, the plastic collapse mode is predetermined by the initial buckling mode which generally goes outwards.

It is also evident from the figures that several T-sections deform symmetrically with large shape distortions of the stringers.

11. ELLIPTICAL CYLINDER WITH DECK AND BULKHEAD

The present test is run in two steps. In the first run the internal elements (bulkhead/deck) are supported at one end, only. In the second run support is given at both ends.

Initial buckling occurs almost simultaneously in the skin adjacent to the bottom - top generator at both ends, Plate 11b. Owing to redistribution of forces to the deck and the bulkhead the deformations cease at one end while folds are developed through distortion of edges at the unsupported end. As can be seen in Fig. 11, stage 1 the load remains almost constant during this process. The subsequent load-displacement relationship can be explained in the same manner as for the previous cylinder test. Due to the lack of support, the folding of the internal elements is not fully completed so that they are partiality squeezed out of the model.

After the collapse of the first half of the model,the bulkhead and deck are compressed fully in a separate run and the test continues in phase 2 with rigid support at both ends.

The different edge conditions have a distinct influence on the shape of the load curve which becomes almost uniform. Neither the peaks nor the minima attain the values of the first phase. The reason for this is that the deformations in the internal members progress faster than in the skin due to a lower degree of compressibility. They also disturb the boundaries of skin plates which have not failed yet. Thus the collapse load of the skin plates is reduced drastically.

The measured average crushing loads of the two phases differ little (830 kN versus 860 kN). Thus the reduced compression of internal members are counteracted by a more complete and regular folding of the skin plates.

The final deformation are visualized by Plage 11c - f.

The particular mechanisms described in the previous test can be studied in the close-up (Plate 11d). The ductility of the material is striking since few samples of fractures can be observed.

The cross-sectional cut shows that several stiffeners have twisted. This is not amazing considering the great thickness of the plate.

12. ELLIPTICAL CYLINDER WITH LONGITUDINAL STIFFENERS

The test is run in two steps. Owing to limited capacity of the ordinary jack initial buckling is run in a manually controlled jack with a maximum capacity of 5000 kN.

The end shortening is measured manually by means of a dial indicator. The first peak in the load diagram, Fig. 12, is reached when local buckles occur in the skin between stiffeners at each end of the model, Plate 12b. Due to low slenderness the failure implies considerable plasticity effects. The load remains almost constant until the stiffeners collapse, followed by steep unloading as the deformations proceeds into the plastic region. The situation at the end of the first phase is shown in Plate 12c. Plate 12d demonstrates the buckling mode. The Poisson effect promotes outwards folds in the skin, while the next wave goes inwards. In the deck and bulkhead asymmetric folds of similar length are generated.

The stiffeners distorts to a large extent by developing local mechanisms but overall tripping of longitudinals is occasionally found.

Beyond stage 2 the model is positioned in the usual test rig. By further compression the model collapses in a series of local folds. Since each buckle is formed at different points of time the load remains almost constant. Plate 12e, f demonstrate the deformation pattern at stage 3 and 4 respectively.

The midframe which remains relatively intact, produces significant load increase as the compression capability of the first field is exhausted. However, the load does not attain the same level as in the fist phase. Plate 12g (stage 5) shows that the failure mode is similar to that of the first buckling with local waves close to the mid-frame.

The subsequent deformations deviate from those observed during the first phase as a mixture of local and interframe folds emerge, Plate 12h. This brings about an oscillating crushing load with a slightly lower mean level.

The final deformations at end of test, stage 6 , are shown in Plate 12i,j. Transition zones which are created in order to overcome mode incompatibility at stiffeners, are visualized. They harmonize very well with the deformation modes assumed for T-sections.

The view of the longitudinal section demonstrates further the different buckling modes in the first and second field.

13. CONICAL BULB

The present specimen consists in fact of two different models. In the frontal part of the model, a deck and a bulkhead are included, while in the second part stringers only are used for longitudinal stiffening. During compression of the first half rigid support of the bulkhead and deck is provided by a stiff cruciform rig.

Similar to other models with transverse framing the bulb collapses by folding of consecutive regions starting in the front. Each fold is associated with a peak load and the average load increases steadily in proportion to the increase of cross-sectional area,Fig. 13. Due to disturbances from previously collapsed fields the maximum load does not reach the level of initial buckling. Correspondingto the observations made with the wedge shaped bow model a so-called secondary collapse occurs when the skin hits the load plate. The first run is terminated when the frontal half is fully compressed. This prevents further development of an inversion type of mechanism.

In the second phase the internal support is removed. As anticipated the lack of internal panels reduces the mean load considerably but the shape of the curve corresponds.

The series of deformation is presented in Plate 13b-f (stage 1 - 3). The final deformations are shown in Plate 13f,g. It appears that the conical shape has facilitated a thorough compression of the model as the folds have been pushed into the structure behind.

Due to the low stiffness of the ringstiffeners these are distorted significantly thus reducing the buckling loads for large indentations.

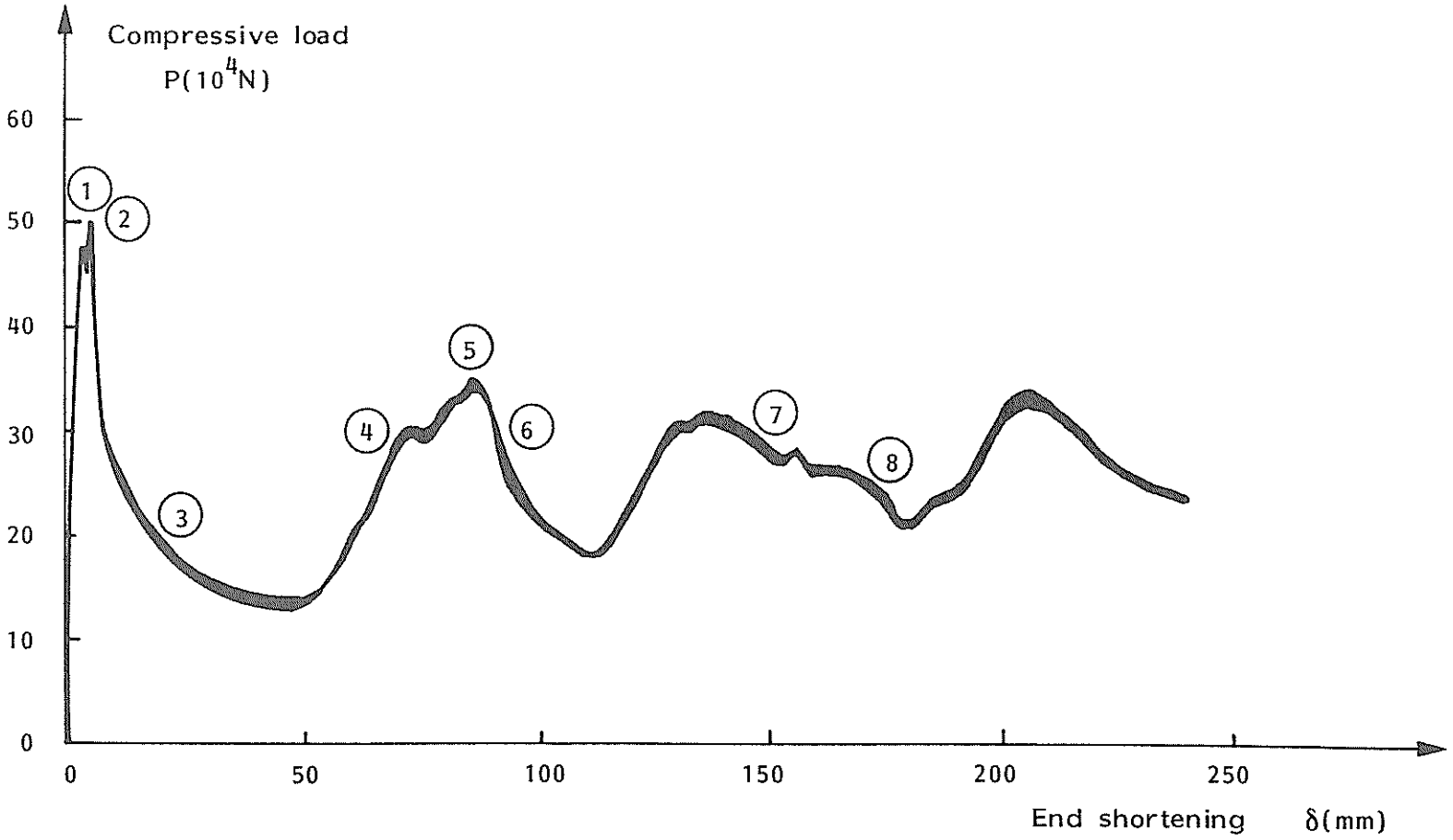

Figure 1 Load displacement curve for box-shaped model (Model no. 1)

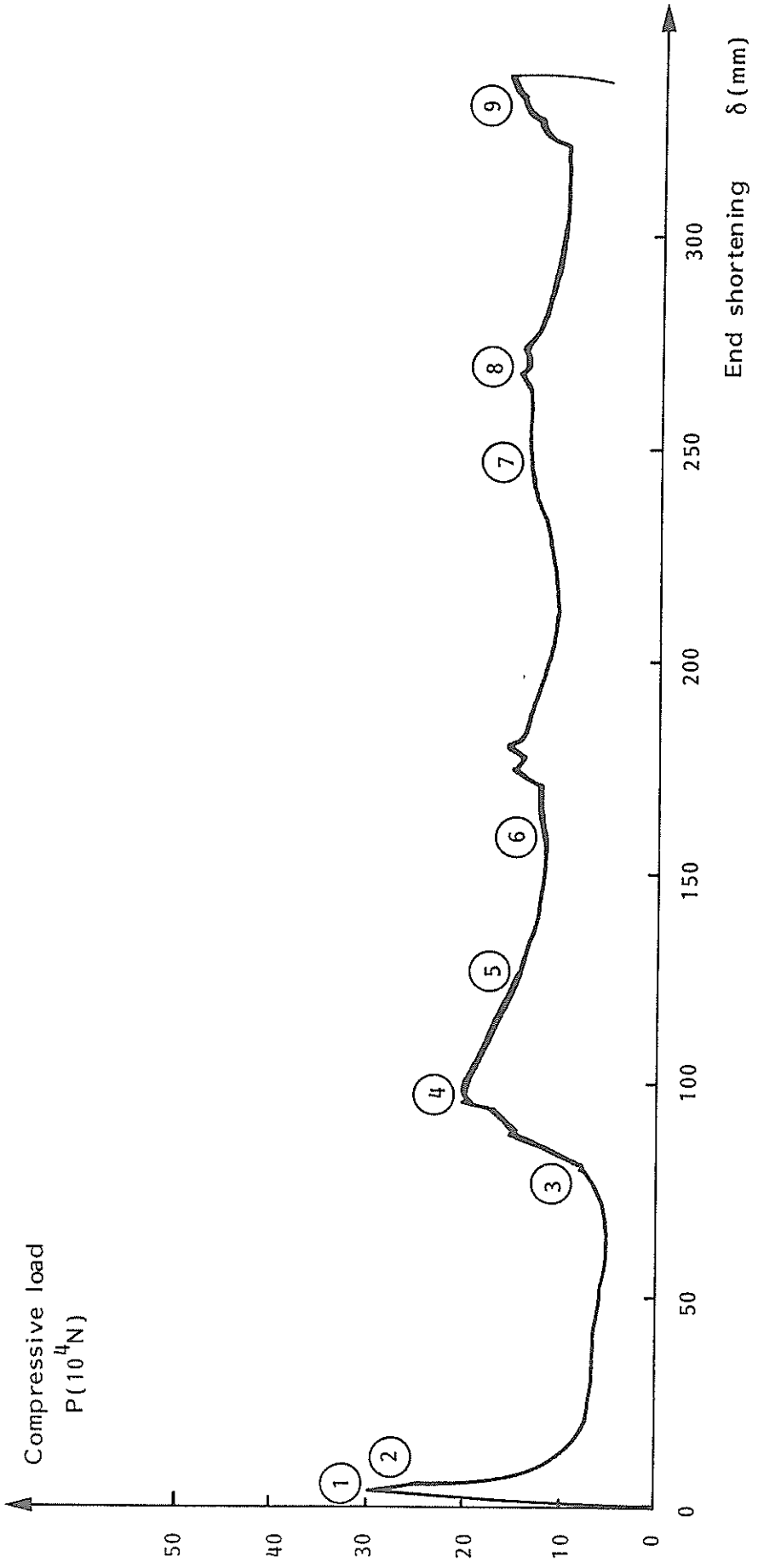

Figure 2 Load displacement curve for bow model with transverse frames (Model no. 2)

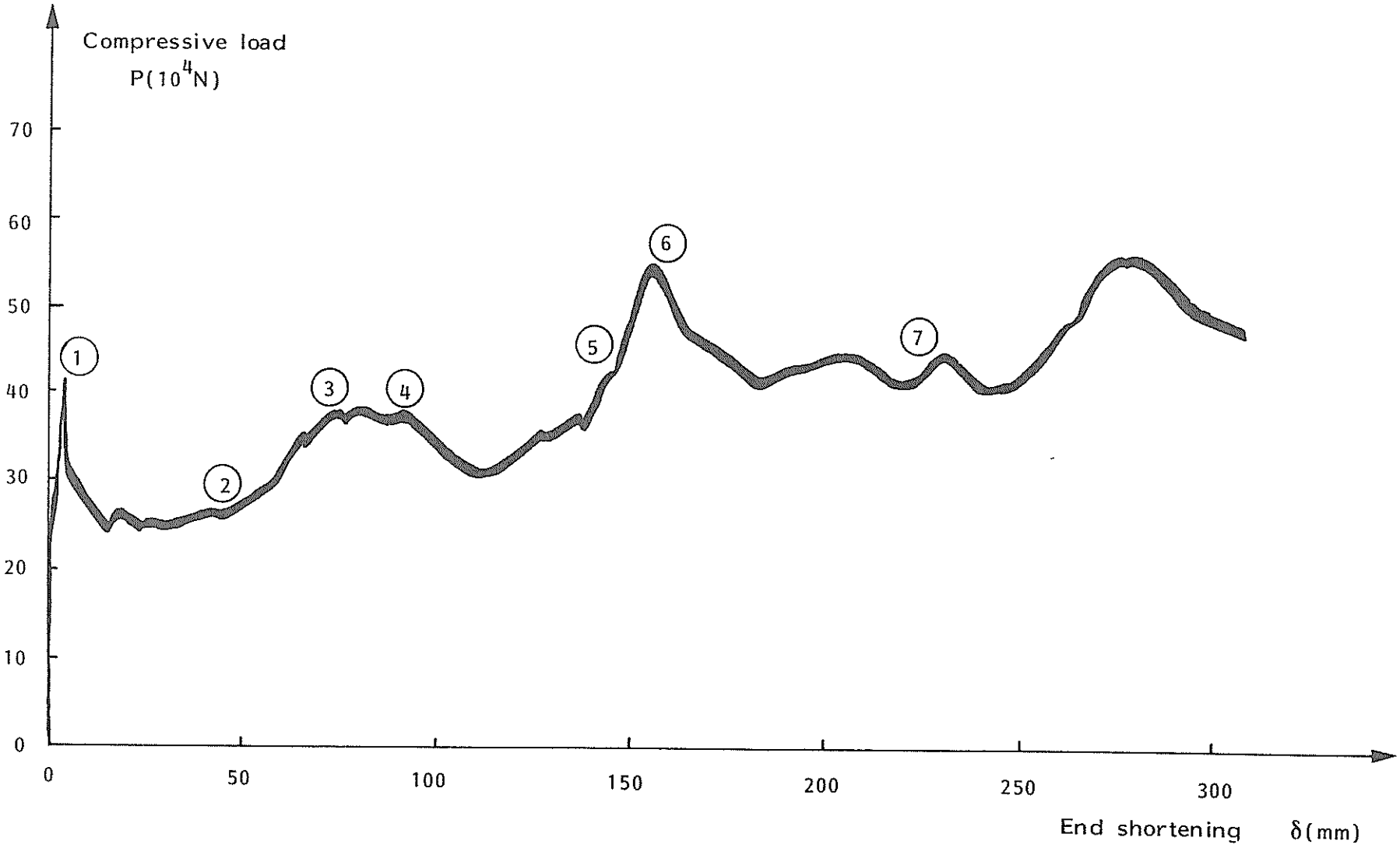

Figure 3 *Load displacement curve for bow model with transverse frames, deck and a longitudinal bulkhead (Model no. 3)*

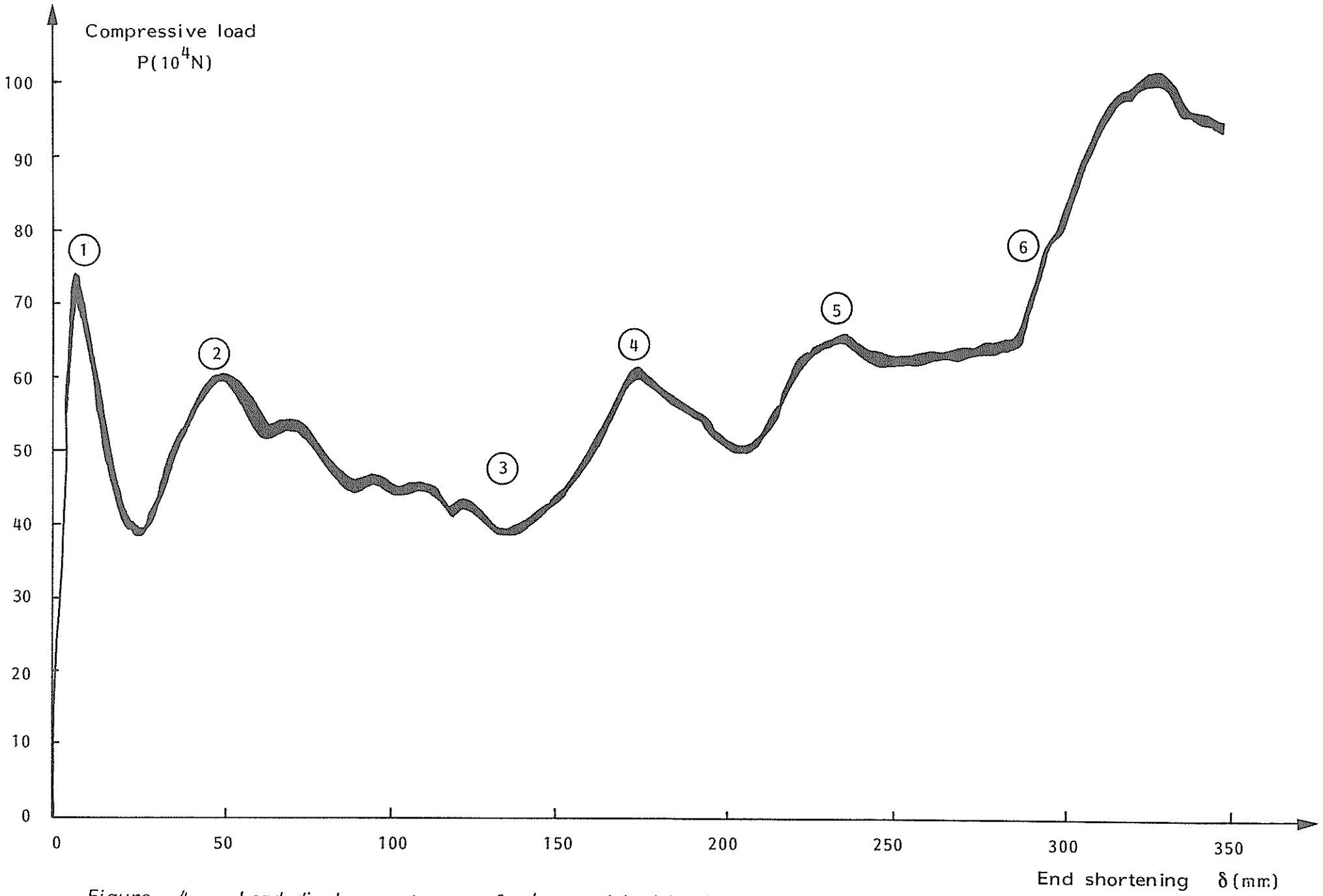

Figure 4 Load displacement curve for bow model with mixed framing (Model no. 4)

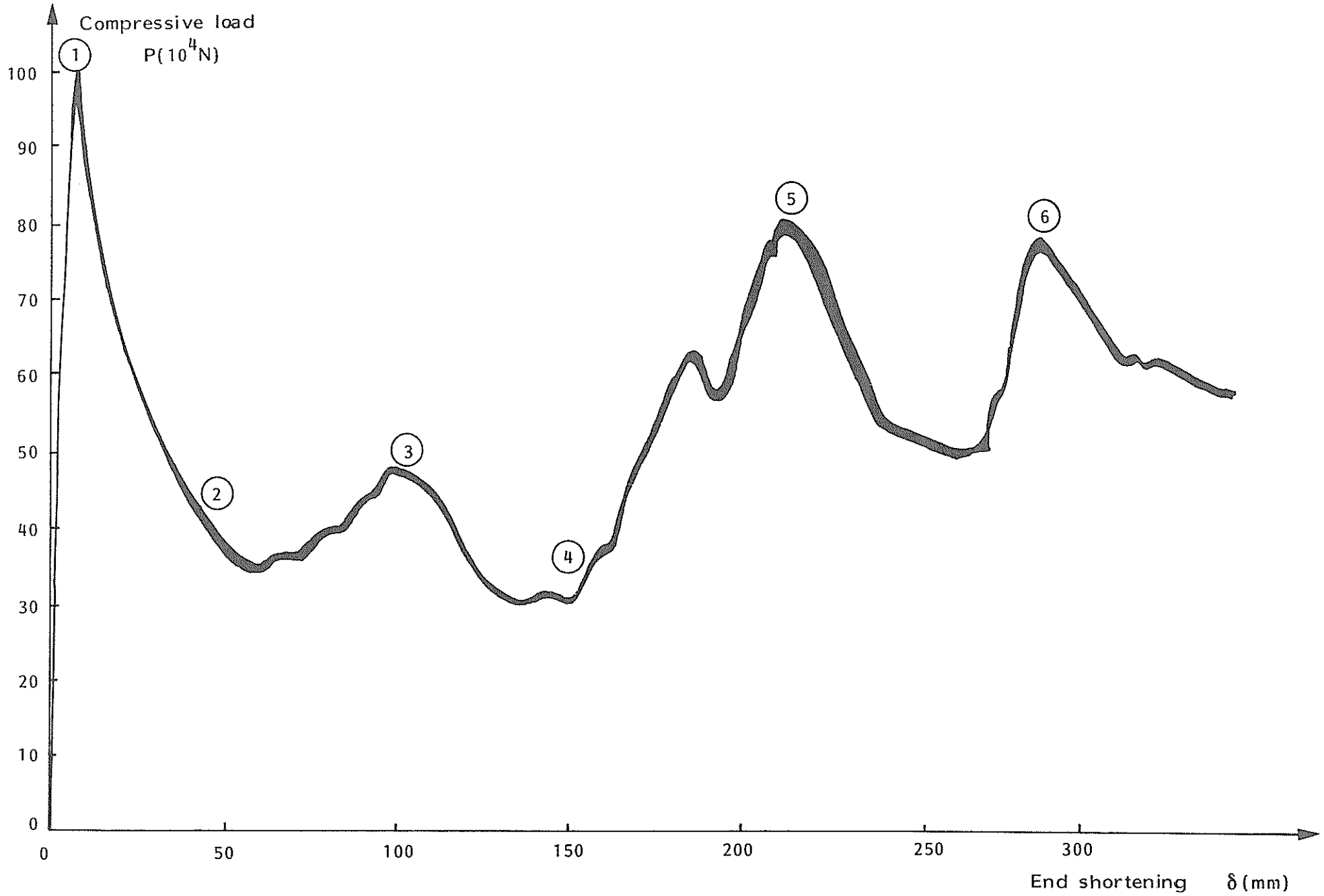

Figure 5 Load displacement curve for bow model with longitudinal stiffeners (model no 5)

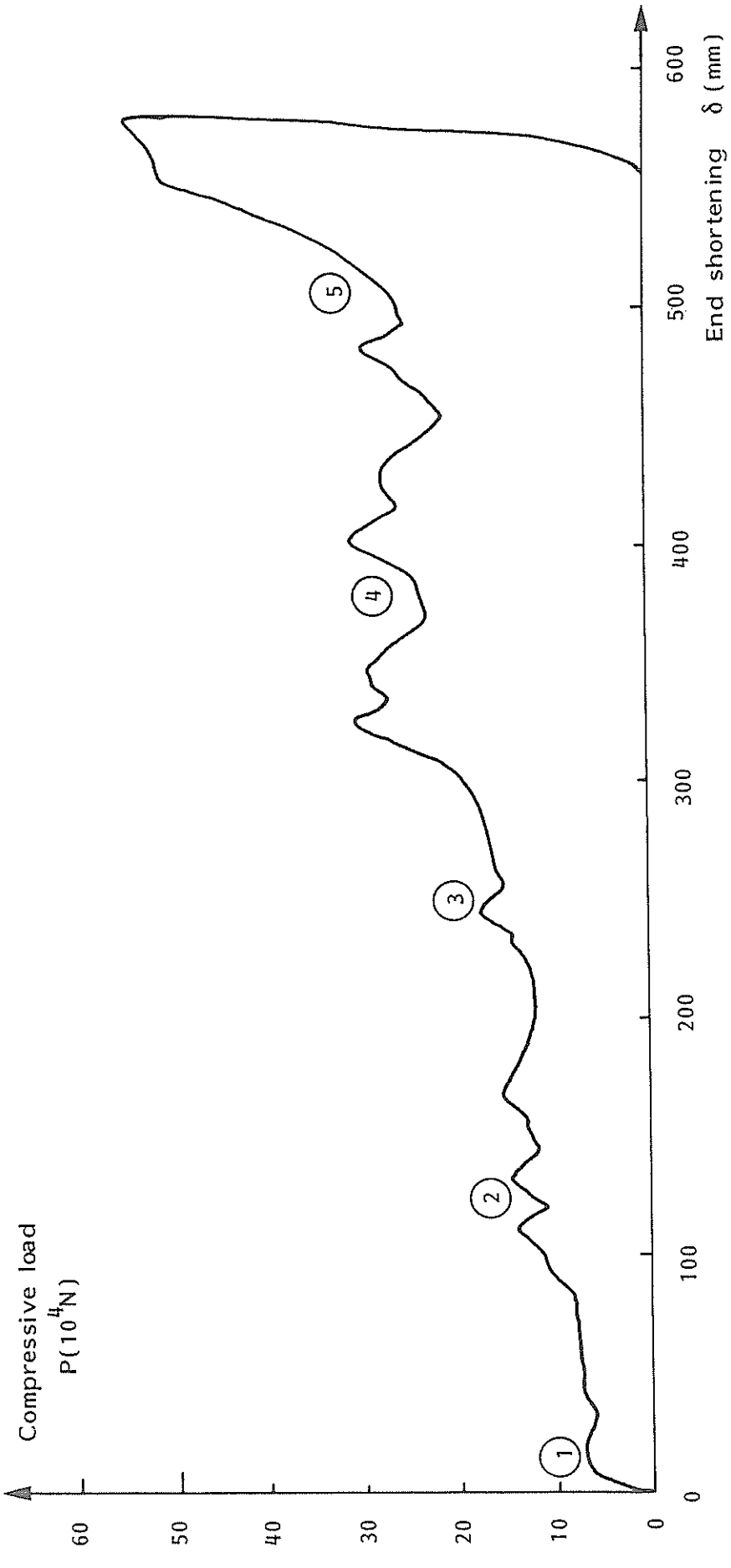

Figure 6 Load displacement curve for raked bow model (Model no.6)

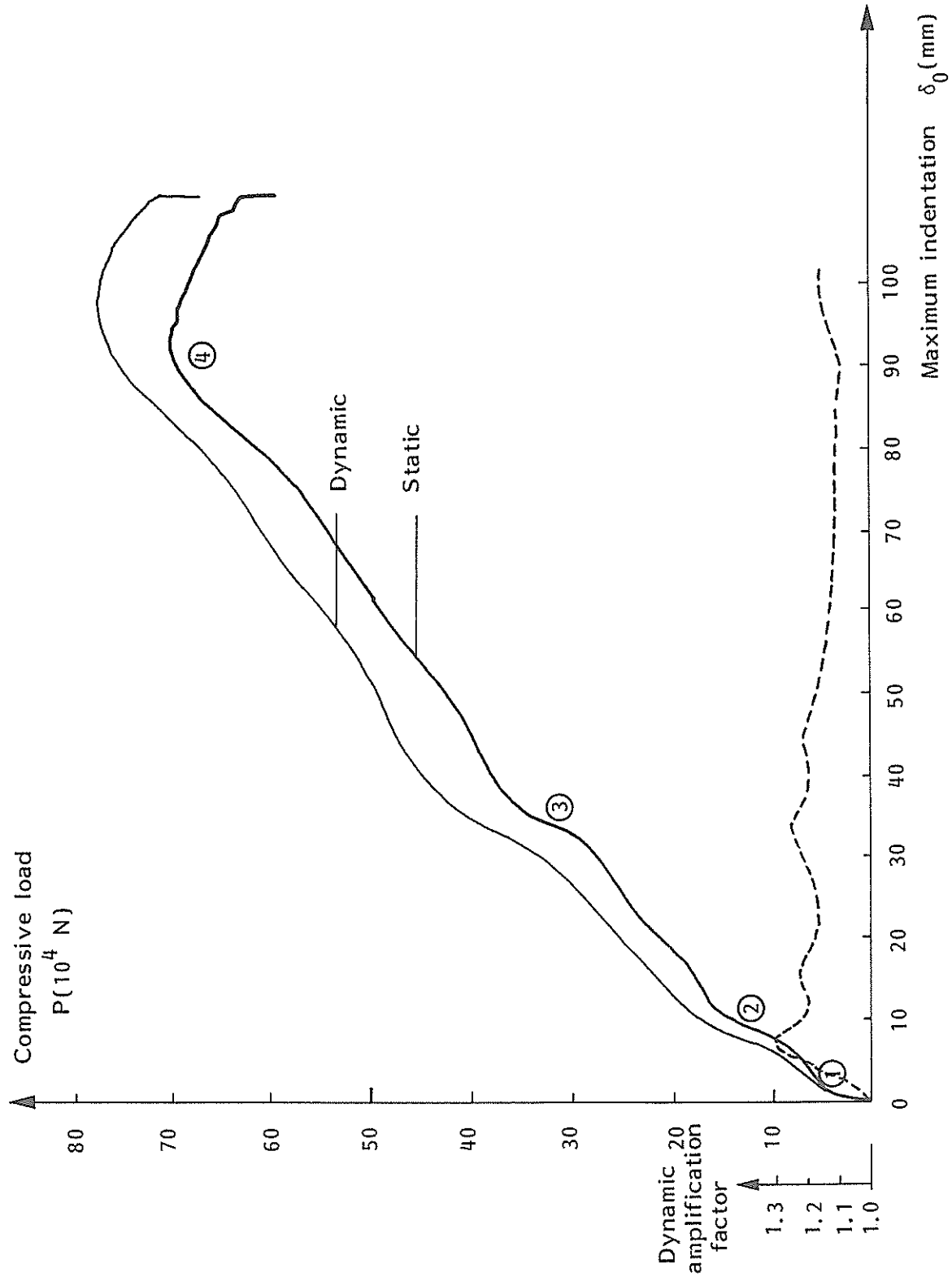

Figure 7 Load versus indentation for stern models

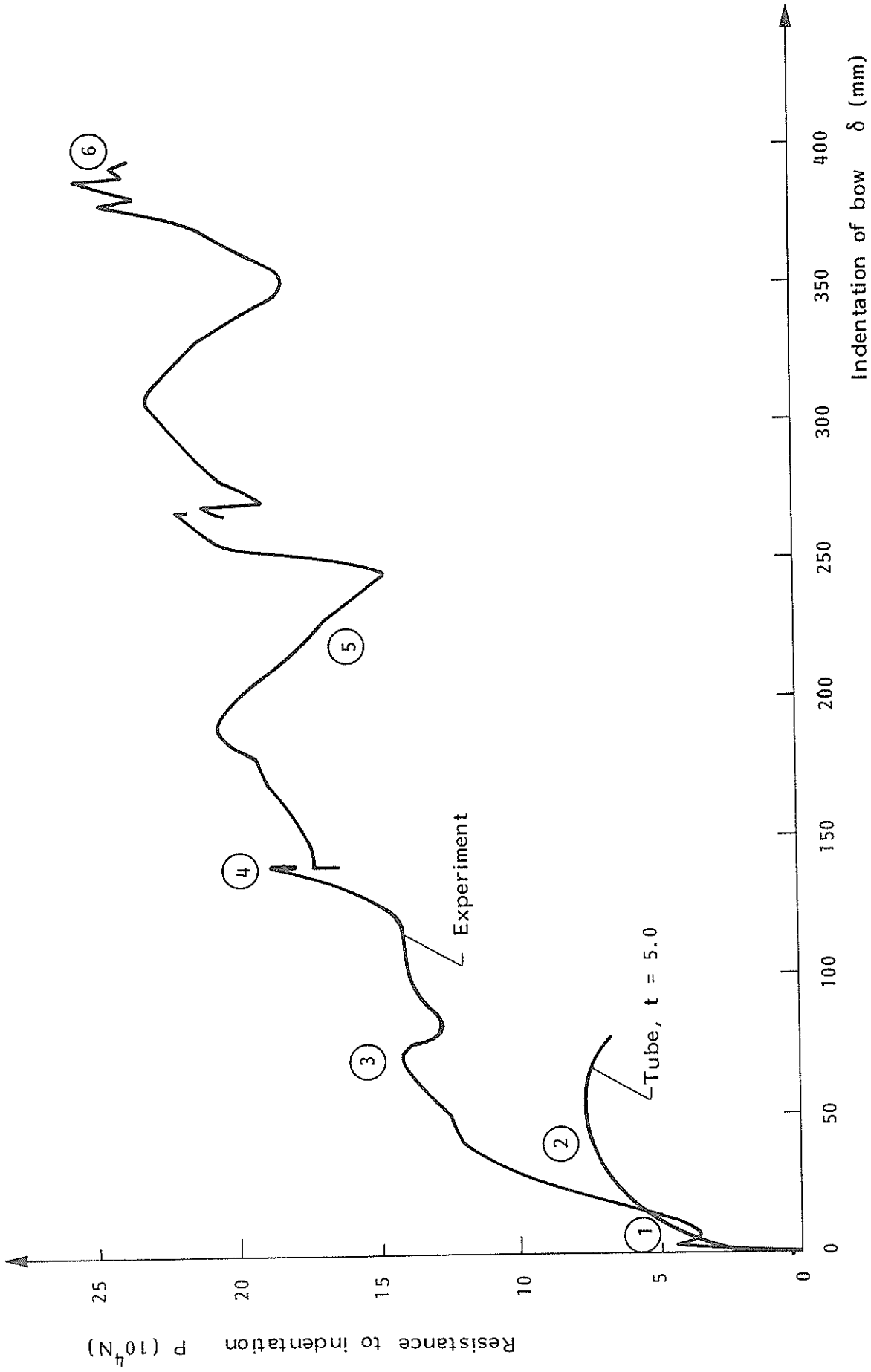

Figure 8 Load versus bracing indentation for medium strength stem

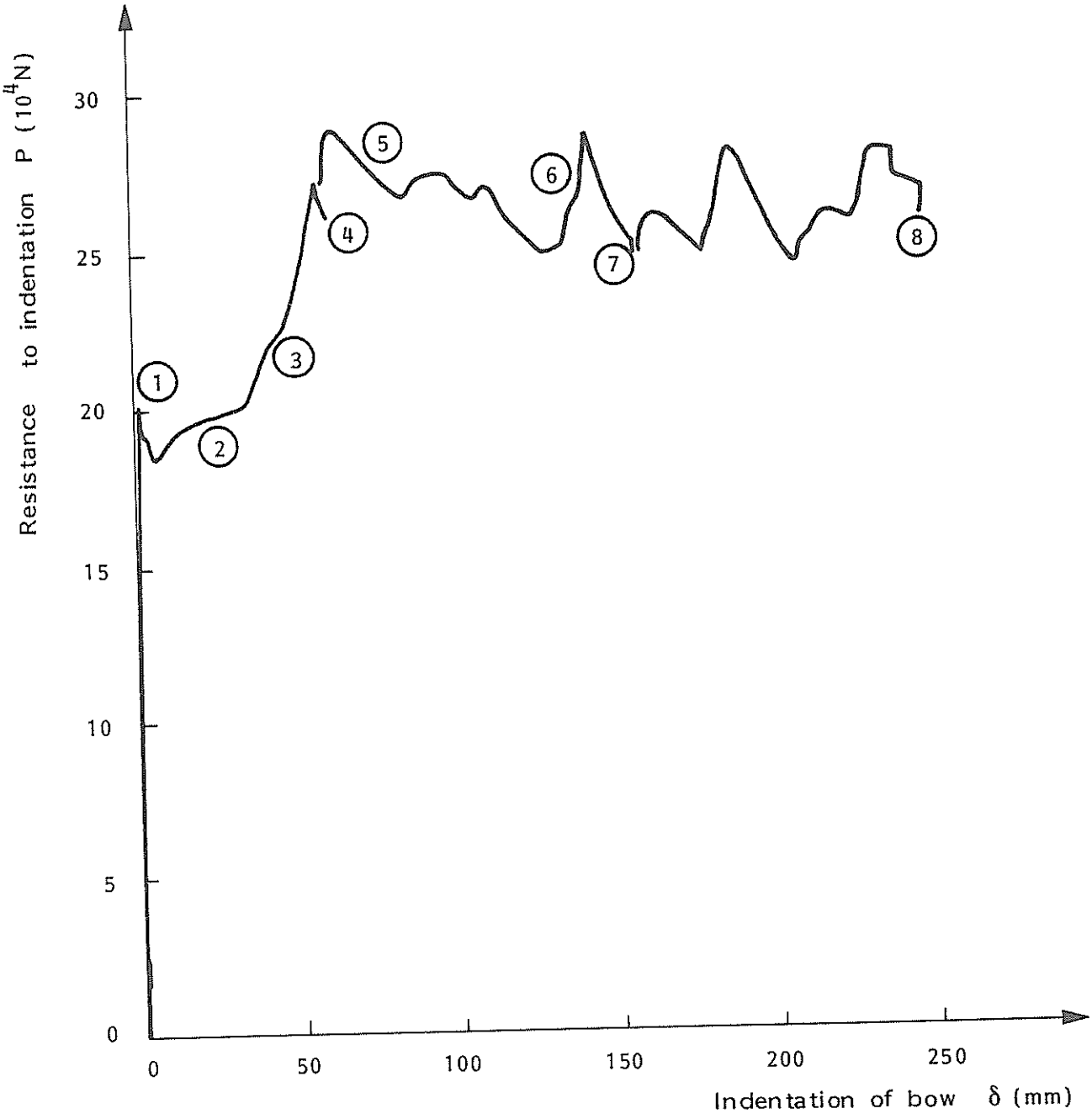

Figure 9 Load versus bracing indentation for strong stem

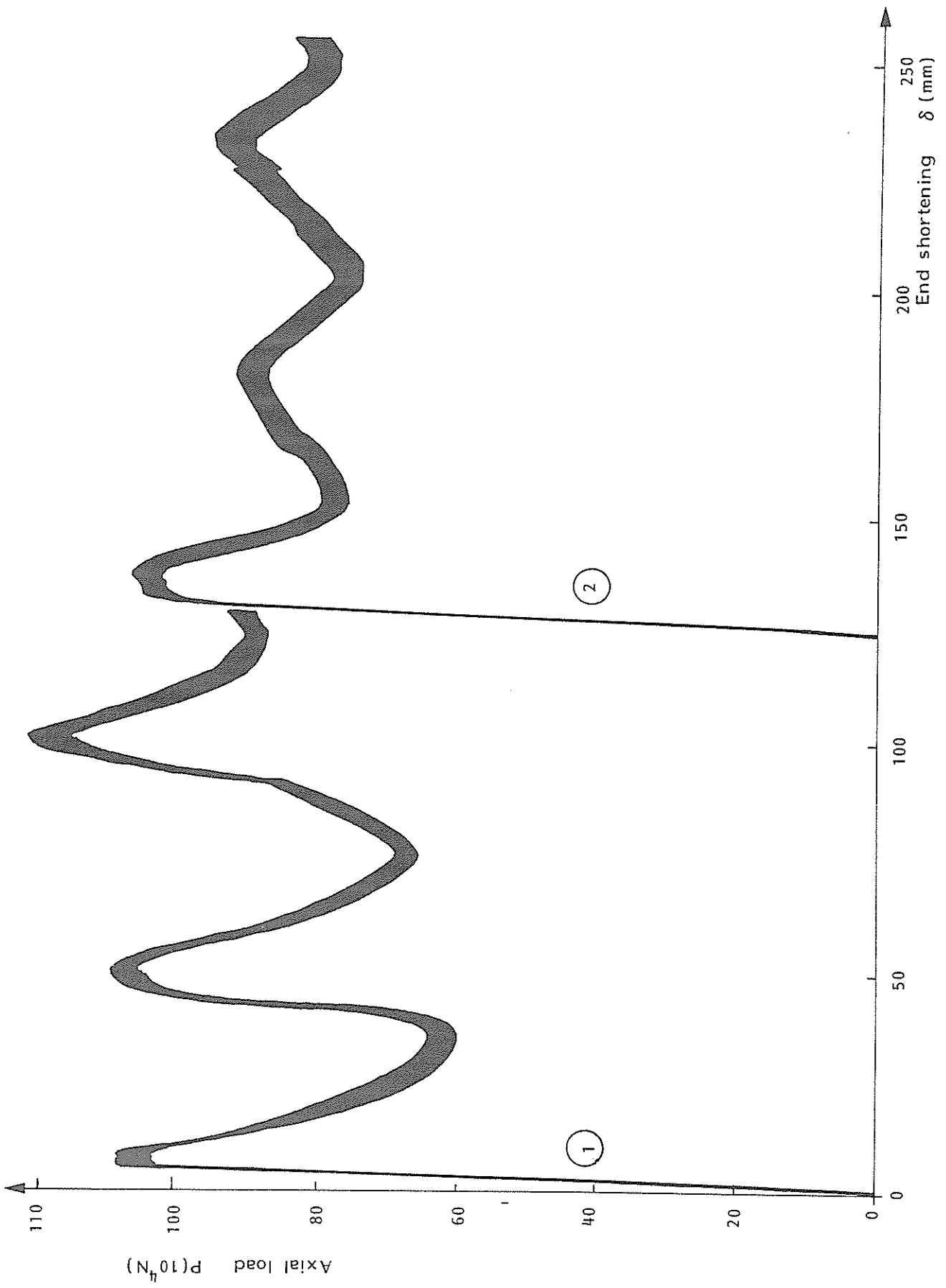

Figure 11 Load displacement curve for elliptical cylinder with deck and bulkhead

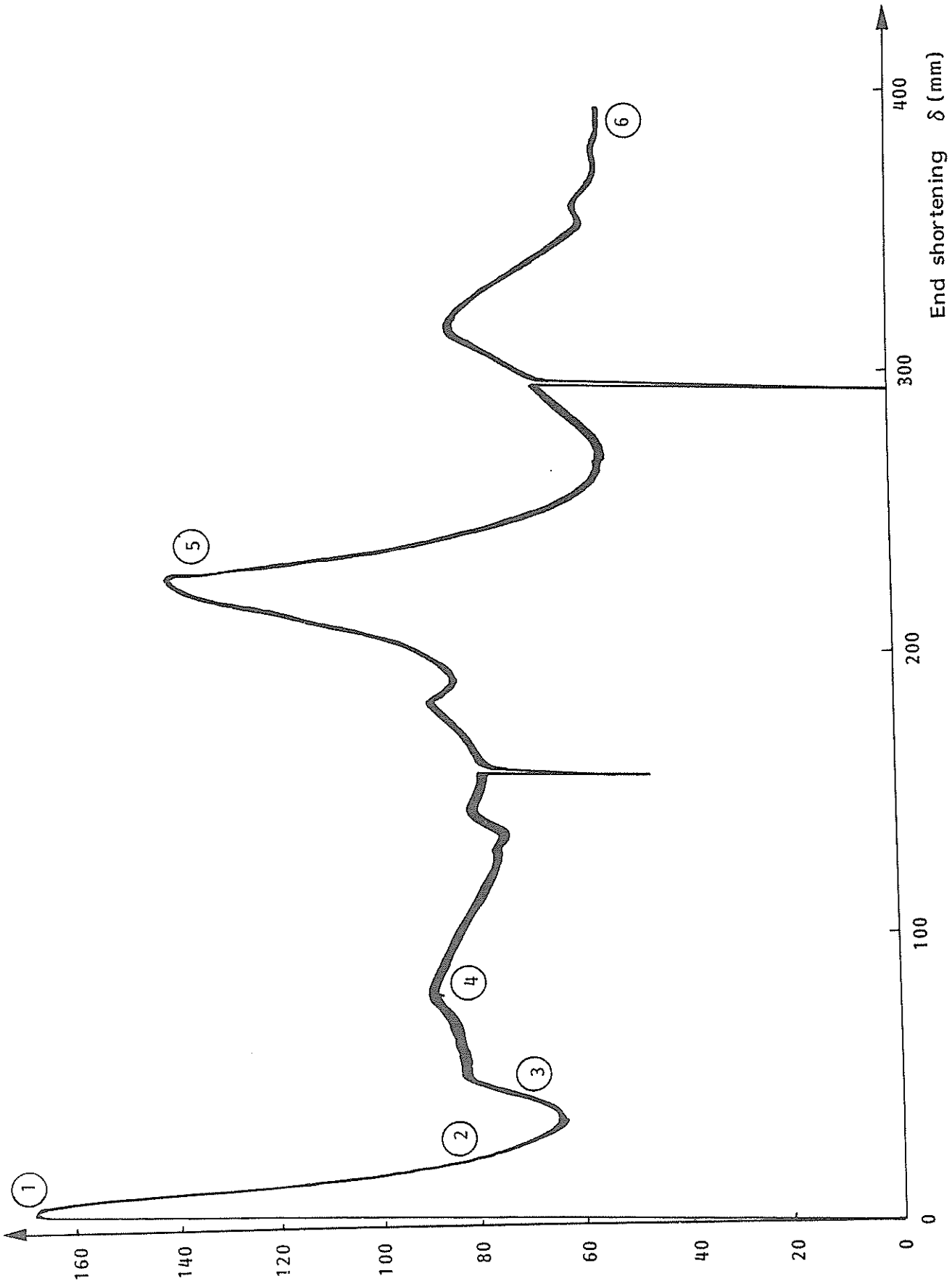

Figure 12 Load-displacement curve for elliptical cylinder with longitudinal stiffeners

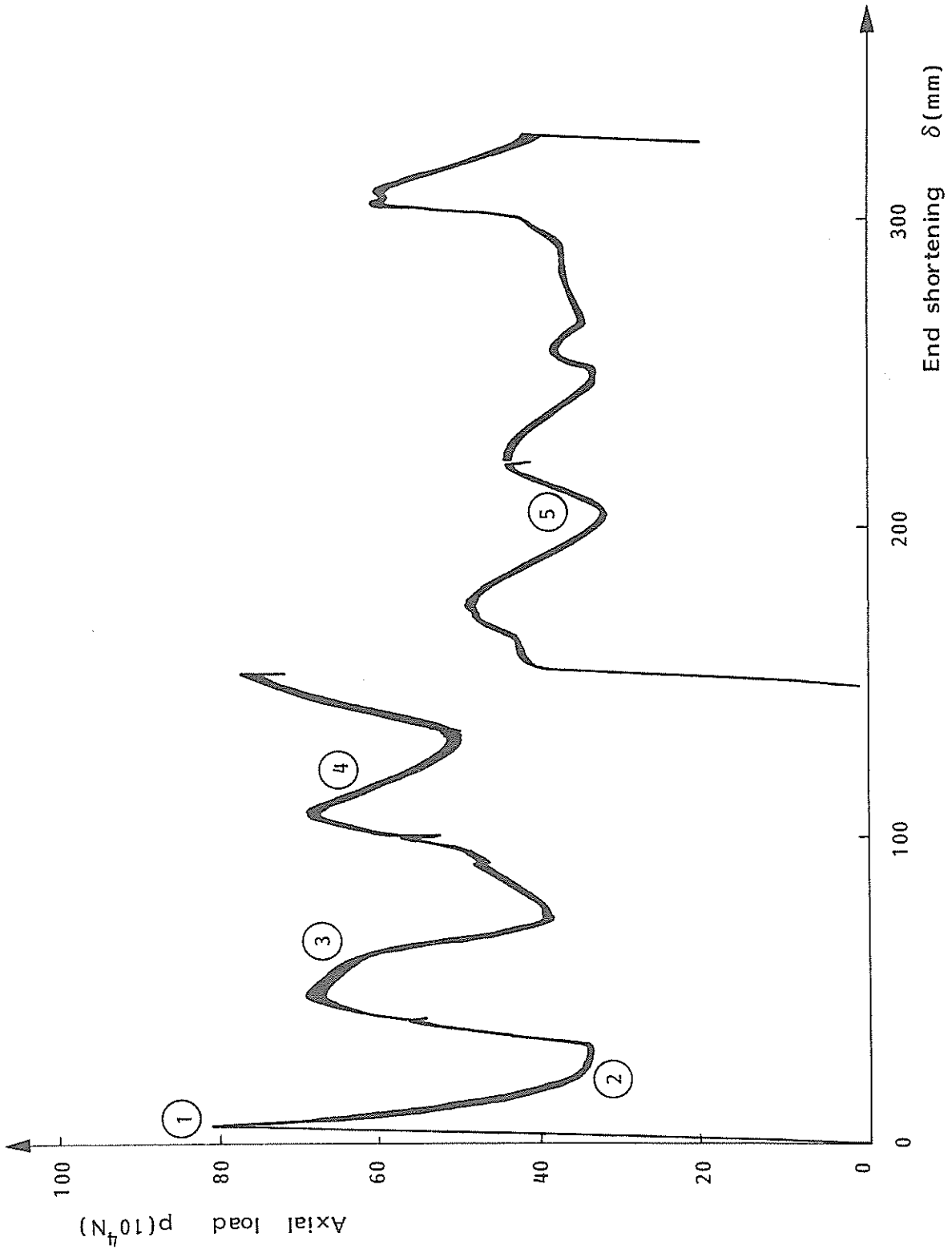

Figure 13 Load displacment curve for conical model